Author:
Young, Nicky

Title:
Elucidating Shallow Volcanic Structures and Dynamics using Geophysics and Numerical Modelling

Elucidating Shallow Volcanic Structures and Dynamics using Geophysics and Numerical Modelling

Nicky K. Young

Supervisors: Joachim Gottsmann & James Wookey

A dissertation submitted to the University of Bristol in accordance with the requirements for award of the degree of Doctor of Philosophy in the Faculty of Science

School of Earth Sciences

March 6, 2019

Word Count:

38096

ABSTRACT

Our understanding of volcano dynamics and structures is frequently measured by how accurately we can model and reproduce volcanic signals. However, both forward and inverse models of volcano movement and mass distributions are inherently non-unique, which means that the best-fit model may not necessarily be the closest to reality. It is imperative that we consider models of volcanoes in the context of plausible geological conditions and integrate these conditions as limiting constraints. With the computing power and sophistication of numerical modeling software available today, options for exploring volcanic processes and structures are endless. I focus on three different volcano types (restless caldera, explosive stratovolcano and persistently active complex volcano) undergoing contrasting activity. I use the most suitable available data to numerically model the mechanics shallow crust at each volcano and retrieve details of fluid distributions and subsurface structures.

First, I process and invert Bouguer gravity data at Campi Flegrei caldera, which has been experiencing restless behaviour symptomatic of hydrothermal fluid perturbations. Using numerical modelling software GROWTH2.0 I retrieve the subsurface locations of low gravity anomalies within the caldera, and show that their position is related to shallow crustal structure. Next, I use volumetric strain data from a magmatic explosion at Soufrière Hills Volcano to investigate conduit dynamics and the shallow structure of Montserrat, through progressively more complicated 2D axisymmetric and 3D models. Collectively, these models demonstrate that the shape of the island's surface and internal heterogeneities, including a weakened halo around the conduit and stiff relict volcanic core, have a quantifiable impact on strain partitioning within the shallow crust and are necessary to reproduce the data at strain benchmarks during the eruption. Migration of this work from 2D axisymmetric to 3D also highlights that the conduit at Soufrière Hills Volcano cannot be cylindrical, with implications for magma flow dynamics both here and at other volcanoes. Lastly, at Masaya Volcano I use InSAR data to find the source of deformation during a phreatic event and reconstruct a joint magmatic and hydrothermal explosion instigator.

The results highlight that shallow structures such as faults and mechanical heterogeneity are key to strain partitioning in the shallow crust and thus the storage of fluid, both magmatic and hydrothermal.

Author's Declaration

I declare that the work in this dissertation was carried out in accordance with the requirements of the University's Regulations and Code of Practice for Research Degree Programmes and that it has not been submitted for any other academic award. Except where indicated by specific reference in the text, the work is the candidate's own work. Work done in collaboration with, or with the assistance of, others, is indicated as such. Any views expressed in the dissertation are those of the author.

.....

Nicky K. Young

March 6, 2019

Acknowledgments

I could not have finished this PhD without the help and encouragement I received from my supervisors, family and friends and accordingly, thanks are in order.

I wish to thank Jo Gottsmann for taking me on as a Masters student many years ago and encouraging my fascination with volcano geophysics - and then for taking me on again for this PhD. I have had many wonderful experiences during the last four years, which would not have been possible without your support. My grateful thanks are also due to my second supervisor, James Wookey, for his support, advice, and proof-reading; it was invaluable. James Hickey also deserves my thanks for always being willing to share his time and COMSOL knowledge.

My parents deserve my endless love and gratitude; their support and encouragement helped me through the infamous 'valley of sh*t' phase of the PhD and I cannot thank them enough for it. I also thank my brother James for thanking me in his PhD acknowledgements; as is only right.

I conservatively estimate that I have shared approximately 3000 cups of tea with my wonderful office mates, Becky, Ery, Keri, Ryan, Serginio and Neil. It is rare to find co-workers who also become close friends and I will miss you all terribly when we go our new exciting ways. Thank you for spending the last four years with me creating such wonderful memories. Thank you in particular to Becky for endlessly patient proof-reading.

I must thank a few stand-out individuals who have listened to my endless gripes about the trials and tribulations of PhD life. Emily, who went through the same journey 6 months ahead and came for countless tea breaks and walks with me, thank you for keeping me sane and reminding me it will be ok at all times. Graham, for always being there to listen, and for rejuvenating take-out and movie nights - I owe you. Jean and Lexi, whose hospitality I shamelessly abuse, for being my haven when I needed to escape the PhD bubble and be looked after, thank you so much. Chanelle, who made my year in Halls of Residence so much more enjoyable than I could have ever imagined, thank you for always being there for hang-outs and chats.

I cannot finish without thanking Mary Benton, who has been a stalwart presence and a source of advice and encouragement throughout my entire time in this department. Her belief in me started me on this Bristol journey, and I will always be thankful for that.

On a more general note I would like to thank the volcanology and geophysics groups of Bristol University. The endless supplies of biscuits and tea involved were fundamental to PhD completion and I cannot tell you all how much I have enjoyed all our conversations, both science and fiction-based. The vibrant social aspects of my research groups at Bristol have been highlights of my time here; it would not have been the same without you all.

Finally, I would like to dedicate this thesis to my Grandfather Roger Sorenson, who together with the assistance of his best friend and geologist Ron Wilden has always supported and encouraged my dreams to become a volcanologist.

Contents

List of Figures

List of Tables

Chapter 1

Introduction

1.1 Background and Motivation

Volcano dynamics, i.e. - the mechanics of how volcanoes move and change, covers a spectrum of activity from unrest to eruption. Phillipson et al. [2013] define volcanic unrest as 'deviation from the background or baseline behaviour of a volcano towards a behaviour which is a cause for concern in the short-term because it might prelude an eruption'. The word 'background' is a nebulous term; what constitutes background for one volcano may herald impending activity at another. For example, a volcano can be classed as active if it has erupted in the last 10,000 years [Global Volcanism Program, 2013]. Therefore an 'active' volcano that has erupted 100s of times is likely to have a very different description of background behaviour compared to one that has only erupted once. To highlight this ambiguity in volcano descriptors further, the difference between a dormant and an extinct volcano, is only the expectation that it will or will not erupt again [Oregon State University, 2019]. Therefore, what constitutes unrest at a volcano is specific to the individual, and the decision to class a volcano as undergoing unrest must be informed by its history and specialist knowledge of volcanology.

These kinds of definition are important for decision making, particularly with reference to volcanic hazards. Most volcano observatories have developed a traffic light system to communicate the status of an active volcano, not only for communities nearby, but also for aviation. The USGS, for example, uses a four tier system going from normal, to advisory, to watch, to warning, where normal refers to a background state, advisory and watch indicate elevated and escalating unrest, and warning means imminent eruption or eruption underway [USGS, 2017]. In contrast, in 1996 Monsterrat Volcano Observatory had a tiered alert system from 0 to 5, where 0 explicitly included background seismicity and levels 2 to 5 ranged from effusive dome building to ongoing large explosive eruptions [MVO, 1997].

The term volcanic eruption encompasses a range of activity involving magma or other fluids at the Earth's surface. What constitutes an individual eruption is a grey area, but the Smithsonian database defines a continuing eruption as one that has not had a pause of more than three months between eruptive events [Global Volcanism Program, 2013]. The median timescale of a volcanic eruption is 7 weeks, but there is a wide variation around this; some volcanoes have been erupting continuously for more than 24 years, and some eruptions end within a day, or even seconds [Sigurdsson et al., 2015]. When discussing volcanic eruptions it is helpful to categorise them as effusive or explosive, where effusive eruptions involve coherent magma flow out of a vent and the magma in explosive eruptions is torn apart [Parfitt and Wilson, 2009]. We can further specify if they are magmatic or phreatic; magmatic eruptions are those which involve the release of magma from the surface, and phreatic eruptions involve explosions of confined steam/gas without the direct involvement of magma (i.e., no juvenile magma is produced, only pre-existing rock) [Barberi et al., 1992]. Phreatic eruptions can have little to no detectable precursors; at Mt. Ontake in September 2014 57 hikers were killed by an unexpected phreatic explosion [Kato

et al., 2015]. A middle-ground, known as a phreatomagmatic or sometimes hydromagmatic eruption occurs when magma interacts with surface or ground water, i.e., juvenile magma will be present [Barberi et al., 1992].

Volcanic eruptions can display different styles which often transition from one to the other as eruption power waxes and wanes. Effusive behaviour can include lava flows, coulees and domes [Sigurdsson et al., 2015]. Strombolian and Hawaiian fountaining is the explosive but low power ejection of low viscosity magma from a vent; this low viscosity permits gas escape and prevents more intense activity [Sigurdsson et al., 2015]. Once the gas is lots from the fountains, they may continue as lava flows [Parfitt and Wilson, 2009]. Higher viscosity magmas can produce highly explosive Vulcanian (short duration), Plinian and subPlinian (sustained) eruptions [Parfitt and Wilson, 2009; Sigurdsson et al., 2015]. Effusive dome eruptions can swiftly transition into explosive behaviour including Vulcanian explosions and pyroclastic flows, should pressure can build up beneath the domes preventing gas escape [Sigurdsson et al., 2015]. Alternatively, if a dome grows too quickly, it can collapse, also causing pyroclastic flows [Sigurdsson et al., 2015].

The primary driver of explosive eruptions is bubbles [Parfitt and Wilson, 2009; Sigurdsson et al., 2015]. As magma ascends from a reservoir towards the surface it will experience a large pressure decrease and this decrease will allow saturated volatiles to come out of solution into a new bubble phase [Parfitt and Wilson, 2009; Sigurdsson et al., 2015]. On further ascent, the gas bubbles may grow in size and the gas becomes overpressured with respect to the liquid [Sigurdsson et al., 2015]. Fragmentation, i.e., the explosive mechanism, occurs when the magma/gas mixture transitions from a fluid carrying dispersed gas bubbles to a gas carrying dispersed liquid drops or solid particles [Sigurdsson et al., 2015]. Fragmentation may occur due to rapid acceleration or decompression; the former involves high strain rates within the magma/gas mixture and tensile failure of the melt, the latter involves sudden decompression of existing bubbles and their rupture [Sigurdsson et al., 2015]. This sudden decompression could be caused by dome collapse, for example [Sigurdsson et al., 2015]. Explosive behaviour, therefore, is governed by the efficiency of gas escape which in turn depends on the permeability of conduit wall rocks, ascent rates and bubble connectivity [Sigurdsson et al., 2015]. It should be noted here that though phreatic eruptions are not magmatic they too are caused by the explosion of trapped gas [Barberi et al., 1992]. How an eruption develops is very dependant on the final stages of ascent in the shallow part of the Earth's crust [Sigurdsson et al., 2015]. The conduit, i.e., the uppermost part of a magmatic system, is also important for mass eruption rates and magma ascent rates [Melnik and Sparks, 2002; Sigurdsson et al., 2015]. Properties of the conduit are important are therefore important for our understanding of how an eruption may proceed and its dynamics.

In this thesis, I study three volcanoes demonstrating different dynamics; Campi Flegrei caldera, Soufrière Hills Volcano, and Masaya Volcano. At the Soufrière Hills Volcano the cause of most unrest is undoubtedly magmatic and eruptions often have short-term precursors [e.g., Cole et al.,

2014; Mattioli et al., 2010; Odbert et al., 2014b; Sparks and Young, 2002; Voight et al., 1999; Watts et al., 2002; Young et al., 1998]. Though there is an active hydrothermal system at the Soufrière Hills Volcano [Chiodini et al., 1996; Hemmings et al., 2015], aside from short-term precipitation and sealing within the conduit [Edmonds et al., 2003], its influence appears to have been limited on eruption dynamics. The Soufrière Hills Volcano has had five eruptive phases in recent history, ranging from months to years in duration, with pauses of similar lengths [Odbert et al., 2014b]. Activity has included cyclic lava extrusion and dome building, dome collapse and pyroclastic flows [Cole et al., 2014]. Eruptions were well monitored and while the opening phases were often phreatic, violent magmatic explosions were the norm [Odbert et al., 2014b]. Unrest periods preceding eruption phases have typically involved inflation, seismicity and persistent degassing [Wadge et al., 2014].

Volcanoes frequently display unrest without eruption, particularly at calderas, e.g., Campi Flegrei, Yellowstone, Long Valley [Biggs et al., 2009; Chaussard et al., 2013, and references within]. Campi Flegrei is a classic example; uplift of 3 m occurred over two periods from 1969-1984, accompanied by building-damaging seismicity and triggering an evacuation [Barberi et al., 1984]. Uplift has continued since 2005, including numerous mini-uplift events each lasting several months, without eruption [Chiodini et al., 2015; INGV, 2016; Travaglino et al., 2018]. The causes of the various episodes of activity remain debated to this day in terms of magmatic vs. hydrothermal unrest instigators, but generally it is accepted that the mini-uplift events are hydrothermal in origin only [e.g., Battaglia et al., 2006; Berrino, 1994; Gottsmann et al., 2006; Todesco and Berrino, 2005]. However, the latest eruption in 1538 produced a scoria cone whose opening eruptive phases were hydromagmatic, and whose later phases may have experienced pyroclastic and strombolian behaviour [Di Vito et al., 1987]. It is therefore of primary importance to understand the provenance of deformation signatures and fluid distribution in the shallow crust.

Campi Flegrei caldera and the Soufrière Hills Volcano represent extreme end-members of volcano dynamics from hydrothermal unrest to eruption. However many volcanoes experience activity which falls somewhere between the two. Masaya Volcano is persistently active and falls within this category. When there is no lava lake present it can experience constant tremor and continuous degassing; it hosts numerous fumaroles, transient and permanent [Caravantes Gonzalez, 2013]. Occasional minor explosions occur at the volcano, at least one of which has been suggested to be phreatic in nature and had no seismic precursors [Duffell et al., 2003].

This thesis investigates shallow-seated crustal processes and structures associated with unrest and eruptive activity at Campi Flegrei caldera, Soufrière Hills Volcano and Masaya Volcano. These examples comprise three volcanoes of broadly dissimilar volcanic type which demonstrate fundamentally differing processes and time-scales. Calderas such as Campi Flegrei caldera are formed by rare catastrophic collapses [Gregg et al., 2012]. These kinds of eruptions

occur every 100,000 years [Gregg et al., 2012], and calderas frequently experience resurgent activity including post-caldera eruptions and exhibit well-developed hydrothermal systems whose activity are interpreted to be connected to magma below [e.g., Hill, 2006; Husen et al., 2004]. The positioning of this activity, magmatic and hydrothermal, is intrinsically linked to caldera structure [e.g., De Siena et al., 2018; Vilardo et al., 2010] which is therefore key to its dynamics. Additionally, calderas are formed by a spectrum of magmatic compositions. Campi Flegrei calderas' major eruptive products have included trachydacites, to basaltic trachyandesites and phonolites, whereas the Masaya volcano (which is a shield within a caldera complex) has produced a narrow compositional range from basalts to andesites [Global Volcanism Program, 2013; Pearson et al., 2012].

Variation in volcano type and composition presents a variety of processes and associated timescales, and correspondingly shifting motivations for how and why different volcanoes are monitored. Masaya volcano differs markedly from Campi Flegrei caldera and Soufrière Hills Volcano in its present activity. Compared to Campi Flegrei caldera and Soufrière Hills Volcano, this volcano is very poorly monitored and data pertaining to deformation is sparse. Hazardous gases at Masaya volcano are perceived to be one of the main concerns [van Manen, 2014] which means that for years attention has been on quantifying gas composition and trends with little focus on deformation. Concern at Campi Flegrei caldera over the provenance of deformation, hydrothermal or magmatic, has resulted in a focus on emissions from hydrothermal zones and intense scrutiny of deformation and seismicity. By comparison, Soufrière Hills Volcano is one of the world's natural laboratories and has a wealth of both geochemical and geophysical data, including high resolution strain data. It is also worth noting that the Soufrière Hills Volcano is part of an island arc, a very different setting to both the Campi Flegrei and Masaya volcanoes which are derived from continental subduction zones [Global Volcanism Program, 2013]. One is part of a volcanic belt [Pérez et al., 2009], the other part of complex collisional dynamics of Europe and Africa [Cello and Mazzoli, 1998]. For this reason it is perhaps unsurprising that these volcanoes demonstrate such different processes and dynamics.

Regardless of these differences, the movement of fluids causes deformation which we can measure, and gives rise to earthquakes in the brittle shallow crust [Segall, 2010]. This makes deformation and seismicity our best tools for forecasting volcanic behaviour [Segall, 2010]. When volcanoes are in remote locations seismometers are often the only type of instrumentation available for monitoring, e.g., Alaska [Dixon et al., 2017]. Indeed, seismometers are the primary instrument used in volcano monitoring networks and they can capture signals related to rock breaking, magma fragmentation, and the movement of fluids and gases among other things [Chouet and Matoza, 2013; Dzurisin, 2006].

Other in situ instruments found at volcanoes include tiltmeters, strainmeters, continuous GPS, and gravimeters [Dzurisin, 2006]. Tiltmeters measure changes in the inclination of the Earth's

surface and take advantage of the fact that volcanoes often inflate prior to eruptions and deflate afterwards. This change in volume due to magma movement through the volcano can be registered as volumetric strain in a borehole volumetric strainmeter. Strainmeters can also detect pressure variations within the volcanic system. Continuous GPS record 3-D surface displacements, and gravimeters are sensitive to ground movement and mass redistributions [Dzurisin, 2006].

Repeat measurements at volcanoes can include levelling, Electronic Distance Measurements (EDM), GPS, and gravity [Dzurisin, 2006]. The first three measure ground movement and the last mass redistribution. Continuous measurements offer the advantage of greater precision and dense temporal coverage, at the cost of spatial coverage and unavoidable long-term drift, while repeat surveys can be adjusted to cover the desired area and provide reliable measurements over long time periods [Dzurisin, 2006]. Lastly, volcano deformation can be measured from space using synthetic aperture radar (SAR).

Clearly there is a large variety of techniques to choose from for volcano monitoring and research, which cannot be covered in their entirety here. The different methods have individual pros and cons which means that instrument coverage must be designed based on the budget available, the type and location of the volcano and of course the budget available. Regardless of the selected instrumentation, where there is unrest and volcanic risk monitoring is crucial, as statistical tests indicate that between 2000-2011, 52-86% of the reported unrest across a spectrum of volcano types (including large calderas, complex volcanoes, shield volcanoes, stratovolcanoes, submarine volcanoes) lead to an eruption [Phillipson et al., 2013].

Within this thesis I use gravity, strain and InSAR data to investigate volcano dynamics and structures due to data availability and suitability, expanded upon later. These techniques fall under the umbrella of geodesy, which ‘measures the geometric shape of the Earth, its orientation in space, and its gravity field, as well as the changes of these properties with time’ [Van Camp et al., 2017]. This category also includes levelling, GPS, EDM, tilt, photogrammetry, water and level gauging [Dzurisin, 2006]. Below I briefly review each of the chosen techniques.

1.1.1 Gravity Data

Gravity is used in volcanology to investigate mass transport and density distribution. When we measure gravity, we are measuring a cumulative effect including the attraction of the Earth, Sun, Moon and planets and the centrifugal effect of Earth rotation [Van Camp et al., 2017]. The exact value of gravitational attraction at the Earth’s surface varies due to tides, geoid variations, earth rotation and mass distribution around the sensor (i.e., it varies spatially and temporally) [Van Camp et al., 2017]. The mass distribution is the object of interest in volcanology, but any

measurement includes all masses around the instrument; therefore 1) signals of interest must be large enough that the remainder can be removed as noise and 2) careful processing must be done to isolate signals of interest [Van Camp et al., 2017]. Modern gravimeters can measure differences up to 0.1 µgal, however this is dependant on the type of gravimeter [Sigurdsson et al., 2015]. Gravimeters can be absolute and measure exactly gravitational attraction at a location, or relative, and measure gravity changes with reference to a base station [Dzurisin, 2006].

Relative gravimeters, such as the CG5 used in Chapter REF, are based on a spring with length (L) suspending a mass (m), as in Fig. 1.1. The spring, with spring constant k, stretches in response to a change in gravity, and this change is proportional to the gravity change, m and k [Van Camp et al., 2017]. Quartz spring gravimeters such as the CG5 experience a strong changing drift and generally relative gravimeters are only stable for a few days and cannot be used for longer term continuous measurements [Van Camp et al., 2017].

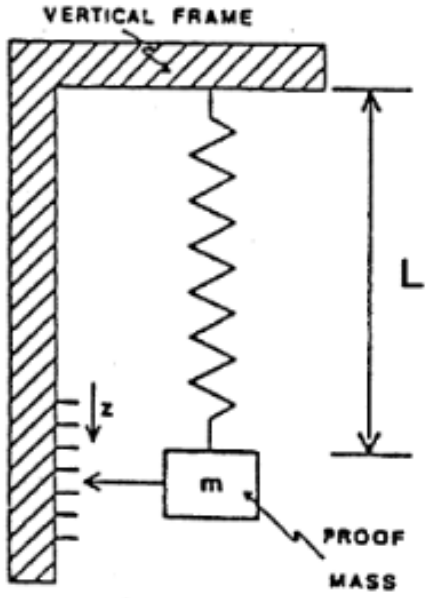

Figure 1.1: Top) A simple representation of a basic gravimeter from Seigel et al. [1995]. A mass (m) hangs from a known length of spring (L) which changes length with changing gravity. This displacement (z) can be measured.

Continuous measurements explore temporal gravity changes, which can be monitored using either in situ continuous gravimeters or repeat microgravity surveys (occupying the same benchmarks). Continuous gravity has been successfully used at Kilauea and Mt Etna (for example) with permanently installed stations [Carbone et al., 2007; Poland and Carbone, 2016]. However permanently installed stations are not common because few types of gravimeters are stable over long time periods or can withstand the mechanical wear, and those that are suitable

are very expensive [Poland and Carbone, 2016; Van Camp et al., 2017]. Alternative uses are defined intervals of continuous measurements such as at Nysiros, where gravity oscillations were linked to the hydrothermal system [Gottsmann et al., 2007]. Microgravity measurements are made at a fixed network and the elevation is accurately measured at the same time. A time period later, the stations are reoccupied and the difference in the measurements is therefore due to subsurface density changes [Sigurdsson et al., 2015]. Kilauea, Mt. Etna, and Piton de la Fournaise Volcano for example, all have microgravity networks which are occupied almost yearly [Bonvalot et al., 2008; Carbone and Greco, 2007; Johnson et al., 2010]. Temporal gravity changes such as these can vary from 10s to 100s of μgal [Sigurdsson et al., 2015], and can be cause by magma intrusion/withdrawal, variations in vesiculation, and changes to the proportions of other fluids [Van Camp et al., 2017].

The above summary of temporal gravity is not comprehensive and the interested reader is referred to Van Camp et al. [2017] and Sigurdsson et al. [2015] for more information; in this thesis Bouguer gravity data is used, which I focus on now. Bouguer gravity surveys generate plan view maps of gravity anomalies due to density variations only, (the effects of topography and latitude have been removed), from which models of the subsurface density distribution can be derived. Benchmarks from this kind of survey are not permanent and generally are not repeated. The data requires a number of corrections to remove unwanted signal contributions. Time dependant components include Earth tides and instrumental drift, which much be carefully calculated and removed [Telford et al., 1976]. Spatially dependant components include the latitude, the elevation and the topography of the surrounding terrain, and of course the density [Telford et al., 1976]. The first three can be removed by reducing the measurements to an equipotential surface and taking into account the mass and elevation changed by doing so [Telford et al., 1976]. The effect of latitude is calculated with reference to normal gravity (g_n), elevation effects are removed using the Free Air Correction (FAC), and the effects of terrain normally require both the Bouguer slab correction (BS) and the terrain correction (TC) [Telford et al., 1976]. These are explained in more detail in Chapter 2, however, it is clear already that gravity measurements include many sources of uncertainty.

Bouguer anomalies have been used to discover various subsurface structures and fluids at volcanoes. Hautmann et al. [2013a] used Bouguer gravity to highlight high density extinct volcanic cores at SHV and their associated low density aprons, and differentiate the active SHV centre as low density. Malengreau et al. [1999] discovered previously unknown volcanic structures beneath Reunion Island, one of which may have represented the ancient volcano Piton de la Fournaise was built on. At Mount Etna, low density anomalies found by Bouguer gravity have been interpreted variously as a bubble and liquid magma mixture and faults [Schiavone and Loddo, 2007]. At Somma Vesuvius, the morphology of the carbonate basement below the volcano was reconstructed [Cella et al., 2007].

1.1.2 Strain

Strain is a dimensionless measure of the change in shape or volume of a body due to an imposed stress [Dzurisin, 2006]. This can be measured by an instrument called a strainmeter. Most strainmeters are extensometers, which measure the change in displacement between two separated points (including rod, wire and optical strainmeters) and are mostly used in tunnels [Agnew, 1986]. Another type is the dilatometer or volumetric strainmeter which uses hydraulic amplification to make borehole measurements [Agnew, 1986]. This instrument is a cylindrical object (so that it couples with the borehole) composed of a sensing volume (liquid filled) and a smaller backing volume (gas filled) connected by a bellows (see Figure 1.2) [Agnew, 1986]. Changes to the sensing volume force liquid in and out of the backing volume - the motion of the bellows is measured as a voltage by a DC LVDT (linear variable differential transformer) or a inductive displacement transducer [Agnew, 1986]. The output voltage of this instrument is a near linear function of displacement.

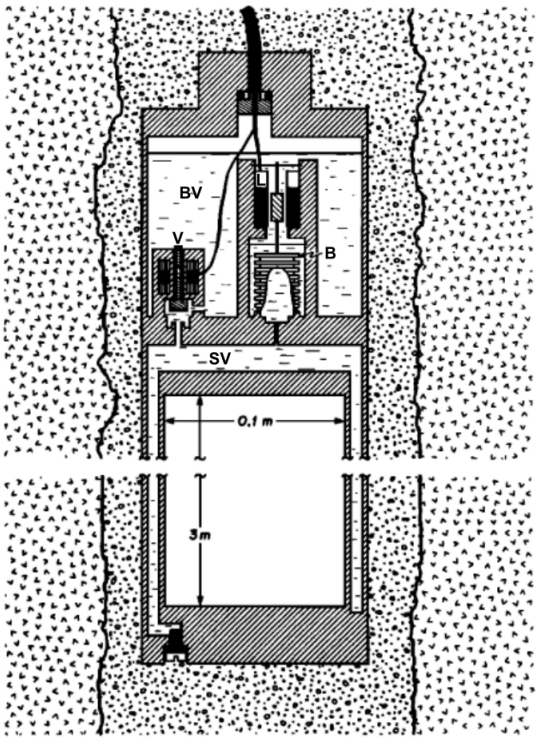

Figure 1.2: Top) Simplified example of a Sacks-Everton borehole dilatometer, adapted from Agnew [1986]. The digram highlights the sensing volume (SV), the backing volume (BV), the bellows (B), the LVDT (L) and the valve (V). The sensing volume (with a hollow insert inside) is connected to the backing volume via the bellows. The movement of the bellows is measured by the LVDT and the valve is available to rezero the bellows, should the volume passing through it be too large [Agnew, 1986].

The method of attachment of the strainmeter to the earth, rather than its sensitivity, limits its

measurements, however borehole strainmeters can detect strain changes $< 10^{-11}$ [Agnew, 1986]. Sacks-Everton dilatometers are the most common, being used at Montserrat, Stromboli, Etna, Izu-Oshima, Hekla and Mauna Loa. They are usually installed deep in boreholes to reduce noise and improve coupling to the substrate [Bonaccorso et al., 2016]. Calibration factors are used to convert the recorded data from counts to strain [Bonaccorso et al., 2016]. These can be obtained by the ratio of theoretical and recorded amplitudes of lunar tidal components [Bonaccorso et al., 2016]. Strainmeters are particularly useful because of their high sensitivity and ability to detect changes some distance away from an erupting volcano [Bonaccorso et al., 2016]. However this makes them very expensive to install (e.g. $618K for four boreholes [Mattia et al., 2004]). At Montserrat, four stations were chosen to maximise scientific return ; however a closer station at a few km from the dome was scrapped due to volcanic risk [Mattia et al., 2004].

Borehole dilatometer data has been used in a number of applications at active volcanoes, most notably at Mt. Etna and SHV [e.g. Bonaccorso et al., 2012, 2013; Chardot et al., 2010; Hautmann et al., 2014b; Linde et al., 2010; Voight et al., 2010]. At Mt. Etna, strain changes during lava fountaining have been used to locate the eruption source depth and volume change (hours), and delineate phases of recharging and discharging (1 month)[Bonaccorso et al., 2016]. The amplitude of the strain changes has been used to show that the source is small and cannot accommodate large volumes, resulting in short-term periodic events [Bonaccorso et al., 2013]. [Bonaccorso et al., 2012] found that strain could monitor an initial phase of pressure growth, step-like overpressure and emptying.

At Montserrat, strain has provided information on Vulcanian explosion dynamics [Gottsmann et al., 2011], demonstrating that despite multiple geophysical records including strain, it is very difficult to provide warnings. Strain also marked the true beginning of the eruption, where the seismic record would have led one to believe an earlier start. When there are multiple sources, strain can be used to distinguish which are active during aa deformation event due to distinct strain ratios imparted at well placed strainmeters Hautmann et al. [e.g., 2014b]. Using these strain ratios and their timings, allowed the author to detect contraction of the deeper chambers and contemporaneous inflation of the shallow system; the short time-span (100s of seconds) of this deformation prior to eruption led the author to infer rapid fluid transport as an explosion trigger rather than magma movement.

One of the most sensational uses of strain data occurred at Hekla in 1991, when clear strain patterns and seismicity led the national radio to issue a warning for an eruption to occur in 15 minutes, and it happened in 17 [Sparks, 2003]. It is clear from the above examples that generally strain is most useful over short time-scales and for increasing our understanding of volcano dynamics, rather than monitoring, as the time-scales are usually too short, with Hekla being a rare exception.

1.1.3 InSAR

Satellite imagery is an excellent monitoring tool, not only in the range of visual light, but particularly within the 0.3-30 cm range of the spectrum, which radar systems use Dzurisin [2006]. The advantage of radar is that the wavelength of the electromagnetic waves used in this technique are not affected by clouds or other atmospheric opacities, which means it can be used in any weather [Massonnet and Feigl, 2001]. Further advantages over visual techniques include its use at night and ability to see through moderate vegetation Dzurisin [2006]. Synthetic Aperture Radar (SAR) satellites follow a sun synchronous low earth polar orbit and have repeating paths which are important for Interferometric Synthetic Aperture Radar (InSAR) which is a particular application of SAR [UNAVCO, 2019]. I will therefore preface an introduction to the InSAR technique with a brief overview of SAR.

SAR measurements retrieve amplitude and phase components for each pixel of an image. The amplitude is a consequence of the reflectivity of the terrain within the pixel, where perfect reflectors appear dark, and scatterers are bright [Massonnet and Feigl, 2001] The amplitude is also governed by the size, shape, roughness, orientation, and dielectric constant of the target [Dzurisin, 2006]. In volcanology, changes in amplitude in successive SAR images indicate alterations to the volcano surface including flow emplacement, dome growth and new vents among other things (see Ebmeier et al. [2018] and references within for more details). SAR data is therefore capable of monitoring topographic change, the distribution of eruptive products and surface displacements [Ebmeier et al., 2018], and has been successfully used to calculate eruption volumes (effusive) and to make inferences on magma storage and supply [e.g., Ebmeier et al., 2018; Lu et al., 2010; Wauthier et al., 2012].

Interferometric Synthetic Aperture Radar 'calculates the interference pattern caused by the difference in phase between two images acquired by a spaceborne synthetic aperture radar at two distinct times' [Massonnet and Feigl, 2001]. The interferogram obtained from this process reflects the change in distance between the ground and the satellite, represented by contours, or fringes (see Fig. 1.3) [Dzurisin, 2006]. Pre-processing, the difference in phase is caused by a superposition of effects, including 1) phase variations in a pixel, 2) orbital trajectories, 3) topography, 4) displacement, 5) atmospheric changes and 6) other contributions such as instrumental artefacts and changes in ground reflectivity [Dzurisin, 2006]. For volcanologists the displacement is the contributor of interest, which means the rest become noise and must be removed via sophisticated processing Dzurisin [2006, see][for more details]. If multiple interferograms are made over an extended time period, a time-series may be produced for locations of interest detailing ground displacement with time.

SAR satellites typically have a temporal resolution of days to weeks, i.e., they revisit the same ground track in this time period [Ebmeier et al., 2018]. The ground track width can range from

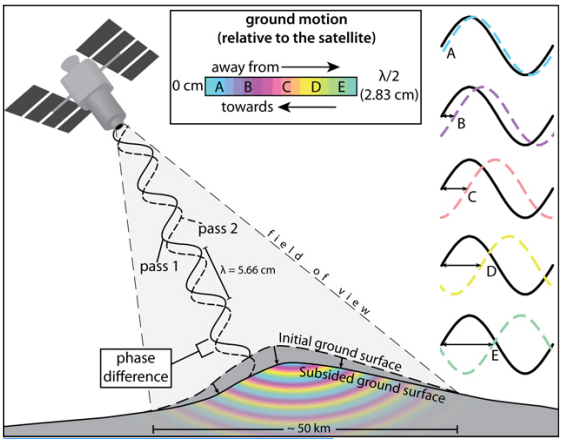

Figure 1.3: This figure demonstrates the InSAR process and is taken from Global Volcanism Program [2012b]. The satellite passes over the same area twice in similar orbital locations and collects phase data each time (pass 1 and pass 2). If there has been deformation in the time interval the collected radar waves will be out of phase with each other. Post processing, the fringes represent the change in distance between the ground and satellite.

10s to 100s of km, and the spatial resolution of a single pixel is on the order of 10 m [Dzurisin, 2006; Ebmeier et al., 2018]. Post-processing, InsAR can measure displacements down to a millimetre resolution, which is very useful for deformation monitoring [Ebmeier et al., 2018]. The main downsides of interferogram data are the delay between satellite acquisition of data and delivery of the images, and the expertise required to properly process and interpret the data [Ebmeier et al., 2018]. Additionally, InsAR can't really be used in areas of dense vegetation and the tropics tend to have more tropospheric water vapour than the equator, which means it is a high magnitude contributor to interferometric phase [Dzurisin, 2006]. The uncertainty in InSAR measurements comes from how well known the contributors to interferometric phase are.

Despite this, InSAR has been used extremely successfully to monitor volcano deformation. For example, two decades of InSAR data have been used over 100000 km^2 of the Andes [Henderson and Pritchard, 2013]. These data continued previous observations at several volcanoes which were known to be deforming, and also discovered deformation at two more as well as 4 areas of deformation unrelated to any edifice [Henderson and Pritchard, 2013]. InSAR is frequently used with GPS observations so that both high spatial coverage and accuracy can be combined Jónsson [e.g., 2009]; Palano et al. [e.g., 2008]. As well as monitoring, InSAR is frequently used to infer magma chamber geometries Wauthier et al. [e.g.,[2012].

1.1.4 Comparison of datasets

The above sections broadly outline the capabilities of the 3 different datasets contained in this thesis. As Bouguer gravity and InSAR data are discrete, and strain is continuous, they are not

directly comparable. However each has advantages and limitations, which I broadly split into 5 categories; temporal resolution, spatial coverage, data resolution, and cost. As already stated, Bouguer gravity and InSAR data are discrete, in that each acquisition is separated from the next by a distinct interval of time. Bouguer gravity is not typically repeated as a survey; microgravity is used for the purpose of evaluating temporal gravity changes. InSAR temporal resolution depends on the repeat time of the satellite, which can range from days to weeks [Ebmeier et al., 2018]. Strain data has a sampling rate of 50 hz at SHV and is telemetered [Dunkley et al., 2006; Gottsmann et al., 2011].

There is a wide variability between the spatial coverage of the 3 techniques. Bouguer gravity surveys can be as large or as small as desired, as can the station spacing, depending on the time and budget available. The placement of benchmarks also depends on accessibility and noise present, which can limit the scope of a survey. As InSAR satellite tracks can be 10s to 100s of km wide they provide excellent coverage. Typically volcano observatories can only invest in a few strainmeters, therefore coverage is limited to spot data and locations must be carefully chosen.

A Scintrex CG5 quartz spring relative gravimeter, as used in this thesis, has a resolution of 0.001 mGal [Scintrex Limited, 2012]. In practice, during a Bouguer survey the uncertainty can be approximately an order of magnitude higher than this. InSAR resolution is on the order of centimetres to millimetres and the noise and therefore the uncertainty will vary from location to location. Strainmeter data can detect transients on the order of ¡ 10^{-11}, however noise in the data due to poor borehole coupling, or oceans for example, can add uncertainty.

The expense of these different techniques can be divided into initial and subsequent costs, although due to the range of difficulties in acquiring the instrumentation this is not a fair comparison. To launch a satellite, for example, is extremely expensive, but sometimes the SAR portion of the payload is not the only one. Once the satellite is operational, the data is often free to download, and the expense is only related to facilities required by the data user. At Montserrat, the cost of installing 4 boreholes was 618 k [Mattia et al., 2004]. Post installation, however, borehole strainmeters only require minimum routine maintenance and again costs are related to user facilities [Mattia et al., 2004]. Gravimeters cost approximately 100 k each, but once purchased only require mains power to run, though maintenance can be expensive. Carrying out a survey involves transport costs as well as the day to day costs of the operator.

This brief synopsis demonstrates that the three techniques have very different advantages and therefore applicability to different volcanic scenarios. Instantaneous volcanic deformation, for example, could only be captured by strain. In contrast, slow deformation over years would be difficult to resolve in strain data, but easily monitored with InSAR. However neither of these

techniques provide information about the density of the subsurface, and therefore the probable deformation instigator, which is where gravity data becomes particularly useful. Despite the differences between these methods, each can provide a unique insight into the state of a volcano.

It is the modelling of retrieved deformation and density data which will provide the most information on volcano dynamics and plumbing systems [e.g., Bonaccorso et al., 2012; Bonforte et al., 2008; Camacho et al., 2011; Elsworth et al., 2014; Patanè et al., 2003; Saxby et al., 2016]. Models can range in sophistication depending on the type of model used. For example, there is a trade-off between mathematically 'correct' solutions i.e. - analytical models, and more geologically plausible representations of volcanic systems i.e. - numerical models. On one hand, analytical models provide a general understanding of how processes work, and as they are closed form they can be used to benchmark numerical models which are open and approximate [Gerya, 2009; Gokhale, 2008]. Common analytical models for volcano deformation include the spherical Mogi model, the ellipsoidal Yang model, and the crack model, which together broadly cover most geometries explored at volcanoes [Lisowski, 2006].

Often, analytical solutions of volcano deformation are sufficient, e.g., when fast retrieval of a deformation source is required for an evolving hazard, or where there is not enough data available to justify a more complicated model. However, to gain insights tailored to individual volcanoes, they are insufficient [Masterlark and Tung, 2018]. Generally, analytical models operate on the assumption of a homogeneous elastic half-space, i.e. - such models obey Hooke's law and assume a flat, infinite surface and isotropic material properties [Lisowski, 2006]. In reality these assumptions are rarely valid and additionally, volcanoes themselves are open systems, not closed [Oreskes et al., 1994]. Volcanoes inherently generate their own topography through edifice building and/or collapse and the manner in which they evolve creates complex, highly individual, and heterogeneous internal structures including fault systems, layering, and relict edifices [e.g., Folch and Gottsmann, 2006; Geyer and Gottsmann, 2010; Hautmann et al., 2013a].

Numerical models are able to take such complexities into account. The use of Finite Element Models or Finite Element Analysis (FEM/A) is becoming more and more prevalent among the volcanology community. FEA takes a continuum and breaks it into a number of discrete elements connected by nodes (in a mesh), which have degrees of freedom; these nodes can be expressed as an approximate system of equations which can then be solved and the object quantities calculated [Avitabile, 2005; Dieterich and Decker, 1975; Lin, 2005]. Alongside the mesh, FEA analysis requires the following: mass properties, boundary conditions or restraints and loading/forcing function details [Avitabile, 2005; Lin, 2005]. The error in this method is dependent on how well the mesh approximates the true boundary and how appropriate the type of mesh is for the problem [Avitabile, 2005; Lin, 2005; Masterlark and Tung, 2018]. The more elements present in the mesh, the better the approximation becomes but this must be balanced against the computational power increase required [Masterlark and Tung, 2018].

State of the art numerical deformation models include topography and thermal and mechanical heterogeneity [e.g., Currenti et al., 2010; Hickey et al., 2016; Odbert et al., 2015]. Increased thermal gradients around long-lived magma chambers can transition surrounding rocks through the brittle-ductile boundary, causing them to permanently deform [Del Negro et al., 2009]. The temporal behaviour of a deforming reservoir embedded in a viscoelastic shell differs markedly from a linear elastic medium, and such heterogeneity requires much lower pressures to obtain the deformation produced by the simpler case [Currenti et al., 2010; Del Negro et al., 2009; Hickey et al., 2016]. Frequently, mechanical heterogeneity is inferred from seismic velocity data [e.g., Bonaccorso et al., 2016; Hautmann et al., 2010b; Hickey et al., 2016]. However, the majority of deformation models focus on events which recover magma chambers at depths > 1 km and do not recover details of the conduit to the surface [e.g., Bonaccorso et al., 2012, 2016; Bonforte et al., 2008; Currenti et al., 2010; Elsworth et al., 2014].

Problematically, the properties of volcanic edifices are poorly known due to the risk and expense associated with recovering core samples and in the case of Soufrière Hills Volcano, poor recovery of seismic velocity properties at very shallow depths [Shalev et al., 2010]. Data from long-period (LP) seismicity, which has often been used to locate moving fluids (particularly in near surface conduits), are distorted by structural heterogeneity in the near-surface which, among other things, can result in the retrieval of incorrect source geometries [Bean et al., 2008]. Additionally, these final transport zones of magma to the surface are volumetrically small and their deformation signals are often hidden by larger, deeper chambers, as well as being invisible to seismic tomography [Odbert et al., 2014a]. Therefore, little is known about the shallowest parts of active volcanoes, both geodetically and mechanically. High resolution strain data is an ideal candidate to investigate such fine detail.

Unlike Soufrière Hills Volcano, at Masaya volcano the entire plumbing system has never been revealed geodetically, and instrumentation is sparse. There is only one option, commonly used at remote volcanoes, which is InSAR. The limit on temporal coverage means inferences on dynamics will be difficult, but the excellent spatial coverage will permit me to try and fit the data to a variety of model geometries.

Deformation is a very useful tool for locating reservoirs and constraining their properties at magmatically active volcanoes [Segall, 2013]. However, at volcanoes such as Campi Flegrei, where deformation sources can be magma and/or aqueous fluids, it is important to discriminate between the two. Where aqueous fluids gather and circulate in the very shallow crust, perturbations to this circulation can cause gravity changes, seismicity and deformation [e.g., Chiodini et al., 2012; Todesco and Berrino, 2005]. Often, the presence of such fluids is manifested by vigorous fumarolic activity, e.g., Yellowstone, Campi Flegrei, White

Island)[Chiodini et al., 2001; Fournier and Chardot, 2012; Hurwitz and Lowenstern, 2014]. However, pervasive hydrothermal sealing can inhibit surface degassing and obscure the presence of subsurface fluids, e.g., the Medicine Lake Volcano [Hulen and Lutz, 1999]. An understanding of the distribution of hydrothermal fluids is thus required to interpret unrest correctly; attempts have been made at Campi Flegrei caldera using seismic velocity, attenuation and Interferometric Synthetic Aperture Radar (InSAR) data [D'Auria et al., 2012; De Siena et al., 2010, 2018]. However the most direct possible measurement, i.e. - gravity, has not been used to elucidate the shallow subsurface structure and therefore the hydothermal system.

Shallow subsurface processes and structures vary with volcano type and setting. This is why there is no stand-alone method for investigating them. Depending on the kind of activity the volcano experiences and the tools that are available, methods for elucidating structural details within the shallow crust are highly volcano-specific. I therefore investigate three individual volcanic systems using gravity, strain and InSAR data to investigate the shallowest parts of each, where fluids, magmatic and hydrothermal, reach the surface; Campi Flegrei caldera, Soufrière Hills Volcano and Masaya Volcano respectively.

1.2 Thesis Aims

As outlined above, interrogating shallow crustal structures and dynamics at volcanoes is important for both advancing our understanding of volcanic processes and hazard mitigation. Models of volume transfer and density distribution at volcanoes have improved significantly since the inception of the simple Mogi model, but such evolved models have rarely been applied at the shallowest parts of volcanoes. Accordingly, the aim of this thesis is to develop appropriate methodologies for examining fluid movement and distribution in the shallow crust and the structures within, including:

- Investigating deformation in the shallow crust while taking into account heterogeneity and if possible topography.
- Using these models within the appropriate geological context to elucidate both structure and dynamics.
- Investigating fluid distribution in the shallow crust using gravity data.

1.3 Thesis Outline

Chapters 3 and 5 are based on work published in international peer-reviewed journals. Chapter 3 is a first author paper and is presented accordingly in its complete form. Chapter 5 is an edited version of my contribution to a larger published article, with additional original material to make a complete chapter. Author contributions and details of the papers are outlined at the beginning

of each relevant chapter. Chapters 2 and 4 are being prepared for publication in the Journal of Volcanology and Geothermal Research and the Journal of Geophysical Research respectively.

Chapter 2 begins at Campi Flegrei. This classic example of a hydrothermally active volcano provides an ideal setting for exploring fluids within the shallow crust. As it is the only chapter where I acquire the data directly, I provide a thorough treatment on gravity data processing and the methodology behind it. I explore classic and more novel methods of gravity data reduction and employ the numerical model software GROWTH2.0 [Camacho et al., 2011, 2002] to invert the data and outline fluid distribution in the shallow crust. I use alternative geophysical data alongside that from this study to help elucidate the influence of caldera structure on this fluid arrangement.

Chapter 3 shifts focus to examine almost purely magmatic activity. I use volumetric strain data from a specific eruption at Soufrière Hills Volcano to investigate the dynamics of the eruption, the geometry of the shallow reservoir and the structure of the shallow crust. I also constrain the effects of topography and heterogeneity on strain partitioning in the shallow subsurface. This study is a first attempt at such an endeavour and is therefore carried out in a 2D axisymmetric domain for simplicity and ease of benchmarking.

Next, Chapter 4 explores the findings of Chapter 3 further. The same concepts of exploring topography and heterogeneity are implemented in a 3D model space and investigated more thoroughly. The transition from a symmetric to a fully 3D, non-symmetric domain allows much greater freedom in the implementation of both topography and heterogeneity. I therefore examine in more geologically plausible detail, the effects of volcano specific topography and heterogeneity and the resultant shallow reservoir geometry and volcano structure.

Penultimately, Chapter 5 takes a step backwards in model complexity but tackles a volcano demonstrating both magmatic and hydrothermal activity, marrying the two topics outlined above. I study a period of time encompassing an eruption of unknown origin, and utilse deformation, temperature, gas, seismic and visual data to understand the dynamics during that time period at Masaya volcano.

Chapter 6 reviews the results and conclusions of the thesis, outlining common themes and similarities at each of the studied volcanoes. The importance of the findings is highlighted and the contribution of this body of work to volcanology is evaluated. Lastly, I outline questions inspired by this research and propose directions subsequent research should follow.

Chapter 2

Imaging the Hydrothermal Plume at Solfatara, Campi Flegrei, using Gravity Data

Author contributions and declaration: J. Gottsmann processed the GPS data and assisted in carrying out the gravity survey.

ABSTRACT

I present the results of a high spatial density gravity survey of Solfatara and the surrounding area within Campi Flegrei, Italy. Campi Flegrei experienced deformation on the order of metres in the 1970s and 80s and numerous mini-uplift events on the order of centimetres have occurred since. This deformation has been attributed to magmatic intrusions, perturbations to the hydrothermal system and a combination of both instigators. Hydrothermal fluids and gases are released most vigorously at Solfatara and at Pisciarelli nearby. Thermo-hydro-mechanical models explaining the measured fumarole emissions and mini-uplift events require a plume of ascending hot H_2O vapour and CO_2 from depth. Geophysical techniques such as electromagnetism, electrical resistivity, and active seismic imaging have resolved the subsurface architecture to depths between a few 100 m to 3 km depth at Solfatara, but no gravity survey has been carried out since 1968. I used a Scintrex CG5 gravimeter and simultaneous benchmark localisation using a GNSS system to create a dense survey grid of stations within Solfatara crater, and a reduced coverage network outside the crater to ~ 4 km distance. Results suggest three anomalous gas bodies beneath Pozzuoli, Pisciarelli and Solfatara; the first two are inferred to be trapped beneath hydrothermal seals and the latter is hypothesised to reach the surface via Solfatara's maar-diatreme structure. This work demonstrates the singular utility of gravity measurements in retrieving the density structure of the subsurface and highlights the influence of faults and fractures on fluid behaviour in the shallow crust.

2.1 Introduction

Unrest at active volcanoes is often characterised by seismicity, altered gaseous emissions and surface deformation, and is usually attributed to magma movement [Sparks, 2003; Sparks et al., 2012]. However, restless calderas have complicated subsurfaces which often host both hydrothermal and magmatic reservoirs [Gottsmann and Battaglia, 2008]. Geophysical and geochemical signals from magma reservoirs may be altered by hydrothermal systems, which can themselves produce measurable signals [Gottsmann and Battaglia, 2008; Todesco, 2008]. Hydrothermal systems are a complex interface between magma reservoirs and the surface [Todesco, 2008], therefore our understanding of the subsurface structure at calderas is critical for the interpretation of unrest. Campi Flegrei caldera (CFc) is a well documented restless caldera where the separation of the signals from magmatic and hydrothermal sources has not been trivial [Bonafede et al., 2013]. Solfatara volcano (Fig. 2.1) hosts the main surface features of the hydrothermal system at CFc and lies just a kilometre away from the focus of deformation for the last 50 years [Di Giuseppe et al., 2015]. A growing body of work has demonstrated the mechanisms by which hydrothermal systems can cause unrest and the form of the hydrothermal system [e.g., Chiodini, 2003; Chiodini et al., 2010, 2015; Ingebritsen et al., 2010; Todesco et al., 2004]. Our current understanding of the hydrothermal system structure at CFc is informed predominantly by geochemical constraints, geophysical data and these models [Bruno et al., 2007; Caliro et al., 2007] . The structure is envisaged as a multiphase plume of gas and liquid fuelled by the interaction of magmatic and meteoric fluids at depth which rise to feed fumaroles and mud-pools at the surface [Chiodini et al., 2015]. Density differences are therefore a significant control on the subsurface architecture of the hydrothermal system. However, the evidence which drives our understanding of the plume has not included gravity data. In this chapter I present the results of a new high resolution gravity survey at Solfatara Volcano, data inversion and the interpretation of results regarding the hydrothermal system structure at CFc.

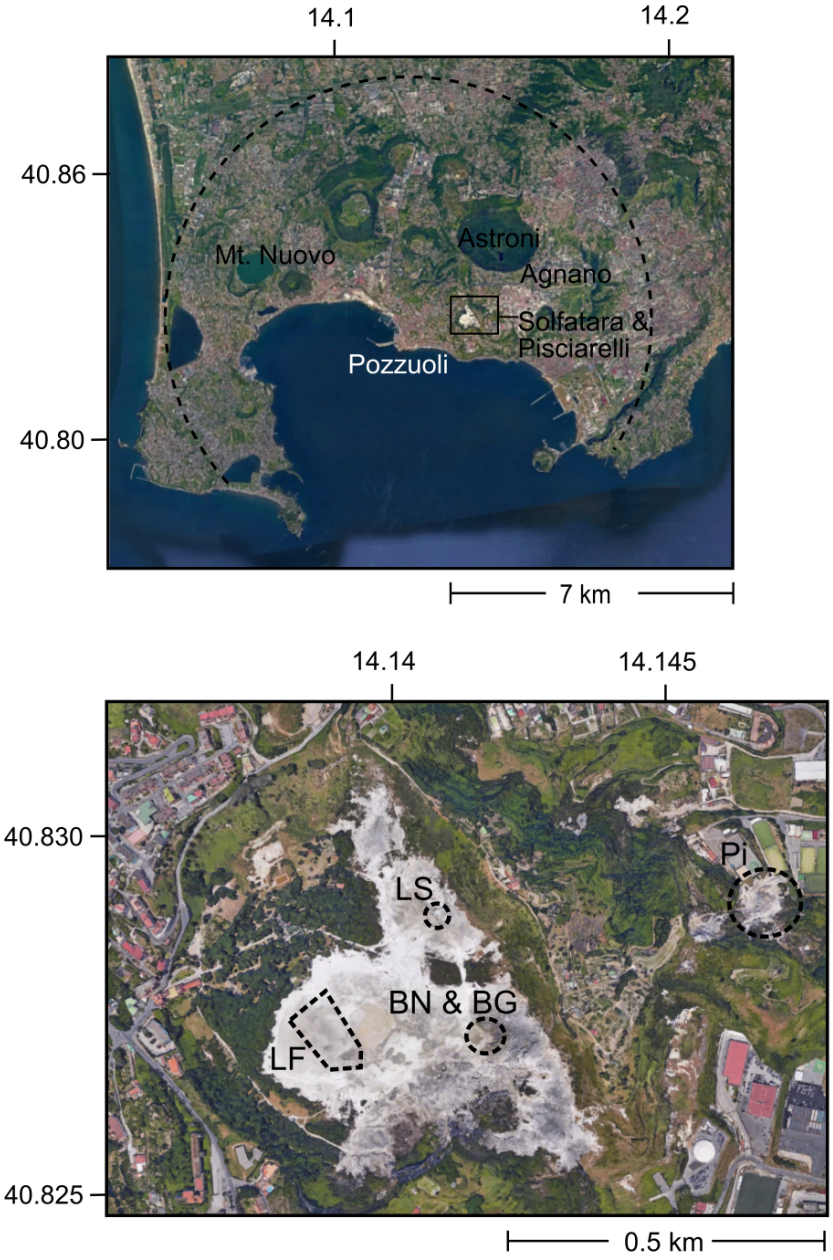

Figure 2.1: Top) Google Earth image of Campi Flegrei. The extent of deformation is marked with a dashed line and Solfatara and Pisciarelli are outlined by a black box. Bottom) Zoomed in Google Earth image of Solfatara. The fumaroles Bocca Nuova (BN), Bocca Grande (BG) and Le Stufe (LS) are circled with dashed lines. The fence around La Fangaia (LF) is marked with a dashed line and Pisciarelli (Pi) (further mud-pools and fumaroles) is circled with a dashed line.

2.1.1 Background and Caldera Structure

Campi Flegrei caldera is a resurgent caldera in the Campanian Plain near Naples, Italy [Orsi et al., 1996]. There is still debate on how the caldera formed [Capuano et al., 2013; De Natale et al., 2016] but some authors consider it to have been formed by two major collapse events,

the Campanian Ignimbrite (CI) at $\sim$ 39 ka, and the Neopolitan Yellow Tuff (NYT) at $\sim$ 12 ka [Acocella, 2008; Orsi et al., 1996; Perrotta et al., 2010]. Subsequent activity has concentrated inside the NYT caldera [Di Vito et al., 1999] and produced monogenetic tuff cones and tuff rings of predominantly trachytic composition [Orsi et al., 1996; Rosi et al., 1983] as well as minor collapse calderas. The latest eruption at the CFc formed the Monte Nuovo tuff cone in 1538 AD, preceded by marked uplift [Barberi et al., 1984; Di Vito et al., 1999].

Long term resurgence has divided the caldera floor into blocks which have had different vertical displacements [Orsi et al., 1999]. The dominant fault trends within the caldera are NW-SE and NE-SW [Di Vito et al., 1999; Isaia et al., 2015]. The presence of the caldera ring faults has been highlighted using gravity data [Barberi et al., 1991; Berrino et al., 2008], V_p tomography [Zollo et al., 2006], and active seismic imaging [Aldo, 2003]. The Mesozoic basement of the caldera begins at $\sim$ 4-5 km depth [Battaglia et al., 2008; Zollo et al., 2008] and seismic reflection studies provide evidence for a 1 km thick magmatic sill within it at 7.5 km depth [Zollo et al., 2008]. The caldera fill is composed of intercalated lava flows, pyroclastic material, and marine and continental sediments [Piochi et al., 2014]. Gravity surveys depict this caldera fill as a low density anomaly [Barberi et al., 1991; Capuano et al., 2013]. Deep borehole drilling has exposed a zone of thermo-metamorphic rocks within the caldera fill at depths of 2.5 km, extending to the bottom of drill holes at a maximum depth of 3.1 km [Piochi et al., 2014]. These boreholes also encountered several small igneous intrusions which were interpreted as possible remnant feeding conduits [Piochi et al., 2014]. Additionally, borehole data permitted assessment of the thermal structure in the caldera [Piochi et al., 2014]. The caldera has a high thermal gradient between 100-170 $^\circ$C km^{-1} and locally raised isotherms in the central-eastern part, particularly the 100 $^\circ$ isotherm which is only a few hundred metres below the surface [Piochi et al., 2014].

Solfatara volcano is positioned above this raised isotherm and is the most thermally active part of the caldera [Di Giuseppe et al., 2015]; it releases ten times more thermal energy than the conductive heat flux across the entire caldera floor [Chiodini et al., 2001]. Hydrothermal gases and fluids are released most vigorously here and at Pisciarelli nearby (Fig. 2.1) [Caliro et al., 2007]. The main features within Solfatara include a mud-pool named La Fangaia (LF) and two main fumaroles named Bocca Nuovo and Bocca Grande (see Fig. 2.1). Detailed geological mapping by Isaia et al. [2015] identifies Solfatara's structure as a maar-diatreme. High angle normal faults characterise the crater edges and fault planes are predominantly NW-SE. Two lava domes reside in the NE and S walls. The crater itself is embedded in the earlier structure of the Agnano-Monte Spina Complex. Isaia et al. [2015] point out that fumaroles and hydrothermal activity are concentrated in the faults zones and their intersections, which are hosted by highly fractured rocks and act as preferred pathways for fluid and gas. An InSAR survey of CFc found that NW-SE faults are reactivated during uplift and subsidence and may be important pathways for the upward movement of gas and magma to the surface [Vilardo et al., 2010]. The authors further observed that caldera rings faults and eruptive fissures are also reactivated during activity.

2.1.2 Unrest History and Deformation Sources

Patterns of uplift and subsidence have been recorded at CFc since Roman times [Bellucci et al., 2006; Parascandola, 1947], though subsidence has been the dominant trend [Barberi et al., 1984]. A permanent geophysical monitoring system was developed at CFc in 1970 in response to an uplift of 1.7 m followed by weak seismicity [Barberi et al., 1984]. In 1982-1984 a further 1.6 m of uplift occurred [Barberi et al., 1984]. The centre of maximum uplift was located in Pozzuoli,

and the area affected by the uplift was essentially that of the caldera (6 km radius) [Barberi et al., 1984]. The seismicity that accompanied the uplift event damaged many buildings and led to the evacuation of 40,000 people [Barberi et al., 1984]. Since 1989 numerous mini-uplift events have occurred producing deformation on the order of centimetres accompanied by seismic activity [Chiodini et al., 2010]. Excluding the isolated mini-uplift events, the overall deformation trend was subsidence from 1984-2005 [Chiodini et al., 2015]. After 2005, a new trend of uplift began. Fumarolic flow rate and discharge temperature increased in Solfatara from 2006 and an increased magmatic contribution was inferred from the composition of the fumarolic gases [Chiodini et al., 2011, 2012, 2015]. The observations of changed fumarolic activity, weak seismicity and inflation led the Italian Civil Defence to raise the alert level at CFc from green to yellow (Chiodini et al., 2015).

The cause of the 1982-1984 unrest at CFc is controversial. The major issues include the geometry and location of the deformation source and more importantly the instigator; hydrothermal vs magmatic activity [Bonafede et al., 2013]. Early work at CFc concluded that the source of the 1982-84 unrest was a magma chamber at 3 km depth [Berrino, 1994]. However the interpretation has evolved since then. Amoruso et al. [2014], for example, suggest a paired deformation source for the time period 1980-2010, with a quasi-horizontal crack at 3.6 km depth causing the large-scale deformation and a small spheroidal source at 1.9 km depth deforming the Solfatara region. Gottsmann et al. [2006] analysed gravity and deformation data from 1981-2001 and argued for the existence of a deep magmatic source at $\sim$5 km depth and a shallow hydrothermal source at $\sim$2 km depth, with varying contributions from both for mass and pressure changes recorded during inflation and deflation at CFc from 1982-84. Battaglia et al. [2006] model levelling, trilateration and gravity data from between 1980-95 and find different best-fit sources for the deflation and inflation events. The former is a horizontal penny-shaped crack at 2.5-3.5 km depth below Pozzuoli and the latter is a vertical prolate spheroid at 1.9-2.2 km depth. The authors propose two separate processes to account for the source disparity; 1) fluid injection from a magmatic source and accumulation in aquifers beneath Pozzuoli and 2) fracturing of a shallow brittle aquifer allowing discharge of hydrothermal fluids.

Many authors suggest that the more recent mini-uplift events have an exclusively hydrothermal origin [Amoruso et al., 2014; Bonafede et al., 2013; Chiodini et al., 2015; D'Auria et al., 2012; De Natale et al., 2006; Gottsmann et al., 2006; Manconi et al., 2010]. Todesco et al. [2004] and Chiodini et al. [2015] for example, have shown through coupled thermo-hydro-mechanical modelling that periods of intense magmatic degassing can change the composition of the fumarole-feeding reservoir, which in turn leads to deformation comparable with mini-uplift events. These perturbations to the hydrothermal system at Solfatara have been successfully modelled using CO_2 and H_2O mixtures undergoing phase changes [e.g., Chiodini, 2003; Todesco et al., 2003]. Todesco and Berrino [2005] and Coco et al. [2016] model the gravity changes induced by evolving fluid density and find that initial fluid injection periods are accompanied by a gravity increase, and later a gravity decrease. Todesco and Berrino [2005] in particular use their model to broadly reproduce the measured gravity changes at Solfatara. These models require a plume of ascending hot water vapour and CO_2 from depth through a porous medium to reproduce measured fumarole emissions, deformation and gravity changes.

2.1.3 The Hydrothermal Plume

The hydrothermal plume at Solfatara was theorised on a geochemical basis in 1984 by Cioni et al. [1984]. This inception of the plume theory proposed that dry steam separates from a geothermal liquid at 236°C in a highly fractured zone and feeds the fumaroles. The modern version of this theory suggests that rising magmatic gases flash hydrothermal liquids in a deep 'mixing zone' and form a gas plume which ascends to the surface [Caliro et al., 2007; Chiodini et al., 2015]. Compelling evidence for the plume is laid out by Chiodini et al. [2015], substantiated by thermo-hydro-mechanical models, fumarole geochemistry, CO_2 release, water table height, seismic velocity and InSAR data.

Thermo-hydro-mechanical models [Chiodini, 2003, 2016; Chiodini et al., 2012, 2015; Rinaldi et al., 2011; Todesco et al., 2016, 2003, 2010] demonstrate that perturbations of the composition, temperature and phase changes of the hydrothermal system drive deformation, changes in fumarole geochemistry/temperature and gravity. Fumarole geochemistry [Caliro et al., 2007; Chiodini et al., 2011, 2010] is an important constraint for these models. It allows the estimation of the temperature, pressure and depth of the mixing zone beneath Solfatara and the temperature of a pure 'vapour zone' above this. Chiodini et al. [2015] argue that the high volume of CO_2 released from diffuse degassing and fumaroles [Aiuppa et al., 2013; Chiodini et al., 2010] demands the presence of a gas reservoir beneath Solfatara. Furthermore, the water table height and temperature are both anomalously high at Solfatara, and Bruno et al. [2007]; Petrillo et al. [2013] assert that they must be sustained by condensates from a pressurised gas reservoir.

Chiodini et al. [2015] cite geophysical evidence for the plume including S-wave seismic velocity models [Battaglia et al., 2008; Zollo et al., 2006], V_p/V_s ratios [Vanorio, 2005] and InSAR [D'Auria et al., 2012]. The S-wave velocity model highlights a quasi-cylindrical high V_s zone beneath Solfatara extending to 1.5 km depth. Similarly, InSAR finds a cylindrical deformation source beneath Solfatara and Pisciarelli with a radius of 0.2 km and extending to 2 km depth [D'Auria et al., 2012]. Chiodini et al. [2015] briefly allude to the deeper structure of the plume with reference to work by Vanorio [2005], who interpret a low V_p/V_s zone 4 km beneath the city of Pozzuoli as a gas-saturated rock formation. Battaglia et al. [2008] find a similar low V_p/V_s zone also at 4 km depth beneath Pozzuoli. Both Battaglia et al. [2008] and Vanorio [2005] find a high V_p/V_s volume at $\sim$ 1 km beneath Pozzuoli which they attribute to steam condensation above the gas reservoir. Fluid reservoirs have also been proposed on the basis of seismic attenuation data [De Siena et al., 2010]. De Siena et al. [2010] suggest that geothermal basins exist beneath Pozzuoli between 0 and -3 km, beneath Mofete and Mt. Nuovo between -0.5 km and -2.5 km, and beneath Agnano between -1 km and -3 km. The authors also find a vertical high attenuation structure between 0-2.5 km depth beneath Solfatara. Zollo et al. [2008] et al detect a highly reflective layer at 3 km depth which they interpret to be the top of a supercritical fluid-bearing rock.

The hypothesised physical structure of the plume according to Chiodini et al. [2015] can be recapitulated briefly as follows. A magmatic source and magmatic gas accumulation zone exists at $\sim$ 4 km depth in ductile material. The magmatic fluids rise and mix with meteoric fluids, vaporising them in a brittle medium at $\sim$ 2 km depth. These fluids continue to rise and feed the fumaroles and mud-pools at Solfatara and Pisciarelli and this fluid migration has been observed seismically [D'Auria et al., 2012]. The delay between geodetic (uplift) and geochemical (gas composition) signals suggests that the hydrothermal response at Solfatara occurs much later

than the initial fluid injection at depth.

The studies cited by Chiodini et al. [2015] focus on the large scale structure of the plume based on data gathered across the caldera. Many smaller scale studies have scrutinized Solfatara and elucidated details of its structure, the hydrothermal circulation and the topmost portion of the plume (see Table 2.1). The types of data used include geoelectrical (ERT (Electrical Resistivity Tomography), MT (Magnetotellurics), CSAMT (Controlled Source Audio-frequency Magnetotellurics), self-potential, resistivity), temperature, CO_2, hydrogeological, seismic (microseismic, P-wave seismic refraction, Raleigh wave, S-wave velocity, seismic noise and S-wave spectra), gravity, structural, stratigraphic, and volcanological (see Table 2.1 for references).

Geoelectrical methods are well suited to track gas and liquid distributions due to their differing electrical properties, and therefore details of the hydrothermal plume at Solfatara. Bruno et al. [2007] carried out a detailed geophysical and hydrogeological study of Solfatara, finding 1) a top dry layer overlying a water saturated layer down to 300 m depth and 2) structural lineaments acting as preferential escape pathways and sources of microseismic noise. Di Giuseppe et al. [2015] further classify Solfatara into regions which are steam/gas dominated, water dominated, and mixed water and vapour dominated using results from an ERT survey. Byrdina et al. [2014] delineate two plume structures, one liquid and one gas, beneath La Fangaia and Bocca Grande respectively. They find resistive bodies at 30-150 m below the surface overlain by conductive bodies, which they suggest are gas reservoirs and condensate aquifers respectively. They also suggest significant downwelling of condensate near Bocca Grande. The results of ERT profiles carried out by Isaia et al. [2015] corroborate the water rich plume beneath La Fangaia, and find gas saturated zones at 0-40 m a.s.l. which connect to a deeper gas-rich zone. Troiano et al. [2014] employ MT and CSAMT and distinguish 3 main bodies; a vertical, plume-like high resistivity body reaching from 2.25 km depth to the fumarole field, a low resistivity body, deepening westwards underneath La Fangaia, and a low resistivity body at 1.2 km depth. These are interpreted as a steam/gas saturated column, a water-saturated, pressurised reservoir, and a mineralized, clay-rich body respectively.

The most recent published gravity survey dedicated to Solfatara [Oliveri del Castillo et al., 1968] found four main anomalies. The Bouguer anomaly map shows an elongate ~ 1 mGal gravity high on the NE crater wall, two connected gravity lows reaching from the southern edge of La Fangaia (~ 0.3 mGal) to Bocca Grande and Bocca Nuovo (~ 0.4 mGal), and a small ~ 0.3 mGal gravity low in the western side of the crater. Bruno et al. [2007] demonstrate correlation of the first three anomalies with maximum seismic noise, and of the first two negative anomalies with high CO2 degassing and temperature. The horizontal derivative of this gravity data, performed by Bruno et al. [2007], highlights the role of faults in concentrating these density anomalies.

There are several common themes in the above studies. Within Solfatara 1) a water-dominated anomaly is consistently found in the vicinity of La Fangaia, 2) gas/steam dominated anomalies are found close to Bocca Grande and 3) anomalies are often co-located with faults and seismicity. Caldera-wide studies persistently detect a seismically anomalous zone, interpreted as a gas column, extending from Solfatara's surface to a few km depth. These findings are coupled to density variations in the subsurface, yet there is little published gravity data related to the hydrothermal system at CFc. Furthermore, several of the above authors compare and contrast their findings with the Bouguer anomaly map of Solfatara from 1968 [Oliveri del Castillo et al., 1968]. CFc and Solfatara have undergone many changes since 1968 and the shallow

hydrothermal system is likely to have been altered by recent inflation events [Bruno et al., 2007]. Updated knowledge of the density structure of the hydrothermal system is required to complement the profusion of recent geophysical and geochemical studies dedicated to the hydrothermal system, and to increase our understanding of the subsurface structure at CFc.

2.2 Methods

2.2.1 Data Acquisition

I performed a gravity survey from 8-12 July 2015 which encompassed the Solfatara crater and surrounding region (Fig. 2.2). I used a Scintrex CG-5 Autograv gravimeter in tandem with a differential TOPCON HiPer Pro GPS receiver and antenna mounted on a 1 m tripod. The survey contained a total of 85 benchmarks laid out in two different spatial settings. Benchmarks within Solfatara crater were ordered in a dense irregular grid with a minimum spacing of 17 m and included a local gravity base station. The remainder of the benchmarks were spaced more widely on the roads around Solfatara with an approximate spacing of 1 km and a maximum spacing of 2.5 km. The purpose of the multiple spatial settings was to 1) investigate the expression of the hydrothermal plume at Solfatara at a similar scale to the many geophysical studies carried out there and 2) to explore the spatial distribution of the hydrothermal system in the wider area. Both the GPS reference receiver and the main gravity base station were located near Monte Nuovo and all gravity measurements were normalised to this main gravity base station. The entire network covered an approximate area of 36 km^2 and the estimated precision of each gravity measurement was 15 µgal (average of 12 repeat measurements of raw data across the survey area, each repeat being taken within a 10 minute window). The average standard error of the raw measurements was 8 µgal.

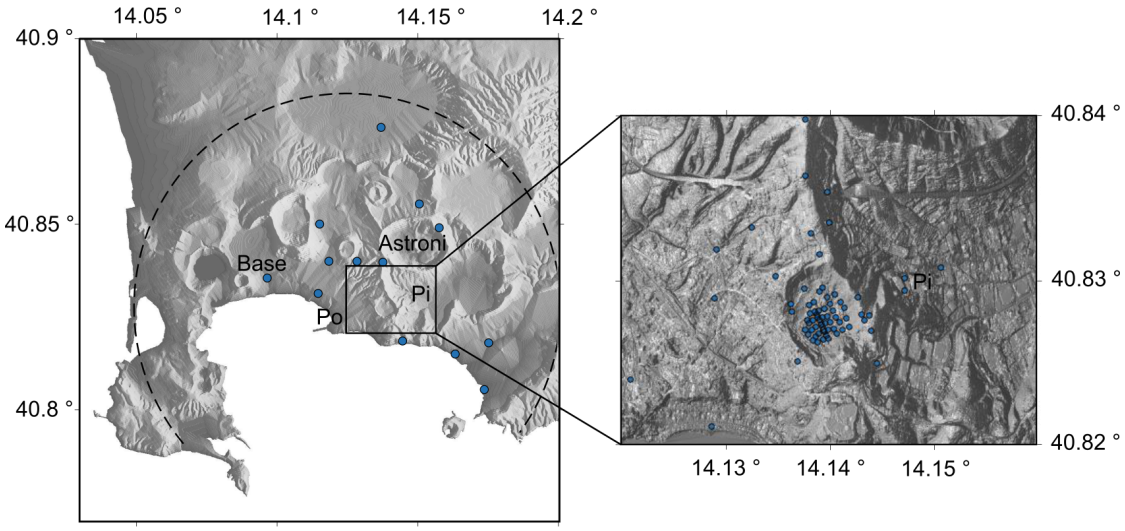

Figure 2.2: Left) 10 m DEM of Campi Flegrei with the outline of the major collapse event and deforming region marked with a dashed line. Survey benchmarks are in blue. Right) 1 m DEM with the densely spaced benchmarks within Solfatara in blue. Pozzuoli (the centre of major deformation events) and Pisciarelli (further mudpools) are labelled Po and Pi respectively

Table 2.1: Surveys within Solfatara (S). Also shown are geophysical surveys outside of Solfatara pertinent to the hydrothermal system (CFc). Question marks indicate where the survey date was not disclosed or unclear.

Survey Type	Survey Location	Year of Survey	Author
Bouguer Gravity	S	1968	Oliveri del Castillo et al. [1968]
	S,CFc	2015	This study
CSAMT	S	2000?	Bruno et al. [2007]
	S	2012	Troiano et al. [2014]
Resistivity	S	2000?	Bruno et al. [2007]
ERT	S	>2008	Di Giuseppe et al. [2015]
	S	2008-2012	Byrdina et al. [2014]
	S	2014?	Isaia et al. [2015]
Magnetotellurics	S	2000?	Bruno et al. [2007]
	S	2012	Troiano et al. [2014]
Self Potential	S	2011	Byrdina et al. [2014]
CO2 Measurement	S	2011	Byrdina et al. [2014]
Hydrogeological	S	2000?	Bruno et al. [2007]
InSAR	CFc	1992-2001, 2003-2007	Vilardo et al. [2010]
	S,CFc	1995-2007	D'Auria et al. [2012]
P/S-wave velocity	S,CFc	2006?	Zollo et al. [2006]
	S,CFc	2008	Battaglia et al. [2008]
	S,CFc	2005	Vanorio [2005]
Seismic reflection	CFc	2008?	Zollo et al. [2008]
Microseismic	S	2000?	Bruno et al. [2007]
P wave seismic refraction	S	2000?	Bruno et al. [2007]
Raleigh wave	S	2000?	Bruno et al. [2007]
Raleigh waves s-wave velocity	S	2001	Petrosino et al. [2006]
Seismic tomography	S	2009	Letort et al. [2012]
Seismic attenuation (passive)	S,CFc	1984	De Siena et al. [2010]
Seismic noise	S	2007	Petrosino et al. [2012]
S-wave spectra (passive)	S,CFc	2004-2006	Saccorotti et al. [2007]
Structural	S	2007?	Petrosino et al. [2012]
	S	2014?	Isaia et al. [2015]
Temperature	S	2009-2011	Byrdina et al. [2014]
Volcanological	S	2007?	Petrosino et al. [2012]
	S	2014?	Isaia et al. [2015]

2.2.2 Data Reduction

The objective of a static gravity survey is to constrain the location of anomalous density contrasts. The magnitude of gravity at any point is influenced by latitude, elevation, topography of the surrounding terrain, and also Earth tides and subsurface density variations [Telford et al., 1976]. The measurement of gravity is affected by instrumental drift. Raw gravity data is therefore composed of many elements and requires careful corrections to obtain the density component only, known as the Bouguer anomaly (BA). Earth tides and instrumental drift are usually removed first. The observed gravity (g_{obs}) is what remains and the following corrections are applied to acquire BA;

$$\text{BA} = g_{\text{obs}} - g_{\text{n}} + \text{FAC} - \text{BS} + \text{TC}, \tag{2.1}$$

where g_{n} is the normal gravity, FAC is the free-air correction, BS is the Bouguer slab correction and TC is the terrain correction.

Earth Tides

Earth tides are the motion in the solid Earth and the changes in its gravitational potential caused by the varying positions of the sun and the moon [Agnew, 2007; Ekman, 1993; Robinson and Coruh, 1988]. Accurate knowledge of their positions allows their influence to be calculated and removed [Agnew, 2007]. Many software packages exist for this (see Broucke et al. [1972]; Harrison [1971]; Longman [1959]; Merriam [1992]; Tamura [1982]; Van Camp and Vauterin [2005]). However, I elected to use the CG-5 Autograv gravimeter's optional inbuilt Earth tide removal algorithm which uses the Longman formula [Longman, 1959]. I do not include the effect of ocean loading as it is negligible in the Mediterranean [Ray, 1999].

Instrumental Drift

Instrumental drift refers to changes in the instrument with time which affect the reproducibility of measurements. The CG-5 Autograv measures the movement of a mass on a spring, caused by a change in gravity [Scintrex Limited, 2012]. However creep can occur in this spring; this usually causes a unidirectional change in gravity readings with time [Scintrex Limited, 2012; Telford et al., 1976]. This means that repeat readings at the same station may not provide an identical result. I assessed the drift by visits to the main gravity base station at the beginning and end of the survey (see Fig. 2.3) and at least three further occupancies at the local gravity base station within Solfatara during the day. These regular repeat measurements allowed the instrument drift to be tracked and removed. Drift corrections also remove residual tidal signals. The drift in the data follows a linear trend of $\sim$ -0.675 mGal/day (Fig. 2.3). The dataset for each day was corrected individually with a single linear trend. A control point (measured multiple times per day) within the dense survey grid was used to estimate the uncertainty on the drift correction. The first control point of each day was normalised to the base station and the subsequent residuals between further control point measurements and the linear trend were averaged. The average of these residuals was 66 µgal. This uncertainty is much larger than the precision of the survey and the standard error of the raw measurements; interpretation of results will therefore have to be made in light of this value.

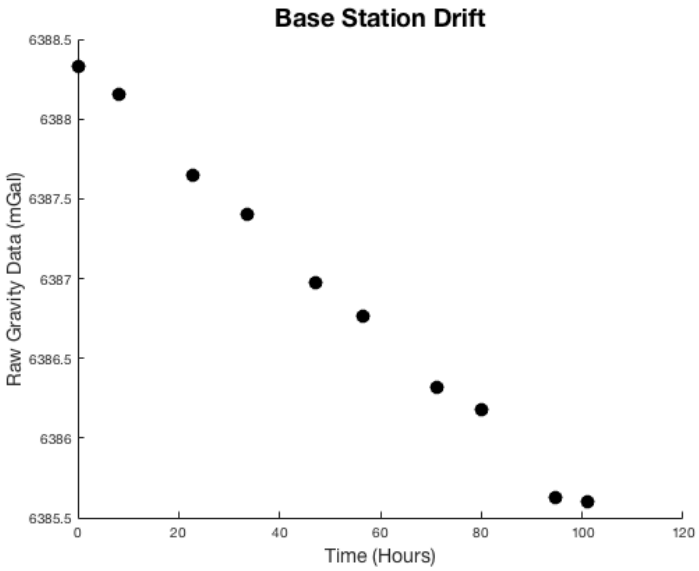

Figure 2.3: Drift at the base station over the course of the survey.

Normal Gravity

Anomalies remaining in g_{obs} may still be caused by latitude, elevation and terrain. These remaining components of gravity data are due to the irregular shape of the Earth. They must be eliminated from g_{obs} by reducing measurements to the reference ellipsoid, or an equipotential surface, while taking into account the elevation and mass lost or gained by doing so. The Earth is flattened at the poles and bulges at the equator, therefore gravity readings will be higher and lower than average due to the reduced or increased distance from the Earth's centre of mass respectively [Telford et al., 1976]. Additionally centrifugal acceleration due to the rotation of the Earth is greatest at the equator and opposes gravitational acceleration, and is zero at the poles [Telford et al., 1976]. I use the International Gravity Formula (IGF) 1980 [Moritz, 1992] to calculate the normal gravity (g_{n}) (which accounts for these effects) at the latitude of each gravity benchmark. Once g_{n} is subtracted from g_{obs}, one can be confident that remaining dissimilarities in the resultant gravity values are not due to latitude. Normal gravity at the main gravity base station was 980244.4306 mGal as calculated in Equation 2.2;

$$g_{\text{n}} = 978032677.14 \, \frac{1 + 0.0019319 \, sin^2\phi}{(0.0066944 \, sin^2\phi)^2}, \tag{2.2}$$

where ϕ is the latitude of the station. The remainder of the stations were normalised to this value.

Free-Air Correction

Smaller scale undulations in the Earth's surface must also be accounted for. The gravity measurements must be compared as if they are at the same equipotential surface, i.e. at the same distance from the Earth's centre of mass and with the same mass of material beneath them. In practice, peaks and troughs in the local terrain mean this is not the case. The free-air correction (FAC) reduces the gravity data to the same elevation as per Equation 2.3;

$$\mathrm{FAC} = 0.3086\,h(mGal), \tag{2.3}$$

where h is the height difference in metres from the reference surface. This correction is added to gravity measurements made above the reference surface and subtracted below the reference surface [Telford et al., 1976]. 0.3086 mGal/m is the theoretical free-air gradient which assumes a perfectly homogenous spherical earth. However, as the earth is not perfectly spherical the free-air gradient varies from location to location; Berrino et al. [1984] directly measured a value of 0.29 mGal/m for the free-air gradient at CFc in 1984. A free-air gradient of 0.289 mGal/m was also calculated by removing the effect of the -30 mGal, 3 km deep Bouguer anomaly (assumed to be spherical) from the theoretical gradient [Berrino et al., 1992]. However I elected to use the theoretical free-air gradient for the correction because this is the standard approach used in most gravity processing. In hindsight, it would have been more correct to use the measured free-air gradient, but as the terrain correction is generally the greatest source of error in obtaining the Bouguer anomaly the choice of free-air is less important. I show the resulting free-air anomaly map in Fig. 2.4. The average error of the vertical GPS measurements (0.24 m), when inserted into the free-air correction, generates an uncertainty of 7 µgal.

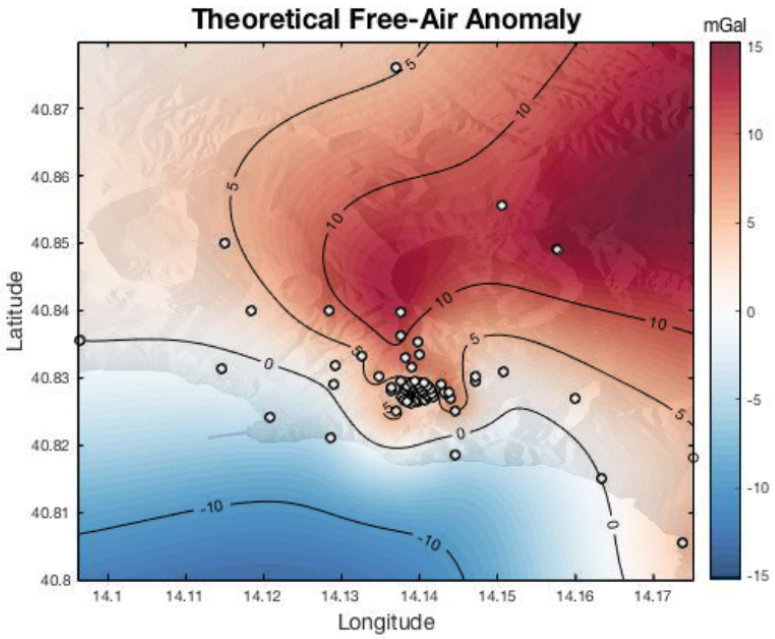

Figure 2.4: Theoretical free-air anomaly map superimposed on the 10 m DEM with benchmarks in white and contours in mGal.

Bouguer Slab and Terrain Correction

The material between the gravity measurements and the reference surface is accounted for by using the Bouguer slab correction (BS) and the terrain correction (TC). The Bouguer slab correction (Bullard A) approximates this material as a plate or slab of infinite horizontal extent, finite thickness and constant density [Robinson and Coruh, 1988] as in Equation 2.4;

$$\mathrm{BS} = -0.0419\,\rho\,h(mGal), \tag{2.4}$$

where ρ is the density of the slab (described later) and h is the height difference from the reference datum. A gravity measurement made above the reference surface will have excess mass beneath it, which exerts additional attraction compared to the reference surface, therefore, the correction must be subtracted at this point. Similarly, a gravity measurement made below the reference surface is missing mass and experiences a lesser attraction compared to the reference station. Therefore the correction must be added at this point. Where there is extreme topography the earth's curvature can cause the topography to fall below the horizon at large distances from the gravimeter. For this case the Bullard B spherical cap correction is required, but it was not needed in this case due to the limited topography. The error on the vertical GPS measurements and the tested density increment (100 kg m^{-3}) generates an uncertainty of 4 μwhen inserted into the Bouguer correction.

However the approximation of the Bouguer slab only holds if the nearby topography is extremely subdued [Robinson and Coruh, 1988]. This is not the case in Campi Flegrei and one must consider an additional terrain correction. Hills near a gravity measurement will exert an upward pull on the gravimeter [Telford et al., 1976]. Valleys (effectively missing mass) fail to exert a downward pull. I perform the terrain corrections in MATLAB using high resolution Digital Elevation Models (DEMs). Within and nearby the steep sided Solfatara crater, I used a 1 m DEM. I also took care to place benchmarks in locations free from significant nearby (within the first Hammer zone) topographic changes to mitigate the effects of near-field topography . A 10 m DEM [Tarquini et al., 2007, 2012] was appropriate for the more distal region surrounding Solfatara. The RMS error between the GPS benchmark heights and heights at the same locations in the DEMs was ∼2 m and ∼0.4 m for the 10 m and the 1 m DEMs respectively. I also incorporated bathymetric data [Ryan et al., 2009] into my corrections. The density of sea water (∼1025 kg m^{-3}) is much lower than that of rock and must be accounted for separately in the terrain correction. I therefore built separate DEMS for the onshore and offshore portions of the terrain correction. To test the uncertainty on the terrain correction I generated two normally distributed random topographies, ranging from 0 m in height to the RMS error between the GPS benchmark heights and co-located 10 m and 1 m DEM height (2 m and 0.4 m respectively). I calculated the terrain correction for two points 1 km apart (representing the 10 m DEM) and 50 m apart (representing the 1 m DEM) and found the difference between the two terrain corrections. This was repeated 10e^2 times and the 1 σ error of each distribution was found to be 130 μgal and 13 μgal for the 10 m and 1 m DEM respectively.

The MATLAB script I used to calculate the terrain correction followed the approach of Hammer [1939], but calculated the terrain correction at each DEM data point rather than for each Hammer chart compartment. The distance from each benchmark to every DEM data point is calculated and used to weight the influence of the height difference between each DEM data point and the benchmark;

$$\mathrm{TC}_1 = \left(\frac{1}{r} - \frac{1}{r^2 + \Delta z^2}\right)\Delta x^2, \tag{2.5}$$

where r is the radial distance from the benchmark to each DEM data point in metres, Δz is the height difference between the benchmark and the DEM data point and Δx is the DEM spacing.

The total terrain correction for each benchmark is then calculated;

$$TC_2 = \rho\, G \sum TC_1, \tag{2.6}$$

where G is the universal gravitational constant. The terrain correction was calculated for the onshore portion of the survey using the onshore DEM and an appropriate density (described below). The offshore portion required a density equal to that of the onshore density minus the density of seawater [Saxby et al., 2016].

The density for both the Bouguer correction and the terrain correction should be close to the average subsurface density [Robinson and Coruh, 1988]. If density data is not available it is possible to estimate it using the Bouguer anomaly and elevation data. Traditionally this is done using the Nettleton method [Nettleton, 1976]. This method involves plotting profiles of Bouguer gravity (for a range of different densities) against topography (Fig. 2.5). The Bouguer gravity profile with the least correlation to topography is the best estimate of the density. However profiles over structurally controlled features may not be appropriate as density might change with elevation [Nettleton, 1976]. While the profiles displayed in Fig. 2.5 show a strong correlation with topography, the least correlated profile is between 1800 and 1900 $\mathrm{kg\,m^{-3}}$. However the interpolation of the Bouguer gravity data, especially where data points are sparse has a smoothing effect and makes correlating the elevation and Bouguer gravity profiles qualititative rather than quantitative.

I also explore the approach of Eshaghzadeh et al. [2015]. This method correlates the Bouguer anomalies of different densities and elevation at each data point, rather than by eye across a profile. This correlation is plotted against the tested densities and a least-squares straight line is fitted to the resultant curve. Once this line is subtracted from the curve, the 'correlation difference' is plotted against the density and returns a unique best-fit density. The resultant best fit terrain density is 1900 $\mathrm{kg\,m^{-3}}$ (Fig. 2.6). The two approaches are in agreement and I proceed with a density of 1900 $\mathrm{kg\,m^{-3}}$.

Densities of various materials from boreholes at Campi Flegrei range from $\sim$1600 $\mathrm{kg\,m^{-3}}$ (tuff) to $\sim$2800 $\mathrm{kg\,m^{-3}}$ (thermometamorphic complex rocks) [Barberi et al., 1991; Piochi et al., 2014]. The average density of the first 500 m of all borehole data is approximately 1800 $\mathrm{kg\,m^{-3}}$ and the average density of all the borehole data is 2300 $\mathrm{kg\,m^{-3}}$ [Barberi et al., 1991], therefore I regard the chosen density as reasonable.

s

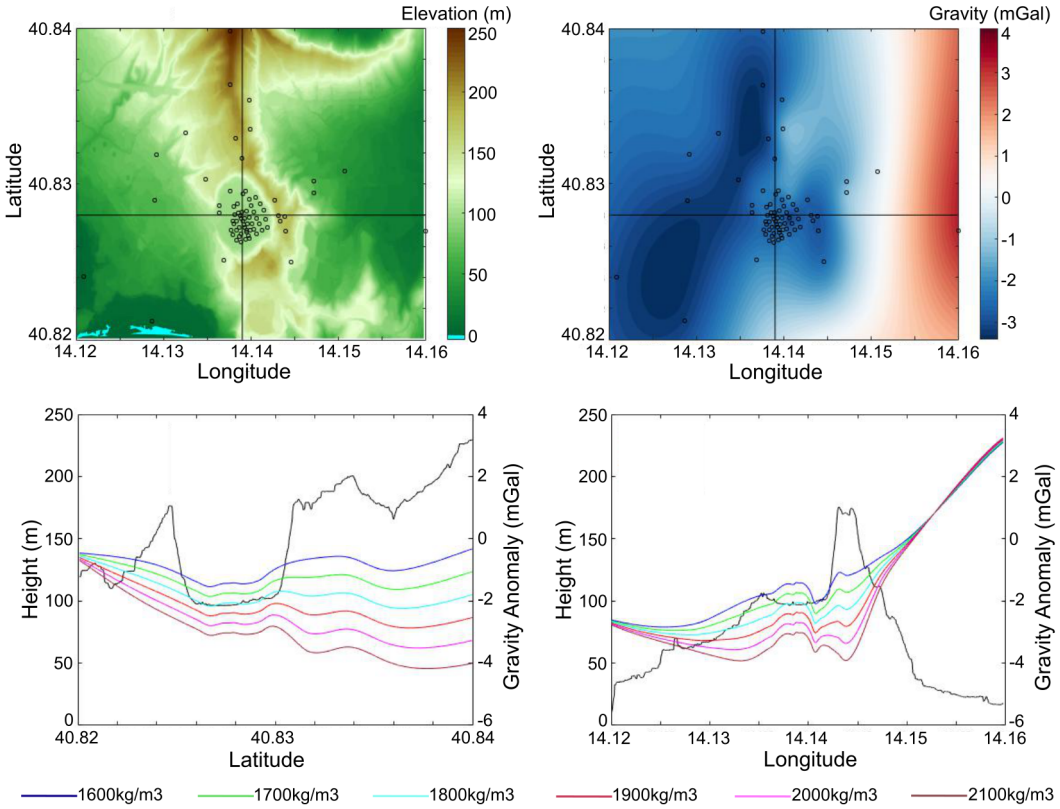

Figure 2.5: Top left) 1m DEM with EW and NS profiles at 40.828° and 14.139° respectively shown as black lines. Top right) Bouguer anomaly map for 1900 kg m^{-3} Bouguer slab and terrain density with NS and EW profiles shown as black lines. Bottom left) NS at 14.139° section though the field area with the topography shown as a black line, and Bouguer anomalies profiles of various densities as per the legend. Bottom right) EW profile at 40.828° through the field area with the topography shown as a black line, and Bouguer anomalies profiles of various densities as per the legend.

Data Detrending

The final step in processing is to detrend the data. Often survey regions will contain long wavelength features (e.g., variations in bedrock thickness) which must be filtered out to reveal the local Bouguer gravity anomalies caused by shallow-seated structures. This can be done by finding the best-fit plane to the Bouguer anomaly and removing it from the data. Once this regional gradient has been removed only the local, or residual anomaly remains. I calculate a regional gradient of 0.86 mGal/km with a strike of N50 °E. Cassano and La Torte [1987] find a different gradient of 0.5 mGal/km with a strike of S35 °W. Regional Topex gravity data [Sandwell et al., 2013, 2014; Sandwell and Smith, 2009] shows a regional gradient of 0.2 mGal/km with a strike of N37 °E. I note that Cassano and La Torte [1987] examined a much larger dataset than ours, reaching as far as Salerno to the east and the Volturno River to the north. The Topex dataset area coincides closely with my own and has a 1.4 km grid spacing.

Removing a linear trend may not be sufficient in complicated areas such as calderas. Large scale gravity surveys at CFc have consistently shown a negative gravity anomaly associated with low

density caldera fill [Berrino et al., 2008; Capuano et al., 2013; Nunziata and Rapolla, 1981]. I explore the effect of this anomaly by building a simple forward model based on the most recent data of Capuano et al. [2013] and borehole density data [Barberi et al., 1991; Piochi et al., 2014]. The caldera fill is simulated by a series of stacked spheroids 2 km deep and 3 km in radius with a density contrast of -300 kg m^{-3}, centered offshore of Pozzuoli (see Appendix A). The results of Capuano et al. [2013] suggest that the uppermost part of the caldera fill contains remnant high density feeder systems, as well as post-collapse lava flows and domes. I therefore set the top of the model at a depth of 1 km. I subtract the simulated Bouguer anomaly from the regional Bouguer gravity data. At the end of this process there are two Bouguer gravity datasets; the linear detrended Bouguer gravity (LBG) and the caldera fill detrended Bouguer gravity (CBG).

2.2.3 Horizontal Derivatives

The first and second horizontal derivatives are useful tools used to study potential fields such as gravity and magnetometry [e.g., Cooper and Cowan, 2008; Setyawan et al., 2015]. The first derivative calculates the rate of change in potential field and thus highlights gradients in the data which may be due to the edges of buried bodies or faults. The second derivative measures the rate of change of the gradient; inflection points are absolute maxima/minima and show the shape of boundaries. Both gradients can be calculated in the x and y direction, however it is more useful to look at the total horizontal derivative;

$$\mathrm{THD1} = \sqrt{\left(\frac{\partial g}{\partial x}\right)^2 + \left(\frac{\partial g}{\partial y}\right)^2}, \tag{2.7}$$

where THD1 is the first total horizontal derivative, $\partial g/\partial x$ is the change in gravity in the x direction and $\partial g/\partial y$ is the change in gravity in the y direction [Cooper and Cowan, 2008]. Similarly;

$$\mathrm{THD2} = \sqrt{\left(\frac{\partial^2 g}{\partial x^2}\right)^2 + \left(\frac{\partial^2 g}{\partial y^2}\right)^2}, \tag{2.8}$$

where THD2 is the second total horizontal derivative [Fedi, 2002]. I calculate TH1 and TH2 within the crater floor data as per the equations above and use the resultant gradient maps to delineate boundaries in the gravity data.

2.2.4 Inverting the Bouguer Anomaly Data

Bouguer gravity data reveals the spatial distribution of gravity anomalies at the reference surface. An inversion is required to transform the gravity variations into the anomalous density contrasts which cause them, which can then be interpreted in the context of geological structures [Gubbins, 2004a]. Inversions are non-unique and have multiple solutions, and should be informed by a priori knowledge of model parameters [Tarantola, 1987]. I use GROWTH2.0 [Camacho et al., 2011, 2002] to invert the Bouguer gravity datasets (LBG and CBG). GROWTH2.0 divides the model space into 3D parallelepiped elements and obtains a 3D anomalous density model using prescribed density contrasts. The issue of non-uniqueness in the inversion process is dealt with by using a mixed minimisation condition which selects a solution based on least squared fitness and 'smoothness', or the total anomalous mass [Camacho et al., 2011, 2002].

Inputs into this model include the Bouguer gravity data, the size of the cells, the density contrast and a balance factor. The balance factor determines the complexity of the model with high balance factors producing simple models. Densities with too high a contrast produce isolated skeletal bodies and densities with too low a contrast produce inflated and interconnected bodies. Both factors must be explored to find an appropriately complex model with a plausible density contrast and low auto-correlation [Camacho et al., 2011]. I explored the model space for each dataset iteratively, searching for suitably complex anomalous bodies and low auto-correlations for a low cell resolution, then repeatedly increasing the resolution and retesting the density contrast and balance factor at every step. I tested densities within $\pm$ 600 kg m^{-3} and balance factors from 10 to 40 (producing in total 119 solutions) and selected the model with the lowest auto-correlation and the most geologically plausible results. This methodology is effectively using a classic trade-off curve between model misfit and model simplicity [Gubbins, 2004b]. While each data point on such a curve is a viable solution, the best solution balances a compromise between adequately fitting the data and producing a suitably simple model. I also implemented a stratified background (density increase 50 kg m^{-3} km^{-1}) to prevent anomalous bodies inflating with depth.

2.3 Results

2.3.1 The Bouguer Anomaly

Fig. 2.7 shows the distribution and comparative magnitudes of the regional anomaly and the local anomalies (LBG and CBG). The NE-SW regional trend is evident in Fig. 2.7a. Removal of the regional trend in Fig. 2.7b reveals a broad $\sim$ -6 mGal negative anomaly (defined as the gravity difference between the base station and the most negative station) centred northwest of Solfatara. It is composed of three distinct gravity lows near Pozzuoli, Solfatara and Astroni. Individual anomalies on the periphery of the survey are supported by single data points and are therefore poorly constrained. In Fig. 2.7c, where the caldera fill trend has been eliminated from the data, the gravity low near Pozzuoli is no longer present and the anomaly is shifted to the northeast. The gravity lows at Solfatara and Astroni persist but the magnitude of the anomaly is reduced to $\sim$ -4 mGal.

Fig. 2.8a and b focus on the local Bouguer anomaly maps of Solfatara (LBG and CBG respectively). The patterns in Fig. 2.8a and b (emphasised by the contours) are similar, though the magnitudes of anomalies present differ. However both Fig. 2.8a and b show a negative anomaly (compared to the average value of all benchmarks on the crater floor) in the eastern side of the crater whose magnitude is $\sim$-1 and -0.5 mGal respectively. It is close to the fumaroles Bocco Nova and Bocco Grande and extends eastwards towards Pisciarelli. There are persistent positive anomalies on the north-northeastern and southern edges of the crater. The southern anomaly is present in both Fig. 2.8a and b, but the north-northeastern anomaly is strongest in Fig. 2.8a and diminishes significantly in Fig. 2.8b.

Lastly there is a small negative anomaly ($\sim$-0.3 mGal) in the vicinity of La Fangaia in Fig. 2.8a. Removal of the crater fill trend almost completely removes this anomaly in Fig. 2.8b where it is positive with regard to the average background value by 0.3 mGal. All anomalies are above the noise level caused by the uncertainty of the measurements; the largest uncertainty within the

1 m DEM area is caused by the drift (0.066 mGal) and would not mask the (0.3 mGal) anomaly in 2.8a or b. Similarly,the largest uncertainty within the 10 m DEM area is caused by the terrain correction (0.130 mGal) and would not mask the anomalies seen (-6 and -4 mGal).

2.3.2 Horizontal Derivatives

The first horizontal derivative (Fig. 2.9a) reveals strong gradients around the edge of the low gravity region and more subdued gradients around La Fangaia and elsewhere on the crater floor. Prevailing NNE and NW trends are highlighted by the rose diagram (Fig. 2.9b). The second horizontal derivative suggests fault trends which are more predominantly NNE (Fig. 2.9c and d). For comparison I show faults mapped by Isaia et al. [2015] and rose diagrams of both faults and fractures measured in the crater, accompanied by the dip angles. The first derivative map (Fig. 2.9a) shows some similar fault locations to those infererred by Isaia et al. [2015] (Fig. 2.9e) and the predominant NW and NNE fault orientations in the rose diagram (Fig. 2.9b) mirror theirs, though admittedly my sample size is much smaller. The second derivative map (Fig. 2.9c) bears less similarity to faults in Fig. 2.9e, however the predominant NNE fault orientation in my rose diagram (Fig. 2.9d) is more similar to the mapped fracture distribution (Fig. 2.9f) than the mapped fault distribution. However it should be noted that the lineaments in Fig. 2.9a and c are picked by hand and are inherently subjective.

2.3.3 Subsurface Distribution of Anomalous Masses

The best fit model, obtained using GROWTH2.0 has a balance factor of 40 and a density contrast of -450 to 450 $kg\,m^{-3}$ (Fig. 2.11). This result was obtained after 3 iterations of increasing cell resolution and was chosen bearing in mind the classic trade-off curve [Gubbins, 2004b]. I relate this to the expected density range extracted from boreholes in Campi Flegrei; $\sim$1600 $kg\,m^{-3}$ to $\sim$2800 $kg\,m^{-3}$ [Barberi et al., 1991; Piochi et al., 2014]. However the maximum rock density from the boreholes relates primarily to thermometamorphic complex rocks [Barberi et al., 1991], which are unlikely to be detected in this survey. If I reduce this maximum to the average borehole density (2300 $kg\,m^{-3}$) the modelled density range ($\pm$450 $kg\,m^{-3}$) is comparable to that seen in the shallow subsurface at CFc ($\pm$350 $kg\,m^{-3}$).

I use density isosurfaces to illustrate the results of the best fit model (Fig. 2.11). I demonstrate that while inversions are inherently non-unique, the model findings are robust, by showing density isosurfaces for models with $\pm$300 and $\pm$600 $kg\,m^{-3}$ density contrasts in Fig. 2.10 and 2.12 respectively. For Fig. 2.10 to 2.12, panels a and b represent negative anomalous bodies responsible for the LBG (blue). Similarly panels c and d represent the CBG (red). Panels d and e show both for ease of comparison.

The main features of each density class remain the same from Fig. 2.10 to 2.12, though they become larger and more interconnected as the range of density contrast decreases. Regarding the LBG, Fig. 2.10a-b and 2.11a-b show three main bodies approximately located beneath Pozzuoli, Astroni and Solfatara. At a density contrast of 300 $kg\,m^{-3}$ (Fig. 2.12a-b) the model becomes inflated and the Pozzuoli and Astroni anomalies become connected. The Solfatara anomaly is approximately 0.5 km wide and extends from close to the surface to -0.8 km below sea level in the best fit model (Fig. 2.11). The anomalous body beneath the Pozzuoli area is 1 km in diameter at its widest and extends from $\sim$ -0.5 km to -1.2 km depth. It is slightly elongated in the NNE-SSW direction. The Astroni anomaly is elongated E-W, 1.75 km across its widest point

and reaches from -0.5 km to -1.4 km depth.

The anomalous bodies retrieved from the CBG inversion (Fig. 2.10c-d to 2.12c-d) are similar to those found for the LBG. However, the Pozzuoli anomaly is not present in this inversion and the anomalous bodies are slightly shallower, as can be seen in Fig. 2.10e-f to 2.12e-f. The long axis of the Astroni anomaly is inclined slightly to the north with respect to the LBG Astroni anomaly.

I compare the different densities in Fig. 2.13. The surface traces of the -600, -450 and -300 $kg\,m^{-3}$ density isosurfaces are shown as dotted, unbroken and dashed lines respectively. Despite the removal of differing trends, both the LBG (Fig. 2.13a) and the CBG (Fig. 2.13b) place the Astroni and the Solfatara anomalies in similar locations for the -450 $kg\,m^{-3}$ isosurface. The Solfatara anomaly covers the SE edge of Solfatara crater and extends to Pisciarelli for both cases. The Astroni anomaly is centered SW of Astroni crater and covers its SW side. The co-location of the Astroni and Solfatara anomalies in both models is an indication of their robustness, while the veracity of the Pozzuoli anomaly remains uncertain.

2.4 Discussion

Inferences on the geometry and location of the hydrothermal system at Solfatara have previously been drawn from a combination of seismic, geochemical and deformation data [e.g., Chiodini et al., 2015; D'Auria et al., 2012; De Siena et al., 2010]. Therefore, gravity data has been almost entirely absent from this endeavour; the density structure of the hydrothermal system has not been interpreted before at Campi Flegrei. I have delineated the hydrothermal system at Campi Flegrei using Bouguer gravity maps and gravity inversions. The results of two detrending techniques (linear detrending (LBG model) and caldera fill detrending (CBG model)) are similar caldera-wide, highlighting features of the gravity data which are robust. I find three separate low-density bodies (Astroni, Solfatara and Pozzuoli) which I interpret as gas reservoirs, one of which reaches the surface (Solfatara). The Pozzuoli anomaly however, is only present in the LBG model, not the CBG model. The lack of offshore data points in this survey prevents certainty about the effect of caldera fill on the data, but the CBG model acts a useful caveat. Both models are plausible and alternative evidence is required to determine the existence of the Pozzuoli anomaly.

2.4.1 Controls on fluid distribution

Hot fluids will rise until they cool and attain neutral buoyancy, reach the surface or encounter a barrier to flow, i.e. a zone of reduced permeability. The results suggest two possible fluid bodies trapped beneath the surface and one which discharges freely at Solfatara. Therefore, the permeability structure of the caldera is key to understanding the present distribution of fluids in the subsurface. Rowland and Sibson [2004] subdivide permeability into intrinsic (lithological), inherited (rock layering) and active structural (faults, fractures and dykes). Each type of permeability is important; for example, at the Taupo Volcanic Zone (a rift system) the basement rock as encountered in drill holes has low intrinsic permeability but holds hydraulically conductive faults. Some rock units of the basin fill have intrinsically high permeability, yet the main fluid flow is via tectonically maintained permeability pathways in accommodation zones of the rift system. This system is quite different from CFc, but as CFc is experiencing extension [Carlino et al., 2015] and deforms regularly, the possibility of tectonically controlled

permeability should not be ignored. Additionally, faults are suggested to be important fluid pathways at CFc on the timescales of both 1-10 years and 10^2-10^3 years [Vilardo et al., 2010]. The influence of faults can be seen in the horizontal gravity gradients within Solfatara (Fig. 2.9), whose derived lineaments show a correlation with the main fault and fracture directions mapped by Isaia et al. [2015].

Permeability in hydrothermal systems is not static; rock permeabilities constantly change due to fracturing and cementation from hydrothermal precipitation as well as tectonic stresses [Rowland and Sibson, 2004]. At Yellowstone intrinsic permeability is important initially, but subsequent hydrothermal alteration reduces lithological permeability and instead focuses flow along fractures [Dobson et al., 2003]. Critically stressed faults can be hydraulically conductive [Jasim et al., 2015], and mineralisation can seal previously connected pathways within or around a fault [Sibson, 1994]. Therefore faults can be both permeable pathways and impermeable inhibitors for fluid flow, depending on the stress regime and degree of alteration. Additionally, fluids can create their own permeability via thermally induced hydraulic fracturing [Knapp and Knight, 1977]. Indeed, both Cusano et al. [2008] and Saccorotti et al. [2007] suggest that a swarm of VT earthquakes in 2006 were caused by this process at Campi Flegrei.

Permeabilities measured from boreholes at CFc range from < 1 mD to 10s of mD [Piochi et al., 2014]. Core samples included welded tuff, depositional layering, and lava bodies, both horizontal and inclined [Carlino et al., 2015; Piochi et al., 2014]. Hydrothermal alteration has not been explicitly noted, though calcite precipitation is mentioned; however none of the boreholes are close to the anomalous bodies. The occurrence of anomalous bodies at shallow depths demands the presence of an impermeable seal preventing access to the surface. Assuming a mineralogical cap is not unreasonable; work at Raoul caldera, Medicine Lake, Ohakuri and Yellowstone for example, has demonstrated hydrothermal sealing at various depths [Christenson et al., 2007; Dobson et al., 2003; Henneberger and Browne, 1988; Hulen and Lutz, 1999]. In particular, a mineralogical seal was assumed at 200 m depth in Raoul Caldera under which a vapor static zone formed (prior to seal rupture), and presently exists hundreds of metres below the surface at Medicine Lake.

Extensive groundwater modelling by Jasim et al. [2015] has shown that faults can be important for fluid and heat distribution in the subsurface at CFc. They modify fault/caldera fill permeability contrasts and basal flux to simulate a range of conditions from steady state to unrest. The authors demonstrate that permeability contrasts alter the distribution and circulation of hydrothermal fluids in the subsurface. In simulations of increased basal heat flux gas-rich pockets develop beneath liquid dominated systems, similar to that found at Pozzuoli by seismic attenuation [De Siena et al., 2010]. Jasim et al. [2015] also find that hot plumes whose radii are no larger than 2 km form due to injection of fluids at the base of faults; the anomalies from this study are 0.25 to 0.875 km in radius. I relate the Astroni, Pozzuoli and Solfatara anomalies highlighted by the inversion to geophysical (see Table 2.1 for details) and geochemical data and discuss their plausibility. The co-location of the Solfatara anomaly and the vigorously degassing fumaroles implies a gas-rich source; I therefore interpret the other anomalies as gas-bearing also.

Pozzuoli

Pozzuoli is the centre of deformation at Campi Flegrei and has experienced intense seismicity during uplift events [Orsi et al., 1996]. Deformation modelling by several authors finds different inflation and deflation sources at depths of approximately 4 km and 2 km respectively, which are both deeper than the source found in this study [Amoruso et al., 2014; Battaglia et al., 2006]. Vanorio [2005] use seismic velocity tomography to delineate a high V_p/V_s (2.3) zone beneath Pozzuoli centered at approximately 0.8 km depth and 0.75 km in radius. Below this, they find a somewhat flat low V_p/V_s (1.4) anomaly at 4 km depth. They interpret these features as brine caused by steam condensation and a gas enriched formation respectively. Chiarabba and Moretti [2006] find a high V_p/V_s region below Pozzuoli at 0-2 km depth, overlying a low V_p/V_s anomaly at 3 km depth which they interpret as steam condensation and gas accumulation respectively. Battaglia et al. [2008] also present very similar results using the same data. This arrangement of fluids has been predicted by groundwater modelling [Jasim et al., 2015].

Seismic attenuation tomography by De Siena et al. [2010] in tandem with V_p/V_s ratios also finds an anomaly 0-2 km below Pozzuoli, approximately 1 km in radius. The anomaly has a high V_p/V_s ratio of $\sim$2.3, high Q_s^{-1} and moderately high Q_p^{-1} (though Q_p^{-1} appears poorly resolved). De Siena et al. [2010] employ the inverse quality factor which is equivalent to attenuation, for which case $Q_p^{-1}/Q_s^{-1} < 1$ implies liquids. The authors suggest that the source is a geothermal basin, but in the same section propose high temperature vapours as the solution for similar seismic properties in another area.

Chiodini et al. [2015] and Caliro et al. [2007] use geochemical models to predict the vaporisation of fluids at 2 km depth which rise to the surface. There is therefore supporting evidence for both a gas and a liquid reservoir beneath Pozzuoli. One aspect that has not been considered is the potential for temporal change in the subsurface. Chiarabba and Moretti [2006] and Battaglia et al. [2006] use combined data from 1984 and 2001, and Vanorio [2005] and De Siena et al. [2010] used data from 1984 only. Not only do the combined datasets risk masking of temporal signals, but 15 years later the system is likely to have changed. Changes in elasticity of the upper crust, for example have been suggested [Di Luccio et al., 2015], which can affect earthquake distribution. Cycles of sealing, fracturing and resealing are suggested to be possible on timescales of years (e.g., Yellowstone cores plugged almost completely after 25 years [Dobson et al., 2003].). Ingebritsen and Sorey [1988] discuss self sealing by deposition of silica due to cooling in shallow parts of hydrothermal systems. Also, conditions can change from liquid to vapour dominated over 10's to 100's of years [Ingebritsen and Sorey, 1988]. I therefore cannot preclude the possibility of the reservoir beneath Pozzuoli having evolved from liquid to gas dominated over the time frame which it has been observed.

Astroni

The Astroni anomaly is unexpected as there are no recorded fumaroles or geothermal manifestations in the region (though this does not mean they do not exist). Additionally, the anomaly is located at the convergence of two crater walls, one might expect high density material here compared to adjacent low density crater fill. However Capuano et al. [2013] find an E-W elongated low-gravity anomaly in the same region as ours at approximately 1-2 km depth, and there have been numerous shallow earthquakes in this area (see Chiodini et al. [2017]; Saccorotti et al. [2007]). There are anomalies associated with Agnano crater, which Astroni is nested into. De Siena et al. [2010], for example, finds an anomaly beneath Agnano at 1-3 km depth which

they relate to a high temperature aquifer noted by Todesco et al. [2003] beneath Agnano plain at -1.4 km. de Lorenzo et al. [2001] show a broad lobe of low Q_p extending from Astroni to Solfatara at 0-1 km depth. They correlate it with high V_p/V_s and attribute it to a fluid saturated volume. However I note that the V_p/V_s and attenuation data are from 1984, and may not be as reliable as more modern data.

Capuano et al. [2013] have already suggested a mechanism for gas to be present in the Astroni region without geothermal manifestations, which I expand upon here. They interpret the anomaly as low density gas at depth, with secondary mineral precipitation as a mechanism for preventing surface expression. They also point towards the earthquakes detected in the area as evidence for the presence of a reservoir here. Furthermore, they suggest that the hot gases condense near the surface and generate a water table emerging within the Agnano plain. The Agnano well has high PCO_2 values, less negative carbon isotope signatures than meteoric water and high HCO_3 concentrations, indicating a contribution of heat and fluids from the magmatic system [Venturi et al., 2017]. Venturi et al. [2017] also point out that the well waters from Agnano plain require the influence of hydrothermal gases and geothermal brines to reconcile measured and theoretical data. However Orlando et al. [2011] argue that Agnano has a more biogenic source, or that secondary processes are modifying the waters composition. In light of the geochemical data at Agnano I hypothesise that the gravity anomaly beneath the Astroni area is a gas reservoir trapped beneath the surface by impermeable hydrothermal precipitates; the gas has therefore gathered beneath the topographically high crater walls. The prevalence of earthquakes in the region may be due to the movement of fluids along faults and it seems likely that there are gas pathways linking Solfatara and Astroni via the network of NW-SE trending faults. It is possible that condensed and compositionally modified gases travel from the reservoir to the Agnano plain, leaving them with a distinct chemical signature.

Solfatara

The anomalous body beneath Solfatara is coincident with a number of source regions found by other authors. InSAR, for example, reveals a network of positive and negative strain sources which evolve through time [D'Auria et al., 2012]. In 2006, a positive strain volume at 2 km depth expanded, and extended two cylindrical volumes towards the surface at Pozzuoli and Solfatara. The Solfatara volume was approximately 0.25 km in radius and 2 km long. The authors correlate this strain volume with an LP swarm in October 2006 at the top of the volume. Similarly Troiano et al. [2014] find a resistive anomaly extending from beneath the fumaroles to 2.25 km depth wth a radius of $\sim$ 0.15 km. Seismic data also finds an anomalous body in the region; Chiodini et al. [2015] show an anomalous V_s zone beneath Solfatara and Pisciarelli which matches well with my modelled anomaly. Chiarabba and Moretti [2006] find low V_p/V_s at sea level beneath Solafatara which they attribute to a shallow gas reservoir. De Siena et al. [2010] also present findings which they suggest are compatible with a small gas reservoir beneath Solfatara using seismic attentuation and V_p/V_s ratios. However, their minimum cell resolution is 0.5 km, similar to the width of the Solfatara crater, and the anomalies they show are offset from the crater and indistinct from the background. I therefore treat this interpretation with caution. My findings at Solfatara are also substantiated by the numerous geochemical models predicting a gas plume there. I suggest that the maar-diatreme structure of Solfatara permits the passage of fluids to the surface unlike the other sources which have no such route. I therefore propose that I have captured the low density signature of hot gas rising from depth to feed the fumaroles at Solfatara.

2.4.2 The Shallow Hydrothermal System at Solfatara

Within Solfatara, the removal of the caldera fill trend imposes a NE trending negative ramp on the data (Fig. 2.8b). This ramp changes the polarity of the anomaly near La Fangaia and reduces the magnitude of the positive north-northeastern crater wall anomaly. It appears that the separation of the simulated caldera fill trend has an adverse impact on the data in the small scale and I therefore interpret only the LBG model (Fig. 2.8a) within Solfatara crater. The key features of the LBG gravity map are the gravity highs on the crater walls ($\sim$ 0.5 mGal), the gravity low on the southeastern side of the crater floor ($\sim$ 1 mGal) and the moderate gravity low near La Fangaia ($\sim$ 0.3 mGal) (Fig. 2.8a). I divide the anomalies into three gravity classes (relative to the average gravity of the crater floor benchmarks). I class the gravity low on the southeastern side of the crater floor as 'low gravity', the moderate gravity low near La Fangaia as 'moderate low gravity', and the gravity highs on the southern and north-northeastern sides of the crater as 'high gravity'. I explore each class in turn and discuss their relationship with other relevant geophysical properties measured within Solfatara (see Fig. 2.14 and Table 2.1).

Low Gravity Class

The low gravity anomaly extends from the eastern side of the crater floor and crosses the crater wall towards Pisciarelli. It coincides with some of the main fumaroles, which are clustered on the eastern side of Solfatara, where the rocks are intensely fractured [Isaia et al., 2015]. I explain the correlation of the gravity low and areas of intense gas emission in two ways. Firstly, upwelling gas-rich fluids replace water in fractures and pore spaces in the rock causing a local decrease in density. Secondly, intense hydrothermal alteration near the fumaroles promotes both the precipitation of light minerals such as amorphous silica and alunite, and creates connected porosities up to 61% [Mayer et al., 2016]. Mayer et al. [2016] conceptualise narrow zones of hydrothermal alteration decreasing in intensity with distance from the fluid pathways. Although the above data is based on surface rocks, Montanaro et al. [2016] suggest that tuffs at 300 m below the surface should have the same properties, since those examined in drill cores at 500 m retain similar porosity, permeability, density and structure. The areas directly around the fumaroles should therefore experience a substantial reduction in density due to the coupled effects of gas and alteration. In the case of Bocca Grande and Bocca Nuova, this low density registers as a gravity low.

However, the low gravity anomaly is associated with some fumaroles and not others. At the time of the survey the most vigorously degassing fumaroles were located at Bocca Nuovo, Bocca Grande and Pisciarelli, though no fumarolic activity was noted on top of the crater wall. These fumaroles are also the hottest of those in the Solfatara area [Chiodini et al., 2011, 2001]. Isaia et al. [2015] have suggested a link between Bocca Nuova, Bocca Grande and Pisciarelli via faulting and fracturing through the crater wall. This region, therefore, may be the main pathway for gases to ascend from deep. The other fumaroles may be fed less voluminously and by narrower, subordinate fracture networks, which are below the resolution provided by the station spacing. I do see strong first horizontal gravity gradient (Fig. 2.9a) extending along the NE crater wall in the region of these other fumaroles; however this could be caused by the contrast between the NE high gravity anomaly and the crater floor. The strongest first and second horizontal gravity gradients (see Fig. 2.9a and b) converge in the vicinity of the low gravity anomaly, indicating that it is strongly influenced by faults and fractures. There is not a strong correlation between gravity gradient and mapping derived faults, indicating perhaps a

more dominant fracture influence.

I compare this low gravity anomaly to resistivity results and the older gravity survey in Solfatara (Fig. 2.14). It overlaps the most eastern lobe of the southern low gravity anomaly (approximately 0.5 mGal) found by the previous survey in 1968 [Bruno et al., 2017; Di Giuseppe et al., 2015; Oliveri del Castillo et al., 1968]. Di Giuseppe et al. [2015] found a high resistivity zone close to Bocca Nuova and Bocca Grande, but little correspondence between resistivity and the other fumaroles. The authors attribute the offset between the resistive body and the 1968 gravity low (see Fig. 2.14) to fluid migration over the time between surveys, but the low gravity anomaly encompasses both the high resistivity body and the 1968 gravity low. Like the 1968 survey however, the gravity low in this study is more intense to the northeast of the fumaroles (Fig. 2.14). It is possible that fluid pathways in the crater continuously evolve over time, however this survey took place within a few years of the resistivity survey. It is more likely that there has not been a shift in the low density source since 1968 but rather that gravity is more sensitive to deeper signals than resistivity.

Other relevant studies in Solfatara that are not possible to depict in Fig. 2.14 include further resistivity, magnetotellurics, temperature, CO_2, self-potential and seismicity. Byrdina et al. [2014] show profiles of resistivity through Solfatara crossing both La Fangaia and Bocca Grande. High resistivity anomalies exist in both the crater walls and beneath the crater floor. Bocca Grande is directly above a narrow zone of moderate resistivity and surrounded by a zone of high temperature, high CO_2 and low self potential. To the east of Bocca Grande is a high resistivity anomaly, and to the west is a low resistivity zone extending towards La Fangaia, overlying a large high resistivity zone; the authors interpret this as a mix of uprising CO_2 and gaseous/liquid water (moderate resistivity) surrounded by gas pockets (high resistivity) and condensate (low resistivity). Although it is difficult to directly compare my results to transects, I suggest that since I do not have data directly east of Bocca Grande, I do not detect the gas pocket there but instead detect the deeper pocket to the west. Additionally, the crater walls to the south of Bocca Grande are high resistivity almost throughout, while the walls to the east are high resistivity within the first 50 m and have variable resistivity below. The authors refer to the high resistivity in the walls as 'vadose zones', I however suggest that they are possible gas rich/high alteration zones. The hypothesis of a gas rich pathway between the main fumaroles and Pisciarelli is not supported by the resistivity measurements of the eastern wall. Additionally, soil and satellite derived temperature data nor CO_2 flux data from 2003-2014 show any significant anomalies here [M. Silvestri et al., 2016]. Troiano et al. [2014] also find a moderately resistive anomaly below the east crater wall and high resistivity anomalies beneath the main fumaroles and Pisciarelli using magnetiotellurics. It seems more likely therefore, that the east crater wall is composed of highly altered rocks with elevated porosity compared to the rest of the rim, indicating relict fluid pathways.

Solfatara demonstrates high levels of seismic noise in an arcuate band from the south to the northeast of the crater floor [Bruno et al., 2007]. Earthquakes are common in and around Solfatara [Chiodini et al., 2017], and Saccorotti et al. [2007] show maximum likelihood locations of LP earthquakes clustered at 500 m depth beneath the SE rim near Bocca Grande. They interpret the LP signals as due to vibrations of fractures in a buried cavity filled by a water-steam mixture. An interpretation of ultra-high resolution seismic imaging of the centre of Solfatara divides the first 30 m into a shallow zone of aerated tephra, a liquid saturated layer below deepening in the direction of La Fangaia and a deeper gas accumulation sloping upwards

towards the eastern side of the crater [De Landro et al., 2017]. On balance, I consider the low gravity anomaly and its gas source interpretation as well supported by alternate geophysical evidence.

High Gravity Class

Interpretation of the high gravity anomalies is inhibited by low benchmarks densities in their vicinity. Additional benchmarks on the south and northeast rims of the crater would have been desirable, but it was not possible due to the rough topography of the crater top and poor accessibility. Co-location of these gravity highs and the Solfatara crytptodome (northeastern) and Mount Olibano lava dome (southern) may therefore be coincidental (see Fig. 2.14). However cross-sections by Isaia et al. [2015] infer that a significant proportion of the southern crater wall is composed of lava dome, and the northeastern gravity high lies in the same region as high gravity from the last gravity survey, which lends support to the theory. The base of the northeastern wall also contains a significant proportion of cryptodome, while the remainder of the walls are composed of tephra deposits. The influence of the cryptodome may be seen in the first horizontal gradient data, where a strong NE crater wall bounding lineament separates the wall and crater fill. I therefore interpret the gravity highs as high density rock volumes.

Moderate Low Gravity Class

The moderate low gravity anomaly is in the vicinity of La Fangaia (Fig. 2.14). The exact location of La Fangaia changes temporally; dried up pits were present during the survey which must previously have been mudpools. I therefore use the fenced-off area to delineate La Fangaia (brown shape in Fig. 2.14), although the most active portion was the southern at the time of the survey. Gentle first and second horizontal gravity gradients bound La Fangaia (Fig. 2.9a and b) and show the same general direction as faults mapped by Isaia et al. [2015], which also mark the approximate boundary of the mudpools. La Fangaia region is encompassed by a zone of low resistivity and low gravity (1968) (Fig. 2.14). The moderate low gravity anomaly of this survey is almost entirely contained by the extent of the 1968 gravity low. Low resistivity suggests high liquid content or the presence of conductive minerals, but Di Giuseppe et al. [2015] infer the former. Intuitively, a low density anomaly here does not make sense; assuming constant porosity, a water rich region should be a higher density than its surroundings.

Di Giuseppe et al. [2015] resolve the issue of conflating resistivity/density/gravity by reasoning that an increased porosity rock filled with volatiles and/or condensates satisfies both the conditions of low resistivity and low density. They do not explain why porosity would be elevated here. However as stated before, hydrothermal alteration promotes the precipitation of light minerals and reduces porosity [Mayer et al., 2016]. Bruno et al. [2007] note that mud and soil samples prove that the interaction between low pH water and Solfatara rocks form alunite among other assemblages, so above background porosity is possible here. Groundwater at Solfatara provides an alternative explanation. The water table is locally raised at Solfatara, outcropping at La Fangaia (97 m a.s.l) and only 7 m below the surface at the OAK well nearby (see Bruno et al. [2017]). This suggests that background densities for the crater are influenced by the presence of liquid water. Therefore, hot, bubble rich water feeding porous rocks at La Fangaia is comparatively less dense and would appear as a low gravity anomaly. Indeed Rinaldi et al. [2011], who base hydrothermal fluid circulation models in TOUGH2 on temperature, degassing and conductivity data, impose two phase (gas and liquid) conditions at La Fangaia.

Anomalies proximal to the moderate low gravity anomaly and not shown in Fig. 2.14 includes high CO_2 flux, low resistivity, low self-potential, high temperature, elevated seismic noise and earthquake clustering (see Table 2.1 for references). Work by Byrdina et al. [2014] includes a cross section (P2 in Byrdina et al. [2014]) which cuts across the middle of the moderate low gravity anomaly and provides a comparison between my data and CO_2 flux, resistivity, self-potential and temperature. Generally, their work shows a positive correlation between CO_2 flux and ground temperature ,which are both anti-correlated with self-potential. The surface of Solfatara demonstrates high CO_2 and ground temperature in the region of La Fangaia, and accordingly low self-potential. The cross section highlights a low resistivity body beneath La Fangaia with a long lobe extending westwards beneath the surface. This lobe approximately matches the portion of the moderate anomaly beyond the boundary of La Fangaia in this study. Byrdina et al. [2014] interpret the confluence of anomalies at La Fangaia as a liquid saturated plume with both a downwelling condensing liquid water and an upwelling vapour and CO_2 mixture. Troiano et al. [2014] also find a low resistivity anomaly on the west side of the crater which they interpret as a hydrothermal aquifer. Seismicity is also anomalous in the region of the moderate anomaly. Although Saccorotti et al. [2007] attribute all three earthquake clusters they find to the SE rim of Solfatara I argue that one is distinctly below La Fangaia. Seismic noise is high near the anomaly, and noise within the crater has been correlated to CO_2 degassing [Bruno et al., 2007]. These factors support my hypothesis that the moderate low density anomaly is due to a combination of low density mud, low density, high porosity altered rock, and a fluid which is gas-rich due to CO_2 outgassing.

2.5 Conclusions

I have carried out the first gravity survey targeted at highlighting the hydrothermal system at Campi Flegrei and updated the only published gravity survey in Solfatara from 1968. My results complement the wealth of geophysical and geochemical data available and strengthen previous findings. The existence of a gas saturated column beneath Solfatara and Pisciarelli has been corroborated by the gravity inversion results. Despite the use of high-quality DEMs, the gravity map of Solfatara crater does not bring to light any more detailed findings than the 1968 survey, though anomaly distributions have evolved. This may indicate that unless fluid pathways are voluminous they remain below the resolution of both survey spacings. I also find a little explored anomaly beneath Astroni crater. As temperature and CO_2 maps outside Solfatara are uncommon there is less evidence than I would like to support this finding; I would highly encourage the production of such maps. I have critically analysed the Pozzuoli anomaly, whose location and size is not unlike other anomalies presented in the literature but requires a different interpretation of a gas body rather than a liquid. Basic caldera fill modelling indicates that the anomaly may be an artefact, however the seismic surveys which suggest a liquid based anomaly are from 2001 at latest. Updated seismic data is ultimately required to verify this particular gravity inversion finding.

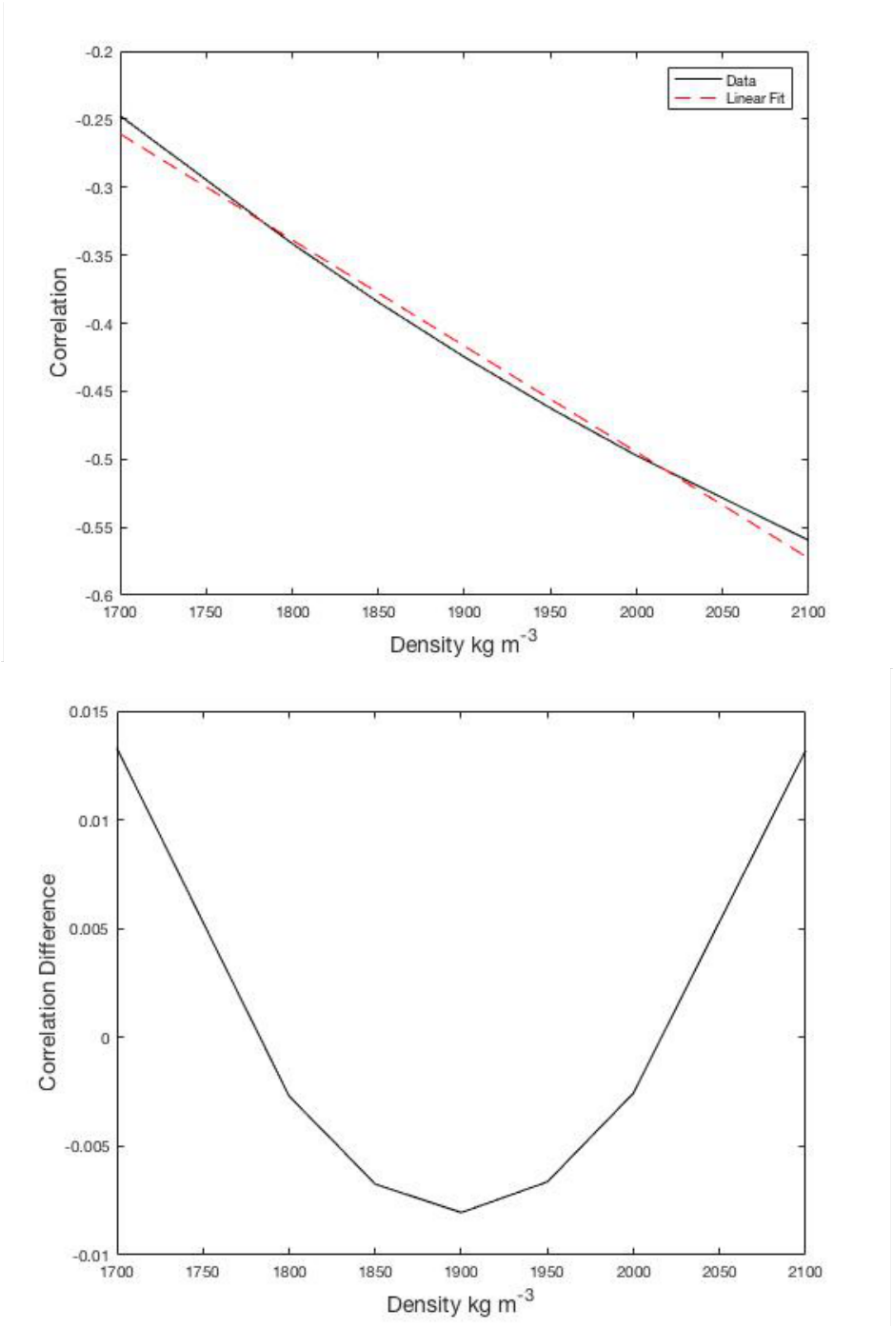

Figure 2.6: Top) Correlation between topography and the density vs. the density, with the best fit line plotted in dashed red, using the method of Eshaghzadeh et al. [2015]. Bottom) The correlation curve less the linear trend plotted against the density. Removal of the trend yields a unique constant which minimises the topographic effects.

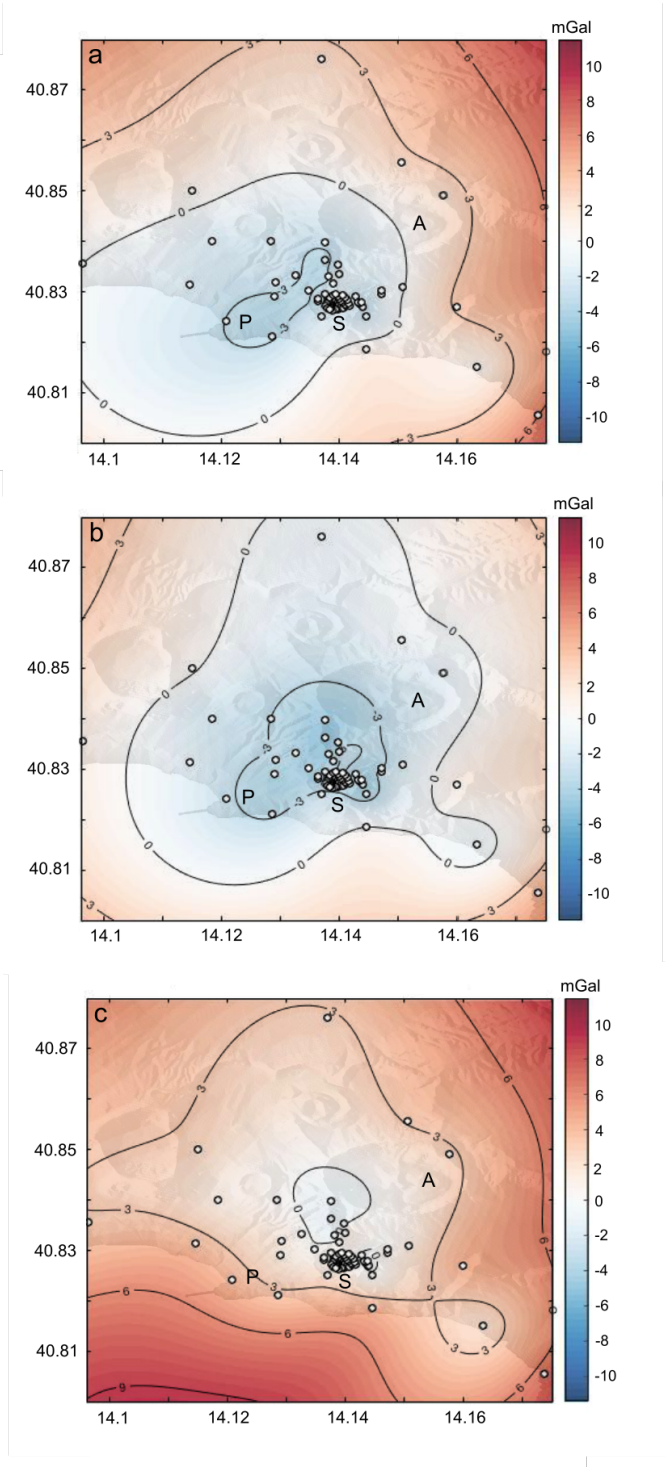

Figure 2.7: a) Regional anomaly. b) Linear Bouguer Gravity (LBG) c) Caldera Bouguer Gravity (CBG). The colourbars are scaled to the maximum absolute gravity of the three datasets. Contours are in mGal and benchmarks are shown in white. The data is overlain on the 10 m DEM and Pozzuoli, Solfatara and Astroni are marked with the letters P, S and A respectively.

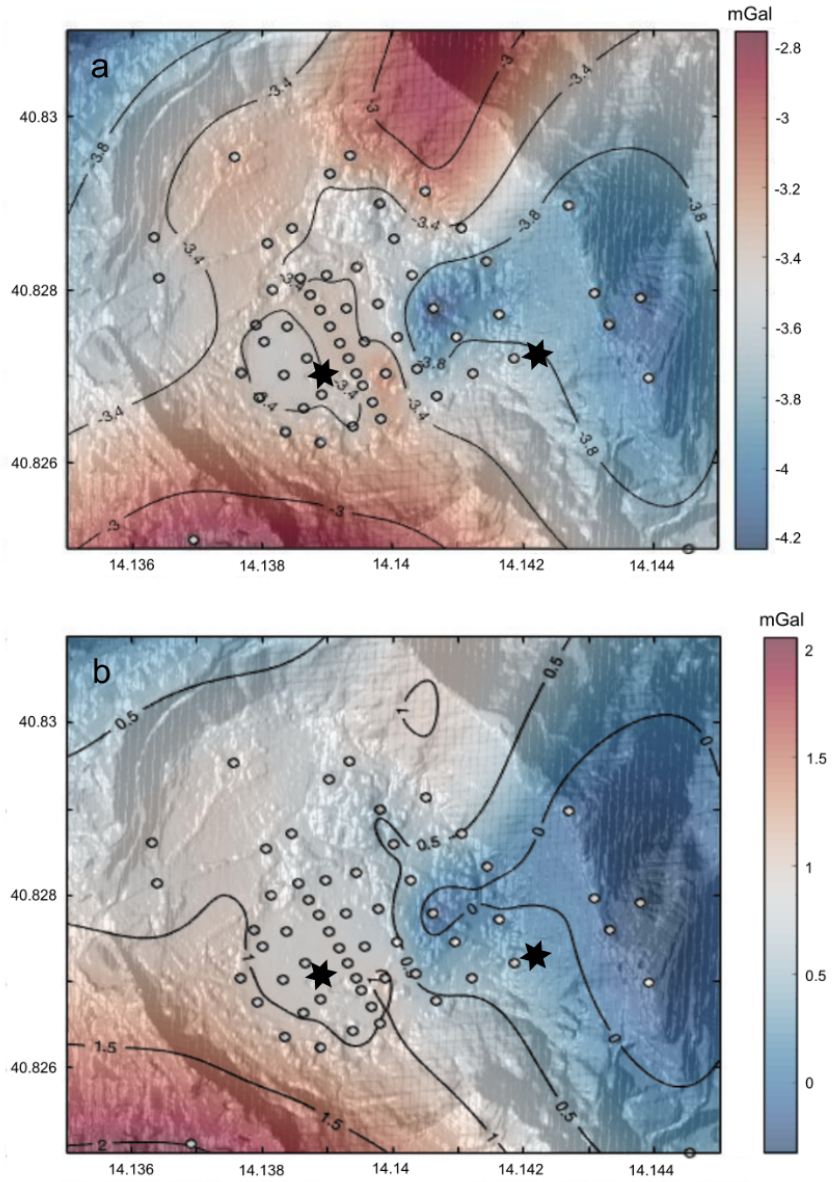

Figure 2.8: Zoom in of Solfatara crater. a) LBG, b) CBG. Colorbars are not scaled. Contours are in mGal and benchmarks are shown in white. The data is overlain on the 1 m DEM and the approximate location of La Fangaia is marked with a black star (left), as is the location of Bocca Grande and Bocca Nuova (right).

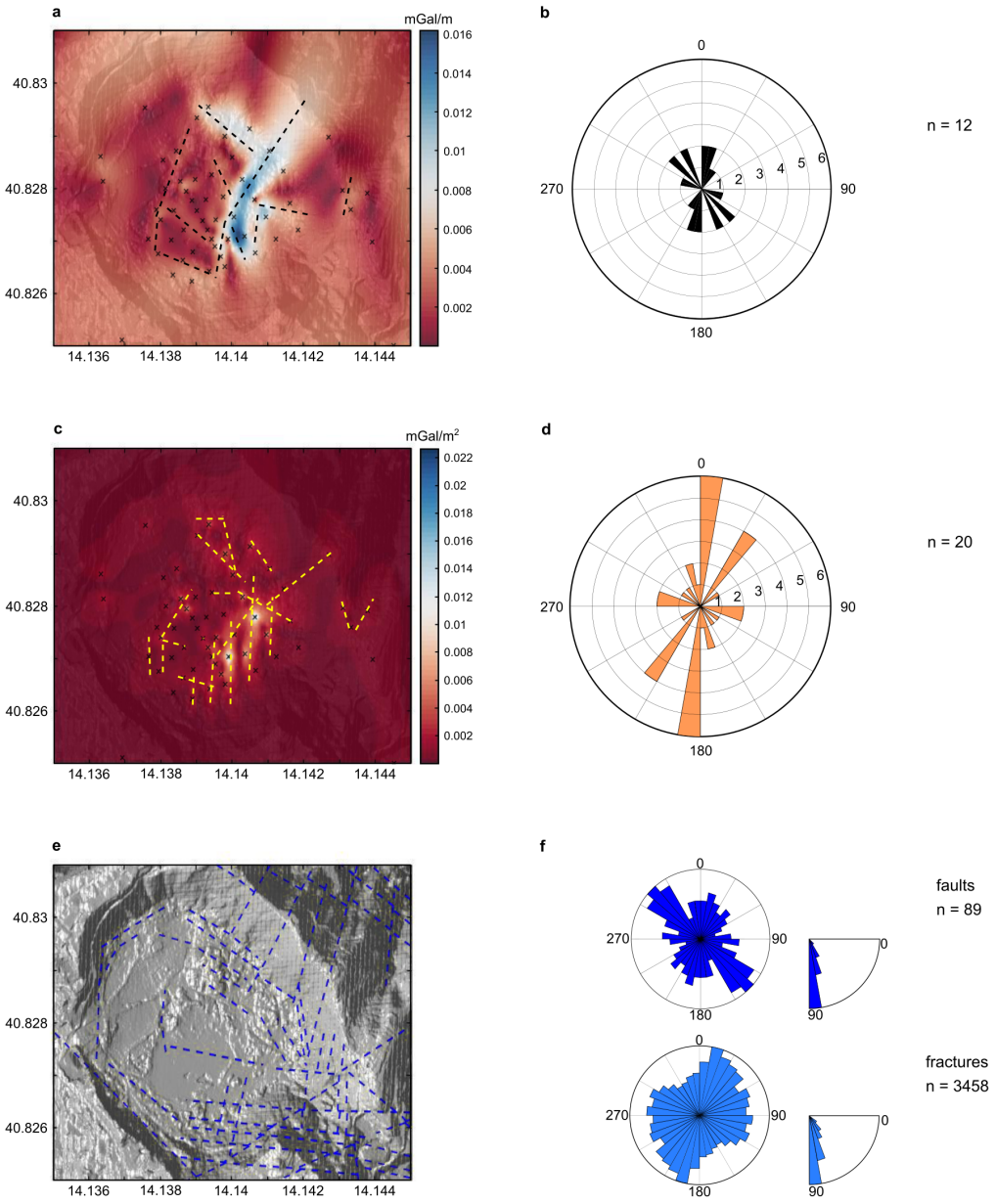

Figure 2.9: Gravity gradient (a,c) and mapping (e) derived faults in Solfatara. a) displays the first total horizontal derivative and faults are shown as dashed black lines, c) displays the second total horizontal derivative and faults are shown as dashed yellow lines and e) displays the DEM of the crater floor and faults mapped by Isaia et al. [2015] as dashed blue lines. b, d and f are the accompanying rose diagrams of the fault strikes, binned in 10 degree increments. f) is adapted from Isaia et al. [2015] and shows the fault strikes (top, dark blue), measured fracture orientations (bottom, light blue) and the accompanying dip angles on the right. Benchmarks are shown as black crosses. Note that peak values in c) are slightly obscured by benchmarks.

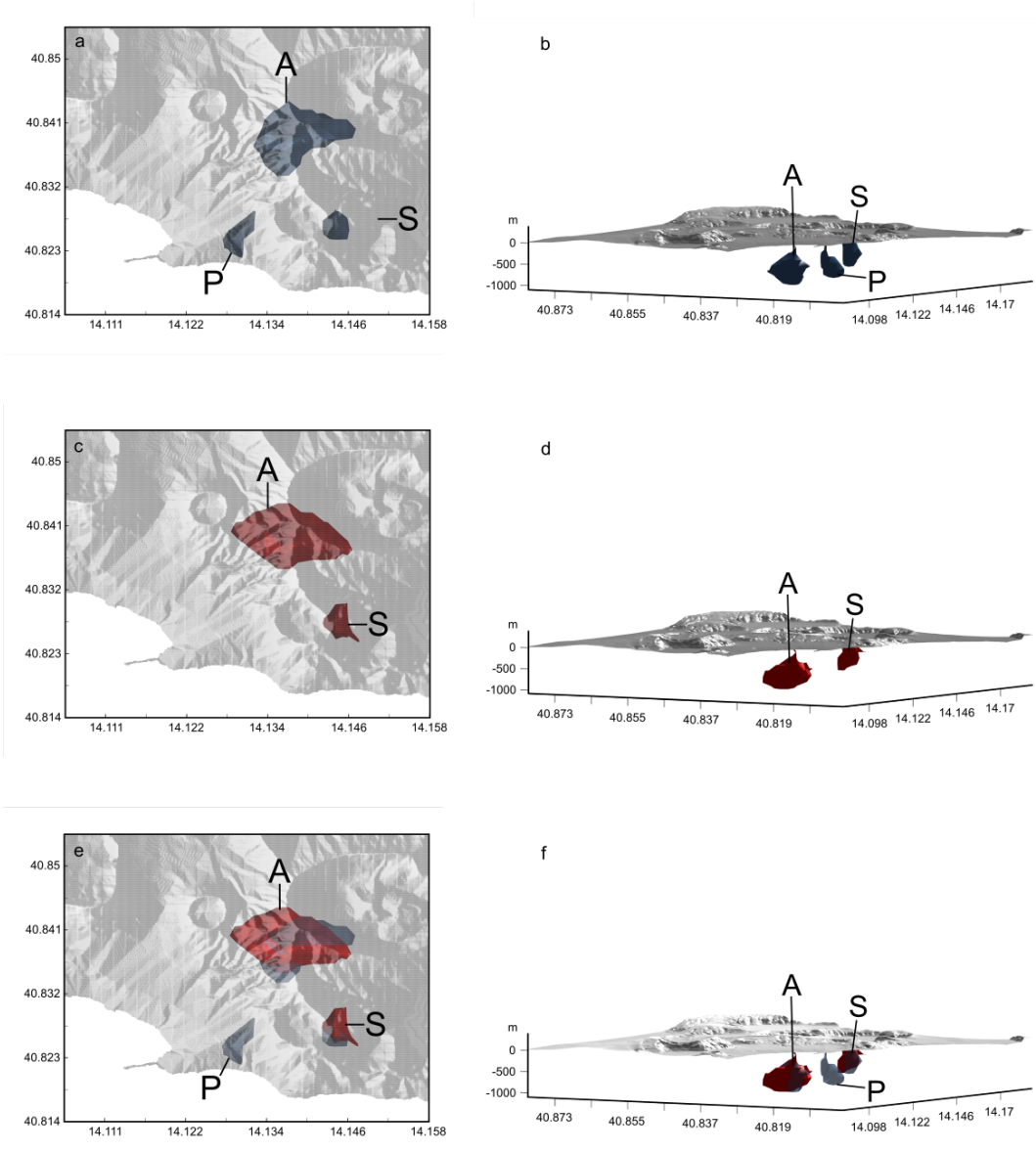

Figure 2.10: a) LBG plan view b) LBG view facing 59 degrees NE c) CBG plan view d) CBG view facing 59 degrees NE e) LBG and CBG plan view e) LBG and CBG view facing 59 degrees NE. The isosurface is set at -550 kg m^{-3} and the a priori density contrasts were $\pm$ 600 kg m^{-3}. The main anomalous bodies are located beneath Pozzuoli, Solfatara and Astroni and are labelled P, S and A respectively.

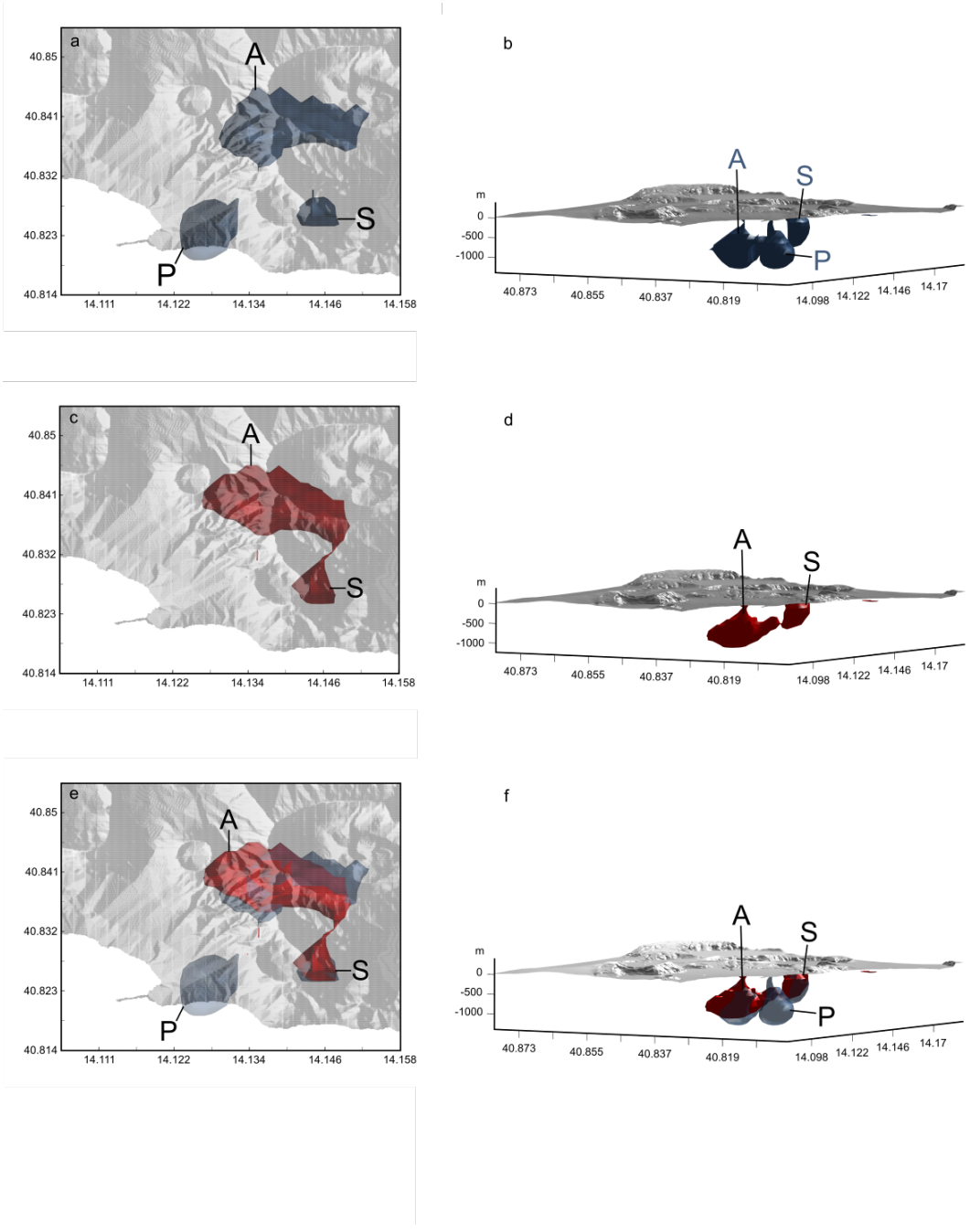

Figure 2.11: a) LBG plan view b) LBG view facing 59 degrees NE c) CBG plan view d) CBG view facing 59 degrees NE e) LBG and CBG plan view e) LBG and CBG view facing 59 degrees NE. The isosurface is set at -400 kg m^{-3} and the a priori density contrasts were $\pm$ 450 kg m^{-3}. The main anomalous bodies are located beneath Pozzuoli, Solfatara and Astroni and are labelled P, S and A respectively.

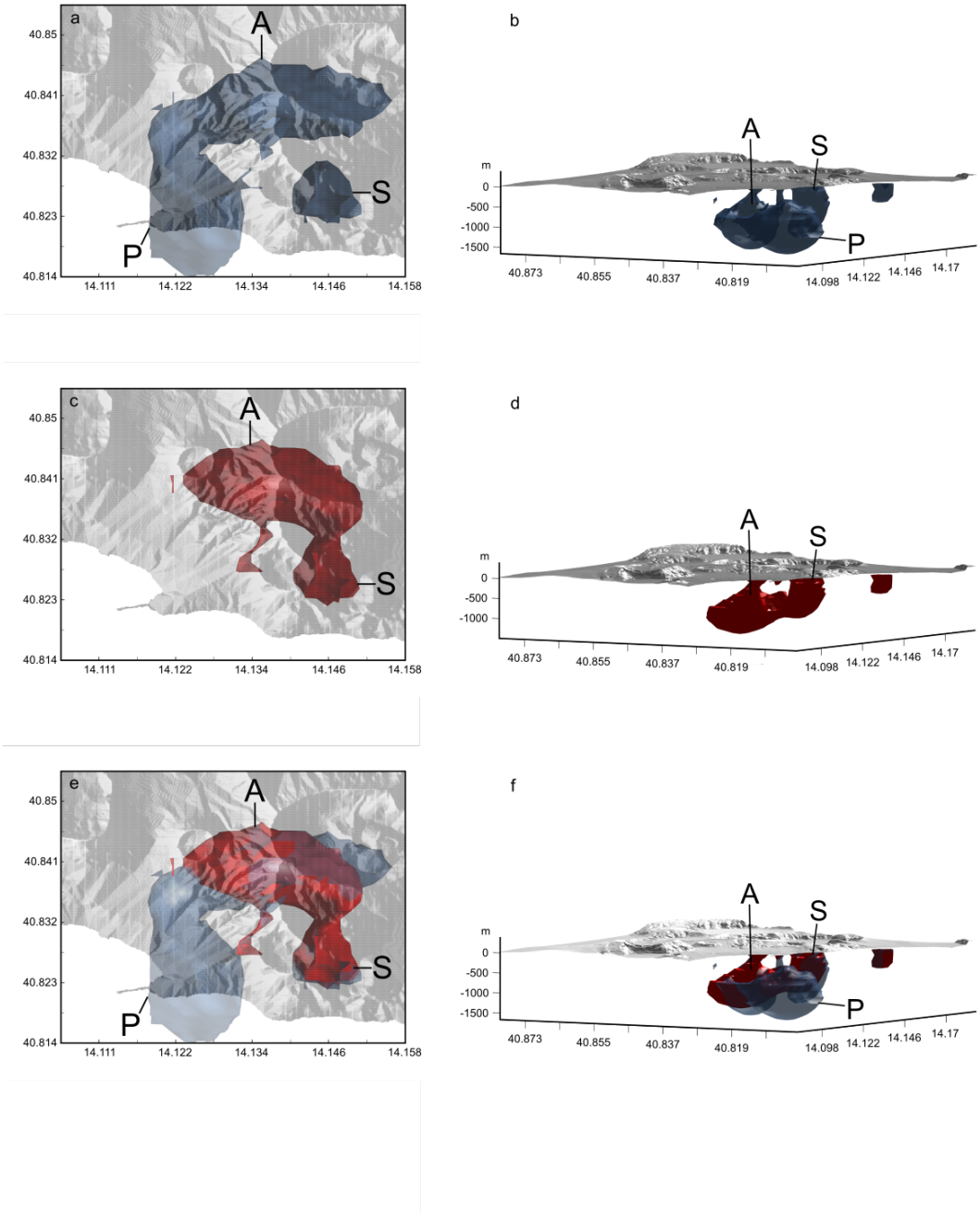

Figure 2.12: a) LBG plan view b) LBG view facing 59 degrees NE c) CBG plan view d) CBG view facing 59 degrees NE e) LBG and CBG plan view e) LBG and CBG view facing 59 degrees NE. The isosurface is set at -250 kg m^{-3} and the a priori density contrasts were $\pm$ 300 kg m^{-3}. The main anomalous bodies are located beneath Pozzuoli, Solfatara and Astroni and are labelled P, S and A respectively.

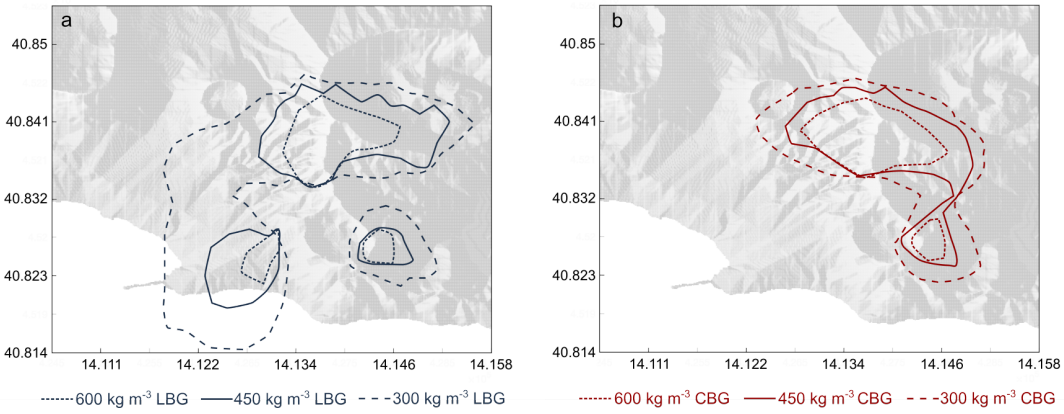

Figure 2.13: a) Surface traces of the LBG anomalous bodies for each density. 600, 450 and 300 kg m^{-3} are represented by dotted, unbroken and dashed lines respectively. b) Surface traces of the CBG anomalous bodies for each density. 600, 450 and 300 kg m^{-3} are represented by dotted, unbroken and dashed lines respectively.

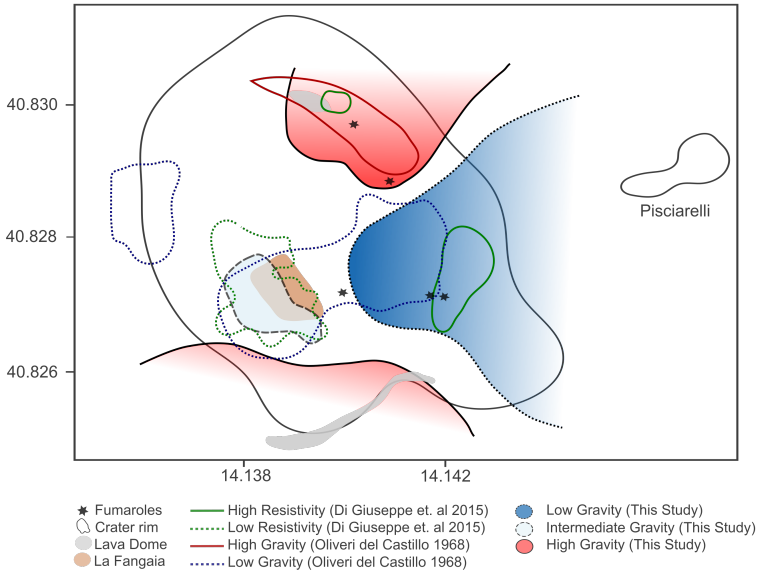

Figure 2.14: Comparison of resistivity and gravity anomalies in Solfatara. Dotted lines denote low magnitude anomalies, dashed lines denote moderate low magnitude anomalies and solid lines denote high magnitude anomalies. The crater outline, Pisciarelli, La Fangaia, fumaroles and lava domes are shown. Colours as in the caption.

Chapter 3

Shallow crustal mechanics from volumetric strain data: Insights from Soufrière Hills Volcano, Montserrat

Young, N. K., & Gottsmann, J. (2015). Shallow crustal mechanics from volumetric strain data: Insights from Soufrire Hills Volcano, Montserrat. *Journal of Geophysical Research: Solid Earth*, 120(3), 1559-1571.

Author contributions and declaration: J. Gottsmann provided supervision and derived the Young's modulus adopted in section 3.3.2, and edited the manuscript for submission. Part of this work came from my MSci research project, but we estimate that this contribution is less than 20% of the paper.

ABSTRACT

Volumetric strain data from the 29 July 2008 Vulcanian explosion of the Soufrière Hills Volcano provide an excellent opportunity to probe the mechanical properties of the volcanic edifice and the shallow crust beneath Montserrat. We use Finite Element Analysis to constrain the geometry of the shallow plumbing system as well as edifice and crustal mechanical properties for mechanically plausible pressure drops associated with dilatational volumetric strains recorded during the explosive activity. Our results from both forward and inverse models indicate a conduit radius of ~ 40 m and a length of ~ 1500 m, and hence much larger conduit dimensions than previously suggested. In order to fit the syn-eruptive volumetric strain data for a conduit pressure drop of < 10 MPa, the conduit needs to be surrounded by a halo of mechanically compliant rocks for which the best-fit models indicate a width of ~ 600 m and a Young's modulus of ~ 1 GPa. Young's Moduli for the main edifice and the shallow crust up to ~ 2000 m b.s.l are found to be ~ 10 GPa. Our best-fit inverse model predicts a syn-eruptive radial conduit contraction by 0.24 m with a corresponding volume loss of ~ 0.1 Mm^3, implying only partial emptying of the conduit upon the explosion. This study demonstrate the critical role of edifice and shallow crustal mechanics for strain partitioning on Montserrat. Our findings may have implications for the assessment of conduit processes at other dome-building volcanoes.

3.1 Introduction

The Soufrière Hills Volcano (SHV; Fig. 3.1) is an andesitic volcano located on the island of Montserrat in the West Indies. The island of Montserrat is a compound volcanic edifice peaking at the SHV whose height currently stands approximately 1 km above sea level [Wadge et al., 2014]. Volcanic activity at the SHV since 1995 has so far involved five phases of dome formation interspersed by periods of eruptive pause [Odbert et al., 2014b].

A wide range of activity has been documented including periods of dome collapses, pyroclastic flows and Vulcanian and sub-Plinian explosions [Sparks and Young, 2002]. Key insights on pre- and syn-eruptive processes of Vulcanian explosions as well as on the size and geometry of SHV's shallow plumbing system have been gained through the analysis of multi-parameter geophysical data [Chardot et al., 2010; Gottsmann et al., 2011; Hautmann et al., 2010a, 2009; Linde et al., 2010; Mattioli et al., 2010; Odbert et al., 2014a; Thomas and Neuberg, 2012; Voight et al., 2010].

The emerging geodetic model of SHV's plumbing system is comprised of vertically stacked magma chambers which connect to a dyke-conduit complex [Elsworth et al., 2008; Gottsmann and Odbert, 2014; Hautmann et al., 2009; Linde et al., 2010; Mattioli et al., 2010]. The concerted view in the published literature regarding the shallowest part of the system indicates that a 1.2 to 2 km long cylindrical conduit connects to the dyke [Costa et al., 2007a; Hautmann et al., 2009; Linde et al., 2010; Voight et al., 2010]. A typical conduit radius of around 15 m has been inferred from the size of extruded andesitic spines [Melnik and Sparks, 2002; Sparks et al., 2000; Voight et al., 1999] though spines of 25 m radius have also been reported [Wadge et al., 2014]. Volumetric strain data have provided important insights on plumbing system dynamics beneath SHV during explosive activity [Chardot et al., 2010; Hautmann et al., 2013b, 2014b; Linde et al., 2010; Voight et al., 2010].

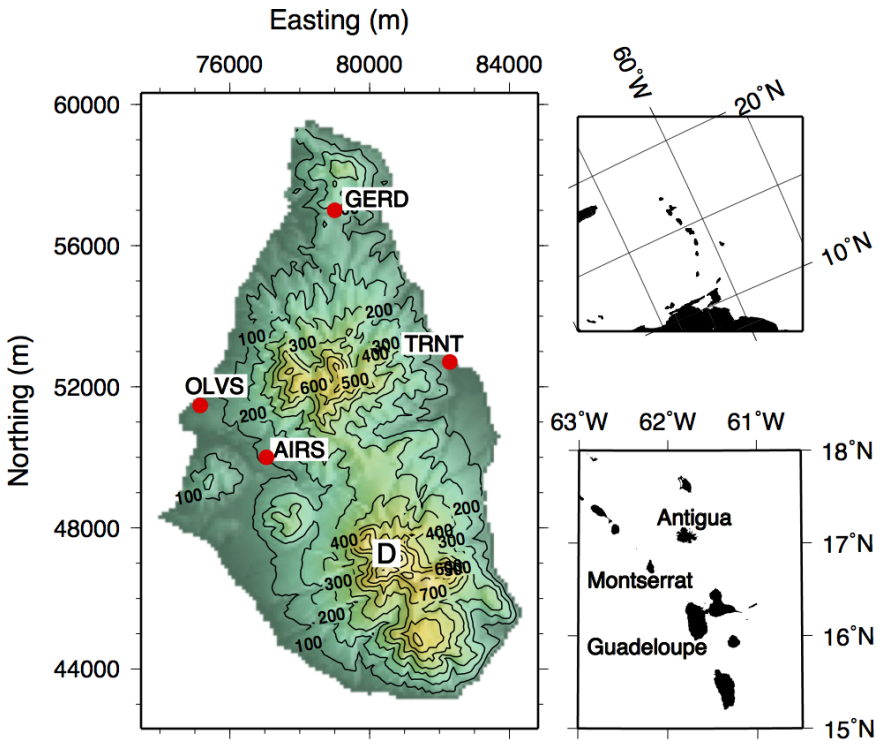

Figure 3.1: Digital elevation model (left panel) of the island of Montserrat as part of the Lesser Antilles volcanic arc (right panels). Locations of strainmeter installations are shown (sites: TRNT, OLVS, GERD and AIRS) as well as the dome complex of Soufrière Hills Volcano (D), which has been the site of recent eruptive activity. Figure adapted from Gottsmann et al. [2011]

Volumetric strains induced by pressure transients in the conduit are thought to be masked when lower sections of the plumbing system are involved in explosions; this has been shown by strain modelling of the various system components of the Soufrière Hills Volcano [Hautmann et al., 2014a; Odbert et al., 2014a]. Consequently the conduit dimensions consistently used in the literature have not been tested by strain modelling [Chardot et al., 2010; Gottsmann et al., 2011; Linde et al., 2010; Voight et al., 2010]. Similarly the effects of topography or mechanical heterogeneity on the strain signature of explosions have so far not been assessed in detail [Chardot et al., 2010; Gottsmann et al., 2011; Linde et al., 2010; Voight et al., 2010].

Topography has been shown to have a measurable effect on strain models [Cayol and Cornet, 1998a], yet, it has commonly been neglected in the analysis of near surface processes at SHV. Many volcano geodetic models applied to explain surface and volumetric strains at SHV ignore mechanical heterogeneity and assume elastic homogenous isotropic mechanics. This is an oversimplification for two main reasons. First, typical rock strengths vary considerably by type and degree of fracturing [Gudmundsson, 2011; Wayne Peter, 2008]. Fracturing in conduit walls is common and some evidence suggests this is the case for the SHV [Widiwijayanti et al., 2005]. Second, layering of mechanically stiff and soft rocks (as is common in stratovolcanoes) has been shown to affect the amplitude of vertical and horizontal surface displacements [Geyer and Gottsmann, 2010; Gudmundsson, 2012a] leading for example to strain amplification with important implications for deduced source pressure changes [Geyer and Gottsmann, 2010; Manconi et al., 2007]. Vertically extended pressure sources in particular can have their strain

signal significantly amplified in the presence of mechanical anisotropies [Folch and Gottsmann, 2006]. Mechanical heterogeneities of the shallow and upper crust beneath Montserrat have been found to significantly influence strain partitioning from the pressurisation of mid and upper crustal reservoirs beneath SHV [Gottsmann and Odbert, 2014; Hautmann et al., 2010a]. Although it is known from recent seismic and gravimetric data that the crustal architecture of Montserrat is very complex, with structures such as horizontal layering [Byerly et al., 2010], stiff andesitic volcanic cores in the island and weakened edifice flanks [Hautmann et al., 2013a; Paulatto et al., 2010; Shalev et al., 2010], geodetic models to explain volumetric strain signals have yet to include such complexities.

In this paper we focus our mechanical analysis on the 29 July 2008 Vulcanian explosion at SHV. This eruption has been interpreted as having been triggered and fed exclusively by dynamics in the shallowest part of the plumbing system; i.e., the conduit [Chardot et al., 2010; Hautmann et al., 2014b]. Extensive strain modelling of the entire SHV plumbing system has isolated and identified the individual signatures of almost every component; conduit signals typically demonstrate a low amplitude strain change on the order of 10s of nS with the same polarity at all sites [Chardot et al., 2010; Hautmann et al., 2014b]. This renders it an ideal candidate for a study on the effects of topography, and heterogeneity.

Using the syn-eruptive volumetric strain signature of this explosion we investigate 1) the effects of topography and mechanical heterogeneity on volumetric strain partitioning in the shallow crust of Montserrat and 2) how volumetric strain data can be used to infer source parameters for shallow conduit mechanics. The aim is to utilise the strain records to inform on the mechanical response of the conduit walls upon decompression, the mechanical properties of the SHV edifice, the amount of conduit closure, pre-eruptive conduit excess pressure and the wavelength and amplitude of resultant surface deformation.

3.2 Background on the 29 July, 2008 eruption

The eruption on 29 July 2008 caused plumes up to 12 km high and generated pyroclastic flows by column collapse [Chardot et al., 2010; Voight et al., 2010]. The eruption produced a total estimated volume of between 0.2 to 1.4 Mm^3 according to field data [Komorowski et al., 2010; Stewart et al., 2009]. Assuming a conduit length of 2000 m and a cylindrical conduit of 15 m radius, the eruption evacuated either a part of the conduit or the entire conduit. The pre-eruptive and syn-eruptive phase of the 29 July explosion was documented in detail by a multi-parameter data set including seismic, barometric, dilatometric, infrasonic and gravimetric observations [Gottsmann et al., 2011]. The eruption was preceded by intense seismicity at 03:32 UTC 29 July 2008 and the first explosion occurred at 03:38 UTC [Chardot et al., 2010], accompanied by a sharp increase in seismicity and acoustic emissions [Gottsmann et al., 2011].

The strain signal showed a six minute long precursory phase, followed by a near linear increase during the main eruption [Chardot et al., 2010]. This syn-eruptive volumetric strain signal (Fig. 3.2) caused the CALIPSO Sacks-Everton borehole strainmeters AIRS (4.6 km radial distance to dome) and TRNT (6 km radial distance to dome) to expand recording maximum strain amplitudes of ~ 31 nS and ~ 12 nS, respectively [Chardot et al., 2010]. Strainmeters GERD and OVLS were not in operation at the time. The signal flattened and then a slow recovery of strain occurred over the next few hours [Chardot et al., 2010; Gottsmann et al., 2011]. For

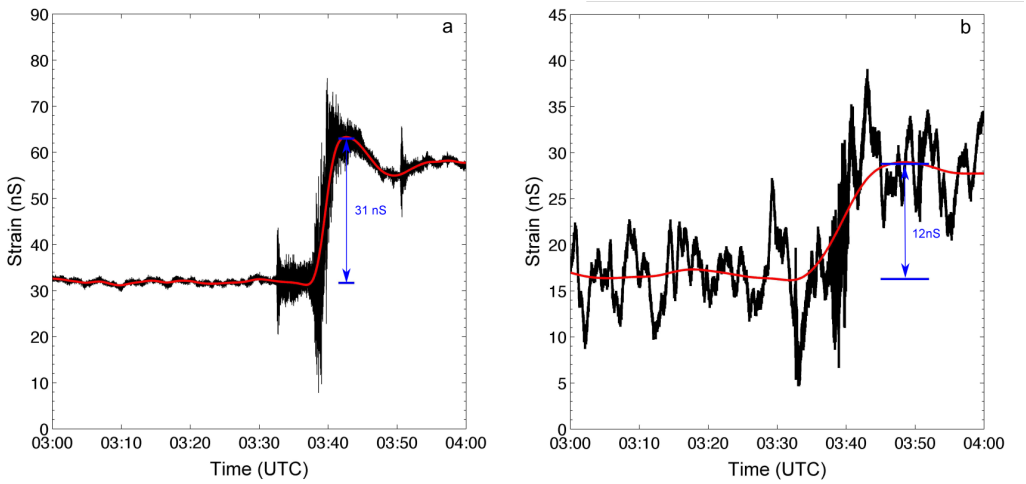

Figure 3.2: Volumetric strains recorded during the eruption on 29 July, 2008 at strainmeters AIRS (a) and TRNT (b). 50 Hz data for AIRS and TRNT is shown in black and filtered data in red. 2nd-order low-pass butterworth filters with a cut-off frequency of 0.0033 Hz for AIRS and 0.000833 Hz for TRNT (to better account for ocean noise) have been applied to derive syn-eruptive strain amplitudes. We derive conservative uncertainty values for the strain amplitudes at the 1σ level of $\pm$ 1 nS and $\pm$ 3 nS at AIRS and TRNT, respectively. Intense seismicity at 03:32 UTC precedes the eruption and is visible in the AIRS 50 Hz record with the first explosion occurring at 03:38 UTC.

this eruption, both strainmeters recorded positive similar amplitude strains (the dike for example typically causes strains on the order of 100 nS at AIRS and TRNT, positive at the former, negative at the latter); therefore the eruption has been attributed to the explosive depressurisation of the conduit only [Chardot et al., 2010; Gottsmann et al., 2011; Hautmann et al., 2014a].

3.3 Methods

3.3.1 Numerical modelling and volumetric strain data

We use a finite-element solver (COMSOL Multiphysics 5.0) to simulate the decompression of a cylindrical conduit as a proxy of the proposed shallow plumbing system at SHV. Because of the quasi-instantaneous response of the strainmeters to the eruption initiation as recorded by seismic and barometric data shown by Gottsmann et al. [2011], we invoke a linear relationship between crustal stress σ and resulting strain ε and attribute elastic mechanical conditions to the modelling domain via Hooke's Law, whereby $\sigma = E \times \varepsilon$ and E is the Young's modulus.

We first explore a series of forward models which have two aims; 1) to test for the effects of topography and heterogeneity and refine the model parameter space and 2) to therefore allow us to define a suitable parameter range of conduit dimensions, pressure drops and domain material properties. We then invert for these properties using the volumetric strain signals from the eruption.

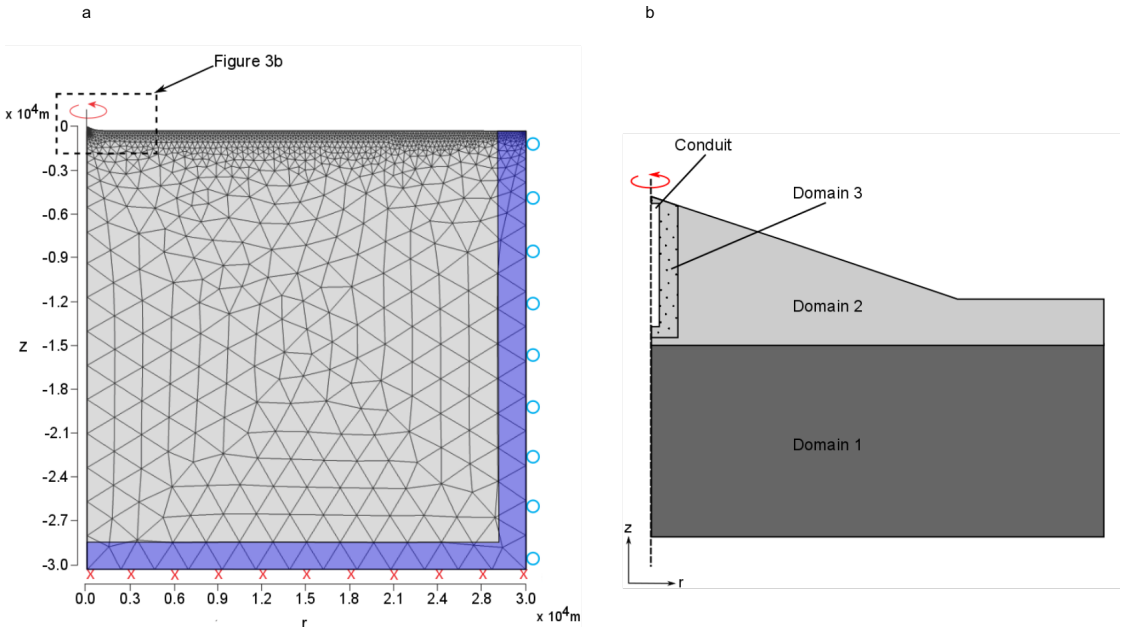

Figure 3.3: a) Finite-Element Model set-up. The 2-D axisymmetric modelling domain was built on a scale large enough to prevent the boundary conditions from interfering with results, but small enough to be computationally quick (ca. 30,000 mesh elements and 100,000 degrees of freedom). This domain obeys Hooke's Law. An infinite element domain is invoked on the lower and right bounds of the halfspace as shown, with the following boundary conditions: (1) a fixed constraint on the bottom boundary to prevent deformation (crosses), (2) a roller on the right boundary to prevent deformation perpendicular to the boundary (circles) and (3) a free top boundary. Values for z are negative and positive for r. b) Zoom-in on model sub-domains including the conduit. Domain 1 has properties which change with depth according to equation 3.4. Domain 2 represents a weak and compliant edifice and shallow crust, extending to z = -1100 m (SCAM and SHAM) and z = -2000 m (DCAM and DHAM) with a Young's modulus of either 1, 5 or 10 GPa. Domain 3 represents a weak and compliant halo and has dimensions of either $2r_c$, $5r_c$, or $10r_c$ and a Young's modulus of either 0.5 or 1 GPa.

Both suites of models are based in a 2-D axisymmetric domain as shown in Fig. 3.3 with dimensions of 30 km in the r and z direction. The top of the domain was set to $z = 0$ m. Fig. 3.3 also shows details of the boundary conditions invoked on the modelling domain according to Hickey and Gottsmann [2014]. The model space size and mesh resolution were tested for conversion and found to be adequate. A series of simple numerical models were benchmarked against analytical models (see supplementary material) for code verification. For simplicity, a cylindrical conduit geometry was used such that uniform boundary conditions, e.g., pressure change could be applied along the conduit wall. Parameters are defined in Table 3.1 and domain properties for the forward and inverse model suites are defined in Table 3.2.

Table 3.1: Model Parameters. EVR = explored value range; m.d. = model dependent

Parameter	Symbol	EVR	Unit
Conduit radius	r_c	15-50	m
Conduit length	l	1000-2000	m
Halo radius	r_h	30-500	m
Young's Modulus	E	m.d. see Table 3.2	GPa
Poisson's Ratio	ν	0.25 (0.4 for domain 3)	-
Pressure Drop	ΔP	m.d.	MPa
Crustal density	ρ_r	m.d.	kg/m^3

Table 3.2: Model parameterisation. The details of each model set-up are shown in terms of invoked topography (Topo.), mechanical heterogeneity (Het.), and geometry (conduit radius r_c and halo radius r_h).

Model ID	Topo.	Het.	Domain 1	Domain 2	Domain 3		r_c	r_h
			E (GPa)	E (GPa)	ν	E (GPa)	(m)	(m)
SBM	none	none	12.5	N/A	N/A	N/A	15	N/A
TBM	yes	none	12.5	N/A	N/A	N/A	15	N/A
HBM	none	yes	Eq. 3.4	N/A	N/A	N/A	15	N/A
CBM	yes	yes	Eq. 3.4	N/A	N/A	N/A	15	N/A
SCAM	yes	yes	Eq. 3.4	1-10	N/A	N/A	15-50	N/A
DCAM	yes	yes	Eq. 3.4	1-10	N/A	N/A	15-50	N/A
SHAM	yes	yes	Eq. 3.4	1-10	0.4	0.5-1	15-50	30-500
DHAM	yes	yes	Eq. 3.4	1-10	0.4	0.5-1	15-50	30-500
ISHAM	yes	yes	Eq. 3.4	1-20	0.4	0.1-5	15-50	75-500
IDHAM	yes	yes	Eq. 3.4	1-20	0.4	0.1-5	15-50	75-500

Volumetric strains at AIRS and TRNT were evaluated by imposing negative pressures on the cylindrical cavity to mimic conduit depressurisation and by varying model geometries and material properties. Best-fit solutions were found by matching the observed strain signals within their 1σ error (AIRS 31 ± 1 nS, TRNT 12 ± 3 nS). We evaluated the quality of fit to the data with a χ^2 test.

$$\chi^2 = \frac{(predicted - observed)^2}{observed} \tag{3.1}$$

Best-fit models hence have χ^2 values < 0.032 for AIRS and < 0.75 for TRNT, respectively.

Using the best-fit model parameters to match data from AIRS and TRNT, we also forward modelled volumetric strains at 9.4 km distance from the vent to predict the signal at strainmeter GERD. Although data from GERD are not available for the eruption, forward-modelling enables

the assessment of strain ratios between the three strainmeters and their comparison against signals from other conduit-dominated Vulcanian explosions such as in July 2003 and January 2009 [Chardot et al., 2010; Voight et al., 2010]. In addition, we also model ground displacements for the best fit-model parameters at all strainmeter sites (see Fig. 3.1; TRNT, OLVS, GERD and AIRS).

3.3.2 Crustal heterogeneity

We adopt a heterogeneous crustal rheological model for those models incorporating heterogeneity. The mechanical properties (density, ρ_r, and Young's modulus, E) of crustal rocks for SHV are parameterised using p-wave velocity (v_p) data by Sevilla et al. [2010] for greater depth ($>$ 7km) and Paulatto et al. [2010] for shallow depths ($<$ 7km) . We use the relationship presented by Brocher [2005] for the ρ_r (kg/m^3) vs. v_p (km/s):

$$\rho_r = 1661.2v_p - 472.1v_p^2 + 67.1v_p^3 - 4.3v_p^4 + 0.106v_p^5. \tag{3.2}$$

and

$$E = \frac{v_p^2\rho_r(1+\nu)(1-2\nu)}{1-\nu} \tag{3.3}$$

Poisson's ratio ν is set at 0.25, consistent with values deduced for Montserrat where the Moho has been imaged at a depth of around 30 km [Sevilla et al., 2010], except for domain 3 where it is set at 0.4 mimicking a very compliant material [Gercek, 2007].

The derived E values were then fitted using a third-order polynomial to obtain a continuous function of E vs z values which then informed the mechanical properties of model domain 1;

$$E = 0.09245 \times 10^{10} - 1.1361 \times 10^7 z - 608.74z^2 - 0.016872z^3. \tag{3.4}$$

where E is in Pa and z is in m.

3.3.3 Forward Models

We explored a series of forward models whose complexities were incrementally increased (see Table 3.2). The Basic Model set examined the effect of topography (Topographic Basic Model TBM), heterogeneity (Heterogenous Basic Model HBM) and a combination of both (Combined Basic Model CBM), compared to the standard model widely used in the literature (Standard Basic Model SBM). SBM is a single domain HoE (Homogenous Elastic) model with a flat surface, TBM is a single domain HoE model with topography, HBM is a single domain heterogenous elastic (HeE) model and CBM is a single domain HeE with topography. The Advanced Model set incorporated more domains with differing material properties. The Shallow Crustal Advanced Model (SCAM) and Deep Crustal Advanced Model (DCAM) are two domain HeE models including topography. The Shallow Halo Advanced Models (SHAM) and Deep Halo Advanced Models (DHAM) are three domain HeE models including topography (see Table 3.2).

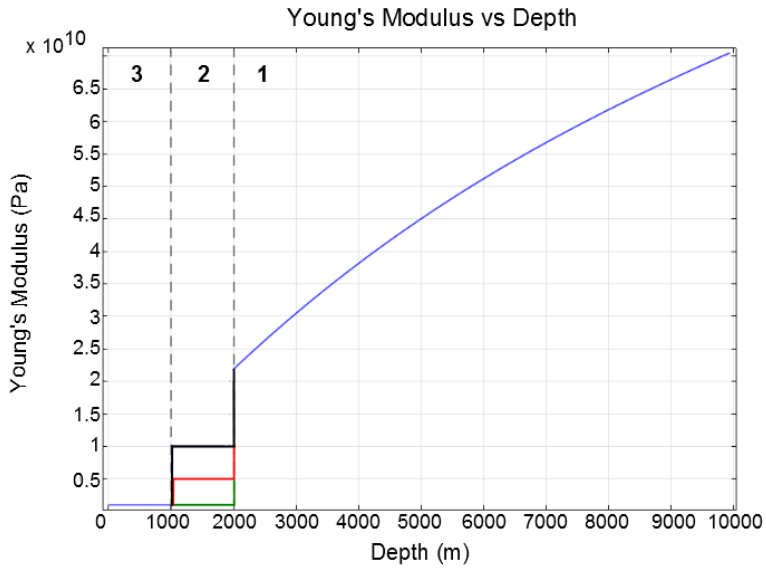

Figure 3.4: Young's modulus vs depth profile for DHAM intersecting all 3 domains. Domain 1 is as per equations 3.2-3.4, domain 2 has E values of 1 GPa (green), 5 GPa (red) or 10 GPa (black) and domain 3 was assigned an E value of either 1 GPa or 0.5 GPa (0.5 GPa not shown).

The simplified topography invoked in models TBM, CBM, SCAM, DCAM, SHAM and DHAM extends to $z = 0$ m (taken as the summit elevation of the SHV edifice in 2008) with a gentle slope towards sea level. Rotation during computation results in an even semi-conical shape. Although we expect erroneous strain results at the intersection between the top of the conduit at $z =$ -10 to -30 m and the top of the edifice due to meshing errors and unstable solutions, solutions at a radial distance $r > 4$ km from the conduit remain unaffected by such effects.

The Advanced Model set is more complex than the Basic Model set, whereby the modelling domain was divided into several sub-domains (Fig. 3.3, Table 3.2) in order to examine the joint effects of different edifice and crustal mechanical properties. Domain 1 represents the crust with mechanical heterogeneity as described in equations 3.2-3.4. Domain 2 represents a fractured edifice and shallow crust invoked by a low Young's modulus between 1 and 10 GPa (to mimic a mechanically compliant and soft material) and extending to $z =$ -1100 m (SCAM) or $z =$ -2000 m (DCAM). The E value range chosen for domain 2 is based on data for Merapi's upper edifice ($E \sim 1$ GPa; Beauducel et al. [2000]), for fractured lavas ($E \sim$ 1-10 GPa; Gudmundsson [2011]), as well as from laboratory measurements of andesitic tuff from SHV (E = 2.25 GPa; Voight et al. [1999]).

Domain 3 represents a cylindrical halo of mechanically compliant and soft material around the conduit with E of either 0.5 or 1 GPa, and with a radius $2r_c$, $5r_c$ and $10r_c$ (SHAM and DHAM). The parameter space presented in Table 3.2 was explored within a Mode-I tensile failure criterion with conduit pressure drops in the range of 1 to 10 MPa, a range consistent with shallow crustal tensile rock strengths [Gudmundsson, 2012a]. See Fig. 3.4 for details of Young's Modulus

change with depth.

3.3.4 Inverse Models

We used the SHAM and DHAM model set-ups as starting points (ISHAM and IDHAM) to invert for geometrical and material properties within set ranges informed by our forward models (Table 3.1 and 3.2). Firstly, we ran a Monte Carlo Simulation inverting for l, r_c, r_h and pressure drop (keeping the material properties constant), and selected those results which were within our 1σ error for the volumetric strain signal. Secondly, we ran a new inversion for material properties of the halo and the edifice, while maintaining a constant geometry provided by the best-fit solution to the prior geometric inverse model. These material properties were permitted to vary from 0.1-5 GPa for the halo and 1-20 GPa for the edifice respectively. We iterated between geometric property inversions and material property inversions given the best-fit solution of each previous model until a solution converged or the iterations remained with the standard deviation of the results.

3.3.5 Conduit Volume Loss

We used the best-fit model parameters from ISHAM and IDHAM to constrain the radial contraction of the conduit during the eruption. By imposing a prescribed radial displacement on the conduit walls instead of negative pressure, we could fit the volumetric strain signals due to a conduit wall contraction and could hence calculate the conduit volume loss.

3.4 Results

3.4.1 Forward Models

The Basic Model set, which assumed $r_c = 15$ m and varying conduit length, did not produce any geologically realistic solutions which fit the volumetric strain data within the 1σ error. SBM, TBM and CBM require pressure drops on the order of 100 MPa to reproduce the strain signal. TBM requires an additional 40 MPa pressure drop in comparison to SBM, similarly CBM requires an additional 50 MPa pressure drop (for $l = 1500$ m). The plausible pressure range (-1 to -10 MPa) was not met for any of the simulations (see Table 3.3). As can be seen in Table 3.3i, the magnitude of the pressure change is controlled by l, whereby the longer the conduit length the lower the required pressure drop. The SBM did not attain the required χ^2 quality of fit for TRNT of < 0.75, however the TBM did match for $l < 2000$ m.The HBM and CBM fitted the data for all explored scenarios (Table 3.3ii).

The Advanced Model set yields satisfactory solutions from DCAM (Table 3.4), SHAM and DHAM (Tables 3.5, 3.6 and 3.7). Model predictions for SCAM do not provide any acceptable fit to the data. Predictions from SHAM and DHAM provide a high number of best-fit solutions. The overall best-fit scenario is obtained by DHAM for a conduit length $l = 1500$-2000 m,conduit radius $r_c = 50$ m, embedded within a mechanically compliant halo with a radius of between $5r_c$ and $10r_c$. The best-fit mechanical properties for the halo are a Young's modulus of 0.5 GPa and a Young's modulus of 5-10 GPa for the shallow crust and edifice. Forward modelling of vertical and horizontal displacement at the strainmeter installations AIRS, TRNT, OLV and

GERD for the best-fit models produces deformation on the order of micrometers to 100s of micrometres, respectively. Forward modelling of the strain signal at GERD produces a strain ratio for AIRS:GERD of $\sim$ 16:1.

Table 3.3: Results from the Basic Model (BM) suite for which model fits to AIRS have χ^2 values < 0.032. Pressure drops reported in MPa and modelled TRNT strain amplitudes in nS with their respective χ^2 value. χ^2 values for TRNT must be $<$ 0.75 to fit the volumetric strain data (shown in bold). See Table 3.2 for model parameterisations.

Model	SBM	TBM	HBM	CBM
i) ΔP (MPa)				
$l = 1000$ m	142	295	95	290
$l = 1500$ m	107	150	70	155
$l = 2000$ m	98	112	60	118
ii) Strain amplitude at TRNT (nS)	SBM	TBM	HBM	CBM
$l = 1000$ m	15.6 (1.11)	**13.4** (0.17)	**11.6** (0.01)	**11.7** (0.01)
$l = 1500$ m	16.1 (1.39)	**13.9** (0.32)	**12.1** (0.00)	**11.8** (0.00)
$l = 2000$ m	18.4 (3.41)	15.1 (0.8)	**122.8** (0.05)	**12.7** (0.04)

Table 3.4: Best-fit results from model suite DCAM for which acceptable pressure drops (1 to 10 MPa) match observed volumetric strains at AIRS within χ^2 values of < 0.032. Predicted volumetric strains at TRNT are shown with the associated χ^2 values. χ^2 values for TRNT must be < 0.75 to fit the volumetric strain data (shown in bold).

Model	l	r_c	E (Domain 2)	TRNT (nS)
DCAM	2000	50	10	**12.1** (0.0009)
DCAM	1500	50	5	**10.3** (0.3)
DCAM	2000	50	5	**10.8** (0.02)
DCAM	1000	25	1	8.5 (1.0)
DCAM	1000	50	1	8.6 (1.0)
DCAM	1500	25	1	8.6 (1.0)
DCAM	1500	50	1	8.7 (0.9)
DCAM	2000	25	1	8.7 (0.9)
DCAM	2000	50	1	8.7 (0.9)

3.4.2 Inverse Models

The solutions from the Monte Carlo simulations for ISHAM and IDHAM converged on similar geometric properties with $r_c \sim 40$ m, $l \sim 1500$ m and $r_h \sim 300$ m (see Table 3.8). These results are very similar to those predicted by our forward models, as shown in Table 3.8. The results on material properties do not converge as well to those obtained by forward modelling, but are reasonably close with E values for the halo of ~ 1 GPa and ~ 10 GPa for the shallow crust and edifice. Based on our inverse model results the best-fit conduit dimensions suggest a conduit volume of ~ 6.5 Mm^3. Furthermore, best-fit modelling of conduit wall displacements (-0.24 m) predicts a volume change within the conduit of 0.1 Mm^3 during the eruption.

Table 3.5: Best-fit results from model suites SHAM and DHAM for halo radius $r_h = 2r_c$, and $\chi^2 < 0.032$ at AIRS and $\chi^2 < 0.75$ at TRNT for predicted volumetric strains. The percentage contribution of tested values (domain 2 E, conduit length l and conduit radius r_c) to the total number of best-fit models (%cbf) is shown. Only results which fit the χ^2 criteria are listed. Results are for a halo with $E = 0.5$ GPa; results for a 1 GPa halo are very similar and available in the supplementary material.

SHAM ($r_h = 2r_c$)						DHAM ($r_h = 2r_c$)					
E	E %cbf	l	l %cbf	r_c	r_c%cbf	E	E %cbf	l	l %cbf	r_c	r_c %cbf
10	33.33	2000	50	50	100	10	37.5	2000	37.5	50	75
5	33.33	1500	50	25	0	5	62.5	1500	37.5	25	25
1	33.33	1000	0	15	0	1	0	1000	25	15	0
No. of best-fit models					6	No. of best-fit models					7

Table 3.6: Best-fit results from model suites SHAM and DHAM for halo radius $r_h = 5r_c$, and $\chi^2 < 0.032$ at AIRS and $\chi^2 < 0.75$ at TRNT for predicted volumetric strains. The percentage contribution of tested values (domain 2 E, conduit length l and conduit radius r_c) to the total number of best-fit models (%cbf) is shown. Only results which fit the χ^2 criteria are listed. Results are for a halo with $E = 0.5$ GPa; results for a 1 GPa halo are very similar and available in the supplementary material.

SHAM ($r_h = 5r_c$)						DHAM ($r_h = 5r_c$)					
E	E %cbf	l	l %cbf	r_c	r_c%cbf	E	E %cbf	l	l %cbf	r_c	r_c %cbf
10	43	2000	43	50	100	10	50	2000	40	50	60
5	28.5	1500	43	25	0	5	50	1500	40	25	40
1	28.5	1000	14	15	0	1	0	1000	20	15	0
No. of best-fit models					7	No. of best-fit models					10

Table 3.7: Best-fit results from model suites SHAM and DHAM for halo radius $r_h = 10r_c$, and $\chi^2 < 0.032$ at AIRS and $\chi^2 < 0.75$ at TRNT for predicted volumetric strains. The percentage contribution of tested values (domain 2 E, conduit length l and conduit radius r_c) to the total number of best-fit models (%cbf) is shown. Only results which fit the χ^2 criteria are listed. Results are for a halo with $E = 0.5$ GPa; results for a 1 GPa halo are very similar and available in the supplementary material.

SHAM ($r_h = 10r_c$)						DHAM ($r_h = 10r_c$)					
E	E %cbf	l	l %cbf	r_c	r_c%cbf	E	E %cbf	l	l %cbf	r_c	r_c %cbf
10	44.44	2000	56	50	78	10	50	2000	40	50	60
5	33.33	1500	33	25	22	5	50	1500	40	25	40
1	22.22	1000	11	15	0	1	0	1000	20	15	0
No. of best-fit models					9	No. of best-fit models					10

3.4.3 Summary of best-fit models

Fig. 3.5 shows our best-fit volumetric strain predictions from model DHAM compared to predictions from models SBM, TBM, HBM, CBM and DCAM. Each model has the same parameter inputs as derived from the best-fit inverse model IDHAM. The latter models predict lower strain amplitudes than observed and require either higher pressures drops and/or lower values of Young's Modulus for domains 1 or 2 to match the observations. Additionally, those models do not appear to partition the volumetric strain according to observations at both AIRS and TRNT. From our set of models, the implementation of the mechanically weak halo in

Table 3.8: Best-fit parameters for inverse model suites ISHAM and IDHAM and associated 1σ uncertainties.

Parameter	ISHAM	IDHAM	Forward Model
r_c (m)	38±7	38±6	25-50
Conduit Length (m)	1550±243	1470 ±275	1500-2000
r_h (m)	283 ±105	263±111	125-500
Pressure drop (MPa)	7±2	6 ±2	-3 to -10
Domain 2 E (GPa)	13±5	8 ±3	5-10
Domain 3 E (GPa)	1±0.2	1±0.7	0.5
AIRS (nS)	31±0.5	31±0.5	31±1
TRNT (nS)	12±0.3	11±0.3	12±3

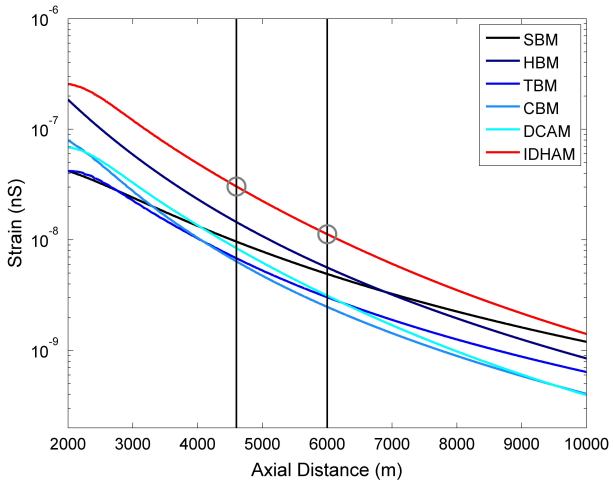

Figure 3.5: A comparison of volumetric strain predictions at sites AIRS and TRNT by best-fit inverse model IDHAM (see Table 3.8) with forward models SBM, TBM, HBM, CBM and DCAM using the model inputs derived from IDHAM.

models (I)DHAM allows us to match the observed strain values within their uncertainties, whilst maintaining geologically and mechanically plausible parameters.

3.5 Discussion

3.5.1 Conduit dimensions and syn-eruptive contraction

The SHV's uppermost plumbing system is thought to be composed of a 1.2 km-2 km long cylindrical conduit [Costa et al., 2007a; Hautmann et al., 2009; Linde et al., 2010; Voight et al., 2010] with $r_c \sim 15$ m matching dimensions of extruded andesitic spines [Melnik and Sparks, 2002; Sparks et al., 2000; Voight et al., 1999]. However, our best-fit models require conduit dimensions that do not fully match those quoted above. The results indicate that the conduit radius might be closer to ~ 40 m, similar to data available from other dome-forming volcanoes. Mount St Helens, for example is postulated to have a conduit of ~ 50 m radius [Scandone and Malone, 1985], although the longevity of this conduit is debated [Scandone et al., 2007]. During the 2006 spine extruding event the conduit exit was thought to be 50-100 m in radius [Pallister et al., 2008]. In our forward models larger conduit widths permit shorter conduit lengths ($<$ 1500 m) and a higher Young's modulus (10 GPa) for the edifice to obtain the same quality of fit.

Here, we only explored conduit radii up to 50 m.The parameter space for radii > 50 m has not been tested.

Furthermore, our best-fit inverse model suggests a conduit length of 1500 ± 299m. Evidence from modelling and seismic data suggests a conduit-to-dyke intersection at between 1 km and 1.5 km depth [Costa et al., 2007a, 2013; Hautmann et al., 2009; Thomas and Neuberg, 2012]. Thomas and Neuberg [2012] and Costa et al. [2007a] propose an abrupt transition from conduit to dyke over a length of 100 m at approximately 1-2 km depth.

A cylindrical conduit of best-fit parameters $r_c \sim 40$ m and $l \sim 1500$ m has a volume of ~ 6.5 Mm^3, and thus is much larger than the estimates for the erupted volume of between 0.2 and 1.4 Mm^3 [Komorowski et al., 2010]. However, we find that by modelling radial contraction of the conduit (mimicking conduit closure), the volume change of the conduit is ~ 0.1 Mm^3 and hence comparable to the lower end of estimates. This would indicate that the conduit only partially emptied during the eruption.

3.5.2 Edifice and shallow crustal mechanics

Published geodetic models for this part of the system commonly neglect topography and mechanical heterogeneities [Chardot et al., 2010; Gottsmann et al., 2011; Voight et al., 2010]. We find these assumptions to be unjustified.

First, we demonstrate that topography and simple mechanical layering affect strain partitioning in the shallow crust. In fact, invoking these complexities required an additional pressure drop of ~ 150 MPa for a conduit of length 1000 m and 20 MPa for a conduit of 2000 m length, compared to a HoE model without topography. We could not achieve solutions yielding mechanically plausible pressure drop values for the Basic Model set, indicating a lack of critical details.

Second, the implementation of sub-domains in the Advanced Model set with distinct mechanical properties significantly improves the quality of fit to the observed volumetric strains for plausible conduit pressure drops ($\sim$ 1-10 MPa). We propose that the way volumetric strain partitions in the shallow crust beneath Montserrat is most sensitive to the mechanical properties of the edifice and the immediate shallow crust. We find best-fit pressure drop solutions for a Young's Modulus of ~ 10 GPa for the volcanic edifice and the immediate shallow crust (ISHAM and IDHAM). We find a greater number of solutions for DHAM than SHAM in our forward models; however, our best-fit inverse models cannot discriminate between them. We do find however, that attributing a Young's modulus of less than 5 GPa to the first 2000 m of the crust does not yield acceptable solutions, particularly to the data recorded at TRNT.

The deduced mechanical properties of the shallow crust do not match the properties suggested by Chardot et al. [2010] and Voight et al. [2010] who invoke very low Young's moduli (~ 3 GPa) for the entire crustal domain. Such a low E value allows these authors to explain volumetric strains recorded during the 29 July, 2008 eruption or similar Vulcanian explosions that are thought to only involve the shallow conduit such as on 13 July, 2003. As we have shown above, invoking such low Young's modulus value for the entire model domain appears to be an oversimplification and unjustified.

3.5.3 Mechanically compliant halo

Our models show the importance of a halo of compliant rocks around the conduit to explain the strain signature during the eruption. The mechanical properties deduced by the modelling indicate a best-fit Young's modulus of ~ 1 GPa, with a radius of ~ 300 m for the halo. This may indicate a zone of mechanically damaged rock around the conduit which profoundly affects strain partitioning. It is conceivable that inelastic effects (including stress corrosion and cyclic fatigue) around the conduit at SHV play a much more crucial role than perhaps hitherto explored. While time-dependent stress corrosion is most sensitive to the mean stress level, cyclic fatigue is most sensitive to the amplitude of the stress cycles [Costin and Holcomb, 1981]. Explosions can cause blasting fractures and loss of cohesion on joints, thus reducing the overall rock strength and country rock stability [Wayne Peter, 2008]. Finally, the conduit wall can also experience erosion due to particles above the fragmentation level and fluid shear stresses [Macedonio et al., 1994].

3.5.4 Volumetric strain ratios

Strain data recorded at GERD for eruptions similar to the 29 July 2008 eruption, such as on 13 July 2003 and 3 January 2009, indicate a ratio of 4:1 between strain amplitudes at AIRS and GERD [Chardot et al., 2010; Voight et al., 2010]. Although data from GERD is not available for the 29 July 2008 eruption, forward modelling of volumetric strain at GERD indicates a ratio of 16:1 between AIRS and GERD. This difference may indicate that the 2-D axisymmetric models employed in this study do not fully capture the three dimensional mechanical complexities such as those discovered by recent seismic and gravimetric studies [Hautmann et al., 2013a; Sevilla et al., 2010]. It will be necessary to test the influence of such structures within the older volcanic edifices on Montserrat as well as large-scale tectonic lineaments on strain partitioning, particularly for eruptions involving the deeper plumbing system.

3.6 Conclusions

This study shows that topography and mechanical heterogeneity fundamentally influence strain partitioning from pressure transients in the near-surface plumbing system of SHV. The results indicate much larger conduit dimensions than have been suggested previously including a halo of damaged and highly compliant rocks around the conduit with a width of ~ 600 m.The immediate shallow crust (to about 1 km b.s.l) of SHV appears to be mechanically compliant with $E \sim 10$ GPa and increasing with depth. Our preferred conceptual model of domain mechanics and conduit dimensions is shown in Fig. 3.6. We find that the exceptional volumetric strain data available for eruptions from SHV provide outstanding opportunities to probe the mechanical properties of the very shallow crust beneath Montserrat and is potentially superior to seismic studies. Invoking mechanical complexities is a necessity to constrain geologically and mechanically plausible conduit pressure drops to fit the volumetric strain signals. Our findings should have implications for the quantification of conduit dynamics and mechanics at other dome-forming volcanoes. In addition, the modeling introduced here may be a useful tool to elucidate shallow crustal mechanics at similar volcanoes.

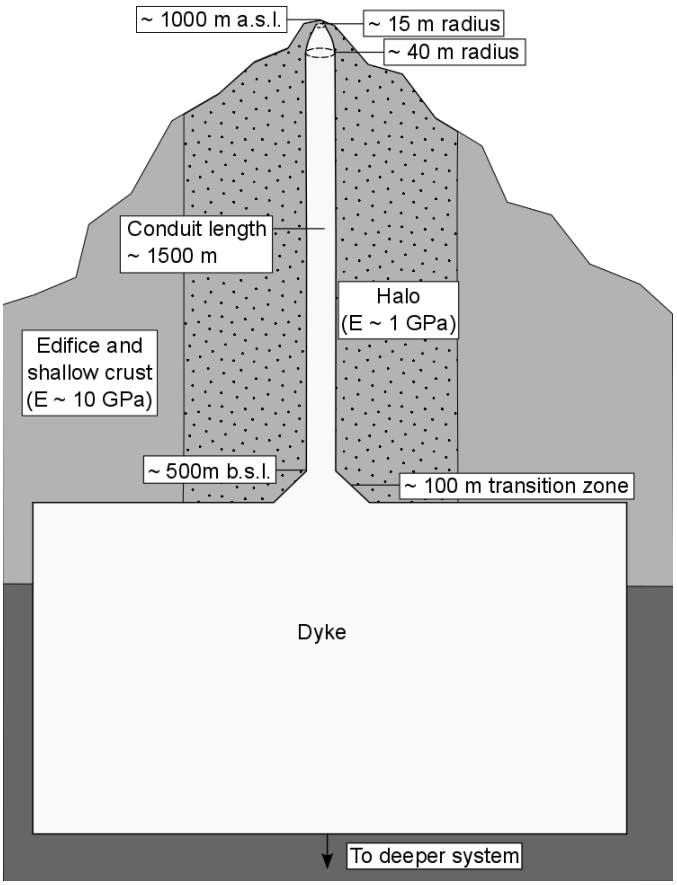

.

Figure 3.6: Proposed conceptual model of the conduit and shallow crustal mechanics at SHV based on best-fit results presented in Table 3.8. The conduit narrows from an average radius of ~ 40 m to about 15 m (based on observed spine dimensions[Melnik and Sparks, 2002; Sparks et al., 2000; Voight et al., 1999] and is embedded within a halo of mechanically compliant material (dotted grey colour). The edifice and the shallow crust are also composed of weakened material (light grey). At depth the rock is mechanically stronger (dark grey). The dyke has not been taken into account in our modelling and is shown here for illustration purposes. The transition zone is drawn after data presented in Thomas and Neuberg [2012] and Costa et al. [2007a]

Chapter 4

Using 3D numerical modelling to test the effect of real topography and volcano specific heterogeneities on volumetric strain partitioning within the shallow crust at Soufrière Hills Volcano, Montserrat

ABSTRACT

Numerical models of deformation at volcanoes experience a difficult trade-off between computational power and mesh complexity when elaborate geometries are involved; therefore they frequently neglect complexities such as real topography and heterogeneity. Additionally, deformation modelling rarely focuses on magma reservoirs shallower than 1 km, therefore knowledge of conduits linking volcano supplies to the surface are largely based on logical inferences, e.g., earthquake clustering. Strain modelling has been used to show that the conduit at Soufrière Hills Volcano is much larger than previously supposed, and that an annulus of weakened rock must exist around it. However this work is limited by symmetry, which inhibits inclusion of complex features such as real topography. In this work, I investigate the same Vulcanian eruption on 29 July 2008 within a 3D model space. I find that the conduit must be asymmetric; I test cylindrical and ellipsoidal geometries and demonstrate that only ellipsoidal solutions fit the volumetric strain data from the eruption. The predominant NE conduit azimuth is in the same orientation as the regional stress in the West Indies, implying that stress regimes at volcanoes may influence conduit formation. Lastly, I integrate the stiff relict volcanic core at Centre Hills into the model and note that this addition allows the previously observed AIRS/GERD strain ratio to be reproduced, a result which was not possible in 2D axisymmetric models nor any other 3D models. The finding of an asymmetric conduit has implications for models of magma transport dynamics, and I suggest that such conduit geometries are likely at other similar volcanoes.

4.1 Introduction

Following a 5 year gap in Vulcanian behaviour, and more than a year's pause in eruptive activity, Soufriere Hills Volcano (SHV) erupted explosively producing well-vesiculated pumice and a 12 km high eruption column [Cole et al., 2014; Komorowski et al., 2010; Wadge et al., 2014]. This eruption on 29 July 2008 provides useful borehole strainmeter data with which to model a depressurising conduit during a Vulanian explosion. In Chapter 3 I extracted useful information from limited axisymmetric models which together highlighted the impacts of simplified topography and mechanical heterogeneity. I acknowledged the limitations of the model set-up and outlined the improvements which would be possible in a more complex 3D model. In this chapter I implement these improvements and explore the benefits of radially unconstrained geometries.

The eruption on 29 July 2008 was extremely well monitored with seismic, barometric, infrasound and gravimetric data, in addition to strain, and occurred as one powerful explosion [see Gottsmann et al., 2011; Komorowski et al., 2010]. Intense seismic swarms occurred on 26-27 July [Komorowski et al., 2010], and on 29 July seismic data showed a gradual onset of activity at approximately 03:32:30 UTC alongside rockfall signals [see Fig. 2 Panel A in Gottsmann et al., 2011]. At 03:38:13 UTC there was a clear increase in activity. This increase was coincident with a pulse in the acoustic trace and the start of the eruption. The barometric record showed a compressive onset marking the opening phase followed by a larger negative pressure wave related to the growing eruptive plume. Gravity data preceding the eruption showed constant values and a 4 minute long perturbation with a peak value of $+40\,\mathrm{nm/s^2}$ at 03:41, which returned to background minutes later. The strainmeter data was similar to the seismic data, in that it demonstrated a 6 minute precursory phase prior to the eruption. The following strain transient during the main phase of the eruption coincided with the pressure wave and the largest seismic

signal. As the strain signal plateaued, the peak gravity signal was reached. The strain signal then recovered over the next few hours and viscous extrusive growth began in early August 2008 [Komorowski et al., 2010]. Gottsmann et al. [2011] point out that strain signature for this Vulcanian eruption is similar to records of other explosions at Monsterrat.

Gottsmann et al. [2011] use the precursory geophysical data to show that the eruption trigger was decoupled from the atmosphere (no acoustic or pressure deviations), and thus were able to rule out dome disintegration or other surface activity. Instead they suggest that the pre-eruptive seismic and strain signal were related to internal conduit processes and internal dome failure. Analysis of eruptive products from preceding explosions in May 2008 showed that 1) juvenile, gas-rich magmatic precursors of the July eruption were already present in the conduit, and 2) the conduit/country rock interface was becoming less permeable due to silicification [Komorowski et al., 2010]. Sealing of permeable pathways due to hydrothermal vapor-phase silification is a plausible mechanism to prevent pre-eruptive degassing and generate overpressure [Komorowski et al., 2010]. Gottsmann et al. [2011] suggest that the 6 minute precursory phase is related to gradual failure of the plumbing system, presumably in response to this overpressure, followed by fragmentation and shallow conduit evacuation. The strain ratios for this eruption clearly rule out involvement of anything deeper than the shallow conduit, making it an ideal candidate to study the mechanics of the shallow crust.

As explained in Chapter 3, volcano deformation models frequently simplify rock mechanics by using a homogeneous elastic half-space. In the case of shallow magma plumbing systems (situated above ~ 2 km depth), I have shown that the assumptions behind this style of model are invalid: i.e., that topography and heterogeneity have a marked effect on strain partitioning in the shallow crust and therefore should not be ignored.

The necessity of incorporating topography has been recognised since the 1990's [e.g., Cayol and Cornet, 1998a; Williams and Wadge, 1998]. However attempts to quantify topographic influences are limited to few volcanoes (in particular Mt. Etna), and range in complexity from analytical Mogi models to fully 3D numerical models (which are few in number) [Bonaccorso et al., 2005; Cayol and Cornet, 1998a,b; Currenti et al., 2011; Lyons et al., 2012; Meo et al., 2008; Trasatti et al., 2003; Williams and Wadge, 1998]. In the case of SHV only one study by Hautmann et al. [2009] includes 3D topography in a ground deformation model, however, its effect is not independently evaluated. Chapter 3 is the first exploration of topographic effects at this volcano and I demonstrate that ignoring topography can lead to an underestimation of modelled pressure drops of up to 150 MPa. However, this model set-up simplifies the edifice geometry to a cone-like feature and cannot fully account for the complexity imparted by real topography. To my knowledge, the effect of fully 3D topography on strain partitioning at any volcano has never been elucidated.

It has become more routine to integrate heterogeneities into volcano deformation models; seismic tomography, for example, is a frequent addition [e.g., Bonaccorso et al., 2016; Hickey et al., 2016]. However this kind of heterogeneity is only applicable to deeper part of the Montserrat volcanic system; tomography fails to capture the details of the top few km of the crust here [Shalev et al., 2010]. Previously investigated shallow mechanical effects include layering of mechanically stiff and soft rocks (e.g. Geyer and Gottsmann [2010]; Manconi et al. [2007]), a compliant halo around volcanic conduits [e.g., Farquharson et al., 2016, Chapter 3], and faults [e.g., Folch and Gottsmann, 2006].

The above list of shallow heterogeneities at SHV is not exhaustive. For example, mechanically stiff andesitic cores representing old volcanic centres have been imaged by gravity and seismic data [Byerly et al., 2010; Hautmann et al., 2013b; Shalev et al., 2010] but their effect on strain partitioning within the island is yet unknown. Modelling this effect was a future aim of Chapter 3 which was not possible before due to the axisymmetric model used.

A 3D model space provides huge scope for exploring the effects of asymmetric domains and their properties, as I have outlined above. An additional avenue of investigation is the geometry of the shallow conduit, and correspondingly its orientation (if the geometry is asymmetric). Most conduits worldwide have more tabular than cylindrical geometries [Gudmundsson, 2012b; Tibaldi, 2015]. Drilling projects and field investigations demonstrate that eruptive paths can be conduit 'zones' composed of brecciated material and multiple dykes, and it has been suggested that a single dyke feeds an eruption rather than the entire conduit [Tibaldi, 2015]. Until now, the conduit at SHV has been assumed to be cylindrical with a radius of 15 m; this width does not deviate in any model except those in Chapter 3.

This assumption is necessary because of a lack of geodetic data [Odbert et al., 2014a]. Any single aspect of the deeper plumbing system (deep chamber, shallow chamber or dyke) produces a deformation signal which must dwarf any concurrent signal from the conduit (see Hautmann et al. [2014b] for a thorough explanation) due to the size discrepancy of the relevant chambers. Eruptions which can be exclusively attributed to the conduit are not common and there is no work aside from that in Chapter 3 which attempts to constrain the conduit width. Instead, the size of extruded andesitic spines is the single constraint used for conduit width [e.g., Melnik and Sparks, 2002; Voight et al., 2010].

The geometry of the conduit is important. Shallow conduit processes have complex relationships with eruptive behaviour [Komorowski et al., 2010] and are linked with short-term risk at SHV [Odbert et al., 2014a]. These processes, which are linked to rapid changes in magma flux within the conduit, take place over hours to tens of hours [Odbert et al., 2014b]. They can include plug-formation, rheological stiffening,stick-slip behaviour and magma fracturing [Odbert et al., 2014b]. However, ascent velocity and discharge rate are strongly influenced by conduit diameter [Melnik and Sparks, 2002; Scandone and Malone, 1985]. Additionally, dyke geometries result in more complex periodic behaviour than cylindrical geometries [Costa et al., 2007a].

Exploring radially asymmetric conduit geometries increases the parameter space and correspondingly the suite of possible solutions compared to Chapter 3. Geological constraints on the solutions include the volumetric strain data accompanying the eruption and details of the emitted volcanic products. I previously used the strain data to limit the solutions and carried out a brief exploration of the resultant conduit volume in the context of the erupted volume. For this chapter, in order to impose plausible limitations on the solution space, I explore the erupted volume in more detail.

Previous work has suggested that the eruption tapped the shallow conduit only [Gottsmann et al., 2011; Komorowski et al., 2010] due to the strain ratios and eruptive products accompanying the event. This theory implies that the eruptive volume is synonymous with the conduit volume.

The dense rock equivalent (DRE) volume of the total eruptive volume and the bulk volume of block and ash flows are reported in the literature for this Vulcanian explosion (see Table 4.1), as well as the average vesicularity of clasts (63% $\pm$ 8, [Komorowski et al., 2010]). I also show bulk volumes for the eruption based on the available porosity and DRE data from Komorowski et al. [2010] in Table 4.1.

In this chapter I will utilise the eruption volume data to constrain plausible conduit geometries (based on syn-eruptive conduit emptying) generated by deformation model solutions fit to volumetric strain data from AIRS, TRNT and GERD during the eruption. I aim to build upon the findings of Chapter 3 and explore the geometry of the conduit at SHV as well as the effects of real topography and volcano-specific heterogeneities (i.e., the stiff cores).

Table 4.1: Recorded and calculated volumes associated with the eruption.

Volume (Mm3)	Details	Reference
1.36	DRE volume of the eruption	Komorowski et al. [2010]
0.2-0.3	Bulk volume of block and ash flows	Stewart et al. [2009]
3.7	Bulk volume of eruption (63% vesicularity)	Komorowski et al. [2010]
3	Bulk volume of the eruption (55% vesicularity)	Komorowski et al. [2010]
4.7	Bulk volume of the eruption (71% vesicularity)	Komorowski et al. [2010]
0.3	Average DRE volume of Vulcanian eruptions in 1997	Cole et al. [2014]; Druitt et al. [
1	Average DRE volume of Vulcanian eruptions between 2008-2010	Wadge et al. [2014]

4.2 Methods

I use COMSOL Multiphysics (v5.1), a finite element solver, to simulate a deforming conduit in an elastic, mechanically heterogeneous volcanic edifice. As in Chapter 3, I explore the effects of topography and heterogeneity sequentially in a series of forward models. However, in this chapter, model attributes are not moderated by rotational symmetry and it is possible to explore more complex and perhaps more realistic geometries.

I first benchmark 3D models against equivalent 2D axisymmetric models from Chapter 3 including the Standard Basic Model (SBM), Topographic Basic Model (TBM), Heterogeneous Basic Model (HBM), Combined Basic Model (CBM), Deep Crustal Advanced Model (DCAM) and Deep Halo Advanced Model (DHAM), which were themselves previously benchmarked against analytical models. I follow methods proposed by Hickey and Gottsmann [2014] for building 3D models, though the basic model set-up and boundary conditions are almost identical to those in Chapter 3, which I briefly outline here. The sides and base of the model are infinite element domains, a fixed constraint is imposed on the base, and the model top acts as a free surface (see Fig. 4.1 a). I use the successfully benchmarked 3D version of the DHAM model from Chapter 3 as a template for further models. It comprises three domains; a deep crustal domain with vertically changing 1D mechanical properties parameterised by seismic P wave data [Paulatto et al., 2010; Sevilla et al., 2010], a shallow crustal domain (to 2 km depth) with homogeneous mechanical properties, and lastly a mechanically weak and compliant halo domain around the conduit. Negative pressure transients imposed on the conduit walls simulate eruptive decompression.

The surface topography for this model was created by transforming the topographic profile from

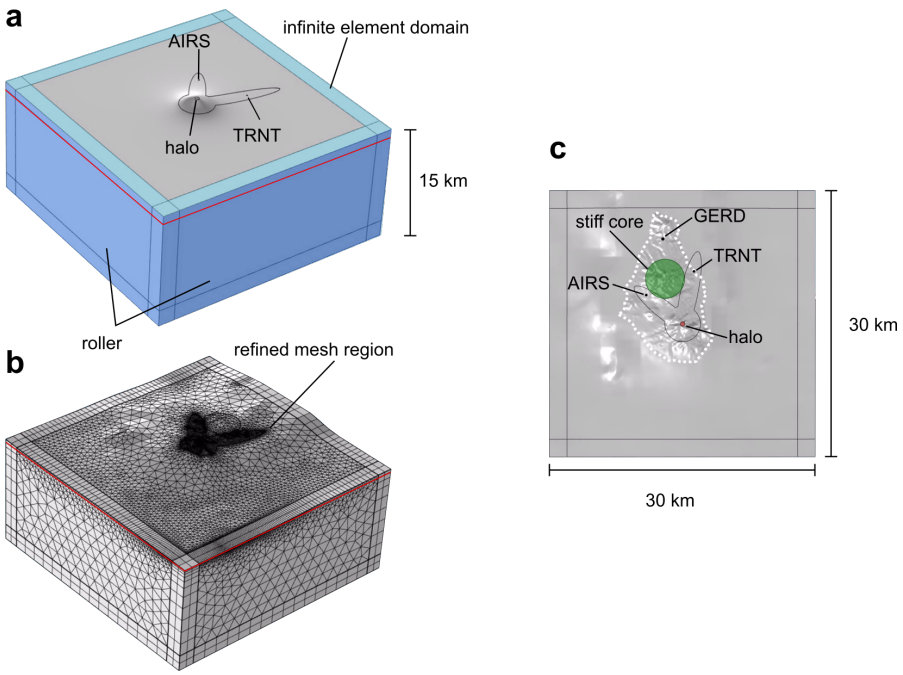

Figure 4.1: The model set-up including (a) boundary conditions, (b) the mesh distrubution and (c) a plan view of the model. a) the Standard Topographic Model (STM) depicting the infinite element domain (shades of blue) and the roller boundaries (dark blue only). The base, (not visible) has a fixed constraint applied, and the model top remains a free surface. The red line indicates the boundary between the shallow and deeper crust, and strainmeters AIRS, TRNT and the halo are indicated. Lastly the mesh refinement is outlined in black. b) The details of the mesh are shown, with a swept mesh on the infinite element domain and a tetrahedral mesh elsewhere. The mesh is refined around the edifice and on the paths between it and the strainmeters. Refinements with a higher mesh density (not visible) are in place locally around the strainmeters. c) the Core Topographic Model (CTM) is shown, with the stiff core and halo in green and red respectively.

Chapter 3 into an xyz grid that was then imported into COMSOL. The resultant surface includes a smooth semi-conical central peak with the same dimensions and slope as in the DHAM model (see Fig. 4.1 a). Similarly, equations 3.2-3.4 (describing crustal heterogeneity) from Chapter 3 were used to generate a series of xyz grids whose Young's moduli change linearly with depth, which were imported into COMSOL as a pseudo-3D tomography for the deep crustal domain.

The size of the complete model is $30\times30\times15$ km. The model space size has been tested for boundary effects which were found to be insignificant. It has $\sim 1.2e^6$ degrees of freedom and is composed of $\sim 2.4e^4$ mesh elements. The complexity and size of the model requires a nested mesh to achieve convergence. This includes a locally refined mesh around each strainmeter and the conduit, and a further mesh refinement around the edifice and in areas between the conduit and the locations of the strainmeters AIRS and TRNT (see Fig. 4.1 b).

Two models were subsequently created based on the template. The first model includes 10 m topography derived from a Digital Elevation Model (DEM) of Montserrat from Le Friant et al. [2004]; hereafter I refer to it as the Real Topographic Model (RTM). The second and last model includes the mechanically stiff core suggested by Hautmann et al. [2013a] at Centre Hills (see

Fig. 4.1 c), hereafter referred to as the Core Topographic Model (CTM). The stiff core is 1.1 km in radius and 2 km in height, with a Young's modulus of 30 GPa. The core was tested for mesh interference and exonerated.

I used the results of Chapter 3 to inform the parameter space explored in the RTM and CTM. I chose to focus on the orientation and ellipticity of the conduit, as it was not possible to do this in the previous axisymmetric model space, and has important implications for conduit processes. The shape of the conduit was therefore approximated by a prolate/tri-axial ellipsoid, with major (vertical) axis c, and minor (horizontal) axes a and b, where $a \leq b$. The azimuth (az) and the minor axes (radii) of the elliptical conduit were explored within pressure conditions commensurate with the tensile strength of rocks [Gudmundsson, 2012a] as shown in Table 4.2. Additionally, I varied the Young's modulus (E) of the shallow crust (see Table 4.2).

The conduit length/semi-major axis (c) of the ellipsoid was kept fixed at 1.5/0.75 km; this parameter has already been explored via modelling and seismic data [Costa et al., 2007a, 2013; Hautmann et al., 2009; Thomas and Neuberg, 2012], while the radius is only assumed based on spine dimensions. For simplicity, the dimensions of the halo were coupled to b, such that the halo radius is $5\times b$. The mechanical properties of the halo were kept constant with a Poisson's ratio of 0.4, and a Young's modulus of 1 GPa. As in Chapter 3, Poisson's ratio was fixed at 0.25 for the remaining domains.

As in Chapter 3, best fit solutions to the observed strain at AIRS and TRNT within their 1σ error (31 ± 1 nanostrain (nS) and 12 ± 3 nS respectively) were evaluated using the standard χ^2 test;

$$\chi^2 = \frac{(predicted - observed)^2}{observed},$$

where AIRS and TRNT have χ^2 values of < 0.032 and < 0.75 respectively.

While the strainmeter GERD was not recording during the eruption, the expected strain ratio between AIRS and GERD is known from other eruptions (4:1) [Hautmann et al., 2014b]. However, in Chapter 3, 2D axisymmetric modelling predicted a strain ratio of 16:1. A desired outcome of 3D modelling stated in Chapter 3 was reducing the discrepancy between predicted and expected strain ratios at GERD. However, meshing a model of $1.35e^4$ km^3 in volume with the object of finding a nanostrain signal from a deforming $5e^{-3}$ km^3 volume is not trivial. The nested mesh configuration shown in Fig. 4.1a is at the limit of computational efficiency and I was unable to include GERD within the refined mesh region (see Fig. 4.1a). Results from GERD cannot be guaranteed to be robust; I therefore limit the use of GERD in modelling and interpretation. As no error data exists, where GERD is used, I apply the same χ^2 criterion as for TRNT.

Using this methodology I iteratively build model complexity and explore the effects of 1) assuming a cylindrical conduit, 2) neglecting real topography, and 3) ignoring shallow heterogeneities in the crust. I use parametric sweeps to explore each combination of azimuth, a and b, where the duration of a single model run time is approximately 7 minutes. Two parametric sweeps are performed for both the RTM and CTM (one sweep per value of E). As the relationship between strain and pressure is linear I explore the pressure parameter in post-processing.

Table 4.2: Model parameter space, where E, a and b have a step size of 5 units, the azimuth (az) has a step size of 10, and the pressure drops have a step size of 1. Note that a and b are semi-minor axes and that pressure drops refer to negative transients.

Model	E (GPa)	a (m)	b (m)	az (°)	Pressure Drop (MPa)
RTM	5-10	5-30	30-55	0-180	1-10
CTM	5-10	5-30	30-55	0-180	1-10

4.3 Results

Parameter sweeps of the RTM and the CTM produced $\sim$4000 individual solutions for each of the chosen shallow crustal Young's moduli. Of these, a small subsection fit the volumetric strain recorded at strainmeters AIRS and TRNT (see Table 4.3) during the eruption on 29 July 2008. The remaining solutions were disregarded. I subdivide the results based on the ellipsoidal conduit volume of each solution; this is based on the inference that the conduit partially or completely evacuated during the eruption [Gottsmann et al., 2011; Komorowski et al., 2010]. I therefore use the eruption volume as a proxy for conduit volume. By this reasoning, I use the dense rock equivalent (DRE) volume ($1.36e^6$ m^3) and the calculated bulk volume ($3.7e^6$ m^3, based on 63% vesicularity, see Table 4.1 for references) for the eruption as upper and lower bounds respectively when selecting plausible solutions from the parametric sweeps. I hereafter refer to solutions whose modelled conduit volumes fall within these bounds as the Volume Fit (VF) solutions.

Table 4.3: Breakdown of the number of solutions which fit the volumetric strain data at AIRS and TRNT (Strain Fit) within the χ^2 criterion and the subset of these solutions whose modelled conduit volumes are between lower and upper bounds of the DRE and bulk volume of the eruption respectively (Volume Fit).

Model	E (GPa)	Iterations	Strain Fit	Volume Fit
RTM	5	3960	53	32
	10	3960	42	25
CTM	5	3960	29	14
	10	3960	17	8

I illustrate the results in Fig. 4.2, which demonstrates the azimuth and eccentricity (with regards to the semi-minor axes) required to fit the data. The DRE volume and bulk volume of the eruption are used to delineate the parameter space which I believe is representative of plausible solutions. There are no solutions for a cylindrical conduit whereby $a = b$ for either the RTM or the CTM. I provide rose diagrams of the conduit azimuths (Fig. 4.3), and histograms of the conduit dimensions, which also demonstrate the frequency of any semi-minor axes pairing (Fig. 4.4).

Raising the rigidity of the shallow crust alters the azimuth distribution of the VF solutions for the RTM (blue segments only) from a primary and secondary peak at 50°E and -10°NW respectively (Fig. 4.3a) to two primary peaks in the previous orientations (Fig. 4.3b). The azimuth distribution of the VF solutions in the CTM model (green segments only) changes from a primary and secondary peak at 60° and -10° respectively (Fig. 4.3c) to two primary peaks at 60° and 50° (Fig. 4.3d) when the rigidity is increased.

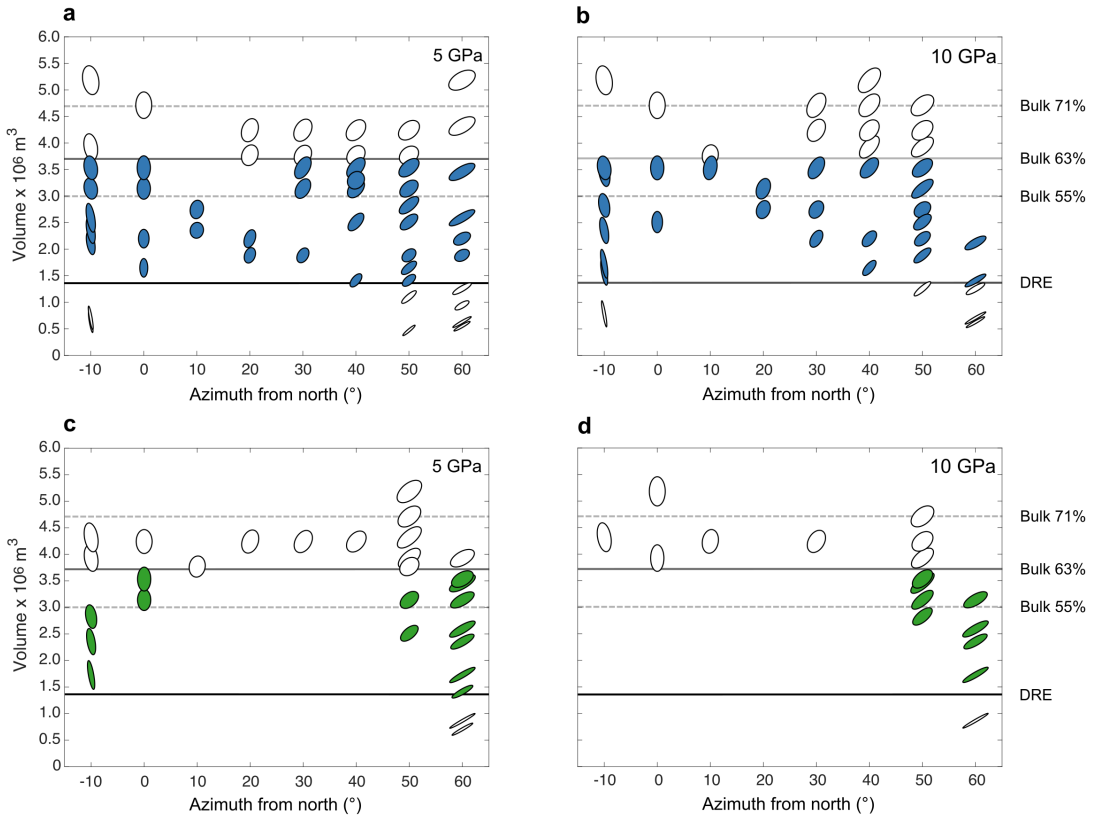

Figure 4.2: The ellipses in each panel show the solutions from a) the RTM for a 5 GPa Young's modulus, b) the RTM for a 10 GPa Young's modulus, c) the CTM for a 5 GPa Young's modulus and d) the CTM for a 10 GPa Young's modulus. Each ellipse represents a plan view of a conduit geometry which fits the data, showing the appropriate azimuth (from north), eccentricity w.r.t. the semi-minor axes, and relative volume. A dark gray (bottom) and a light gray (top) line indicate the DRE volume of the eruption and the calculated bulk volume of the eruption respectively. The dotted lines delineate the uncertainty (8%) on the vesicularity of the erupted products and the corresponding bulk volumes. Blue (a and b) and green (c and d) ellipses represent conduit volumes $\geq 1.36e^6$ m^3 and $\leqslant 3.7e^6$ m^3 (Volume Fit solutions) for the RTM and CTM respectively.

The RTM histograms (Fig. 4.4a and b) demonstrate that VF solutions for a 5 GPa and 10 GPa shallow crust have a peak frequency where $a = 25$ and $b = 40$ or 45. The CTM histograms imply that VF solutions for a Young's modulus of 5 Gpa display no preference for a specific semi-minor axis pairing (Fig. 4.4c) and a weak preference for $a = 20$ and $b = 50$ for a Young's modulus of 10 Gpa (Fig. 4.4d). I compare the range of ellipticities for VF solutions within each histogram in Table 4.4. I define the ellipticity by the axial ratio (ar), where ar = 1 indicates a circle and ar = 0 indicates a line. Higher Young's moduli require conduits with high ellipticity, and overall, the addition of the stiff core promotes more elliptical conduits.

Although I am unable to mesh the models as appropriately for GERD as I have for AIRS and TRNT, I evaluate volumetric strain at the strainmeter location VF solutions. The resultant subset of best-fit models are shown in Table 4.5. Th average ellipticity of the CTM solutions within this subset is 0.45 and a NE conduit orientation is favoured.

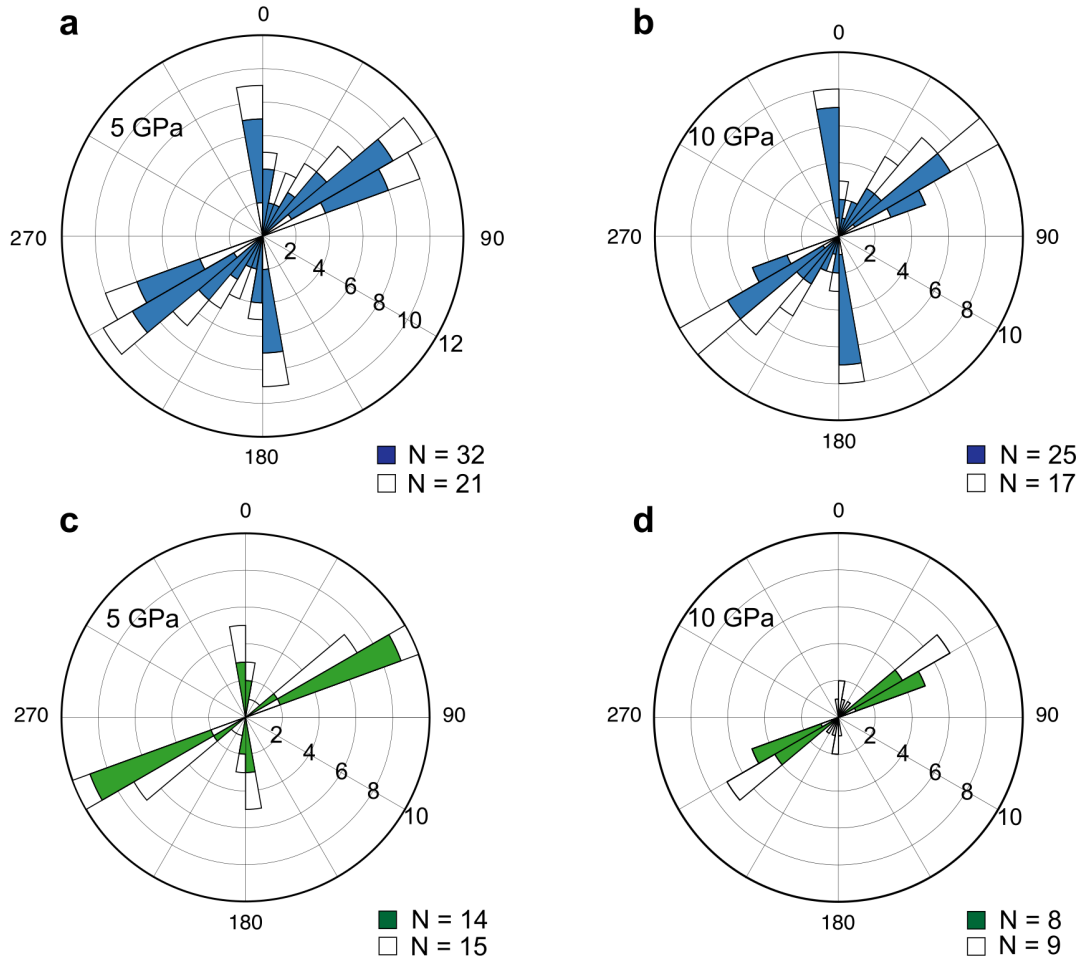

Figure 4.3: Rose diagrams for solutions from a) the RTM for a 5 GPa Young's modulus, b) the RTM for a 10 GPa Young's modulus, c) the CTM for a 5 GPa Young's modulus and d) the CTM for a 10 GPa Young's modulus. The colours are as in the previous figure; blue (a and b) and green (c and d) segments represent conduit volumes $\geq 1.36e^6$ m^3 and $\leqslant 3.7e^6$ m^3 (VF solutions), and white segments represent conduit volumes $< 1.36e^6$ m^3 (closest to diagram centre) or $> 3.7e^6$ m^3 (closest to diagram edge). The entire half length of each bar represents the total number of models which fit any one azimuth as indicated by the segment labels; the individual colours have a population represented by the discrete segment space they occupy.

Table 4.4: Ellipticity of VF solutions by model and Young's modulus. The ellipticity is defined by the axial ratio (ar), where ar = 1 indicates a circle and ar = 0 indicates a line

Model	E	Min Ellipticity	Max Ellipticity	Prevailing Ellipticity
RTM	5	0.86	0.27	0.63 or 0.55
	10	0.71	0.18	0.55
CTM	5	0.63	0.18	N/A
	10	0.55	0.18	0.4

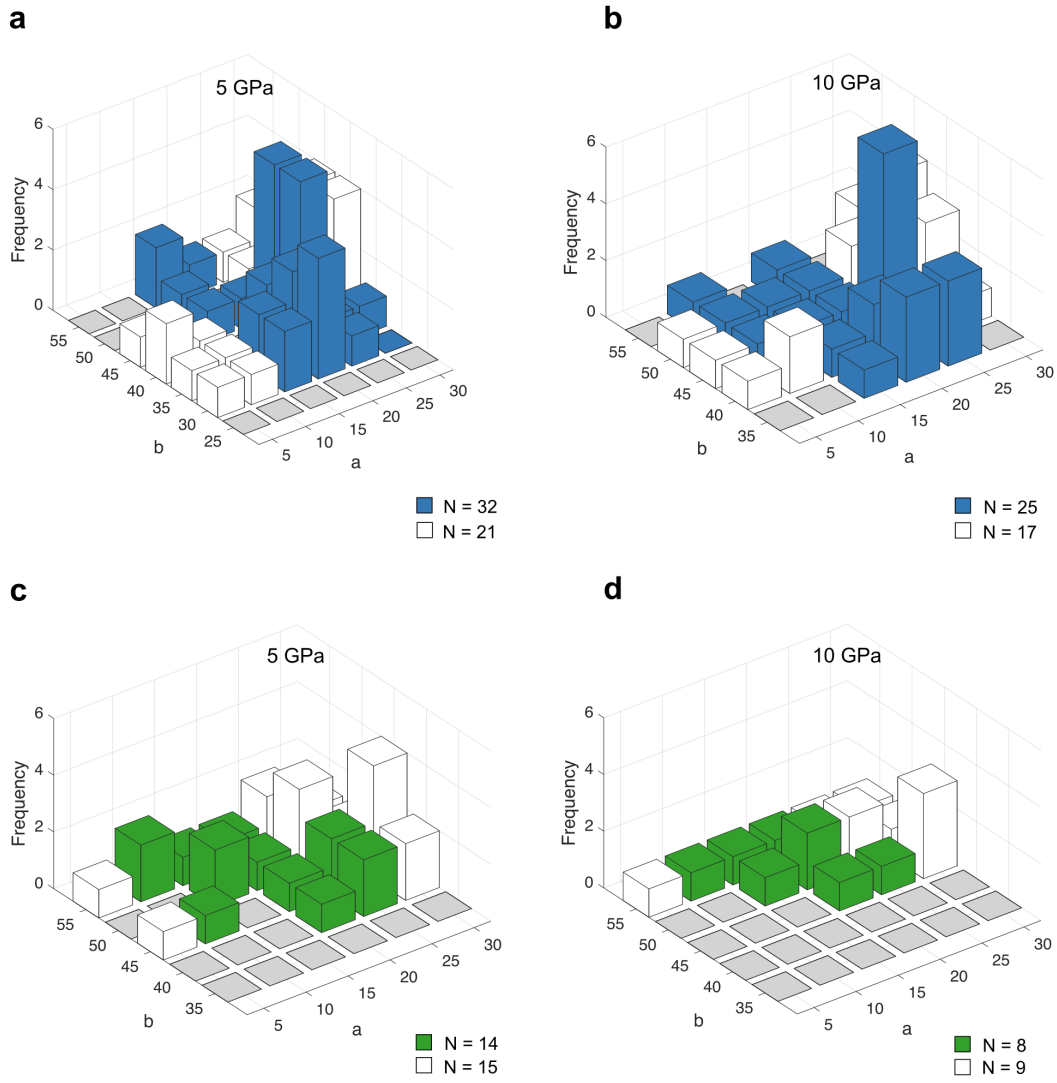

Figure 4.4: Histograms displaying the frequency of semi-minor axes pairings where a) is the RTM for a 5 GPa Young's modulus, b) is the RTM for a 10 GPa Young's modulus, c) is the CTM for a 5 GPa Young's modulus and d) is the CTM for a 10 GPa Young's modulus. The colours are as previously shown; blue (a and b) and green (c and d) bars represent conduit volumes $\geq 1.36e^6$ m^3 and $\leqslant 3.7e^6$ m^3 (VF solutions), and white bars represent conduit volumes $< 1.36e^6$ m^3 or $> 3.7e^6$ m^3.

Lastly, I perform a direct comparison between the STM, RTM and CTM to demonstrate the impact of disregarding real topography and heterogeneity. I select two solutions from Table 4.5 which are representative of the CTM results. I evaluate volumetric strain at all three strainmeters in the RTM and STM using identical starting parameters to those used to produce the CTM solutions (azimuth, a, b, pressure drop).

There are notable variations between model outputs (see Table 4.6). Firstly, both the RTM and STM overestimate volumetric strain compared to the CTM. Secondly, volumetric strain partitioning varies widely by model, as demonstrated by the strain ratios. For reference, I permit

Table 4.5: Subset of best fit-models which also fit the expected volumetric strain at GERD within its χ^2 value

Model	E (GPa)	Azimuth (°)	a (m)	b (m)	Ellipticity	Volume (Mm^3)
RTM	10	60	10	45	0.22	1.41
RTM	10	60	15	45	0.33	2.12
RTM	10	50	25	35	0.71	2.75
CTM	5	0	25	40	0.63	3.14
CTM	5	0	25	45	0.55	3.53
CTM	5	-10	20	45	0.44	2.83
CTM	5	60	10	55	0.18	1.73
CTM	5	60	15	50	0.3	2.36
CTM	5	60	25	45	0.55	3.53
CTM	5	50	20	40	0.50	2.51
CTM	5	50	25	40	0.63	3.14
CTM	10	50	20	45	0.44	2.83
CTM	10	50	20	50	0.40	3.14
CTM	10	50	20	55	0.36	3.46

strain ratios of 2-3.5 and 2.79-6.7 for AIRS/TRNT and AIRS/GERD respectively.

Table 4.6: Direct comparison of STM and RTM against CTM for the same starting parameters.Strain ratios in bold fit within the expected range (2-3.5 and 2.79-6.7 for AIRS/TRNT and AIRS/GERD respectively).

Fixed Parameters				
Solution	E	Azimuth	a	b
1	5	60	15	50
2	5	-10	20	45

Predicted Volumetric Strain						
Solution	Model	AIRS	TRNT	GERD	AIRS/TRNT	AIRS/GERD
	CTM	3.03e-8	1.22e-8	1.07e-8	**2.5**	**2.8**
1	RTM	5.85e-8	2.46e-8	7.51e-9	**2.4**	7.8
	STM	3.89e-8	1.45e-8	2.44e-9	**2.7**	16
	CTM	3.02e-8	1.18e-8	5.41e-9	**2.5**	**6**
2	RTM	4.77e-8	1.94e-8	3.56e-9	**2.5**	13
	STM	3.11e-8	1.09e-8	8.13e-10	**2.9**	38

4.4 Discussion

The results demonstrate the interplay of shallow crustal mechanics and conduit geometry and their impact on strain partitioning in near-surface volcanic systems. I show that a) the conduit must be asymmetric, b) the assumed crustal rigidity affects the conduit azimuth of model solutions and the eccentricity of the conduit geometry, c) the addition of the stiff core greatly reduces the number of viable solutions and increases the eccentricity of the resultant conduit geometries and d) the island-wide distribution of strain varies greatly depending on the inherent assumptions of the model. The CTM solutions suggest that the best fit to the observed volumetric strain at AIRS and TRNT (and the proposed volumetric strain at GERD) is an elliptical conduit orientated NE. This is contrary to the assumed cylindrical geometry that has been solely used for modelling conduit/magmatic processes at the shallowest part of SHV.

4.4.1 Shallow Conduit Geometry

As explained previously, this assumed cylindrical geometry is based on the width of extruded spines; andesitic spines at Montserrat have typical diameters of 30 m, though an anomalously large 50 m diameter spine has been reported [Loughlin et al., 2002]. The small size of the conduit relative to the rest of the magmatic system has led to most of its geodetic signals being masked or undetectable [Hautmann et al., 2014b; Odbert et al., 2014a]. Until now, the spine based cylindrical geometry has been the best possible assumption and the most mathematically convenient to model.

There is substantial evidence for a dyke beneath the shallow conduit [e.g., Hautmann et al., 2009; Roman et al., 2011]. The nature of the junction between them is unclear, but the transition is assumed to take place over ~ 100 m [Costa et al., 2007a]. The assumption of a paired dyke/cylindrical conduit geometry has also been adopted at Colima Volcano by Zobin et al. [2011], despite a previous interpretation of a conduit composed of connected dykes [Zobin et al., 2008]. The cylindrical assumption at Colima is largely driven by observations of spine geometry at SHV and a coupled dyke-conduit model by Costa et al. [2007a]. I also note that the conduit geometry at Mt. St. Helens is also assumed to be cylindrical [Scandone and Malone, 1985].

More generally, cylindrical geometries are often assumed at explosive volcanoes where mechanical erosion by magma excavates the conduit [Cashman et al., 2013]. However, there are examples of explosive volcanoes with dyke-like conduits; Lahr et al. [1994] show that the conduit at Mt. Redoubt is likely to be narrow rather than cylindrical and Chouet et al. [1997] demonstrate a crack-like conduit at Stromboli. The pioneering conduit drilling project at Mt. Unzen discovered a conduit 'zone' 0.5 km wide hosting multiple plate-like dacite dykes which were interpreted to have fed individual eruptions. These dykes are up to 40 m thick and trend perpendicular to the minimum horizontal stress on the volcano. The majority of the solutions trend parallel to the regional compressive stress (NE) and have a thickness < 50 m.

Additionally, most conduits are assumed to be vertical, despite there being plentiful evidence for inclined conduits, [e.g. Chouet et al., 2003; Scheu et al., 2006; Yamamoto et al., 1999]. There is no evidence for or against an inclined conduit at SHV, and it was not possible test a dipping ellipsoid due to time constraints and too little data. Synthetic tests could provide information on how an inclined conduit may partition strain, and if the difference between an inclined and a vertical pipe is detectable above the noise level of the strain data at SHV.

4.4.2 The Importance of Conduit Geometry

The cylindrical conduit at Montserrat and other locations was surmised based on available data, and this assumption has been incorporated into models of magma transport, conduit drawdown and conduit resonance among others [e.g., Chardot et al., 2010; Melnik and Sparks, 2002; Neuberg et al., 2000]. The discovery of a more dyke-like geometry has implications for conduit and magma dynamics. Shallow conduit processes such as plug formation, rheological stiffening, magma fracturing and stick-slip behaviour cause short-term (hours to tens of hours) changes to lava flux [Costa et al., 2007a; Odbert et al., 2014b]. However the geometry of magmatic conduits also influences magma ascent velocity, discharge rate and style of eruption [de' Michieli Vitturi et al., 2008; Melnik and Sparks, 2002; Scandone and Malone, 1985]. For example, Costa et al.

[2007a] show that dykes promote more complex periodic behaviour than cylindrical conduits using models of magma ascent. An additional layer of complexity is the geometry of the junction between the dyke and the shallower conduit. Changes in conduit geometry are strongly coupled to ascent dynamics [Costa et al., 2007a; de' Michieli Vitturi et al., 2008] and this particular junction is theorised to be responsible for past sub-daily cyclic activity[Wadge et al., 2014] and linked to the fragmentation depth during explosions [Thomas and Neuberg, 2012]. Additionally, research on basaltic volcanoes shows that inclined conduits have different flux coefficients than vertical conduits [Palma et al., 2011].

Furthermore, the geometry of the conduit has implications for calculations of conduit drawdown. Using the simplified cylindrical conduit Chardot et al. [2010] estimate a drawdown depth of 2.3-3.5 km for the 29 July 2008 explosion. Chardot et al. [2010] quote DRE volumes (0.93-1.42 Mm^3); I extrapolate from these bulk volumes of 1.6-2.5 Mm^3 and a vesicularity of 44%. I perform the same calculation for an equivalent cylindrical volume of our most and least elliptical conduit models ($a = 5/25$, $b = 55/35$, $c = 750$) using the DRE and bulk volumes. These result in a drawdown depths of 2.4 /0.75 km (DRE) or 6.5/2.0 km (bulk). The variance in calculated drawdowns is large, as is the uncertainty on the erupted volume. Calculations of conduit drawdown depths are heavily dependent on the semi-minor axis or radius of the conduit (which in the literature is always taken to be 15 m). I therefore cannot discriminate between solutions based on their modelled volume; I do suggest however, that the narrowest geometries seem less likely.

4.4.3 Conduit Evacuation/Volume

Although conduit drawdowns are commonly calculated for Vulcanian eruptions at SHV it is not clear if the entire conduit evacuates fully, and eruption processes are not fully understood. Vulcanian eruptions at SHV are short-lived and violent, with plumes extending as high as 15 km and ballistics travelling up to 3 km laterally [Chardot et al., 2010]. Explosion products from 1997 included tabular or platy forms of fallout pumice, and it was thought that these shapes were formed during brittle fragmentation of upper conduit magmatic foam [Druitt et al., 2002]. Lavallée et al. [2012] suggest based on physical experiments that magma may fragment in response to fracturing of wall rock, though they do not suggest where in the conduit this may take place. Due to the consistent location of low frequency (LF) seismic events fragmentation of pumice has been theorised to commence at the conduit/dyke junction at ~ 1.5 km [Thomas and Neuberg, 2012]. The more common view however is that the fragmentation front moves downwards [Burgisser et al., 2011].

Regardless, there are authors who believe the conduit emptied during the eruption [e.g., Gottsmann et al., 2011; Komorowski et al., 2010], and many authors refer to an 'evacuation' of the upper conduit [e.g., Cole et al., 2014; Watts et al., 2002]. The consistency of Vulcanian eruption volume through the history of Montserrat suggests a controlling mechanism on the maximum possible emission; eruptions in the 1900's and 2008-2010 had mean volumes of 0.3 Mm^3 and 1 Mm^3 respectively [Cole et al., 2014]. The change in geometry from shallow conduit to dyke seems a reasonable explanation as put forward by Thomas and Neuberg [2012]. Additionally, the increase in average volume from the 1900's to 2008-2010 could be explained by a change in conduit geometry, more specifically conduit widening due to erosion [e.g., Macedonio et al., 1994; Watts et al., 2002; Wilson et al., 1980].

In the models I impose a pressure change on the boundaries of the conduit geometry. What this boundary is equivalent to in natural systems is not straightforward. Although deforming geometries are almost always simplified to regularly shaped objects, realistically they are likely to be complex zones influenced by heterogeneities such as layering within the volcanic edifice which must cause, for example, local variations in conduit wall strength. Changes in the temperature regime can also cause (centimetric) changes in conduit radius and in wall rock strength [Heap et al., 2017]. Additionally, it has been suggested that not all the magma in the conduit empties during an eruption, but that the high vesicularity core material exits first while the low-porosity lining is less likely to escape [Kennedy et al., 2005].

Clearly the issue of conduit evacuation is not straightforward. This makes it difficult to concisely link the eruption volume and the volume of the conduit. I do not know what the porosity distribution was within the conduit, though it was likely to be complex. I therefore must be satisfied that the true bulk volume of the conduit is somewhere between the quoted approximate DRE and the bulk volume assuming maximum porosity throughout.

4.4.4 The Azimuth Debate

The results broadly favour two conduit azimuths, 60°E and 10°NW. These orientations mirror those debated in the literature for the established long axis of the dyke at SHV. The orientation of the dyke is a controversial topic which has by no means been resolved. The evidence in favour of a NE azimuth lies in the regional stress field, dyke orientations, stress field modelling, and strain models [Chardot et al., 2010; Roman et al., 2011; Wadge, 1986]. Evidence promoting a NW orientation is given by shear wave splitting, NW oriented fault zones, strain and ground deformation modelling [Baird et al., 2015; Hautmann et al., 2010a, 2009, 2014b; Le Friant et al., 2004; Mattioli, 1998]. Mattioli [1998] outlines how NE and NW trending extension may both be common features, discussing Lesser Antilliean dyke orientations and sector collapse features including the NE opening English Crater.

The orientation and alignment of spines exiting the shallow conduit do not constrain the azimuth. Explosion craters and magma discharge followed a NNW alignment during the early stages of the eruption, however growth directions of magma lobes have followed all directions [Watts et al., 2002]. Additionally, NE-SW lineaments have been highlighted by earthquake alignment [Aspinall et al., 1998].

Nakamura [1977] suggests that the trend of dykes may be normal to the minimum compressive stress, or in the direction of the maximum compressive stress. For Montserrat, the regional stress orientation is NE/SW, however the local stress regime at the volcano is dynamic and debated. The polarisation of shear wave splitting (thought to be controlled by structural features) can change with time, some changes have been attributed to pressurisation of a dyke [Baird et al., 2015; Roman et al., 2011]. Baird et al. [2015] point out that while Wadge [1986] found an overall trend of NE orientated dykes in the Lesser Antilles no dykes were measured on Montserrat and while they do find NE trends on the island, seismic stations closest to the volcano suggest a NW orientation of structures. However, it does not necessarily follow that the shallow conduit must have the same orientation as the lower system, or be influenced by the regional stress regime. It is located chiefly within the volcanic edifice; deposit loading deforms the first few km of the crust and is inferred to influence degassing in the shallow conduit [Odbert et al., 2015]. Indeed, dykes

are often observed to be radial around the central edifice due to the stresses and gravitational force they impose [Galgana et al., 2013; Nakamura, 1977; Poland et al., 2008].

CTM solutions which fit the volumetric strain data at AIRS and TRNT favour a predominant NE conduit orientation for a shallow crust with both a 5 and 10 GPa Young's modulus. However a 10 GPa shallow crust has no solutions for a NW orientation, where a 5 GPa shallow crust does. As in Chapter 3, I based the explored Young's moduli on measurements of andesitic tuff from SHV (E$\sim$ 2.3 GPa), values for fractured lavas (E$\sim$ 1-10 GPa) and data for Merapi's upper edifice (E$\sim$ 1 GPa) [Beauducel et al., 2000; Gudmundsson, 2011; Voight et al., 1999]. Pyroclastic rocks from Tenerife and elsewhere in the literature are quoted to have Young's moduli between 3.4 -14.1 GPa (see [del Potro and Hürlimann, 2008]) and measurements of andesitic rocks from Bodrum peninsula found a range of Young's moduli from 8-18 GPa [Dinçer et al., 2004]. With such a range of rock stiffness it is not possible to select solutions by Young's modulus.

The addition of GERD does not help discriminate between solutions by Young's modulus, and therefore preferentially select an azimuth as solutions which also fit the strain data at GERD have similar azimuth distributions to those for AIRS and TRNT only. To summarise, the solutions favour a NE direction and a subsidiary NNW orientation. Although the latter orientation is less supported by the data, it has more endorsement from the literature than the former NE orientation. Costa et al. [2007b]; Hautmann et al. [2009, 2014b]; Linde et al. [2010]; Mattioli [1998] among others support a NW-SE lower dyke azimuth. Rock mechanics, the regional and local stress field and existing structures are equally supportive of both orientations. However, due to the prevalence of the NE azimuth in the solutions I favour it over the less frequent NW azimuth.

4.4.5 Strain Partitioning

The effects of conduit azimuth, topography and heterogeneity on modelling shallow strain partitioning are made particularly clear in Fig. 4.5. The variation by model, strainmeter path and conduit azimuth are complex and unpredictable. The effect of the stiff core is particularly well illustrated; the strain transported by the core plummets, but unexpectedly also rises before and after encountering the stiff core. The largest difference appears to be due to the addition of real topography. The largest discrepancy is close to the conduit, indicating that a simplified cone topography in the STM is a poor substitute for the real ground surface. The different azimuths also promote very different strain evolution, particularly for the path between the strainmeter and GERD.

I theorised in Chapter 3 that further heterogeneities may have been responsible for the poorly fitting strain fit at GERD produced by the axisymmetric model. The best fit for the DHAM model was a ratio of 1:16 (AIRS:GERD) when a ratio of 1:2.79-6.7 is compatible with eruption data. I have shown that the addition of real topography followed by the stiff core progressively lowers the ratio to acceptable levels in the CTM. I note that GERD is not meshed as appropriately as AIRS and TRNT, however since the axisymmetric model in Chapter 3 and the 3D STM models find similarly large ratios (see Table 4.6 for comparison) I am confident that meshing insufficiencies are not unduly affecting the results.

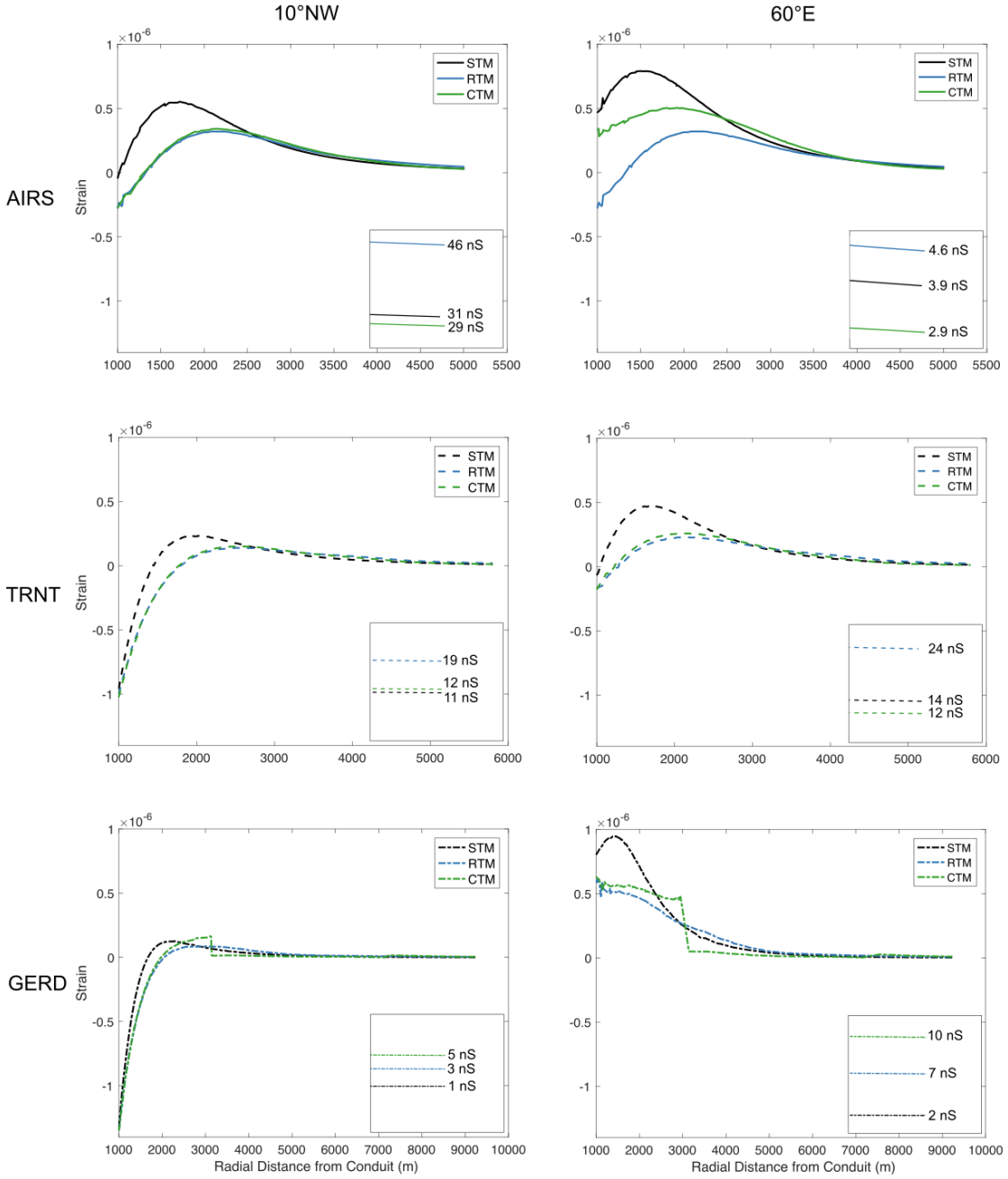

Figure 4.5: Strain partitioning between each strainmeter and the conduit for the plausible NNW and NE conduit azimuths at the approximate depth of the strainmeters. The x axis represents the radial distance between the strainmeter and each core beginning at 1000 m (solutions are unstable close to the conduit). STM, RTM and CTM solutions are shown in each graph in black, blue and green respectively and the paths to AIRS, TRNT and GERD are indicated by solid, dashed and dotted lines respectively. Insets show the resultant strain at the approximate strainmeter location.

4.5 Conclusions

Models of volcanic systems and processes are often simplified to idealised 2D forms for the purposes of reducing computation time and simplifying the parameter space. I have

shown here that 2D models fail to capture the complexity of the shallow volcanic system at Montserrat and neglect the asymmetry of the conduit; a key factor in how strain partitions in the shallow crust. Shallow conduit processes are regularly approximated as radially symmetric, as such, many inferences made about magma flow dynamics (among other things) may be based on unrepresentative models. Furthermore, I also demonstrate the effects of volcano specific complexities in the shallow crust (i.e. real topography and the stiff core). The effects are particularly dramatic near the conduit and have implications for interpreting near-vent measurements of deformation.

These results represent one aspect of conduit geometry which can be modelled. Another method, which could provide useful constraints on the geometry, would be to model the change in conduit semi-minor axis required to fit the volumetric strain signal. I also assume that the conduit is essentially uniform throughout its length which as I discussed is unlikely to be true. Future work should therefore include modelling asperities in the conduit and modelling changes in conduit width during the eruption. Additionally, future studies should not restrict themselves to one eruption. It may be possible to use other conduit driven eruptions and their accompanying strain data to constrain a narrower field of solutions. It would be particularly useful to install tiltmeters close to the summit and record an eruption of this kind. The region closest to the conduit undergoes the largest strains and shows the largest discrepancies between the two plausible azimuths (see Fig. 4.5); near vent deformation data would therefore be a useful discriminator.

Chapter 5

Capturing the shallow deformation source at Masaya with InSAR data

Stephens, K. J., Ebmeier, S. K., **Young, N. K.,** & Biggs, J. (2017). Transient deformation associated with explosive eruption measured at Masaya volcano (Nicaragua) using Interferometric Synthetic Aperture Radar. *Journal of Volcanology and Geothermal Research*, 344, 212-223.

Author contributions and declaration: K. Stephens processed and interpreted the interferogram data. This work is adapted from the paper cited above. I include sections from the paper which I wrote; the modelling methods and results. The introduction, discussion and conclusions are original work written for the thesis and independent of those in the paper.

ABSTRACT

Volcanoes are often sparsely monitored due to inaccessibility or the expense of a comprehensive monitoring network. Seismology is the primary tool used, due to the close relationship between magma movement and seismic signals. This is to the detriment of deformation monitoring, which also provides vital information about the location of fluid reservoirs. However a lack of ground-based instruments can be overcome with high-resolution satellite data. I examine an explosive episode at the Masaya Volcano in May 2012, which is accompanied by continuous seismic data and semi-monthly alternative data and create numerical models of the deformation obtained from Interferometric Synthetic Aperture Radar data. With these models I am able to retrieve geodetic source locations at Masaya for the first time. The first iteration of models outlines a selection of possibilities, all of which lie below sources suggested by geochemical and seismic data. However, in the second iteration when I employ a weakened halo of material around the source I observe that model solutions are plausible in the region outlined by other forms of data. This work demonstrates the utility of deformation modelling at sparsely monitored volcanoes and highlights how integrating all available data sources can provide important inferences on volcano dynamics; in this case a joint magmatic hydrothermal explosion instigator.

5.1 Introduction

Deformation observations are among the most important tools in volcano monitoring and forecasting today [Segall, 2013; Sparks, 2003; Sparks et al., 2012]. Modelling of deformation data is an excellent way to estimate approximate source size, geometry and location. Just as importantly, deformation models improve our understanding of magma transport and eruption dynamics [Segall, 2013]. Typical instrumentation includes tiltmeters, Global Positioning Systems (GPS), Electronic Distance Measurement (EDM) and less commonly, strainmeters [Sparks et al., 2012]. While GPS and tiltmeters are common at the well studied volcanoes, e.g., Hawaii, instrumentation at remote or sparsely monitored volcanoes is often focused on seismicity, e.g., Alaska [Dixon et al., 2017]. However, improved access to satellite data has opened up new avenues in deformation monitoring at difficult to access volcanoes [e.g., Biggs et al., 2011].

Typically volcanic eruptions are preceded by seismicity and inflation [Segall, 2013]. Recognition of repetitive precursory signals is key in eruption forecasting [Segall, 2013]; such signals have been characterised at a variety of timescales from hours (e.g., deflation/inflation events at Hawaii) to years (e.g., Soufriere Hills Volcano) [Anderson et al., 2015; Sparks, 2003]. The style, duration and frequency of eruptions and precursory signals varies greatly with volcanic setting, magmatic composition and if the system is open or closed [e.g., Behncke and Neri, 2003; Chaussard et al., 2013; Costa et al., 2013]. Our understanding of eruption precursors, and indeed eruption mechanisms, comes primarily from well studied natural laboratories such as Hawaii and Soufrière Hills Volcano. Sparsely monitored volcanoes that exhibit behaviour atypical of these natural laboratories are therefore difficult to forecast as their eruption dynamics are less well constrained.

Masaya is one such poorly monitored volcano which fulfils these criteria. Degassing at Masaya is cyclical [Rymer et al., 1998]; the average daily SO_2 flux from 1996-2013 was 1000 tons/day, representing nearly 3 percent of global SO_2 emissions [van Manen, 2014]. Many scientific

studies on Masaya therefore focus on the hazard to nearby residents from the emitted gases. Though seismic, gravity, self potential and resistivity data exist [e.g., Lewicki, 2003; Mauri et al., 2012; Métaxian et al., 1997; Rymer et al., 1998], there are no deformation monitoring networks permanently installed at Masaya, therefore deformation data is sparse. Seismicity is the only continuous measurement made at Masaya, the remainder of data (temperature and gas) is campaign style, measured only once or twice a month. From 30 April to 17 May 2012 Masaya experienced a series of explosions emitting ash and rocks. The immediate precursors of the event were an unusual drop in Real-time Seismic Amplitude Measurements (RSAM), deflation and a rise in temperature [Global Volcanism Program, 2012a; INETER, 2012a]. Explosions at Masaya have previously been related to blockage of the active vents by rockfalls from the crater edges, but a lack of coincident geodetic data accompanying these earlier explosions renders a more complex explanation untenable.

InSAR (Interferometric Synthetic Aperture Radar) is a satellite based technique which has been used successfully to highlight deformation globally (see Ebmeier et al. [2018]) and has a resolution of millimetres to centimetres [Ebmeier et al., 2018; Massonnet and Feigl, 2001]. For example, InSAR has uncovered movement at poorly monitored volcanoes (previously believed to be entirely dormant) in the East African Rift [Biggs et al., 2009, 2011]. At Masaya, InSAR data has previously highlighted slow subsidence within the inner ring fault (see Fig. 5.1) at Masaya on the order of 4 cm from 2007-2010 [Ebmeier et al., 2013]. The data from this time period did not detect deformation at the volcano itself despite explosions occurring during this time frame as the temporal resolution, of minimum 46, days may have been too low. For the first time, InSAR data from the satellite COSMO-SkyMed, with a temporal resolution of 1-14 days, is available for the explosive period in 2012. The increased resolution renders InSAR a plausible technique to a) measure deformation at Masaya, and b) provide data for deformation source modelling and investigating the shallow volcanic plumbing system.

5.1.1 Background

Masaya is a basaltic shield volcano composed of multiple pit craters with an ephemeral lava lake in Nicaragua. It sits in an elliptical caldera approximately 10 km wide on the long axis (Fig. 5.1). Within the last 150 years activity at Masaya has been confined to the formation of two pit craters, ephemeral lava lakes, weak strombolian eruptions and large gas emissions [Rymer et al., 1998]. However in the past it has experienced pyroclastic cone formation, Plinian eruptions and caldera forming eruptions; therefore it is capable of much more destructive events than those that presently occur [Pérez et al., 2009; Rymer et al., 1998].

The volcano is divided into two cones, Nindirí and Masaya. The name Masaya is frequently applied to the caldera, the cone, the crater within the cone and the volcano as a whole, though some authors divide Masaya cone into the San Fernando crater and the subsidiary San Juan crater [Caravantes Gonzalez, 2013]. Hereafter, I use the terms Masaya caldera, Masaya cone and San Fernando crater in specific reference to these features and Masaya as a volcano wide term. The inactive pit craters (San Fernando, San Pedro and Nindirí) are composed of pyroclastic spatter, scoria, fine ash layers and lava flows. Nindirí hosts frozen lava lakes and exhibits downsagging on circular faults while San Fernando and San Pedro are unfilled [Rymer et al., 1998]. The Santiago pit crater is the site of current activity. Layers of scoria, fine ash, lava flows or thin lava lakes are visible within the walls, as well as massive breccias [Rymer et al., 1998]. The main crater is $\sim$600 m wide and 150 m deep, and contains a secondary crater a further 150 m deep

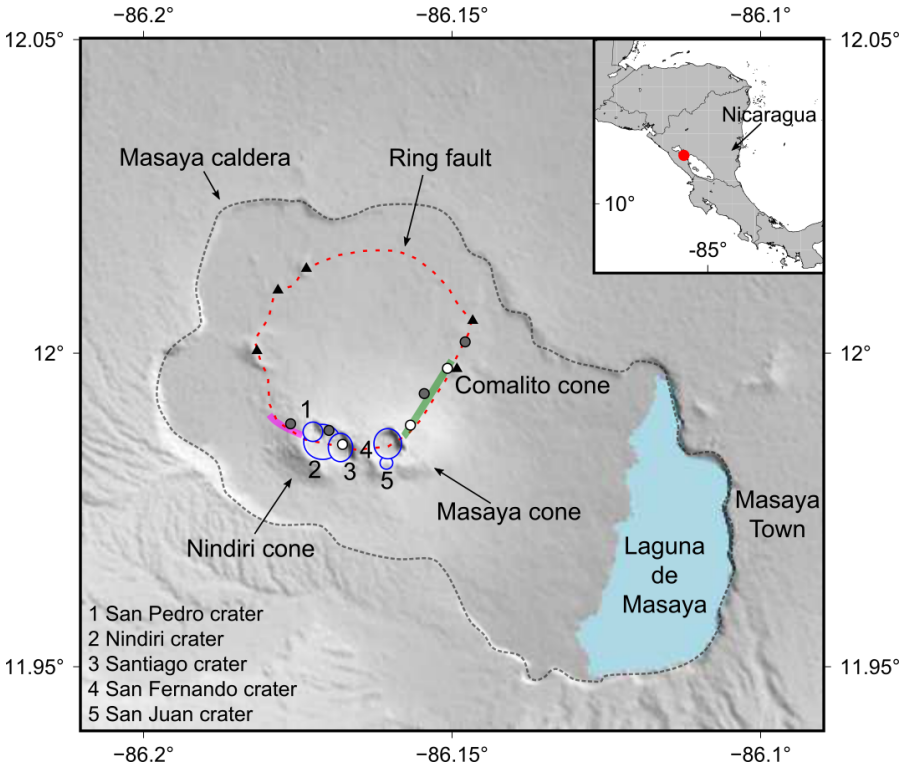

Figure 5.1: DEM of Masaya caldera with inset location of the study area in western Nicaragua (top left). Masaya caldera, lake and town are labelled as are the two cones, Nindirí and Masaya. The ring fault inferred by Caravantes Gonzalez [2013] is shown with a red dashed line. The numbers indicate the individual craters (blue circles) within the cones as per the key on the bottom left. Triangles represent minor cinder cones including Comalito and the filled circles depict the locations of active (white) and transient (gray) fumaroles as presented by Caravantes Gonzalez [2013]. Lastly the pink/purple line to the left of Nindirí cone and the green line to the NE of Masaya cone show the approximate locations of the San Pedro rift and a fumarole bearing fracture zone respectively [Caravantes Gonzalez, 2013; Pearson et al., 2012]. Figure prepared with the Generic Mapping Tools (GMT) software [Wessel and Smith, 1998]

which contains the active vent [Rymer et al., 1998]. This inner crater was formed by episodic multiple chamber unroofing events, which usually began with the formation of a hole, followed by collapse to a cavern sometimes exposing lava [Rymer et al., 1998]. Currently, the Santiago pit crater hosts an active lava lake which was formed in 2015 [Aiuppa et al., 2018].

5.1.2 The Hydrothermal System and Caldera Structure

Recent work at Masaya has focused on the hydrothermal system which is manifested by numerous fumaroles and diffuse degassing. There are seven known fumarole sites within Masaya caldera (see filled circles in Fig. 5.1), three of which are permanently present [Caravantes Gonzalez, 2013]. These include Santiago, Comalito and a fumarole field on the north slope of Masaya cone. Transient sites are located on the northern frozen lava lake border fault in Nindirí and the San Pedro rift valley; the two remaining sites are close to Comalito [see Caravantes Gonzalez, 2013, for more details]. Caravantes Gonzalez [2013] suggests the fumaroles are 'superficial manifestations' of the hydrothermal system and links their positions to the fault

network.

Diffuse degassing has been noted in a semi-circular pattern following the path of cinder cones in the caldera (see dashed red line in Fig. 5.1) [Mauri et al., 2012]. Degassing is not only confined to the cones, it is also seen in the NW-orientated fracture zone on Masaya cone (green line, Fig. 5.1) and inferred in both San Pedro rift (purple line, Fig. 5.1) and another rift between the most northwesterly cinder cones [Mauri et al., 2012]. Self-potential (SP) and CO_2 measurements within the NW fracture zone have been modelled in TOUGH2 to reproduce diffuse degassing regions via convection (to 3500 m depth) [Pearson et al., 2012]. In the shallower subsurface (< 250 m), the SP and CO_2 data show that faults can behave impermeably at Masaya, creating partitions with elevated self potential and CO_2 on one side, and an absence of CO_2 on the other [Pearson et al., 2012]. However alternative evidence from SP and soil gas measurements suggests that faults also promote the upward movement of fluids whereas dykes act as barriers [Mauri et al., 2012]. In any case it seems clear that fluid flow in Masaya caldera is structurally controlled, and that the circular ring fault which is theorised to control the distribution of cinder cones in the caldera may also control the current movement of fluids [Mauri et al., 2012]. Caravantes Gonzalez [2013] point out that a structural control on degassing is a framework which both dissipates heat and pressure and promotes fluid circulation, and this framework may maintain steady state behaviour within the caldera. Additionally, the NW fracture zone and diffuse degassing structures across the caldera are thought to be fed by a common shallow magmatic source or hydrothermal reservoir which is aerially extensive [Mauri et al., 2012; Pearson et al., 2012].

The caldera walls act to hydrologically isolate groundwater within Masaya caldera from the surrounding area [MacNeil et al., 2007]. Various estimates of the water table depth have been made based on SP and transient electromagnetic method (TEM) data. [MacNeil et al., 2007]. Resistivity finds an interface between a dry overlying basalt and an underlying saturated zone (aka the water table) at a depth between 100 m to 200 m below the surface. Generally, the water table is a subdued replica of topography within the caldera with some exceptions [Lewicki, 2003; MacNeil et al., 2007; Mauri et al., 2010, 2012]. These exceptions are touched on above, i.e. the fumaroles and diffuse degassing areas. The Nindiri and Masaya cones have been traversed extensively; collective resistivity and SP studies of both cones have found an anomalous region near the active vent, interpreted to be a vapour dominated zone [MacNeil et al., 2007; Mauri et al., 2010]. Additionally, Very Low Frequency (VLF) electromagnetic data has found evidence of the hydrothermal system in the San Pedro fracture and of fault driven fluid migration in Nindiri [Caravantes Gonzalez, 2013]. Fumarole soil temperature monitoring of the most actively degassing Comalito cone demonstrates temperatures up to 80°C and evidence that volcanic activity drives rapid changes in pore pressure, dilating and/or creating fractures and increasing hot fluid transport to the surface [Pearson et al., 2008]. Furthermore, the active Santiago crater vaporises water, acting as a sink and drawing in groundwater from Comalito and the fracture region[Pearson et al., 2012].

It is possible that the dynamics of the hydrothermal system and explosions at Masaya are related. Anecdotal reports suggest that explosions are more common in the rainy season, which may be related to groundwater recharge [MacNeil et al., 2007]; however, Rymer et al. [1998] and Williams-Jones et al. [2003] favour a magmatic explanation caused by pressure release after vent blockages. MacNeil et al. [2007] also prefer a magmatic mechanism; they point out that exposed walls in the active vent do not show clay alteration which would evidence an

active hydrothermal system, but do not mention sulphur deposits in the neighbouring San Pedro rift [Caravantes Gonzalez, 2013], nor the nearby transient fumarole at Nindiri. Additionally, enhanced scavenging of volcanic gas preceding the 2001 phreatic explosion was attributed to an invigorated hydrothermal system [Duffell et al., 2003]. The contribution and connection of the hydrothermal system to explosive activity at Masaya should therefore not be discounted.

5.1.3 The Shallow Plumbing System

Geodetic studies at Masaya are few; evidence for the geometry and depth of the plumbing system is therefore limited. InSAR data from 2007-2010 detected deformation on the ring fault, but none at the volcano itself [Ebmeier et al., 2013]. However, the characteristics of eruptive products at Masaya caldera are indicative of an open-system shallow (upper-crustal depth) magma chamber with a volume of $\sim$10 km^3 [Walker et al., 1993] and gas composition data suggests magma storage at minimum depths of 0.36-1.4 km [Aiuppa et al., 2018]. There is one broadband seismometer at Masaya, near the Santiago crater, which makes source locating difficult and poorly constrained. In the late 1990's field campaigns by Métaxian et al. [1997] found a permanent source within the Santiago crater at the lava lake level (at that time) which the author related to superficial magma activity.

Useful information has come from sporadic gravity surveys during the periods 1993-1997 and 1997-1999 [Rymer et al., 1998]. GPS from the first period showed height changes < 6 cm during a gravity decrease > 90 μGal, followed by an indistinct increase of 30 μGal until 1997 [Rymer et al., 1998]. Source modelling suggested a reduced density region a few 10's of metres below the active vent with a diameter of 440 m, though it is important to note that no measurements were made inside the craters which limits the depth and size resolution of the gravity anomaly. Two scenarios were suggested for the source region: 1) a 100 m thick body with a density contrast of -300 kg m^{-3}, and 2) a 25 m thick body overlying a 200 m thick body with density contrasts of -600 kg m^{-3} and -100 kg m^{-3} respectively. The second period of gravity data collection found a similar pattern with a gravity decrease from 1997-1999 and no significant change until 2001 [Williams-Jones et al., 2003]. These density contrasts were interpreted as changes in vesiculation. Interestingly, some of the changes were centred under Nindirí crater rather than Santiago. The authors' final interpretation of the data suggested a stratified vesiculated region beneath Santiago, Nindirí and San Pedro craters connected at depth to a magma chamber at $\sim$1 km b.s.l.. Locke et al. [2003] however, interpreted two sources, one at 500 m depth below the volcano and another at 1-2 km depth, as responsible for gravity changes over the entire time period. A separate gravity study found a positive gravity anomaly 300 m below Nindirí plateau which was interpreted as degassed magma on its way from Santiago to a recycling zone at depth [Caravantes Gonzalez, 2013].

Microgravity measurements at the summit have been used to monitor gravity changes over different timescales between 1993 to 2012. These fluctuations are divided into short term (small annual, < 60 μGal), mid-term (2-5 yr, < 100 μGal) and long term fluctuations (> 10 year periodicity)[Caravantes Gonzalez, 2013]. The various timescales are attributed to different source mechanisms. The short term station localised gravity changes are thought to be caused by changes in the highly vesiculated magma layer at the top of the magma column [Caravantes Gonzalez, 2013, and references within]. Mid-term gravity decreases could be explained by a gradual reduction in the thickness of vesiculated magma layers, alternatively, magma injection or withdrawal across the whole of the plumbing system is a plausible mechanism for both mid-

term gravity increases and decreases [Caravantes Gonzalez, 2013]. Lastly, long term changes are interpreted as re-organisation of the plumbing system and generation of new convection cells due to new, hot, gas-rich magma [Caravantes Gonzalez, 2013].

Additional work by the same author found evidence for an elongate dense intrusion NE of the volcano underneath the caldera rim which was also found by others in similar locations [Métaxian et al., 1997, and references within]. The spatial coincidence of this anomaly and recent magmatism leads the author to hypothesise an elongate dense magma body here, which has may have fed recent volcanism mainly via the ring fault which is a structural weakness [Caravantes Gonzalez, 2013]. Removal of this strong anomaly by band-pass filtering demonstrates smaller positive anomalies which align NNW-SSE and encompass Nindirí, Masaya and the NW cones.

Alternative evidence for the geometry, or past geometry, of magma reservoirs comes from analogue an mathematical modelling [Roche et al., 2001; Stix, 2007]. Analogue modelling of pit craters relates the aspect ratio of the magma chamber roof (thickness/width) to the type of pit crater collapse and resultant pit crater [Roche et al., 2001]. Results suggest that the original Santiago crater floor hosted a magma chamber less than 600 m below the surface at the time of collapse, and that the newer inner crater was underlain by magma at 100-150 m depth. A mathematical model of coupled conduit convection and foam accumulation also infers a general geometry of the shallow plumbing system; although depths and volumes are not calculated, the model suggests a conduit 2-6 m in radius feeding a shallow reservoir, which is connected to the surface by another conduit (radius unspecified) [Stix, 2007].

5.1.4 Shallow Magmatic Processes

The rate, quantity and composition of degassing, the density state of the subsurface and seismic tremor at Masaya, are directly correlated with magmatic processes in the shallow subsurface [Aiuppa et al., 2018; Métaxian et al., 1997; Rymer et al., 1998; Stix, 2007; Williams-Jones et al., 2003]. This is also true for other basaltic volcanoes, e.g., Hawaii [Patrick et al., 2016]. Theories behind the behaviour of persistently degassing volcanoes are broadly split into two categories, the foam collapse model and convective overturn model [Jaupart and Vergniolle, 1989; Kazahaya et al., 1994; Stevenson and Blake, 1998; Stix, 2007].

The convective overturn model suggests that degassed, densified magma sinks, driving convection, and the comparatively less dense non-degassed magma rises buoyantly through the degassed magma [Kazahaya et al., 1994]. The authors suggest that the process will only halt if the entire magma reservoir becomes degassed or the conduit becomes blocked. Further laboratory modelling of such a process for both a basaltic and dacitic magma shows that this process is plausible [Stevenson and Blake, 1998]. These fluid convection models showed that the undegassed magma rises up through the centre of the conduit while the dense magma sinks along the walls [Stevenson and Blake, 1998]. Additionally, observations at Hawaii have shown that spattering at the surface of the lava lake bursts bubbles, creating void space and promoting downwelling [Patrick et al., 2016]. Observations of gas emissions at Masaya suggests that plume composition is remarkably consistent through time, which fits with degassing-driven convection in a conduit [Horrocks et al., 1999; Horrocks, 2001].

The convective model favours continuous processes. The foam collapse model is an alternative which provides a better explanation for abrupt transitions in behaviour, e.g., fire fountains [Andronico and Corsaro, 2011]. Experiments with a tube topped tank and magma/gas analogues demonstrated three different regimes based on differing styles of foam accumulation [Jaupart and Vergniolle, 1989]. The first is bubbly flow in the conduit, the second, foam build-up and collapse and the third, slug flow of coalesced gas pockets. Stix [2007] apply this model to Masaya to show that gas input into the foam can be balanced by gas output to the surface, resulting in passive degassing, but that destabilisation of the foam layer can cause explosive eruptions. The mechanism offered for destabilisation in this case is an injection of volatile rich magma from deep; other authors have suggested earthquakes are another possible explanation [Namiki et al., 2016]. Horrocks et al. [1999] suggest a combination of both models at Masaya; open system conduit convection reflects the persistent degassing trends overtime, and discrete overturns of gas-rich magma are superimposed on this process, affecting the shallowest part of the plumbing system. Other processes recognised at persistently degassing, open basaltic systems include compression dilation sequences at Stromboli, interpreted as passage of gas through a pressurising and depressurising conduit [Chouet et al., 1999].

5.1.5 Data

Classically volcanoes pressurise, inflate, erupt and deflate, in sequence, often with subsequent re-pressurisation. I obtained InSAR deformation data covering the 2012 eruption at Masaya from 14 January to 1 August from Kirsten Stephens who produced interferograms, displacement profiles and time-series plots for different deformation signals during the time period (see Fig. 5.2 and 5.3e). Profiles of line of sight (LOS) displacement were created using the averaged cumulative displacement in a 105° arc to the north of the central vent at Santiago (Fig. 5.2a). Unusually, the time period preceding the explosion at Masaya followed an inflation-deflation trend, with inflation measured at the end of the explosions, as seen in Fig. 5.3e.

Sporadic geophysical and geochemical data overlap the deformation observations. These include real-time seismic amplitude measurements (RSAM), CO_2, SO_2 and temperature (Fig. 5.3a, b, c and d respectively), as reported by INETER [2012a]. RSAM data were acquired from the broadband seismometer near the Santiago crater. Diffuse CO_2flow data were measured in the nearby Comalito cone but errors are not provided, and only a passing reference is made to a flowmeter by West System. However portable fluxmeters by West System have a measurement accuracy of $\pm$ 10% for the data range seen during the deformation time period [INETER, 2012b; West Systems, 2016]. SO_2 data were measured by transverses under the plume with a mobile DOAS; again errors were not explicitly stated, however repeat measurements varied within 30% of the average over a 2 hour window, and previous measurements using the same instrument at Masaya quote a flux error of 30% due to plume height uncertainty [INETER, 2012b,c; McGonigle et al., 2002] The following errors for gas measurements are therefore estimates. Temperature data were observed by an infrared sensor at the Santiago crater [Global Volcanism Program, 2012a; INETER, 2012a; Pearson et al., 2008]. Although no errors are quoted, at the nearby Telica Volcano (also monitored by INTETER) the TESTO 845 infrared gun has been used, and has an accuracy 0.75 percent of the measured value in the temperature range from +100 to +950 °C) [Geirsson et al., 2014; Testo, 2019]. Temperature errors are therefore $\leq$1°C and I do not provide them. The timeline of events from January 2012 to July 2012 is summarised in Fig. 5.3.

Preceding the eruption, in January RSAM was steady with an average of 60 RSAM units. SO_2

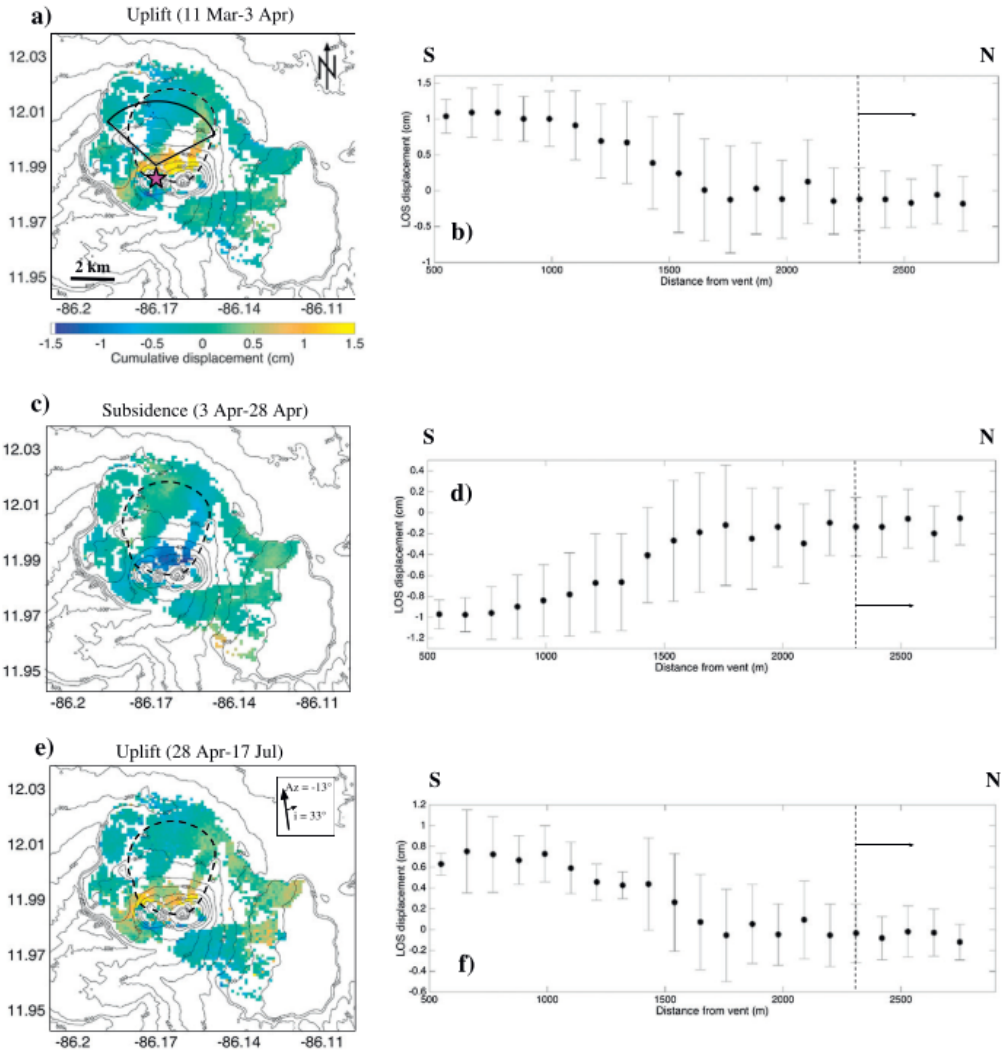

Figure 5.2: Figure and caption from Stephens et al. [2016]. Profiles for each stacked interferogram deformation period. LOS displacement for all the profiles is the radially averaged cumulative displacement according to the arc indicated in (a). The location at which the deformation values outside the inferred large ring fault begin to contribute to the radially averaged profiles are indicated on the profiles by the arrows. a) Uplift (11 March-3 April) stacked interferogram with the 105° arc region outlined. The pink star indicates the location of the active vent at the Santiago crater pit. b) Uplift profile (11 March-3 April) with relative errors. c) Subsidence (11 March-3 April) stacked interferogram. d) Subsidence profile (11 March-3 April) with relative errors. e) Uplift (28 April-17 July) stacked interferogram. f) Uplift profile (28 April-17 July) with relative errors.

was on the rise from 640±192 tons/day in the previous year to 801±240 tons/day in late January and reached a peak at 1002±301 tons/day in March. The first available CO_2 data point in February was the highest measurement made in the entire observation period at 51±5 tons/day; no further data is available until late April. The temperature fluctuated between 100°C and 70°C during the months of February and March and inflation began in late March.

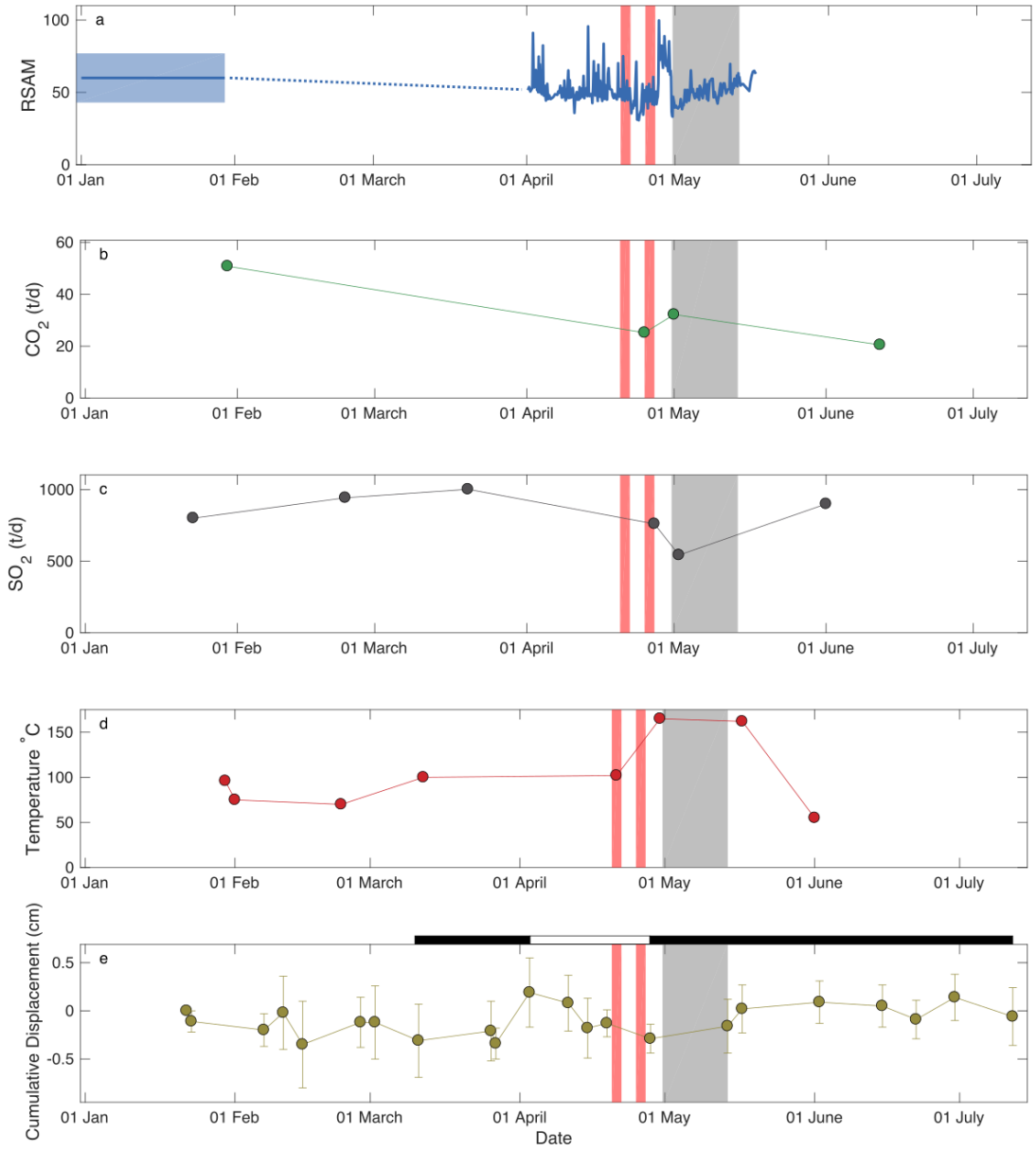

Figure 5.3: Timeline of events preceding and following the explosions at Masaya including a) RSAM b) CO_2 in Comalito cone c) SO_2 d) temperature and e) LOS displacement. a-d are adapted from data provided in reports by INETER [2011, 2012a,b,c,d,e,f,g]. The data in e) was provided by Kirsten Stephens who calculated the errors by computing the standard deviation of the caldera with the crater pit region masked out, and the horizontal black bars and white bar denote the inflation and deflation periods respectively. The thin red bars in in each figure indicate when incandescence was noted in the Santiago crater and the wide grey bars represent the explosion period. Note that the RSAM data is averaged in January and the standard deviation is shaded either side. No data is available in February and March.

Inflation reached its peak in early April (0.5 cm LOS) and quickly switched to subsidence; the last acquisition before the eruption recorded a maximum subsidence of -0.5 cm LOS 48 hours

prior. Incandescence was reported by rangers in the Santiago crater on 21 April for the first time since October 2010 (Fig. 5.3, 1st red bar) and jetting noises were also heard at this time [INETER, 2012a]. The incandescence was corroborated by scientists on 26 April (Fig. 5.3, second red bar) [INETER, 2012a]. Incandescence has been used as a proxy for lava level [Duffell et al., 2003], therefore, lava may have risen within the system at this time. Just prior to the second sighting of incandescence, CO_2 was measured at 25±3 tons/day, decreasing from February and SO_2 also showed a decrease after the second incandescence sighting. The temperature in the Santiago crater rose from 102 to 165°C between 21 April and just prior to the first explosion.

RSAM averaged 55 RSAM units in the early half of April and peaked several times at 100 on 27, 28 and 29 April. These peaks were related to monochromatic tremor, which INETER suggested was characteristic of magma movement underneath the volcano [INETER, 2012a]. INETER also reported seismic events located at approximately 3-4 km below the surface, just prior to the tremor increase and related them to rupture beneath the volcano. Tremor dropped to 30 RSAM units on 30 April (which was noted as unusual by INETER [Global Volcanism Program, 2012a] and 7 hours later the first explosion occurred.

The eruption column reached 1 km in height and ash travelled up to 3 km away from the Santiago crater. Incandescent debris as large as 60 cm in diameter was thrown from the crater. It is not clear if the explosion products contained juvenile material, though they were reported to be pink and yellow in colour suggesting hydrothermally altered products (see Fig. 5.4) [INETER, 2012a]. The explosions continued sporadically through to 17 May, with 68 explosions between 30 April to 3 May alone. RSAM varied between 75 and 120 RSAM units for the first part of May, steadying at 70 from the 25th onwards.

Figure 5.4: Photograph of explosion debris from INETER [2012a].

CO_2 increased slightly to 32±3 tons/day at the start of the explosions and temperature in the crater remained high until they ceased, dropping to below pre-eruptive levels by the end of May. The next InSAR interferogram showed a resumption of inflation close to the end of the explosions. SO_2 continued to drop at the start of the explosions to 543±163 tons/day, but recovered to 90±2700 tons/day by the end of May. INETER, however, cautioned that inconsistent wind direction may have influenced the data during this time. CO_2 declined to 21±2 tons/day by the beginning of June.

The ground-based data accompanying the explosion period are sparse and does not provide a clear picture of the causative mechanism. Previous work on similar explosions have debated causative mechanisms including groundwater recharge (hydrothermal) and vent blockages (magmatic). The accompanying deformation data for this eruption has an unusual pattern and is difficult to interpret without information about its source. I therefore forward model the deformation signal to investigate the causative body. Correlation plots of the subsidence and uplift profiles by Kirsten Stephens demonstrated high linear regressions indicating a common source for each deformation period. I select the subsidence period (Fig. 5.2c) for deformation modelling.

5.2 Methods

I used COMSOL Multiphysics 5.1, a Finite Element Analysis software, to numerically model the observed subsidence in InSAR profiles at Masaya (Fig. 5.2b). The decompression of a magma reservoir in homogeneous media was simulated to replicate the observed InSAR deformation by imposing a pressure change on a buried cavity. I tested for various geometries and depths of reservoirs since the shape and amplitude of the deformation is dependent on the size, shape and depth of the deformation source, the rock mechanics and the imposed pressure change. I tested two different numerical models: a homogeneous (single domain) model and a heterogeneous (two domain) model. The model is a 2D axisymmetric domain, 30 km in radius and in height, with boundary conditions as set out by Hickey and Gottsmann [2014]. The size of the model and the mesh were tested for convergence and found to be satisfactory. I used a simple ellipse shaped cavity which becomes an ellipsoid by rotation during computation, and started with the simplest model setting of a homogenous elastic halfspace. It is important to state, however, that the assumption of symmetry in the deformation field would not necessarily hold for all origins of deformation. Ignoring topography and heterogeneities in near surface deformation modelling has been shown to have a detrimental impact on the results (Chapter 3), however the topography at Masaya is complicated and the simplifications necessary to render it in an axisymmetric setting could themselves introduce errors. As mentioned in Section 5.1.5, the profile used for modelling is an average of a 105-degree swath, and does not take into account variations in topography that are not axisymmetric. Additionally, when tested, the effect of topography on predicted displacements is within the expected InSAR error. I therefore neglect the topography for this model setting.

There is little available information about Masaya's crustal properties (e.g., seismic tomography, borehole data), and I therefore use constant material properties for the model (i.e. the properties do not change with depth). The chosen material properties of the model are based upon the natural rock strength of basalts. Estimates of Young's modulus range from 22 GPa for Etnean basalts [Heap et al., 2009, 2007] to 36 GPa for fresh Icelandic basalt [Heap et al., 2007], and a Poisson's ratio for volcanoes in Nicaragua of 0.25 [Cailleau et al., 2007]. However, experimental pressurisation and depressurisation cycles on Etnean basalts have the effect of lowering the Young's modulus by 30 percent (from 33 to 22 GPa) and raising the Poisson's ratio by a factor of 3 (from 0.2 to 0.5) [Heap et al., 2009]. Mechanical testing of basalts from Pacaya volcano shows that rock strength decreases with porosity, increases with strain rate and temperature, and has a variable response to thermal stressing [Schaefer et al., 2015]. I therefore selected 20 GPa as an appropriate lower limit of Young's modulus for the whole model domain (E1), and 0.25 for Poisson's ratio. The pressure change imposed is constrained by the tensile strength of the rocks. Subsidence of the volcano implies a depressurisation event, and therefore tensile

deformation of the surrounding rock. Natural rocks have a maximum tensile strength of up to -10 MPa [Gudmundsson, 2011]. As the subsidence was not accompanied by an eruption, and consequently rock failure, I assumed that the tensile strength limit was not reached and selected -10 MPa as the maximum pressure.

For the homogeneous model, I performed parametric sweeps of the reservoir length, reservoir radius and reservoir top depth (meters below the surface) in COMSOL. Incremental sweeps of 200 m for reservoir length, 100 m for reservoir top depth and 50 m for reservoir radius were performed, with the parameter limits expanded until the upper and lower limits of each parameter was found. Resultant models were only selected if they fell within the expected InSAR error at every data point using a weight sum of squared errors as per Eq. (1):

$$\chi^2 = \sum_{i=1}^{n} \frac{(O_i - E_i)}{\sigma_i^2} \tag{5.1}$$

where O is the observed (COMSOL) data and E is the expected (InSAR) data. $\chi^2 = 0$ means a perfect fit to the InSAR data, and at each data point, if χ_i^2 is <1, the observed data fits within the InSAR error. Therefore, if χ^2 is $<$n and each χ_i^2 is <1, the model fits the InSAR data, and the closer χ^2 is to 0, the better the fit.

I then explored modelling a heterogeneous halfspace as the contribution of the shallow subsurface required further examination according to previous Masaya models [Rymer et al., 1998; Williams-Jones et al., 2003]. The heterogeneous model was constructed to include the shallow vertical reservoir surrounded by a cylindrical domain with a lower Young's modulus to represent fractured rocks from repeated pit collapse, which has been previously suggested by Rymer et al. [1998]; Williams-Jones et al. [2003]. The effect of a halo of weakened rock around a shallow conduit style reservoir was tested using the concepts given by Young and Gottsmann [2015] (Chapter 3). The halo radius is fixed at 500 m, approximating the extent of recent pit craters. The halo extends from the model surface to 200 m below the base of the conduit to prevent boundary errors. Incremental sweeps of 100 m for reservoir length, 10 m for reservoir reservoir depth, and 20 m for reservoir radius were performed, again expanding the parameter limits until the upper and lower limits of each parameter was found. However, for this model, the upper radius limit was set to 250 m, as this approaches the Santiago crater radius. The halo Young's modulus was also tested (E2) at 5, 10 and 15 GPa. Again, the resultant model was only selected if it fell within the expected InSAR error.

5.3 Results

The results for the homogeneous and heterogeneous domain models for the subsidence period are shown in Fig. 5.5, with the final model parameters given in Table 5.1.

For the homogeneous models, the best fit radius and length (according to the χ^2 criteria) for both the shallowest and deepest possible models are shown, as well as the best fit model with best fit radius, length and depth (Fig. 5.5a, c and Table 5.1a). Since the model is a homogeneous halfspace, the depths are with reference to the surface at 0 m. The horizontal and vertical reservoirs vary the shape and amplitude of the resultant deformation signal, as does the depth of the modelled reservoir. All of these models fall within the expected InSAR error, with the best-

Table 5.1: Homogenous and heterogeneous model results.

a) Homogeneous model results				
Model	Radius (m)	Length (m)	Top depth (m)	χ^2
Shallow limit	110	1400	100	3
Best fit	300	200	1500	1.6
Deep limit	370	200	2200	6

b) Heterogeneous model results					
Model	Radius (m)	Length (m)	Top depth (m)	E2 (GPa) Halo	χ^2
Best Fit	160	700	450	15	1.9

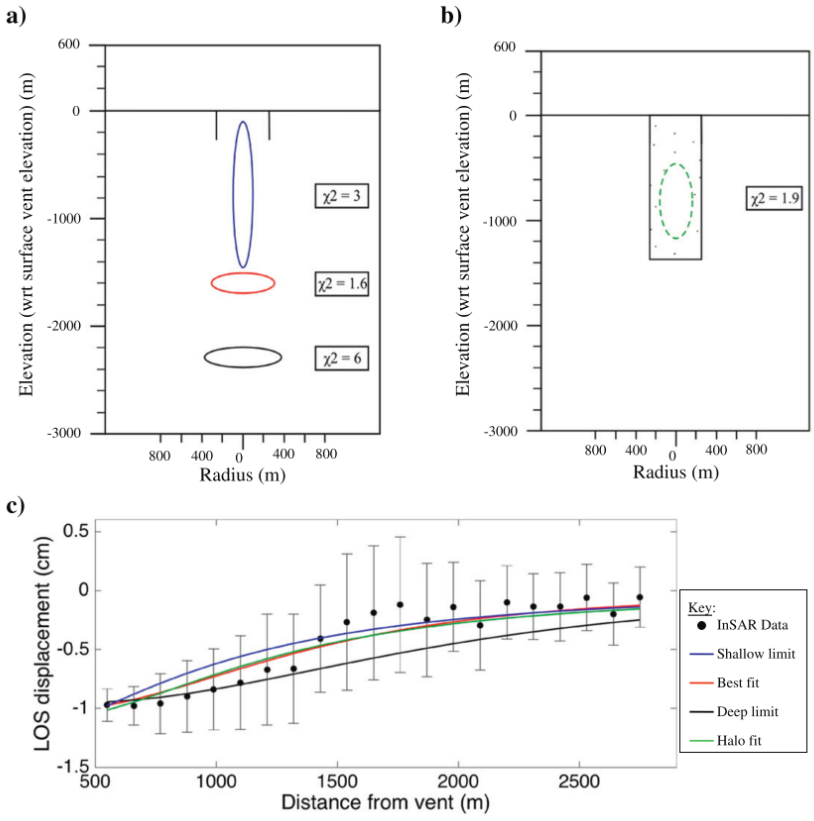

Figure 5.5: Models obtained for the homogeneous and heterogeneous domain parameter runs. a) Homogeneous domain models, with the shallowest limit vertical reservoir (top blue), best-fit sill reservoir (middle red) and deepest limit sill reservoir (bottom black) models. b) Heterogeneous domain model, where the vertical reservoir (dashed green lines) is surrounded by the halo domain (dotted black rectangle). c) Resultant displacement with distance from the vent for the homogeneous and heterogeneous domain models, overlain on the pre-eruptive subsidence profile from Fig. 5.2d. LOS displacement is the radially averaged cumulative displacement for the profile. Blue indicates shallow homogeneous model, red indicates best-fit homogeneous model, black indicates deep homogeneous model, and dark green indicates the heterogeneous model.

fit model being a sill at 1500 m depth with a χ^2 of 1.6. However, because I expect magma to be present in the shallow subsurface [e.g., Métaxian et al., 1997; Rymer et al., 1998; Williams-Jones et al., 2003], I examined the possibility of a shallower deformation source further. The

homogeneous shallow vertical reservoir fit is greatly improved by the addition of the halo domain (Fig. 5.5b, c and Table 5.1b), where a χ^2 of 1.9 approaches the χ^2 obtained for the best-fit homogeneous sill model (Fig. 5.5c). The conduit radius of 160 m is well confined to the width of the Santiago crater pit (radius $\sim$ 300 m), and the depth to the top of the conduit, 450 m, falls in the same approximate location as the base of the gravity changes shown by Williams-Jones et al. [2003] (Fig. 10 in text). The length of the conduit, 700 m, corresponds well with the depicted length for the conduit region connecting the shallow 1 km b.s.l. reservoir to the region of gravity changes [Williams-Jones et al., 2003, Fig. 10]. All four models presented above fit within the expected InSAR error, and highlight the non-uniqueness of modelling solutions and the importance of modelling using apriori knowledge from previous studies to find the most plausible best-fit. While I recognise that the deformation field observed at a volcano can be the superposition of multiple sources at different depths and locations [Bonaccorso and Davis, 1999], I do not consider that the CSK interferograms contain information sufficient to constrain any deeper source. I consider the heterogenous shallow source model as the best model because it both accounts for the majority of the displacement signal, and agrees well with previous models of the shallow subsurface at Masaya [e.g., Métaxian et al., 1997; Rymer et al., 1998; Williams-Jones et al., 2003].

5.4 Discussion

I performed FEA in COMSOL Multiphysics to model the source of the deflation preceding the explosive period at the Masaya Volcano. Details of the plumbing system beneath Masaya have been resolved for the first time from deformation data and I compare it here with contemporaneous seismic, temperature, and gas data, as well as previous gravity data. This model is limited by the lack of data on rock and seismic properties; I make assumptions based upon similar basaltic systems. Additionally, the axisymmetric model could not incorporate the ring fault, an important structural feature of the caldera, or the topography of Masaya. Although I tested a 2D simplification of the topography and found it within the InSAR data error, the edifice of Masaya is complex and composed of multiple pit craters; the stress imposed by the complete 3D topography is unknown and its influence on the deformation field is unaccounted for in the model. The region of misfit between the model predictions and the InSAR data may therefore be due to some combination of the complex volcanic edifice and the ring fault. I also assume the deformation is centred only beneath the Santiago crater, when 1) Williams-Jones [2001] showed that magma foams are centred beneath all of the Santiago, San Pedro and Nindiri craters and 2) the subsidence source is slightly north of the crater (fig.5.2. However, the centre of the crater is unresolved in the interferogram and the full deformation pattern is unknown, therefore the source was modelled as beneath the pit craters. This does bias interpretation towards crater activity, but in Chapter 4 the issue of inclined conduits is touched upon; since magma has been hypothesised to feed degassing structures (exclusively north of Santiago crater) it is plausible that a northerly inclined conduit connects the active crater to a deeper magma body, producing the subsidence pattern we see[Mauri et al., 2012; Pearson et al., 2012], though this was not possible to model.

The unknown influence of the pit craters, and the assumption of a source beneath Santiago, mean that the depth and inclination of the reservoir may vary from that predicted by the best fit models. Despite this, the best-fit and most plausible source falls in a similar region as those found by Métaxian et al. [1997],Williams-Jones [2001] and Aiuppa et al. [2018]. If the conduit is inclined, as mentioned above, this region may represent where the conduit meets the sub-crater foam storage region.

Though I have elucidated a source for the InSAR recorded inflation and deflation phases spanning the eruption period, the relationship between this deformation and the pre, syn and post-eruptive data seismic, temperature, and gas data is still not straightforward. The timing of inflation and deflation does not follow the classic inflation-deflation-inflation pattern and it is not immediately clear if, and how, it relates to the subsequent explosions. Deformation data is unfortunately absent during the explosion period itself with important information is missed. Additionally, each SAR capture has a minimum time step of several days. Volcanic processes occur on a variety of time-scales from minutes through to years (see Table 5.2), and often explosive mechanisms are preceded by hours of precursory signals only [e.g., Bonaccorso et al., 2012]. The time-scale over which these events take place is of primary importance and a key tool for distinguishing shallow volcanic processes. At Masaya, aside from RSAM, none of the available data is continuous over the period of interest (see Fig. 5.3). However the RSAM behaviour is unusual, and cannot be used alone to decipher the ongoing processes. It is highly likely that crucial volcanic processes were undetected by the available data, particularly in the hours preceding the explosions, due to the temporal resolution of the measurements. Therefore, I discuss the findings and how they relate to the recorded ground deformation and explosions in the context of both detected long term (month long) and poorly/undetected short term (hour long) processes. To aid interpretation of the short term processes, I make inferences based on past behaviour at Masaya, and better recorded explosions at similar open system basaltic volcanoes.

Table 5.2: Timescales over which various observations at volcanoes show fluctuations due to different volcanic processes. These processes range from magma intrusion to aqueous fluid migration.

Property Measured	Timescale	References
Deformation	Minutes to years	Anderson et al. [2015]; Bonaccorso et al. [2012]; Sparks [2003]
Gravity	Minutes to years	Gottsmann et al. [2007]; Locke et al. [2003]; Rymer et al. [1998]
Gas Flux	Weeks to months	Aiuppa et al. [2010]; Carapezza et al. [2004]; Scandone et al. [2007]
Temperature	Days to months	Calvari et al. [2005]; Geirsson et al. [2014]
Magma Column Height	Hours to months	Patrick et al. [2016]

Previous work by Kirsten Stephens suggests the same source for the inflation-deflation-inflation phases. However, I note that crucial data is missing from the explosive period and it is possible that the deflation and subsequent inflation was of greater magnitude than recorded. The position of the source during the first and subsequent deformation phases may therefore vary slightly. It is also possible that the deformation is decoupled from the explosive processes. Inflation and deflation at volcanoes can have a multitude of source mechanisms occurring at a variety of time-scales; I explore the different possibilities below and use the accompanying data to accept or reject them. Such mechanisms include magma intrusion/withdrawal, gas accumulation/escape, fault slip, pore pressure variations in hydrothermal systems and thermoelastic heating/cooling [Lyons et al., 2012; Masterlark, 2007]. It is difficult to distinguish between magmatic and hydrothermal processes as they both can be accompanied by seismicity, variations in gas emission and gravity changes, and can occur over time-scales of minutes to years [e.g., Bonaccorso et al., 2005; Lyons et al., 2012; Todesco and Berrino, 2005; Wadge et al., 2014].

5.4.1 Magma Movement

Intrusion

Magma intrusion is the most common explanation for inflation at volcanoes [Segall, 2013] and is often presaged by rock-fracturing induced seismicity [Scandone et al., 2007]. No significant seismic events were noted during the first inflation phase at Masaya, nor is RSAM reported. However, since Masaya maintains open system convection, fracturing may not be required to transport magma. Additionally, aseismic injection is possible particularly if the magma batches are small [Dzurisin, 2003; Power et al., 1994; Scandone et al., 2007]. At the start of the second inflation phase, just prior to the tremor increase, INETER located seismic events at 3-4 km below the surface, and related them to rupture beneath the volcano [Global Volcanism Program, 2012a]. This depth is well below any of the sources I fit to the data, and as there is only one seismometer, it is not clear how well located these events are. As a result, I am hesitant to over-interpret this sesimicity; however it may be related to stress changes within the volcano preceding the explosive period.

Often rising magma batches are heralded by increased volcanic gas emissions, particularly CO_2 and SO_2 from months to weeks beforehand [Aiuppa et al., 2010; Burton et al., 2009; Carapezza et al., 2004; Scandone et al., 2007; Swanson et al., 1985]. There can be a time lag between the appearance of increased CO_2 and SO_2 at the surface due to their different exsolution depths (on the order of 10 km and 1 km respectively) [Bruno et al., 2001]. Depending on the depth of magma supply at Masaya, I would therefore expect to see increased CO_2 emissions followed by increased SO_2 preceding the eruption, or simply enhanced SO_2 measurements prior to the arrival of fresh magma. I find that SO_2 rose from 640 ± 192 tons/day in late 2011 to 1002 ± 300 tons/day in late March 2012 preceding the eruption, but these measurements are within error, and I do not have enough CO_2 data from 2011 to make any interpretations.

However, this SO_2 rise (if it is real) could be due to processes unrelated to the explosions. Degassing crises at Masaya last years to decades [Stix, 2007] and the SO_2 flux varies greatly within these degassing episodes [Williams-Jones, 2001]. Intra-degassing variations may be related to convective overturn and/or trapping of gas in a shallow storage zone beneath the craters [Williams-Jones, 2001] and do not seem to be correlated with explosions. Additionally, incandescence was seen at same time as the gravity surveys by [Williams-Jones et al., 2003] and no explosions occurred, implying heating of the shallow subsurface alone may not be enough to trigger explosions.

Gravity changes accompanying magma intrusion can be both positive and negative depending on the pre-existing conditions and accompanying processes. Rymer and Williams-Jones [2000] demonstrate that intruding a high viscosity magma into an existing chamber will cause inflation and either a density increase or no change. A low viscosity magma is likely to induce vesiculation and thus an overall density decrease. Alternatively, magma entering pre-existing voids will induce a gravity increase, as will magma rising through conduits [Carbone and Greco, 2007; Rymer et al., 1995]. At Masaya, measured gravity transients, positive and negative, are cyclical and discussed in increments of years though there are noteworthy changes on monthly time-scales [Rymer et al., 1998; Williams-Jones et al., 2003]. GPS and levelling measurements accompanying gravity measurements at Masaya from 1994-2001 detected uplifts of 2-3 cm at the summit, and deformation was not resolved below 1 cm. The height correction engendered by

this uplift was negligible compared to the gravity changes and therefore discarded.

There were no concurrent gravity measurement during the 2012 InSAR acquisition period, but as I observe sub-centimetre uplift at Masaya preceding the eruption, deformation accompanying the gravity changes from 1994-2001 may have been missed. It is therefore possible that the processes responsible for gravity changes at Masaya, i.e., trapping and storage of gas due to blockages within the volcano or gas rich magma emplacement near the surface, may also be related to deformation [Williams-Jones et al., 2003]. Trapping of gas rich magma has been observed at Stromboli, where a build up of such magma below a pile of rock caused inflation and eruption [Bonaccorso et al., 2012]. No gravity data accompanies this phenomenon and I do not infer that the mechanisms are directly comparable. However, I do suggest that some inflation might be expected from shallow, low density magma accumulation.

Interpretations of gravity changes and gas flux at Masaya imply that trapping and storage of gas might be accompanied by decreased gas flux [Williams-Jones, 2001]. If I examine the gas data, the highest measurement of SO_2 was taken just prior to inflation (1002$\pm$300 tons/day) and the next measurement, showing a decrease in SO_2 (761$\pm$228 tons/day), was not taken until close to the end of deflation. The only measurement of SO_2 during the explosions is even lower (534$\pm$163 tons/day), although inconsistent wind directions are cited at this time [INETER, 2012e] indicating that this measurement may not be accurate. The first measurement after the explosions end recovers almost to the previous high (900$\pm$270 tons/day). Unfortunately, as the above SO_2 measurements are within their estimated errors and inconsistent windspeeds were noted, these results must be viewed with caution.

I propose that the above observations are consistent with inflation due to magma pressurising the source region. The possible increase in SO_2 in the months preceding the inflation could be indicative of fresh magma migrating from depth, but it is impossible to separate this from intra-degassing crisis variations, and the pressurisation may be caused by an alternative mechanism, discussed later. Additionally this interpretation must be consistent with any hypothesis for the subsequent deflation.

Withdrawal

The removal of magma from a reservoir, via eruption or drainage (i.e., upwards or downwards magma migration), is a frequent explanation for volcanic deflation. I rule out eruption as no material, juvenile or not, left the volcano until nearly a month after the start of deflation. Drainage is also extremely unlikely as incandescence was noted in the Santiago crater towards the end of the deflation period, which infers that magma rose within the system and approached the surface. This interpretation is supported by temperature data; the temperature rose sharply at the end of the inflation period and remained high throughout the explosive events.

Magma eruption and drainage cannot be inferred as a mechanism to explain the observed deflation in the source region. The temperature rise and incandescence following deflation, however, suggest that magma withdrew from the source reservoir and moved upwards in the system without eruption. Increasing ground temperatures at other volcanoes, e.g., Mt. Etna and Stromboli, have been related to the rise of magma in dykes and conduits respectively [Calvari et al., 2003, 2005]. However this interpretation of rising magma seems to conflict with the

concurrent deflation; at Hawaii, another open basaltic system, increases in lava lake level are correlated with summit inflation [Patrick et al., 2016].

I propose two plausible explanations for the lack of inflation: 1) the magma left its reservoir, which deflated, and rose to higher levels in the system which contained enough void space to hold the ascended volume without ground movement; 2) there was inflation but it was extremely localised and not visible in interferograms or the profiles which begin at 500 m distance from the Santiago crater. Due to the low magnitude of the deformation I favour low volumes of causative rising magma which could be accommodated in the proposed brecciated zone beneath the craters [Williams-Jones et al., 2003]. For example, Lascar volcano experienced very localised low magnitude (17 mm) subsidence which was interpreted as due to a low volume change of 2.1 m^3 [Pavez et al., 2006].

Magma Convection

I have discussed magma movement in terms of isolated magma migration in and out of a reservoir imposing volume changes. However magma does not cause deformation purely due to this kind of volume change. At silicic volcanoes stick slip mechanisms are commonly inferred to pressurise and depressurise the conduit resulting in inflation and deflation respectively [Voight et al., 1999]. This process is largely linked to rheological stiffening of conduit magma driven by gas loss. The Masaya volcano is basaltic and it is unlikely that the resident magma has high enough viscosity to become lodged in the conduit. In any case, inflation/deflation cycles at mafic volcanoes are inferred to be driven by gas bubble growth and magma ascent in open conduits [Lyons et al., 2012].

As explained in section 5.1.4, a mixture of degassing driven convection and foam collapse are theorised to drive shallow processes at Masaya [Horrocks et al., 1999]. A magma intrusion therefore seems less likely than a perturbation to normal convection, but the paucity of explosions at Masaya suggests that their trigger is not derived from normal processes. This perturbation might take the form of a blockage in the plumbing system. A partial or complete blockage may cause magma to accumulate in the shallow storage region, perturbing normal circulation or causing inflation. Subsequent relaxation/removal of the blockage would allow the magma to ascend to shallower levels into void space permitting overall deflation of the reservoir.

Later re-inflation of the same source region is difficult to explain. It is not clear from the InSAR time series what can be considered background behaviour, nor where equilibrium lies. It is possible that it represents a resumption of normal circulation, redistribution of the post-eruptive stress, downwelling of rapidly degassed magma or another unknown mechanism.

5.4.2 Gas Accumulation and Escape

Inflation and deflation by gas accumulation and loss is an alternative mechanism to magma migration [Johnson et al., 2014]. Gas exsolution at the Soufriere Hills Volcano, Montserrat, drives pressurisation of the conduit and inflation of the edifice [Voight et al., 1999]; this mechanism is related to the presence of magma in the conduit. However fluid driven inflation and deflation also occurs at Campi Flegrei with no associated magma intrusion [Todesco, 2008]. Trapping and pressurising of fluids is often due to sealing of permeable pathways [Edmonds

et al., 2003]. A previous explosion at Masaya in 2001 has been related to rockfalls blocking the vent and halting gas escape [Duffell et al., 2003]. Rockfall was noted at Masaya in 2012, but not until 21 April towards the end of the deflation [Global Volcanism Program, 2012a]; while I cannot rule out earlier missed rockfalls, they do not seem like a likely mechanism for the observed deformation.

Fluids exsolved from rising magma may create permeability due to fluid dissolution of minerals in the surrounding wallrock. This would provide a pathway to permit the escape of fluids. A concurrent rise in temperature of the crater would be expected associated with the exsolved fluids. Alternatively, the inflation reached a critical pressure, cracks opened, fluids were released and depressurisation occurred instantaneously. There is no seismicity data available for the transition from inflation to deflation, which could have helped evaluate the plausibility of this particular hypothesis. However, the explosions themselves imparted very little seismic signatures and crack opening may not have promoted above average RSAM values anyway. The delayed rise in temperature of nearly a month after peak inflation does not seem to support this mechanism; [Hautmann et al., 2014b] suggest that rapid fluid transport can cause deformation, but on the time-scale of tens to hundreds of seconds.

While the fluid-derived mechanisms discussed above appear plausible, they do not explain the incandescence in the crater following deflation at Masaya. For this reason, accumulation of exsolved fluids alone does not seem relevant to the deformation seen close to the explosive period at Masaya. I prefer the simpler explanation of magma pressurisation due to a blockage in the conduit and subsequent magma escape to higher levels.

Short-Term Explosion Mechanisms

I have found plausible explanations for the activity preceding the explosions, but none of the suggested mechanisms explain the explosions themselves. As shown in Table 5.2, various geophysical and geochemical signals can occur over weeks and months, which is visible in the data, but they can also occur over minutes to days. Change from inflation to deflation caused by gas escape from new or pre-existing fractures can take place over less than an hour prior to explosion [Lyons et al., 2012]. Sudden fluid release on a time-scale of hundreds of seconds has been proposed to generate a pressure change affecting large portions of volcanic systems [Hautmann et al., 2014b]. Neither of these examples could have been captured within the temporal resolution of the InSAR data. I propose that processes associated with the explosions were transient and undetected by the InSAR and geochemical data, and were only observed in the RSAM.

The RSAM data demonstrates a peak in activity shortly after incandescence was seen and a dramatic low immediately preceding the explosions. The monochromatic tremor related peaks were suggested to be characteristic of magma movement beneath the volano [INETER, 2012d]. However, many authors relate monochromatic tremor to resonance of hydrothermal fluids in cracks [Alparone et al., 2010; Chouet and Matoza, 2013; Ibáñez et al., 2000; Saccorotti et al., 2007]. At Galeras volcano in Colombia, monochromatic signals were related to pressurisation due to gas release into confined pore space [Stix et al., 1997]. The monochromatic tremor was suggested to be an indication that a pressurisation threshold had been reached. Chouet and Matoza [2013] discuss a phreatic event at Ontake volcano in Japan, which was interpreted as

the response of its hydrothermal system to hot gases released by an intruding body. Heating and pressurisation of the hydrothermal system resulted in long period (LP) events and tremor followed later by a small phreatic eruption.

Therefore, I do not consider it unreasonable to suggest that rising magma at Masaya may have interacted with the shallow hydrothermal system, heating and pressurising fluids present in the near subsurface. The high RSAM preceding the explosions may have been related to trapped heated fluids resonating in cracks before escaping in the explosions. However the drop in RSAM before the explosions remains unaccounted for. At the neaby Telica volcano, a similar persistently active volcano, low hourly seismic event rates were noted prior to individual phreatic explosions, though these also occurred without explosions [Geirsson et al., 2014]. Some of the explosions at Telica did not appear in the seismic data recorded 450 m from the crater, indicating low energy. This low explosion energy is attributed to the low strength of hydrothermal sealing and low pressures building between events [Geirsson et al., 2014]. This is markedly similar to Masaya where the explosions do not appear clearly in the RSAM data which also dropped before the first explosion. The only seismometer at Masaya is > 1 km away from the Santiago crater rim [Pearson et al., 2008].

If the explosion series at Telica is somewhat analagous to Masaya, this implies there was low strength hydrothermal sealing present. Hydrothermal minerals can precipitate due to cooling [Henneberger and Browne, 1988; Ingebritsen and Sorey, 1988]; as incandescence had not been seen at Masaya after October 2010, sealing of the shallow subsurface may have occurred while the magma level was low. A timescale of months to years is required to reduce permeability via cooling and precipitation of hydrothermal minerals, which is plausible for this scenario [Edmonds et al., 2003]. This does not explain the repetitive nature of the explosions, which was not elucidated at Telica either [Geirsson et al., 2014].

5.5 Conclusions

I use InSAR data to forward model the deformation during the period encompassing explosions at Masaya volcano and present the first deformation derived source. The resultant reservoir sizes and locations are non-unique and depend on the assumptions of the model. I show that including heterogeneities in the model set-up permits a satisfactory source location which fits with findings in the literature better than sources found by simple models. By examining deformation scenarios and time-scales at other volcanoes, I interpret the nature of deformation pattern at Masaya in terms of volcanic processes. I suggest that the inflation-deflation pattern prior to the explosions may be caused by a blockage in the system and accumulation of magma, followed by release and ascent to the shallow subsurface. It is plausible that the arrival of magma near the surface, indicated by incandescence heated and pressurised the sealed hydrothermal system resulting in the subsequent explosions. The short duration of the InSAR time series means that it is difficult to discern what is normal background activity and what is unusual; therefore I cannot rule out that the deformation represents regular basaltic circulation and that the explosions were coincidental. However, the lack of juvenile material found and close timing of magma and temperature rise points compellingly towards a hydrothermal trigger.

Chapter 6

Concluding Remarks

6.1 Summary

In this thesis I examine the structure and dynamics of the shallow subsurface at three uniquely different volcanoes; Campi Flegrei caldera, Soufrière Hills Volcano and Masaya Volcano. The activity at these volcanoes covers a spectrum from unrest to eruption, and though each individual study represents a snapshot in time, I demonstrate methods for understanding the architecture of shallow crustal volcanic systems and their dynamics according to the most suited tools available.

In Chapter 2 I use gravity data and high resolution DEMs to reveal the position of the shallow hydrothermal system at the Campi Flegrei caldera. I highlight the role of pre-existing structures in promoting the accumulation and passage of fluids. The fluid batches a) feed the Solfatara, b) may have evolved from condensate to gas beneath Pozzuoli, and c) present a little recognised hazard in the form of trapped gas beneath the Astroni area. While previous studies including seismic surveys and InSAR have recognised possible fluid volumes in similar areas, this is the only gravity study in Solfatara since 1968, and the first gravity survey targeted at illuminating the hydrothermal system across the caldera. In Chapter 1 I outlined the need to understand the fluid distribution in the shallow crust at Campi Flegrei due the potential hazard posed by new opening phases. This work contributes to our knowledge of where phreatic or phreatomagmatic hazards may exist.

Shifting focus from non-magmatic unrest to purely magmatic activity, in Chapters 3 and 4 I use volumetric strain data from a vigorous Vulcanian explosion to build models of increasing complexity at the Soufrière Hills Volcano. I focus on the topmost few km and am able to not only make discoveries about the geometry of the depressurising conduit, but also the mechanical structure of the Soufrière Hills Volcano itself. The island structure is key in Chapter 4 to fitting the volumetric strain data at the distal strainmeter GERD, and the use of more sophisticated 3D models allow me to show, for the first time, that the conduit geometry is asymmetric rather than cylindrical, as many have believed for more than 20 years. In Chapter 1 I highlighted the role of conduit geometry in magma ascent rates and mass eruption rates; my findings about the conduit have implications for how these are calculated at Soufrière Hills Volcano and for assumptions about conduit geometries at other volcanoes. Additionally my addition of volcano specific heterogeneity is novel compared to any methods of modelling heterogeneity listed in Chapter 1.

Lastly, in Chapter 5 I examine an intermediate case, where persistent activity and limited signs of unrest preceded a small phreatic explosion. Using the methods and findings outlined and developed in Chapter 3, I find the shallow deforming reservoir at Masaya for the first time geodetically with InSAR data. Compared to the Campi Flegrei caldera and Soufrière Hills Volcano, available data (including geophysical and structural) at Masaya is sparse and explosion drivers are poorly understood. Therefore, this chapter requires a careful analysis of all available

data during the explosion time-frame and thoughtful comparison to similar volcanoes. My reconstructed order of events highlights a dual magmatic and hydrothermal explosion instigator within the shallow subsurface. As I pointed out in Chapter 1, often at remote volcanoes seismometers are the only permanent instrumentation, which makes it hard to investigate the subsurface. However the use of InSAR and InSAR time series for modelling and interpretation of dynamics much more information can be coaxed from limited data than previously thought.

Chapters 3, 4 and 5 demonstrate the effect of mechanical heterogeneity on deformation models and for the cases of Chapters 3 and 4, topography. I show that where possible, topography should be used for deformation models of the shallow surface, particularly when high resolution data such as strain is involved. Models using the homogenous half-space assumption at the nanostrain level may underestimate the causative pressure changes by 10's to 100's of MPa (Table 3.3), and the variation caused by true topography imparts a very different strain profile to that caused by even an approximated cone shape (Fig. 4.5).

Furthermore heterogeneity fundamentally affects the way strain partitions in volcanic edifices. The addition of the mechanically weak halo around the conduit in Chapters 3 and 4 permits geologically realistic implementation of Young's modulus in the shallow crust domain, compared to many models which exploit a low Young's modulus throughout the model [e.g., Voight et al., 2010]. The finding of a weak annulus or halo around the conduit has been suggested before [e.g., Rust et al., 2004; Widiwijayanti et al., 2005], but has since been echoed in the literature following rock stressing experiments [e.g., Farquharson et al., 2016; Heap et al., 2015; Heap and Wadsworth, 2016]. I apply the same principle to Masaya Volcano in Chapter 5. I iteratively test a range of appropriate Young's Modulus for basalts and find values of the halo Young's modulus which fit the deformation data at Masaya. Inclusion of the halo also makes shallower models within the sub-crater region of Santiago (in a similar location to gravity variation and geochemically derived sources) viable.

In Chapter 4 I take the next step in heterogeneity application, i.e., applying volcano-specific mechanical irregularities, by developing a 3D model for nanostrain level deformation at the Soufrière Hills Volcano. Freedom from the constraint of symmetry allow the stiff core at Centre Hills to be built into the model, and its influence tested on strain partitioning. I find that the stiff core was fundamental to reproducing predicted volumetric strain at strainmeter GERD. Previous 2D axisymmetric models (Chapter 3) and the STM and RTM were unable to do this.

This thesis addresses the shallow structure and dynamics of three different volcano types and highlights commonalties. Fundamentally, the passage and accumulation of fluids in the shallow crust is governed by its structure. Both Masaya and Campi Flegrei caldera demonstrate a prevalence of resurgent activity along intra-caldera wall faults as well as preferential passage of

hydrothermal fluids in these locations. The time-scales and lack of obvious precursory activity at Masaya prior to a series of explosions is a stark warning for potential evolution of activity at Campi Flegrei caldera, should magma rise within the caldera.

I have shown that the presence of a mechanically weakened halo around near surface volcanic conduits is plausible at both Masaya and Soufrière Hills Volcano. Although more testing is required at more volcanoes, I suggest that this is a feature that may be common to most volcanoes with a long-lived central vent. Although the scope of the study at Masaya did not require a fully 3D model and I could not infer anything other than a symmetrical conduit geometry, the findings at Soufrière Hills Volcano are thought provoking. The alignment of best-fitting conduit azimuths with proposed regional stress orientations imply a fundamental control on conduit development. I challenge the cylindrical conduit paradigm and suggest that conduits world-wide are likely to have geometries influenced by their local stress directions (I acknowledge that the exit geometry is probably cylindrical).

Fault orientations at Campi Flegrei caldera are also heavily influenced by regional tectonics. Structurally controlled fluid movement and accumulation is therefore a theme throughout this thesis, and highlights the importance of shallow volcanic structures in understanding near surface volcano dynamics. The new inferences on conduit geometry have implications for conduit flow modelling and magma dynamics close to the surface and show a new potential hazard close to the surface at Campi Flegrei Caldera. Through investigation of three different examples of volcanic activity, I demonstrate that volcano dynamics represent a complex spectrum of activity from non-eruptive fluid movements through to magmatic explosions.

While this thesis addresses quite specific situations, these findings are widely applicable elsewhere. Hydrothermal systems are very common, but are not often imaged using Bouguer gravity. Uturuncu volcano has a vigorous hydrothermal system and an unsolved question about the nature of some of the deformation occuring; Bouguer gravity is the perfect candidate to explore this problem. Yellowstone Caldera, one of the most famous calderas in the world only has Bouguer data from a national grid [Phillips et al., 1993]; a high density survey could provide fascinating insights into its subsurface.

Vulcanian explosions such as the one at Soufrière Hills Volcano have occurred extremely often in its history, and should it resume activity will very likely happen again. They are also common occurrences at summit craters in stratovolcanoes generally, and sometimes in summit crater lakes or lava domes. While the information provided by two strainmeters at Soufrière Hills Volcano limits what can be discovered about the geometry of the conduit, any further eruptions with more active instrumentation could pin down the conduit orientation, and possible allow testing of conduit inclination. The more extensive strainmeter network at Mount Etna, although basaltic,

is an avenue of exploration with regards to plumbing system geometry and volcano architecture.

The results at Masaya volcano (both magma chamber and eruption instigator retrieval) are extremely applicable at other volcanoes. Masaya itself has had previous explosions for which InSAR data is not available, and its current lava lake is likely to preclude phreatic explosions. If the lava lake disappears again, subsequent activity could be modelled using this method. However, if the deformation seen was instead related to circulation, continued InSAR monitoring of the volcano could reveal this. While deformation modelling is commonly done using InSAR data at poorly monitored volcanoes, it is not often attempted at this scale of ground movement. Remote sensing based exploration of small scale signals from shallow volcanic processes, particularly at remote volcanoes, would be an intriguing avenue of research which would require little operating costs.

Upon reflection, some recommendations can be made based on the datasets used. While strain data was the only deformation data available during the particular eruption I studied at Soufrière Hills Volcano , it would have been of particular utility to have had concurrent deformation measurements near the summit of the volcano to help constrain the orientation of the conduit. InSAR would have had the wrong temporal resolution, but continuous GPS or tilt could have provided the necessary information. The comparative cheapness of these instruments (to strainmeters) means they could be used to fill in strainmeter gaps, provided they are close enough to the volcano centre to detect deformation. The gravity dataset at Campi Flegrei, in hindsight, would have been vastly complimented by concurrent CO2 and temperature measurements. This could have helped evaluate the prospect of trapped reservoirs. However, given the survey was static, further deformation data would not have been useful. With regards to Masaya Volcano, as highlighted in Chapter 5, any further data would have been very useful. Ground truthing is always desirable for remote sensing data; the Masaya work would have benefited intensely from even a single continuous GPS or tiltmeter near the summit.

Without the geophysical data utilised and incorporated into the geologically plausible models tailored to each volcano, it would not have been possible to retrieve this information. In 1997, Dvorak and Dzurisin [1997] were of the opinion that geodetic measurements were rarely of sufficient spatial quality to identify anything more complicated than a point source. Dvorak and Dzurisin [1997] also pointed out that at that time, only half a dozen volcanoes had been monitored well enough to gain useful understanding of the meaning of surface displacements. More than 20 years later, advances in the sophistication of geophysical models and our knowledge of volcanic processes have proved these views outdated. Where geophysical data are sparse (e.g., Chapters 3-5), one can still use advanced models to coax the maximum amount of information out of them, and where data are plentiful (e.g. Chapter 2), not only can models be used to their full potential, but comparisons with other available data becomes much more powerful. Geophysics and models of geophysical data, are unsurpassed windows into volcanic

plumbing systems and key tools to improve our understanding of shallow volcanic systems.

6.2 Outlook

Although I have made a number of discoveries at each volcano studied, there is always scope for more. The finding of an asymmetric conduit at Soufrière Hills Volcano demands further investigation into its geometry. Thus far I have only explored a tri-axial ellipsoid, but as I have explained in Section 4.4.2, the change in conduit radius is key to magma dynamics. Therefore, the change in conduit geometry with depth must be explored. As suggested in Section 6.1, I believe that conduits volcano-wide have geometries determined by the regional stress regime. Examples of similar volcanoes include Mt. Redoubt, Mt. St. Helens and Sakurajima. I have identified the latter as suitable for the next 3D strain model due to its record of extensional strain.

Two of these studies (Chapters 3 and 4) are applicable to nanostrain level deformation data. I consider one of the next fundamental steps to be to apply the methodologies explored in the chapters above to larger deformation signals from deeper parts of the volcanic plumbing system and explore at what level topography and different types of heterogeneity become unimportant, if at all. I have taken a first step in applying the methods from Chapter 3 only to Masaya volcano and it is encouraging to find that heterogeneities matter on a millimetre deformation scale. The next step at Masaya volcano is to explore a fully 3D model with real topography and elucidate the edifice effect on strain partitioning there.

I carried out the first gravity survey in Solfatara since 1968 and delineated its feeding structure, as well as two other subsurface gas reservoirs. I am unable to make meaningful direct comparisons of the data from this study and the early survey due to missing information on its genesis. It would therefore be informative to carry out another survey of the same area in the future using the same methodology to investigate how the hydrothermal system changes with time. Additionally, this method could be applied at other volcanoes with active hydrothermal systems to image their fluid distributions. If multiple datasets were acquired an important comparison could be made against modelled hydrothermal structures.

I also propose a temperature and CO_2 survey of the Pozzuoli and Astroni area in to investigate the finding of a gas reservoir below. However, CO_2 anomalies may not exist, if CO_2 is, as I suggest, trapped under a hydrothermal seal. I would also encourage a new seismic tomography survey of the Pozzuoli area to elucidate if the anomaly I show has evolved from a liquid to a gas reservoir.

Lastly, I suggest that my results show that it is important to understand the shallow crust at volcanic systems. Fluids stored here have a short distance to travel before exiting at the surface,

and commensurate with this, can do so over very brief time-scales. Often emphasis is placed on finding and delineating large source regions of magma rather than elucidating the near-surface storage zones where the more immediate hazard lies.

References

Acocella, V. (2008). Activating and reactivating pairs of nested collapses during calderaforming eruptions: Campi Flegrei (Italy). *Geophysical Research Letters*, 35(17):1–5.

Agnew, D. C. (1986). Strainmeters and tiltmeters. *Reviews of Geophysics*, 24(3):579–624.

Agnew, D. C. (2007). Earth Tides. In *Treatise on Geophysics*, volume 3, pages 163–195.

Aiuppa, A., Cannata, A., Cannavò, F., Di Grazia, G., Ferrari, F., Giudice, G., Gurrieri, S., Liuzzo, M., Mattia, M., Montalto, P., Patanè, D., and Puglisi, G. (2010). Patterns in the recent 2007-2008 activity of Mount Etna volcano investigated by integrated geophysical and geochemical observations. *Geochemistry Geophysics Geosystems*, 11(9).

Aiuppa, A., de Moor, J., Arellano, S., Coppola, D., Francofonte, V., Galle, B., Giudice, G., Liuzzo, M., Mendoza, E., Saballos, A., Tamburello, G., Battaglia, A., Bitetto, M., Gurrieri, S., Laiolo, M., Mastrolia, A., and Moretti, R. (2018). Tracking formation of a lava lake from ground and space: Masaya volcano (Nicaragua), 2014-2017. *Geochemistry Geophysics Geosystems*, pages 1–20.

Aiuppa, A., Tamburello, G., Di Napoli, R., Cardellini, C., Chiodini, G., Giudice, G., Grassa, F., and Pedone, M. (2013). First observations of the fumarolic gas output from a restless caldera: Implications for the current period of unrest (2005-2013) at Campi Flegrei. *Geochemistry, Geophysics, Geosystems*, 14(10):4153–4169.

Aldo, Z. (2003). Evidence for the buried rim of Campi Flegrei caldera from 3-d active seismic imaging. *Geophysical Research Letters*, 30(19):8–11.

Alparone, S., Cannata, A., Gambino, S., Gresta, S., Milluzzo, V., and Montalto, P. (2010). Time-space variation of volcano-seismic events at La Fossa (Vulcano, Aeolian Islands, Italy): New insights into seismic sources in a hydrothermal system. *Bulletin of Volcanology*, 72(7):803–816.

Amoruso, A., Crescentini, L., and Sabbetta, I. (2014). Paired deformation sources of the Campi Flegrei caldera (Italy) required by recent (1980-2010) deformation history. *Journal of Geophysical Research: Solid Earth*, 119(2):858–879.

Anderson, K. R., Poland, M. P., Johnson, J. H., and Miklius, A. (2015). Episodic deflation-inflation events at Klauea Volcano and implications for the shallow magma system. In *Hawaiian Volcanoes: From Source to Surface*.

Andronico, D. and Corsaro, R. A. (2011). Lava fountains during the episodic eruption of South–East Crater (Mt. Etna), 2000: insights into magma-gas dynamics within the shallow volcano plumbing system. *Bulletin of Volcanology*, 73(9):1165–1178.

Aspinall, W. P., Miller, A. D., Lynch, L. L., Latchman, J. L., Stewart, R. C., White, R. A., and Power, J. A. (1998). Soufrière Hills eruption, Montserrat, 1995 - 1997: Volcanic earthquake locations and fault plane solutions. *Geophysical Research Letters*, 25(18):3397–3400.

Avitabile, P. (2005). Some Brief Finite Element Modelling Notes. retrieved from http://faculty.uml.edu/pavitabile/22.403/web_downloads/FEM_Brief_Notes.PDF, Accessed 2012-10-10.

Baird, A. F., Kendall, J. M., Sparks, R. S. J., and Baptie, B. (2015). Transtensional deformation of Montserrat revealed by shear wave splitting. *Earth and Planetary Science Letters*, 425:179–186.

Barberi, F., Bertagnini, A., Landi, P., and Principe, C. (1992). A review on phreatic eruptions and their precursors. *Journal of Volcanology and Geothermal Research*, 52(4):231–246.

Barberi, F., Cassano, E., La Torre, P., and Sbrana, A. (1991). Structural evolution of Campi Flegrei caldera in light of volcanological and geophysical data. *Journal of Volcanology and Geothermal Research*, 48(1-2):33–49.

Barberi, F., Corrado, G., Innocenti, F., and Luongo, G. (1984). Phlegraean Fields 1982-1984: Brief chronicle of a volcano emergency in a densely populated area. *Bulletin Volcanologique*, 47(2):175–185.

Battaglia, J., Zollo, A., Virieux, J., and Dello Iacono, D. (2008). Merging active and passive data sets in traveltime tomography: The case study of Campi Flegrei caldera (Southern Italy). *Geophysical Prospecting*, 56(4):555–573.

Battaglia, M., Troise, C., Obrizzo, F., Pingue, F., and De Natale, G. (2006). Evidence for fluid migration as the source of deformation at Campi Flegrei caldera (Italy). *Geophysical Research Letters*, 33(1):1–4.

Bean, C., Lokmer, I., and O'Brien, G. (2008). Influence of near-surface volcanic structure on long-period seismic signals and on moment tensor inversions: Simulated examples from Mount Etna. *Journal of Geophysical Research: Solid Earth*, 113(8).

Beauducel, F., Cornet, F.-H., Suhanto, E., Duquesnoy, T., and Kasser, M. (2000). Constraints on magma flux from displacements data at Merapi volcano, Java, Indonesia. *Journal of Geophysical Research: Solid Earth*, 105(B4):8193–8203.

Behncke, B. and Neri, M. (2003). Cycles and trends in the recent eruptive behaviour of Mount Etna (Italy). *Canadian Journal of Earth Sciences*, 40(10):1405–1411.

Bellucci, F., Woo, J., Kilburn, C. R. J., and Rolandi, G. (2006). Ground deformation at Campi Flegrei, Italy: implications for hazard assessment. *Geological Society, London, Special Publications*, 269(1):141–157.

Berrino, G. (1994). Gravity changes induced by height-mass variations at the Campi Flegrei caldera. *Journal of Volcanology and Geothermal Research*, 61(3-4):293–309.

Berrino, G., Corrado, G., Luongo, G., and Toro, B. (1984). Ground deformation and gravity changes accompanying the 1982 Pozzuoli uplift. *Bulletin Volcanologique*, 47(2):187–200.

Berrino, G., Corrado, G., and Riccardi, U. (2008). Sea gravity data in the Gulf of Naples. A contribution to delineating the structural pattern of the Phlegraean Volcanic District. *Journal of Volcanology and Geothermal Research*, 175(3):241–252.

Berrino, G., Rymer, H., Brown, G. C., and Corrado, G. (1992). Gravity-height correlations for unrest at calderas. *Journal of Volcanology and Geothermal Research*, 53(1-4):11–26.

Biggs, J., Anthony, E. Y., and Ebinger, C. J. (2009). Multiple inflation and deflation events at Kenyan volcanoes, East African Rift. *Geology*, 37(11):979–982.

Biggs, J., Bastow, I. D., Keir, D., and Lewi, E. (2011). Pulses of deformation reveal frequently

recurring shallow magmatic activity beneath the Main Ethiopian Rift. *Geochemistry, Geophysics, Geosystems*, 12(9):n/a–n/a.

Bonaccorso, A., Calvari, S., Linde, A., Sacks, S., and Boschi, E. (2012). Dynamics of the shallow plumbing system investigated from borehole strainmeters and cameras during the 15 March, 2007 Vulcanian paroxysm at Stromboli volcano. *Earth and Planetary Science Letters*, 357-358(2012):249–256.

Bonaccorso, A., Cianetti, S., Giunchi, C., Trasatti, E., Bonafede, M., and Boschi, E. (2005). Analytical and 3-D numerical modelling of Mt. Etna (Italy) volcano inflation. *Geophysical Journal International*, 163(2):852–862.

Bonaccorso, A., Currenti, G., Linde, A., and Sacks, S. (2013). New data from borehole strainmeters to infer lava fountain sources (Etna 2011–2012). *Geophysical Research Letters*, 40(14):3579–3584.

Bonaccorso, A. and Davis, P. M. (1999). Models of ground deformation from vertical volcanic conduits with application to eruptions of Mount St. Helens and Mount Etna. *Journal of Geophysical Research*, 104(B5):10531–10542.

Bonaccorso, A., Linde, A., Currenti, G., Sacks, S., and Sicali, A. (2016). The borehole dilatometer network of Mount Etna: A powerful tool to detect and infer volcano dynamics. *Journal of Geophysical Research: Solid Earth*, 121(6):4655–4669.

Bonafede, M., Gottsmann, J., Todesco, M., Trasatti, E., Amoruso, A., and Crescentini, L. (2013). Ground deformation , gravity changes and source modeling.

Bonforte, A., Bonaccorso, A., Guglielmino, F., Palano, M., and Puglisi, G. (2008). Feeding system and magma storage beneath Mt. Etna as revealed by recent inflation/deflation cycles. *Journal of Geophysical Research: Solid Earth*, 113(B5):B05406.

Bonvalot, S., Remy, D., Deplus, C., and Diament, M. (2008). Insights on the March 1998 eruption at Piton de la Fournaise volcano (La Reunion) from microgravity monitoring. 113(March 1998):1–20.

Brocher, T. M. (2005). Empirical Relations between Elastic Wavespeeds and Density in the Earth's Crust. *Bulletin of the Seismological Society of America*, 95(6):2081–2092.

Broucke, R. A., Zürn, W. E., and Slichter, L. B. (1972). Lunar tidal acceleration on a rigid earth. *Flow and Fracture of Rocks*, 16:319–324.

Bruno, N., Caltabiano, T., Giammanco, S., and Romano, R. (2001). Degassing of SO2 and CO2 at Mount Etna (Sicily) as an indicator of pre-eruptive ascent and shallow emplacement of magma. *Journal of Volcanology and Geothermal Research*, 110(1-2):137–153.

Bruno, P. P. G., Maraio, S., and Festa, G. (2017). The shallow structure of Solfatara Volcano, Italy, revealed by dense, wide-aperture seismic profiling. *Scientific Reports*, 7(1):1–10.

Bruno, P. P. G., Ricciardi, G. P., Petrillo, Z., Di Fiore, V., Troiano, A., and Chiodini, G. (2007). Geophysical and hydrogeological experiments from a shallow hydrothermal system at Solfatara Volcano, Campi Flegrei, Italy: Response to caldera unrest. *Journal of Geophysical Research: Solid Earth*, 112(6):1–17.

Burgisser, A., Arbaret, L., Druitt, T. H., and Giachetti, T. (2011). Pre-explosive conduit conditions of the 1997 Vulcanian explosions at Soufrière Hills Volcano, Montserrat: II. Overpressure and depth distributions. *Journal of Volcanology and Geothermal Research*, 199(3-4):193–205.

Burton, M. R., Caltabiano, T., Murè, F., Salerno, G., and Randazzo, D. (2009). SO2 flux

from Stromboli during the 2007 eruption: Results from the FLAME network and traverse measurements. *Journal of Volcanology and Geothermal Research*, 182(3-4):214–220.

Byerly, K., Brown, L., Voight, B., and Miller, V. (2010). Reflection imaging of deep structure beneath Montserrat using microearthquake sources. *Geophysical Research Letters*, 37(12).

Byrdina, S., Vandemeulebrouck, J., Cardellini, C., Legaz, A., Camerlynck, C., Chiodini, G., Lebourg, T., Gresse, M., Bascou, P., Motos, G., Carrier, A., and Caliro, S. (2014). Relations between electrical resistivity, carbon dioxide flux, and self-potential in the shallow hydrothermal system of Solfatara (Phlegrean Fields, Italy). *Journal of Volcanology and Geothermal Research*, 283:172–182.

Cailleau, B., Lafemina, P. C., and Dixon, T. H. (2007). Stress accumulation between volcanoes: An explanation for intra-arc earthquakes in Nicaragua? *Geophysical Journal International*, 169(3):1132–1138.

Caliro, S., Chiodini, G., Moretti, R., Avino, R., Granieri, D., Russo, M., and Fiebig, J. (2007). The origin of the fumaroles of La Solfatara (Campi Flegrei, South Italy). *Geochimica et Cosmochimica Acta*, 71(12):3040–3055.

Calvari, S., Lodato, L., Burton, M. R., and Andronico, A. (2003). Dike emplacement at Mount Etna before the 2002 flank eruption revealed by surveys with a portable thermal camera. In *EGS - AGU - EUG Joint Assembly, Abstracts from the meeting held in Nice, France, 6 - 11 April 2003, abstract id. 5329*.

Calvari, S., Spampinato, L., Lodato, L., Harris, A. J., Patrick, M. R., Dehn, J., Burton, M. R., and Andronico, D. (2005). Chronology and complex volcanic processes during the 2002-2003 flank eruption at Stromboli volcano (Italy) reconstructed from direct observations and surveys with a handheld thermal camera. *Journal of Geophysical Research: Solid Earth*, 110(2):1–23.

Camacho, A. G., Fernández, J., and Gottsmann, J. (2011). The 3-D gravity inversion package GROWTH2.0 and its application to Tenerife Island, Spain. *Computers & Geosciences*, 37(4):621–633.

Camacho, A. G., Montesinos, F. G., and Vieira, R. (2002). A 3-D gravity inversion tool based on exploration of model possibilities. *Computers and Geosciences*, 28(2):191–204.

Capuano, P., Russo, G., Civetta, L., Orsi, G., D'Antonio, M., and Moretti, R. (2013). The active portion of the Campi Flegrei caldera structure imaged by 3-D inversion of gravity data. *Geochemistry, Geophysics, Geosystems*, 14(10):4681–4697.

Carapezza, M. L., Inguaggiato, S., Brusca, L., and Longo, M. (2004). Geochemical precursors of the activity of an open-conduit volcano: The Stromboli 2002-2003 eruptive events. *Geophysical Research Letters*, 31(7):1–4.

Caravantes Gonzalez, G. (2013). *Geophysical constraints on the structural evolution and hazards of Masaya volcano, Nicaragua*. PhD thesis.

Carbone, D., Budetta, G., Greco, F., and Zuccarello, L. (2007). A data sequence acquired at Mt. Etna during the 2002–2003 eruption highlights the potential of continuous gravity observations as a tool to monitor and study active volcanoes. *Journal of Geodynamics*, 43(2):320–329.

Carbone, D. and Greco, F. (2007). Review of Microgravity Observations at Mt. Etna: A Powerful Tool to Monitor and Study Active Volcanoes. *Pure and Applied Geophysics*, 164(4):769–790.

Carlino, S., Kilburn, C. R., Tramelli, A., Troise, C., Somma, R., and De Natale, G. (2015). Tectonic stress and renewed uplift at Campi Flegrei caldera, southern Italy: New insights

from caldera drilling. *Earth and Planetary Science Letters*, 420:23–29.

Cashman, K. V., Stephen, R., and Sparks, J. (2013). How volcanoes work: A 25 year perspective. *Bulletin of the Geological Society of America*, 125(5-6):664–690.

Cassano, E. and La Torte, P. (1987). Geophysics. In Rosi, M. and Sbrana, A., editors, *Phlegrean Fields*, chapter 6, pages 104–131. Quaderni della Ricerca Scientifica.

Cayol, V. and Cornet, F. H. (1998a). Effects of topography on the interpretation of the deformation field of prominent volcanoes - Application to Etna. *Geophys. Res. Let*, 25(11):1979–1982.

Cayol, V. and Cornet, F. H. (1998b). Three-dimensional modeling of the 19831984 eruption at Piton de la Fournaise Volcano, Réunion Island. *Journal of Geophysical Research*, 103(B8):18025.

Cella, F., Fedi, M., Florio, G., Grimaldi, M., and Rapolla, A. (2007). Shallow structure of the Somma-Vesuvius volcano from 3D inversion of gravity data. *Journal of Volcanology and Geothermal Research*, 161(4):303–317.

Cello, G. and Mazzoli, S. (1998). Apennine tectonics in southern Italy: a review. *Journal of Geodynamics*, 27(2):191–211.

Chardot, L., Voight, B., Foroozan, R., Sacks, S., Linde, A., Stewart, R., Hidayat, D., Clarke, A., Elsworth, D., Fournier, N., Komorowski, J. C., Mattioli, G., Sparks, R. S., and Widiwijayanti, C. (2010). Explosion dynamics from strainmeter and microbarometer observations, Soufréire Hills Volcano, Montserrat: 2008-2009. *Geophysical Research Letters*, 37(18).

Chaussard, E., Amelung, F., and Aoki, Y. (2013). Characterization of open and closed volcanic systems in Indonesia and Mexico using InSAR time series. *Journal of Geophysical Research: Solid Earth*, 118(8):3957–3969.

Chiarabba, C. and Moretti, M. (2006). An insight into the unrest phenomena at the Campi Flegrei caldera from Vp and Vp/Vs tomography. *Terra Nova*, 18(6):373–379.

Chiodini, G. (2003). Magma degassing as a trigger of bradyseismic events: The case of Phlegrean Fields (Italy). *Geophysical Research Letters*, 30(8):1–4.

Chiodini, G. (2016). Geochemical clues on the origin of the current accelerating deformation of Campi Flegrei caldera. *EGU General Assembly Conference Abstracts*, 18:12762.

Chiodini, G., Avino, R., Caliro, S., and Minopoli, C. (2011). Temperature and pressure gas geoindicators at the Solfatara fumaroles (Campi Flegrei). *Annals of Geophysics*, 54(2):151–160.

Chiodini, G., Caliro, S., Cardellini, C., Granieri, D., Avino, R., Baldini, a., Donnini, M., and Minopoli, C. (2010). Long-term variations of the Campi Flegrei, Italy, volcanic system as revealed by the monitoring of hydrothermal activity. *Journal of Geophysical Research: Solid Earth*, 115(3):1982–1984.

Chiodini, G., Caliro, S., De Martino, P., Avino, R., and Gherardi, F. (2012). Early signals of new volcanic unrest at Campi Flegrei caldera? Insights from geochemical data and physical simulations. *Geology*, 40(10):943–946.

Chiodini, G., Cioni, R., Frullani, A., Guidi, M., Marini, L., Prati, F., and Raco, B. (1996). Fluid geochemistry of Montserrat Island, West Indies. *Bulletin of Volcanology*, 58(5):380–392.

Chiodini, G., Frondini, F., Cardellini, C., Granieri, D., Marini, L., and Ventura, G. (2001). CO2 degassing and energy release at Solfatara volcano, Campi Flegrei, Italy. *Journal of*

Geophysical Research, 106(B8):16213–16221.

Chiodini, G., Selva, J., Del Pezzo, E., Marsan, D., De Siena, L., D'Auria, L., Bianco, F., Caliro, S., De Martino, P., Ricciolino, P., and Petrillo, Z. (2017). Clues on the origin of post-2000 earthquakes at Campi Flegrei caldera (Italy). *Scientific Reports*, 7(1):1–10.

Chiodini, G., Vandemeulebrouck, J., Caliro, S., D'Auria, L., De Martino, P., Mangiacapra, A., and Petrillo, Z. (2015). Evidence of thermal-driven processes triggering the 2005-2014 unrest at Campi Flegrei caldera. *Earth and Planetary Science Letters*, 414:58–67.

Chouet, B., Dawson, P., Ohminato, T., Martini, M., Saccorotti, G., Giudicepietro, F., De Luca, G., Milana, G., and Scarpa, R. (2003). Source mechanisms of explosions at Stromboli Volcano, Italy, determined from moment-tensor inversions of very-long-period data. *Journal of Geophysical Research: Solid Earth*, 108(B1):ESE 7–1–ESE 7–25.

Chouet, B., Saccorotti, G., Dawson, P., Martini, M., Scarpa, R., Luca, G. D., Milana, G., and Cattaneo, M. (1999). Broadband measurements of the sources of explosions at Stromboli Volcano, Italy. *Geophysical Research Letters*, 26(13):1937–1940.

Chouet, B., Saccorotti, G., Martini, M., Dawson, P., De Luca, G., Milana, G., and Scarpa, R. (1997). Source and path effects in the wave fields of tremor and explosions at Stromboli Volcano, Italy. *Journal of Geophysical Research: Solid Earth*, 102(B7):15129–15150.

Chouet, B. A. and Matoza, R. S. (2013). A multi-decadal view of seismic methods for detecting precursors of magma movement and eruption. *Journal of Volcanology and Geothermal Research*, 252:108–175.

Christenson, B. W., Werner, C. A., Reyes, A. G., Sherburn, S., Scott, B. J., Miller, C., Rosenburg, M. J., Hurst, A. W., and Britten, K. A. (2007). Hazards from hydrothermally sealed volcanic conduits. *Eos*, 88(5):53–55.

Cioni, R., Corazza, E., and Marini, L. (1984). The gas/steam ratio as indicator of heat transfer at the Solfatara fumaroles, Phlegraean Fields (Italy). *Bulletin Volcanologique*, 47(2):295–302.

Coco, A., Gottsmann, J., Whitaker, F., Rust, A., Currenti, G., Jasim, A., and Bunney, S. (2016). Numerical models for ground deformation and gravity changes during volcanic unrest: Simulating the hydrothermal system dynamics of a restless caldera. *Solid Earth*, 7(2):557–577.

Cole, P. D., Smith, P. J., Stinton, A. J., Odbert, H. M., Bernstein, M. L., Komorowski, J.-C. C., and Stewart, R. C. (2014). Vulcanian explosions at Soufrière Hills Volcano, Montserrat between 2008 and 2010. In *The Eruption of Soufriere Hills Volcano, Montserrat from 2000 to 2010*, volume 39, chapter 5, pages 93–111.

Cooper, G. R. J. and Cowan, D. R. (2008). Edge enhancement of potential-field data using normalized statistics. *Geophysics*, 73(3):H1.

Costa, A., Melnik, O., and Sparks, R. S. (2007a). Controls of conduit geometry and wallrock elasticity on lava dome eruptions. *Earth and Planetary Science Letters*, 260(1-2):137–151.

Costa, A., Melnik, O., Sparks, R. S., and Voight, B. (2007b). Control of magma flow in dykes on cyclic lava dome extrusion. *Geophysical Research Letters*, 34(2):L02303.

Costa, A., Wadge, G., Stewart, R., and Odbert, H. (2013). Coupled subdaily and multiweek cycles during the lava dome eruption of Soufrière Hills Volcano, Montserrat. *Journal of Geophysical Research: Solid Earth*, 118(5):1895–1903.

Costin, L. S. and Holcomb, D. J. (1981). Time-dependent failure of rock under cyclic loading. *Tectonophysics*, 79(3-4):279–296.

Currenti, G., Bonaccorso, A., Del Negro, C., Scandura, D., and Boschi, E. (2010). Elasto-plastic modeling of volcano ground deformation. *Earth and Planetary Science Letters*, 296(3-4):311–318.

Currenti, G., Napoli, R., Di Stefano, A., Greco, F., and Del Negro, C. (2011). 3D integrated geophysical modeling for the 2008 magma intrusion at Etna: Constraints on rheology and dike overpressure. *Physics of the Earth and Planetary Interiors*, 185(1-2):44–52.

Cusano, P., Petrosino, S., and Saccorotti, G. (2008). Hydrothermal origin for sustained Long-Period (LP) activity at Campi Flegrei Volcanic Complex, Italy. *Journal of Volcanology and Geothermal Research*, 177(4):1035–1044.

D'Auria, L., Giudicepietro, F., Martini, M., and Lanari, R. (2012). The 4D imaging of the source of ground deformation at Campi Flegrei caldera (southern Italy). *Journal of Geophysical Research: Solid Earth*, 117(B8):B08209.

De Landro, G., Serlenga, V., Russo, G., Amoroso, O., Festa, G., Bruno, P. P., Gresse, M., Vandemeulebrouck, J., and Zollo, A. (2017). 3D ultra-high resolution seismic imaging of shallow Solfatara crater in Campi Flegrei (Italy): New insights on deep hydrothermal fluid circulation processes. *Scientific Reports*, 7(3412):1–10.

de Lorenzo, S., Gasparini, P., Mongelli, F., and Zollo, A. (2001). Thermal state of the Campi Flegrei caldera inferred from seismic attenuation tomography. *Journal of Geodynamics*, 32(4-5):467–486.

de' Michieli Vitturi, M., Clarke, A. B., Neri, A., and Voight, B. (2008). Effects of conduit geometry on magma ascent dynamics in dome-forming eruptions. *Earth and Planetary Science Letters*, 272(3-4):567–578.

De Natale, G., Troise, C., Mark, D., Mormone, A., Piochi, M., Di Vito, M. A., Isaia, R., Carlino, S., Barra, D., and Somma, R. (2016). The Campi Flegrei Deep Drilling Project (CFDDP): New insight on caldera structure, evolution and hazard implications for the Naples area (Southern Italy). *Geochemistry, Geophysics, Geosystems*, 17(12):4836–4847.

De Natale, G., Troise, C., Pingue, F., Mastrolorenzo, G., Pappalardo, L., Battaglia, M., and Boschi, E. (2006). The Campi Flegrei caldera: unrest mechanisms and hazards. *Geological Society, London, Special Publications*, 269(1):25–45.

De Siena, L., Del Pezzo, E., and Bianco, F. (2010). Seismic attenuation imaging of Campi Flegrei: Evidence of gas reservoirs, hydrothermal basins, and feeding systems. *Journal of Geophysical Research*, 115(B9):B09312.

De Siena, L., Sammarco, C., Cornwell, D. G., La Rocca, M., Bianco, F., Zaccarelli, L., and Nakahara, H. (2018). Ambient Seismic Noise Image of the Structurally Controlled Heat and Fluid Feeder Pathway at Campi Flegrei Caldera. *Geophysical Research Letters*, 45(13):6428–6436.

Del Negro, C., Currenti, G., and Scandura, D. (2009). Temperature-dependent viscoelastic modeling of ground deformation: Application to Etna volcano during the 1993-1997 inflation period. *Physics of the Earth and Planetary Interiors*, 172(3-4):299–309.

del Potro, R. and Hürlimann, M. (2008). Geotechnical classification and characterisation of materials for stability analyses of large volcanic slopes. *Engineering Geology*, 98(1-2):1–17.

Di Giuseppe, M. G., Troiano, A., Fedele, A., Caputo, T., Patella, D., Troise, C., and De Natale, G. (2015). Electrical resistivity tomography imaging of the near-surface structure of the Solfatara crater, Campi Flegrei (Naples, Italy). *Bulletin of Volcanology*, 77(4):27.

Di Luccio, F., Pino, N. A., Piscini, A., and Ventura, G. (2015). Significance of the 1982-2014 Campi Flegrei seismicity: Preexisting structures, hydrothermal processes, and hazard assessment. *Geophysical Research Letters*, 42(18):7498–7506.

Di Vito, M., Isaia, R., Orsi, G., Southon, J., de Vita, S., D'Antonio, M., Pappalardo, L., and Piochi, M. (1999). Volcanism and deformation since 12,000 years at the Campi Flegrei caldera (Italy). *Journal of Volcanology and Geothermal Research*, 91(2-4):221–246.

Di Vito, M., Lirer, L., Mastrolorenzo, G., and Rolandi, G. (1987). The 1538 Monte Nuovo eruption (Campi Flegrei, Italy). *Bulletin of Volcanology*, 49(4):608–615.

Dieterich, J. H. and Decker, R. W. (1975). Finite element modeling of surface deformation associated with volcanism. *Journal of Geophysical Research*, 80(29):4094–4102.

Dinçer, I., Acar, A., Çobanolu, I., and Uras, Y. (2004). Correlation between Schmidt hardness, uniaxial compressive strength and Young's modulus for andesites, basalts and tuffs. *Bulletin of Engineering Geology and the Environment*, 63(2):141–148.

Dixon, J. P., Cameron, C. E., Lezzi, A. M., and Wallace, K. (2017). 2015 Volcanic Activity in Alaska : Summary of Events and Response of the Alaska Volcano Observatory. Technical report, U.S. Geological Survey Scientific Investigations Report 2017-5104.

Dobson, P. F., Kneafsey, T. J., Hulen, J., and Simmons, A. (2003). Porosity, permeability, and fluid flow in the Yellowstone geothermal system, Wyoming. *Journal of Volcanology and Geothermal Research*, 123(3-4):313–324.

Druitt, T. H., Young, S. R., Baptie, B., Bonadonna, C., Calder, E. S., Clarke, a. B., Cole, P. D., Harford, C. L., Herd, R. a., Luckett, R., Ryan, G., and Voight, B. (2002). Episodes of cyclic Vulcanian explosive activity with fountain collapse at Soufrière Hills Volcano, Montserrat. *Geological Society, London, Memoirs*, 21(April 2016):281–306.

Duffell, H. J., Oppenheimer, C., Pyle, D. M., Galle, B., McGonigle, A. J., and Burton, M. R. (2003). Changes in gas composition prior to a minor explosive eruption at Masaya volcano, Nicaragua. *Journal of Volcanology and Geothermal Research*, 126(3-4):327–339.

Dunkley, P., Shalev, E., Voight, B., Norton, G., Steven, R., Johnston, W., Mattioli, G. S., Linde, A., Widiwijayanti, C., Herd, R., Neuberg, J., Hidayat, D., Sparks, J., Elsworth, D., Sacks, S., Malin, P., and Young, S. R. (2006). Prototype PBO instrumentation of CALIPSO project captures world-record lava dome collapse on Montserrat Volcano. *Eos, Transactions American Geophysical Union*, 85(34):317.

Dvorak, J. J. and Dzurisin, D. (1997). Volcano geodesy: The search for magma reservoirs and the formation of eruptive vents. *Reviews of Geophysics*, 35(3):343–384.

Dzurisin, D. (2003). A comprehensive approach to monitoring volcano deformation as a window on the eruption cycle. *Reviews of Geophysics*, 41(1):1001.

Dzurisin, D. (2006). *Volcano deformation: new geodetic monitoring techniques*. Springer Science & Business Media.

Ebmeier, S. K., Andrews, B. J., Araya, M. C., Arnold, D. W. D., Biggs, J., Cooper, C., Cottrell, E., Furtney, M., Hickey, J., Jay, J., Lloyd, R., Parker, A. L., Pritchard, M. E., Robertson, E., Venzke, E., and Williamson, J. L. (2018). Synthesis of global satellite observations of magmatic and volcanic deformation: implications for volcano monitoring & the lateral extent of magmatic domains. *Journal of Applied Volcanology*, 7(1):2.

Ebmeier, S. K., Biggs, J., Mather, T. A., and Amelung, F. (2013). On the lack of InSAR observations of magmatic deformation at Central American volcanoes. *Journal of*

Geophysical Research: Solid Earth, 118(5):2571–2585.

Edmonds, M., Oppenheimer, C., Pyle, D. M., Herd, R. A., and Thompson, G. (2003). SO2 emissions from Soufrière Hills Volcano and their relationship to conduit permeability, hydrothermal interaction and degassing regime. *Journal of Volcanology and Geothermal Research*, 124(1-2):23–43.

Ekman, M. (1993). A concise history of the theories of tides, precession-nutation and polar motion (from antiquity to 1950). *Surveys in Geophysics*, 14(6):585–617.

Elsworth, D., Foroozan, R., Taron, J., Mattioli, G. S., and Voight, B. (2014). Geodetic imaging of magma migration at Soufrière Hills Volcano 1995 to 2008. *The Eruption of Soufrière Hills Volcano, Montserrat from 2000 to 2010*, 39:219–227.

Elsworth, D., Mattioli, G., Taron, J., Voight, B., and Herd, R. (2008). Implications of magma transfer between multiple reservoirs on eruption cycling. *Science*, 322(5899):246–248.

Eshaghzadeh, A., sadat Kalantari, R., and Hekmat, Z. M. (2015). Optimum density determination for bouguer correction using statistical methods: a case study from north of Iran. *International Journal of Advanced Geosciences*, 3(2):25–29.

Farquharson, J., Heap, M. J., Baud, P., Reuschlé, T., and Varley, N. R. (2016). Pore pressure embrittlement in a volcanic edifice. *Bulletin of Volcanology*, 78(1):1–19.

Fedi, M. (2002). Multiscale derivative analysis: A new tool to enhance detection of gravity source boundaries at various scales. *Geophysical Research Letters*, 29(2):2–5.

Folch, A. and Gottsmann, J. (2006). Faults and ground uplift at active calderas. *Geological Society, London, Special Publications*, 269(1):109–120.

Fournier, N. and Chardot, L. (2012). Understanding volcano hydrothermal unrest from geodetic observations: Insights from numerical modeling and application to White Island volcano, New Zealand. *Journal of Geophysical Research: Solid Earth*, 117(11).

Fung, Y. C. (1977). *A first course in continuum mechanics*. Englewood Cliffs, N.J., Prentice-Hall, Inc., 1977. 351 p.

Galgana, G. A., Grosfils, E. B., and McGovern, P. J. (2013). Radial dike formation on Venus: Insights from models of uplift, flexure and magmatism. *Icarus*, 225(1):538–547.

Geirsson, H., Rodgers, M., LaFemina, P., Witter, M., Roman, D., Muñoz, A., Tenorio, V., Alvarez, J., Jacobo, V. C., Nilsson, D., Galle, B., Feineman, M. D., Furman, T., and Morales, A. (2014). Multidisciplinary observations of the 2011 explosive eruption of Telica volcano, Nicaragua: Implications for the dynamics of low-explosivity ash eruptions. *Journal of Volcanology and Geothermal Research*, 271:55–69.

Gercek, H. (2007). Poisson's ratio values for rocks. *International Journal of Rock Mechanics and Mining Sciences*, 44(1):1–13.

Gerya, T. (2009). *Introduction to numerical geodynamic modelling*. Cambridge University Press.

Geyer, A. and Gottsmann, J. (2010). The influence of mechanical stiffness on caldera deformation and implications for the 1971-1984 Rabaul uplift (Papua New Guinea). *Tectonophysics*, 483(3-4):399–412.

Global Volcanism Program (2012a). Report on Masaya (Nicaragua). In Wunderman, R., editor, *Bulletin of the Global Volcanism Network*. 37:6. Smithsonian Institution. https://doi.org/10.5479/si.GVP.BGVN201206-344100, Accessed 2018-10-02.

Global Volcanism Program (2012b). Report on Mauna Loa (United States). In Wunderman,

R., editor, *Bulletin of the Global Volcanism Network*. 37:5. Smithsonian Institution. https://doi.org/10.5479/si.GVP.BGVN201205-332020, Accessed 2019-28-02.

Global Volcanism Program (2013). Volcanoes of the World, v. 4.7.2. In Venzke, E., editor. Smithsonian Institution. https://doi.org/10.5479/si.GVP.VOTW4-2013. Accessed 2018-08-14.

Gokhale, N. S. (2008). *Practical finite element analysis*. Finite To Infinite.

Gottsmann, J. and Battaglia, M. (2008). Deciphering Causes of Unrest at Explosive Collapse Calderas: Recent Advances and Future Challenges of Joint Time-Lapse Gravimetric and Ground Deformation Studies. In *Developments in Volcanology*, volume 10, chapter 12, pages 417–446. Elsevier.

Gottsmann, J., Carniel, R., Coppo, N., Wooller, L., Hautmann, S., and Rymer, H. (2007). Oscillations in hydrothermal systems as a source of periodic unrest at caldera volcanoes: Multiparameter insights from Nisyros, Greece. *Geophysical Research Letters*, 34(7):L07307.

Gottsmann, J., De Angelis, S., Fournier, N., Van Camp, M., Sacks, S., Linde, A., and Ripepe, M. (2011). On the geophysical fingerprint of Vulcanian explosions. *Earth and Planetary Science Letters*, 306(1-2):98–104.

Gottsmann, J., Folch, A., and Rymer, H. (2006). Unrest at Campi Flegrei: A contribution to the magmatic versus hydrothermal debate from inverse and finite element modeling. *Journal of Geophysical Research*, 111(11).

Gottsmann, J. and Odbert, H. (2014). The effects of thermomechanical heterogeneities in island arc crust on time-dependent preeruptive stresses and the failure of an andesitic reservoir. *Journal of Geophysical Research: Solid Earth*, 119(6):4626–4639.

Gregg, P., de Silva, S., Grosfils, E., and Parmigiani, J. (2012). Catastrophic caldera-forming eruptions: Thermomechanics and implications for eruption triggering and maximum caldera dimensions on Earth. *Journal of Volcanology and Geothermal Research*, 241-242:1–12.

Gubbins, D. (2004a). Introduction. In *Time Series Analysis and Inverse Theory for Geophysicists*, pages 1–14. Cambridge University Press, Cambridge.

Gubbins, D. (2004b). The under-determined problem. In *Time Series Analysis and Inverse Theory for Geophysicists*, volume 2, pages 110–124. Cambridge University Press, Cambridge.

Gudmundsson, A. (2011). *Rock Fractures in Geological Processes*. Cambridge University Press.

Gudmundsson, A. (2012a). Magma chambers: Formation, local stresses, excess pressures, and compartments. *Journal of Volcanology and Geothermal Research*, 237-238:19–41.

Gudmundsson, A. (2012b). Strengths and strain energies of volcanic edifices: Implications for eruptions, collapse calderas, and landslides. *Natural Hazards and Earth System Science*, 12(7):2241–2258.

Hammer, S. (1939). Terrain Corrections for Gravimeter Stations. *Geophysics*, 4(3):184–194.

Harrison, J. (1971). *New computer programs for the calculation of earth tides*. Cooperative Institute for Research in Environmental Sciences.

Hautmann, S., Camacho, A. G., Gottsmann, J., Odbert, H. M., and Syers, R. T. (2013a). The shallow structure beneath Montserrat (West Indies) from new Bouguer gravity data. *Geophysical Research Letters*, 40(19):5113–5118.

Hautmann, S., Gottsmann, J., Camacho, A. G., Fournier, N., Sacks, I. S., and Sparks, R. S. J. (2010a). Mass variations in response to magmatic stress changes at Soufrière Hills Volcano,

Montserrat (W.I.): Insights from 4-D gravity data. *Earth and Planetary Science Letters*, 290(1-2):83–89.

Hautmann, S., Gottsmann, J., Camacho, A. G., Van Camp, M., and Fournier, N. (2014a). Continuous and campaign-style gravimetric investigations on Montserrat 2006 to 2009. In *Geological Society, London, Memoirs*, volume 39, chapter 14, pages 241–251.

Hautmann, S., Gottsmann, J., Sparks, R. S. J., Costa, A., Melnik, O., and Voight, B. (2009). Modelling ground deformation caused by oscillating overpressure in a dyke conduit at Soufrière Hills Volcano, Montserrat. *Tectonophysics*, 471(1-2):87–95.

Hautmann, S., Gottsmann, J., Sparks, R. S. J., Mattioli, G. S., Sacks, I. S., and Strutt, M. H. (2010b). Effect of mechanical heterogeneity in arc crust on volcano deformation with application to Soufrière Hills Volcano, Montserrat, West Indies. *Journal of Geophysical Research-Solid Earth*, 115.

Hautmann, S., Hidayat, D., Fournier, N., Linde, A. T., Sacks, I. S., and Williams, C. P. (2013b). Pressure changes in the magmatic system during the December 2008/January 2009 extrusion event at Soufrière Hills Volcano, Montserrat (W.I.), derived from strain data analysis. *Journal of Volcanology and Geothermal Research*, 250:34–41.

Hautmann, S., Witham, F., Christopher, T., Cole, P., Linde, A. T., Sacks, S., and Sparks, R. S. J. (2014b). Strain field analysis on Montserrat (W.I.) as tool for assessing permeable flow paths in the magmatic system of Soufrie‘re Hills Volcano. *Geochemistry, Geophysics, Geosystems*, pages 1–15.

Heap, M., Vinciguerra, S., and Meredith, P. (2009). The evolution of elastic moduli with increasing crack damage during cyclic stressing of a basalt from Mt. Etna volcano. *Tectonophysics*, 471(1-2):153–160.

Heap, M. J., Farquharson, J. I., Baud, P., Lavallée, Y., and Reuschlé, T. (2015). Fracture and compaction of andesite in a volcanic edifice. *Bulletin of Volcanology*, 77(6):55.

Heap, M. J., Lewis, O., Meredith, P. G., and Vinciguerra, S. (2007). Elastic and mechanical properties of Etna basalt. *Geophysical Research Abstracts*, 9(1).

Heap, M. J., Violay, M., Wadsworth, F. B., and Vasseur, J. (2017). From rock to magma and back again: The evolution of temperature and deformation mechanism in conduit margin zones. *Earth and Planetary Science Letters*, 463:92–100.

Heap, M. J. and Wadsworth, F. B. (2016). Closing an open system: Pore pressure changes in permeable edifice rock at high strain rates. *Journal of Volcanology and Geothermal Research*, 315:40–50.

Hemmings, B., Whitaker, F., Gottsmann, J., and Hughes, A. (2015). Hydrogeology of Montserrat review and new insights. *Journal of Hydrology: Regional Studies*, 3:1–30.

Henderson, S. T. and Pritchard, M. E. (2013). Decadal volcanic deformation in the central andes volcanic zone revealed by InSAR time series. *Geochemistry, Geophysics, Geosystems*, 14(5):1358–1374.

Henneberger, R. and Browne, P. (1988). Hydrothermal alteration and evolution of the Ohakuri hydrothermal system, Taupo volcanic zone, New Zealand. *Journal of Volcanology and Geothermal Research*, 34(3-4):211–231.

Hickey, J. and Gottsmann, J. (2014). Benchmarking and developing numerical Finite Element models of volcanic deformation. *Journal of Volcanology and Geothermal Research*, 280:126–130.

Hickey, J., Gottsmann, J., Nakamichi, H., and Iguchi, M. (2016). Thermomechanical controls on magma supply and volcanic deformation: application to Aira caldera, Japan. *Scientific Reports*, 6(March):32691.

Hill, D. P. (2006). Unrest in Long Valley Caldera, California, 1978-2004. *Geological Society London, Special Publications*.

Horrocks, L., Burton, M., Francis, P., and Oppenheimer, C. (1999). Stable gas plume composition measured by OP-FTIR spectroscopy at Masaya Volcano, Nicaragua, 1998-1999. *Geophysical Research Letters*, 26(23):3497–3500.

Horrocks, L. A. (2001). *Infrared Spectroscopy of Volcanic Gases at Masaya, Nicaragua*. PhD thesis, The Open University.

Hulen, J. B. and Lutz, S. J. (1999). Altered Volcanic Rocks as Hydrologic Seals on the Geothermal System of the Medicine Lake Volcano. *Geothermal Resources Council Bulletin*, Sept./Oct.:217–222.

Hurwitz, S. and Lowenstern, J. B. (2014). Dynamics of the Yellowstone hydrothermal system. *Reviews of Geophysics*, 52(3):375–411.

Husen, S., Taylor, R., Smith, R. B., and Healser, H. (2004). Changes in geyser eruption behavior and remotely triggered seismicity in Yellowstone National Park produced by the 2002 M 7.9 Denali fault earthquake, Alaska. *Geology*, 32(6):537–540.

Ibáñez, J. M., Pezzo, E. D., Almendros, J., La Rocca, M., Alguacil, G., Ortiz, R., and García, A. (2000). Seismovolcanic signals at Deception Island volcano, Antarctica: Wave field analysis and source modeling. *Journal of Geophysical Research*, 105(B6):13905.

INETER (2011). Boletín Mensual Sismos y Volcanes de Nicaragua. Technical report, Instituto Nicaragüense de Estudios Territoriales. http://webserver2.ineter.gob.ni/geofisica/sis/bolsis/bolsis.html, Accessed 2018-28-02.

INETER (2012a). Boletín Mensual Sismos y Volcanes de Nicaragua. Technical report, Instituto Nicaragüense de Estudios Territoriales. http://webserver2.ineter.gob.ni/geofisica/sis/bolsis/bolsis.html, Accessed 2018-28-02.

INETER (2012b). Boletín Mensual Sismos y Volcanes de Nicaragua. Technical report, Instituto Nicaragüense de Estudios Territoriales. http://webserver2.ineter.gob.ni/geofisica/sis/bolsis/bolsis.html, Accessed 2018-28-02.

INETER (2012c). Boletín Mensual Sismos y Volcanes de Nicaragua. Technical report, Instituto Nicaragüense de Estudios Territoriales. http://webserver2.ineter.gob.ni/geofisica/sis/bolsis/bolsis.html, Accessed 2018-28-02.

INETER (2012d). Boletín Mensual Sismos y Volcanes de Nicaragua. Technical report, Instituto Nicaragüense de Estudios Territoriales. http://webserver2.ineter.gob.ni/geofisica/sis/bolsis/bolsis.html, Accessed 2018-28-02.

INETER (2012e). Boletín Mensual Sismos y Volcanes de Nicaragua. Technical report, Instituto Nicaragüense de Estudios Territoriales. http://webserver2.ineter.gob.ni/geofisica/sis/bolsis/bolsis.html, Accessed 2018-28-02.

INETER (2012f). Boletín Mensual Sismos y Volcanes de Nicaragua. Technical report, Instituto Nicaragüense de Estudios Territoriales. http://webserver2.ineter.gob.ni/geofisica/sis/bolsis/bolsis.html, Accessed 2018-28-02.

INETER (2012g). Boletín Mensual Sismos y Volcanes de Nicaragua. Technical report, Instituto Nicaragüense de Estudios Territoriales.

http://webserver2.ineter.gob.ni/geofisica/sis/bolsis/bolsis.html, Accessed 2018-28-02.

Ingebritsen, S. E., Geiger, S., Hurwitz, S., and Driesner, T. (2010). Numerical simulation of magmatic hydrothermal systems. *Reviews of Geophysics*, 48(1):RG1002.

Ingebritsen, S. E. and Sorey, M. L. (1988). Vapor-Dominated Zones Within Hydrothermal Systems: Evolution and Natural State. *Journal of Geophysical Research: Solid Earth*, 93(B11):13635–13655.

INGV (2016). Bollettino di Sorveglianza Vulcani Campani Maggio 2016. Technical Report 50, Istituto Nazionale di Geofisica e Vulcanologia. http://www.ov.ingv.it/ov/en/bollettini/275.html, Accessed 2017-01-05.

Isaia, R., Vitale, S., Di Giuseppe, M. G., Iannuzzi, E., D'Assisi Tramparulo, F., and Troiano, A. (2015). Stratigraphy, structure, and volcano-tectonic evolution of Solfatara maar-diatreme (Campi Flegrei, Italy). *Geological Society of America Bulletin*, (X):1–20.

Jasim, A., Whitaker, F. F., and Rust, A. C. (2015). Impact of channelized flow on temperature distribution and fluid flow in restless calderas: Insight from Campi Flegrei caldera, Italy. *Journal of Volcanology and Geothermal Research*, 303:157–174.

Jaupart, C. and Vergniolle, S. (1989). The Generation and Collapse of a foam Layer at the Roof of a Basaltic Magma Chamber. *Journal of Fluid Mechanics*, 203(347):347–380.

Johnson, D. J., Eggers, A. A., Bagnardi, M., Battaglia, M., Poland, M. P., and Miklius, A. (2010). Shallow magma accumulation at Kilauea Volcano , Hawaii , revealed by microgravity surveys. (12):1139–1142.

Johnson, J. B., Lyons, J. J., Andrews, B. J., and Lees, J. M. (2014). Explosive dome eruptions modulated by periodic gas-driven inflation. *Geophysical Research Letters*, 41(19):6689–6697.

Jónsson, S. (2009). Stress interaction between magma accumulation and trapdoor faulting on Sierra Negra volcano, Galápagos. *Tectonophysics*, 471(1-2):36–44.

Kato, A., Terakawa, T., Yamanaka, Y., Maeda, Y., Horikawa, S., Matsuhiro, K., and Okuda, T. (2015). Preparatory and precursory processes leading up to the 2014 phreatic eruption of Mount Ontake, Japan. *Earth, Planets and Space*, 67(1).

Kazahaya, K., Shinohara, H., and Saito, G. (1994). Excessive degassing of Izu-Oshima volcano: magma convection in a conduit. *Bulletin of Volcanology*, 56(3):207–216.

Kennedy, B., Spieler, O., Scheu, B., Kueppers, U., Taddeucci, J., and Dingwell, D. B. (2005). Conduit implosion during Vulcanian eruptions. *Geology*, 33(7):581–584.

Knapp, R. B. and Knight, J. E. (1977). Differential thermal expansion of pore fluids: Fracture propagation and microearthquake production in hot pluton environments. *Journal of Geophysical Research*, 82(17):2515–2522.

Komorowski, J. C., Legendre, Y., Christopher, T., Bernstein, M., Stewart, R., Joseph, E., Fournier, N., Chardot, L., Finizola, A., Wadge, G., Syers, R., Williams, C., and Bass, V. (2010). Insights into processes and deposits of hazardous vulcanian explosions at Soufrière Hills Volcano during 2008 and 2009 (Montserrat, West Indies). *Geophysical Research Letters*, 37:6.

Lahr, J., Chouet, B., Stephens, C., Power, J., and Page, R. (1994). Earthquake classification, location, and error analysis in a volcanic environment: implications for the magmatic system of the 19891990 eruptions at redoubt volcano, Alaska. *Journal of Volcanology and Geothermal Research*, 62(1-4):137–151.

Lavallée, Y., Benson, P. M., Heap, M. J., Flaws, A., Hess, K. U., and Dingwell, D. B. (2012). Volcanic conduit failure as a trigger to magma fragmentation. *Bulletin of Volcanology*, 74(1):11–13.

Le Friant, A., Harford, C., Deplus, C., Boudon, G., Sparks, R., Herd, R., and Komorowski, J. (2004). Geomorphological evolution of Montserrat (West Indies): importance of flank collapse and erosional processes. *Journal of the Geological Society*, 161(1):147–160.

Letort, J., Roux, P., Vandemeulebrouck, J., Coutant, O., Cros, E., Wathelet, M., Cardellini, C., and Avino, R. (2012). High-resolution shallow seismic tomography of a hydrothermal area : application to the Solfatara , Pozzuoli. *Geophysical Journal International*, 189(3):1725–1733.

Lewicki, J. L. (2003). Self-potential, soil CO 2 flux, and temperature on Masaya volcano, Nicaragua. *Geophysical Research Letters*, 30(15):1817.

Lin, L. (2005). Introduction to Finite Element Modelling [PDF]. http://www.me.berkeley.edu/ lwlin/me128/FEMNotes.pdf, Accessed 2012-10-10.

Linde, A. T., Sacks, S., Hidayat, D., Voight, B., Clarke, A., Elsworth, D., Mattioli, G., Malin, P., Shalev, E., Sparks, S., and Widiwijayanti, C. (2010). Vulcanian explosion at Soufrière Hills Volcano, Montserrat on March 2004 as revealed by strain data. *Geophys. Res. Lett.*, 37:L00E07.

Lisowski, M. (2006). Analytical volcano deformation source models. In *Volcano Deformation*, chapter 8. Springer.

Locke, C. A., Rymer, H., and Cassidy, J. (2003). Magma transfer processes at persistently active volcanoes: Insights from gravity observations. *Journal of Volcanology and Geothermal Research*, 127(1-2):73–86.

Longman, I. M. (1959). Formulas for computing the tidal accelerations due to the moon and the sun. *Journal of Geophysical Research*, 64(12):2351.

Loughlin, S., Calder, E., Clarke, A., Cole, P., Luckett, R., Mangan, M., Pyle, D., Sparks, R., Voight, B., and Watts, R. (2002). Pyroclastic flows and surges generated by the 25 June 1997 dome collapse, Soufrière Hills Volcano, Montserrat. *Geological Society, London, Memoirs*, 21(1):191–209.

Lu, Z., Dzurisin, D., Biggs, J., Wicks, C., and McNutt, S. (2010). Ground surface deformation patterns, magma supply, and magma storage at Okmok volcano, Alaska, from InSAR analysis: 1. Intereruption deformation, 19970-2008. *Journal of Geophysical Research: Solid Earth*, 115(5):B00B02.

Lyons, J. J., Waite, G. P., Ichihara, M., and Lees, J. M. (2012). Tilt prior to explosions and the effect of topography on ultra-long-period seismic records at Fuego volcano, Guatemala. *Geophysical Research Letters*, 39(8).

M. Silvestri, Cardellini, C., Chiodini, G., and Buongiorno, M. F. (2016). Satellite-derived surface temperature and in situmeasurement at Solfatara of Pozzuoli (Naples, Italy) M. *Geochemistry Geophysics Geosystems*, 17:2095–2109.

Macedonio, G., Dobran, F., and Neri, A. (1994). Erosion processes in volcanic conduits and application to the AD 79 eruption of Vesuvius. *Earth and Planetary Science Letters*, 121(1-2):137–152.

MacNeil, R. E., Sanford, W. E., Connor, C. B., Sandberg, S. K., and Diez, M. (2007). Investigation of the groundwater system at Masaya Caldera, Nicaragua, using transient electromagnetics and numerical simulation. *Journal of Volcanology and Geothermal*

Research, 166(3-4):217–232.

Malengreau, B., Lénat, J. F., and Froger, J. L. (1999). Structure of Reunion Island (Indian Ocean) inferred from the interpretation of gravity anomalies. *Journal of Volcanology and Geothermal Research*, 88(3):131–146.

Manconi, A., Walter, T. R., and Amelung, F. (2007). Effects of mechanical layering on volcano deformation. *Geophysical Journal International*, 170(2):952–958.

Manconi, A., Walter, T. R., Manzo, M., Zeni, G., Tizzani, P., Sansosti, E., and Lanari, R. (2010). On the effects of 3-D mechanical heterogeneities at Campi Flegrei caldera, southern Italy. *Journal of Geophysical Research: Solid Earth*, 115(8):B08405.

Massonnet, D. and Feigl, K. L. (2001). Radar interferometry and applications to changes in the Earth's surface. *Reviews of Geophysics*, 36(4):441–500.

Masterlark, T. (2007). Magma intrusion and deformation predictions: Sensitivities to the Mogi assumptions. *Journal of Geophysical Research: Solid Earth*, 112(6):1–17.

Masterlark, T. and Tung, S. (2018). Finite Element Models of Elastic Volcano Deformation. In *Volcanoes - Geological and Geophysical Setting, Theoretical Aspects and Numerical Modeling, Applications to Industry and Their Impact on the Human Health*.

Mattia, M., Rossi, M., Guglielmino, F., Aloisi, M., and Bock, Y. (2004). The shallow plumbing system of Stromboli Island as imaged from 1 Hz instantaneous GPS positions. *Geophysical Research Letters*, 31(24):1–4.

Mattioli, G. (1998). GPS measurement of surface deformation around Soufrière Hills volcano, Montserrat from October 1995 to July 1996. *Geophysical Research Letters*, 25(18):3417–3420.

Mattioli, G. S., Herd, R. A., Strutt, M. H., Ryan, G., Widiwijayanti, C., and Voight, B. (2010). Long term surface deformation of Soufrière Hills Volcano, Montserrat from GPS geodesy: Inferences from simple elastic inverse models. *Geophysical Research Letters*, 37(19).

Mauri, G., Williams-Jones, G., and Saracco, G. (2010). Depth determinations of shallow hydrothermal systems by self-potential and multi-scale wavelet tomography. *Journal of Volcanology and Geothermal Research*, 191(3-4):233–244.

Mauri, G., Williams-Jones, G., Saracco, G., and Zurek, J. M. (2012). A geochemical and geophysical investigation of the hydrothermal complex of Masaya volcano, Nicaragua. *Journal of Volcanology and Geothermal Research*, 227-228:15–31.

Mayer, K., Scheu, B., Montanaro, C., Yilmaz, T. I., Isaia, R., Aßbichler, D., and Dingwell, D. B. (2016). Hydrothermal alteration of surficial rocks at Solfatara (Campi Flegrei): Petrophysical properties and implications for phreatic eruption processes. *Journal of Volcanology and Geothermal Research*, 320:128–143.

McGonigle, A. J. S., Pyle, D. M., Mather, T. A., Oppenheimer, C., and Galle, B. (2002). Walking traverse and scanning DOAS measurements of volcanic gas emission rates. *Geophysical Research Letters*, 29(20):46–1–46–4.

Melnik, O. and Sparks, R. S. J. (2002). Dynamics of magma ascent and lava extrusion at Soufrière Hills Volcano, Montserrat. *Geological Society, London, Memoirs*, 21(1):153–171.

Meo, M., Tammaro, U., and Capuano, P. (2008). Influence of topography on ground deformation at Mt. Vesuvius (Italy) by finite element modelling. *International Journal of Non-Linear Mechanics*, 43(3):178–186.

Merriam, J. B. (1992). An ephemeris for gravity tide predictions at the nanogal level. *Geophysical Journal International*, 108(2):415–422.

Métaxian, J. P., Lesage, P., and Dorel, J. (1997). Permanent Tremor Of Masaya Volcano, Nicaragua - Wave Field Analysis and Source Location. *Journal of Geophysical Research-Solid Earth*, 102(97):22529–22545.

Montanaro, C., Scheu, B., Mayer, K., Orsi, G., Moretti, R., Isaia, R., and Dingwell, D. B. (2016). Experimental investigations on the explosivity of steam-driven eruptions: A case study of Solfatara volcano (Campi Flegrei). *Journal of Geophysical Research: Solid Earth*, 120(1):326–343.

Moritz, H. (1992). Geodetic Reference System 1980. *Bulletin Geodesique*, 66(2):187–192.

MVO (1997). Montserrat Volcano Alert System Soufriere Hills Volcano. http://www.geo.mtu.edu/volcanoes/west.indies/soufriere/govt/miscdocs/old/alert.htmlprejuly97, Accesed 2019-12-02.

Nakamura, K. (1977). Volcanoes as possible indicators of tectonic stress orientation - principle and proposal. *Journal of Volcanology and Geothermal Research*, 2(1):1–16.

Namiki, A., Rivalta, E., Woith, H., and Walter, T. R. (2016). Sloshing of a bubbly magma reservoir as a mechanism of triggered eruptions. *Journal of Volcanology and Geothermal Research*, 320:156–171.

Nettleton, L. L. (1976). *Gravity and Magnetics in Oil Prospecting*. McGraw-Hill Companies.

Neuberg, J., Luckett, R., Baptie, B., and Olsen, K. (2000). Models of tremor and low-frequency earthquake swarms on Montserrat. *Journal of Volcanology and Geothermal Research*, 101(1-2):83–104.

Nunziata, C. and Rapolla, A. (1981). Interpretation of gravity and magnetic data in the Phlegraean fields geothermal area, Naples, Italy. *Journal of Volcanology and Geothermal Research*, 10(1-3):209–225.

Odbert, H., Taisne, B., and Gottsmann, J. (2015). Deposit loading and its effect on co-eruptive volcano deformation. *Earth and Planetary Science Letters*, 413:186–196.

Odbert, H. M., Ryan, G. A., Mattioli, G. S., Hautmann, S., Gottsmann, J., Fournier, N., and Herd, R. A. (2014a). Volcano geodesy at the Soufrière Hills Volcano, Montserrat: a review. *Geological Society, London, Memoirs*, 39(1):195–217.

Odbert, H. M., Stewart, R. C., and Wadge, G. (2014b). Cyclic phenomena at the Soufrière Hills Volcano, Montserrat. *Geological Society, London, Memoirs*, 39(1):41–60.

Oliveri del Castillo, A., Palumbo, A., and Percolo, E. (1968). Contributo allo studio della Solfatara di Pozzuoli (Campi Flegrei) mediante osservazione gravimetrichei. *Annali Osservatorio Vesuviano*, 22:217–225.

Oregon State University (2019). How is a volcano defined as being active, dormant, or extinct? http://volcano.oregonstate.edu/, Accessed 2019-04-03.

Oreskes, N., Shrader-Frechette, K., and Belitz, K. (1994). Verification, validation, and confirmation of numerical models in the earth sciences. *Science*, 263(5147):641–646.

Orlando, V., Franco, T., Dario, T., Robert, P. J., and Antonio, C. (2011). Submarine and inland gas discharges from the Campi Flegrei (southern Italy) and the Pozzuoli Bay: Geochemical clues for a common hydrothermal-magmatic source. *Procedia Earth and Planetary Science*, 4(1):57–73.

Orsi, G., Civetta, L., Del Gaudio, C., de Vita, S., Di Vito, M., Isaia, R., Petrazzuoli, S., Ricciardi, G., and Ricco, C. (1999). Short-term ground deformations and seismicity in the resurgent Campi Flegrei caldera (Italy): an example of active block-resurgence in a densely populated area. *Journal of Volcanology and Geothermal Research*, 91(2-4):415–451.

Orsi, G., De Vita, S., and di Vito, M. (1996). The restless, resurgent Campi Flegrei nested caldera (Italy): constraints on its evolution and configuration. *Journal of Volcanology and Geothermal Research*, 74(3-4):179–214.

Palano, M., Puglisi, G., and Gresta, S. (2008). Ground deformation patterns at Mt. Etna from 1993 to 2000 from joint use of InSAR and GPS techniques. *Journal of Volcanology and Geothermal . . .* , 169(3-4):99–120.

Pallister, J. S., Thornber, C. R., Cashman, K. V., Clynne, M. A., Lowers, H. A., Mandeville, C. W., Brownfield, I. K., and Meeker, G. P. (2008). Petrology of the 2004-2006 Mount St. Helens lava dome-implications for magmatic plumbing and eruption triggering. *US Geological Survey professional paper*, (1750):647–702.

Palma, J. L., Blake, S., and Calder, E. S. (2011). Constraints on the rates of degassing and convection in basaltic open-vent volcanoes. *Geochemistry, Geophysics, Geosystems*, 12(11):n/a–n/a.

Parascandola, A. (1947). *I Fenomeni Bradisismici del Serapeo di Pozzuoli*. Stabilmento tipografico G. Genovese.

Parfitt, L. and Wilson, L. (2009). *Fundamentals of physical volcanology*. John Wiley & Sons.

Patanè, D., De Gori, P., Chiarabba, C., and Bonaccorso, A. (2003). Magma Ascent and the Pressurization of Mount Etna's Volcanic System. *Science*, 299(5615):2061–2063.

Patrick, M. R., Orr, T., Swanson, D. A., and Lev, E. (2016). Shallow and deep controls on lava lake surface motion at Klauea Volcano. *Journal of Volcanology and Geothermal Research*, 328:247–261.

Paulatto, M., Minshull, T. A., Baptie, B., Dean, S., Hammond, J. O., Henstock, T., Kenedi, C. L., Kiddle, E. J., Malin, P., Peirce, C., Ryan, G., Shalev, E., Sparks, R. S., and Voight, B. (2010). Upper crustal structure of an active volcano from refraction/reflection tomography, Montserrat, Lesser Antilles. *Geophysical Journal International*, 180(2):685–696.

Pavez, A., Remy, D., Bonvalot, S., Diament, M., Gabalda, G., Froger, J. L., Julien, P., Legrand, D., and Moisset, D. (2006). Insight into ground deformations at Lascar volcano (Chile) from SAR interferometry, photogrammetry and GPS data: Implications on volcano dynamics and future space monitoring. *Remote Sensing of Environment*, 100(3):307–320.

Pearson, S. C., Kiyosugi, K., Lehto, H. L., Saballos, J. A., Connor, C. B., and Sanford, W. E. (2012). Integrated geophysical and hydrothermal models of flank degassing and fluid flow at Masaya volcano, Nicaragua. *Geochemistry, Geophysics, Geosystems*, 13(5):1–21.

Pearson, S. C. P., Connor, C. B., and Sanford, W. E. (2008). Rapid response of a hydrologic system to volcanic activity: Masaya volcano, Nicaragua. *Geology*, 36(12):951–954.

Pérez, W., Freundt, A., Kutterolf, S., and Schmincke, H. U. (2009). The Masaya Triple Layer: A 2100 year old basaltic multi-episodic Plinian eruption from the Masaya Caldera Complex (Nicaragua). *Journal of Volcanology and Geothermal Research*, 179(3-4):191–205.

Perrotta, A., Scarpati, C., Luongo, G., and Morra, V. (2010). Stratigraphy and volcanological evolution of the southwestern sector of Campi Flegrei and Procida Island, Italy. *Geological Society of America Special Papers*, 464:171–191.

Petrillo, Z., Chiodini, G., Mangiacapra, A., Caliro, S., Capuano, P., Russo, G., Cardellini, C., and Avino, R. (2013). Defining a 3D physical model for the hydrothermal circulation at Campi Flegrei caldera (Italy). *Journal of Volcanology and Geothermal Research*, 264:172–182.

Petrosino, S., Cusano, P., and Saccorotti, G. (2006). Shallow shear-wave velocity structure of Solfatara volcano (Campi Flegrei , Italy), from inversion of Rayleigh-wave dispersion curves. *Bollettino Di Geofisica Teorica Ed Applicata*, 47(1-2):89–103.

Petrosino, S., Damiano, N., Cusano, P., Di Vito, M. A., De Vita, S., and Del Pezzo, E. (2012). Subsurface structure of the Solfatara volcano (Campi Flegrei caldera, Italy) as deduced from joint seismic-noise array, volcanological and morphostructural analysis. *Geochemistry, Geophysics, Geosystems*, 13(7):1–25.

Phillips, J., Duval, J., and Ambroziak, R. (1993). Phillips, J.D., Duval, J.S. and Ambroziak, R.A., 1993. National geophysical data grids; gamma-ray, gravity, magnetic, and topographic data for the conterminous United States. Technical report, US Geological Survey.

Phillipson, G., Sobradelo, R., and Gottsmann, J. (2013). Global volcanic unrest in the 21st century: An analysis of the first decade. *Journal of Volcanology and Geothermal Research*, 264:183–196.

Piochi, M., Kilburn, C., and Vito, M. D. (2014). The volcanic and geothermally active Campi Flegrei caldera: an integrated multidisciplinary image of its buried structure. *International Journal of Earth Sciences*, pages 401–421.

Poland, M. P. and Carbone, D. (2016). Insights into shallow magmatic processes at Klauea Volcano, Hawaii, from a multiyear continuous gravity time series. *Journal of Geophysical Research : Solid Earth*, pages 1–16.

Poland, M. P., Moats, W. P., and Fink, J. H. (2008). A model for radial dike emplacement in composite cones based on observations from Summer Coon volcano, Colorado, USA. *Bulletin of Volcanology*, 70(7):861–875.

Power, J. A., Lahr, J. C., Page, R. A., Chouet, B. A., Stephens, C. D., Harlow, D. H., Murray, T. L., and Davies, J. N. (1994). Seismic evolution of the 1989-1990 eruption sequence of Redoubt Volcano, Alaska. *Journal of Volcanology and Geothermal Research*, 62(1-4):69–94.

Ray, D. (1999). *Ocean Tide Model From Altimetry TOPEX /POSEIDON Altimetry: GOT99.2*. NASA.

Rinaldi, A., Todesco, M., Vandemeulebrouck, J., Revil, A., and Bonafede, M. (2011). Electrical conductivity, ground displacement, gravity changes, and gas flow at Solfatara crater (Campi Flegrei caldera, Italy): Results from numerical modeling. *Journal of Volcanology and Geothermal Research*, 207(3-4):93–105.

Robinson, E. S. and Coruh, C. (1988). *Basic Exploration Geophysics*. Somerset, NJ (US); John Wiley and Sons, Inc.

Roche, O., van Wyk de Vries, B., and Druitt, T. (2001). Sub-surface structures and collapse mechanisms of summit pit craters. *Journal of Volcanology and Geothermal Research*, 105(1-2):1–18.

Roman, D. C., Savage, M. K., Arnold, R., Latchman, J. L., and De Angelis, S. (2011). Analysis and forward modeling of seismic anisotropy during the ongoing eruption of the Soufrière Hills Volcano, Montserrat, 1996-2007. *Journal of Geophysical Research: Solid Earth*, 116(3):1996–2007.

Rosi, M., Sbrana, A., and Principe, C. (1983). The phlegraean fields: Structural evolution,

volcanic history and eruptive mechanisms. *Journal of Volcanology and Geothermal Research*, 17(1-4):273–288.

Rowland, J. V. and Sibson, R. H. (2004). Structural controls on hydrothermal flow in a segmented rift system, Taupo Volcanic Zone, New Zealand. *Geofluids*, 4(4):259–283.

Rust, A. C., Cashman, K. V., and Wallace, P. J. (2004). Magma degassing buffered by vapor flow through brecciated conduit margins. *Geology*, 32(4):349–352.

Ryan, W. B., Carbotte, S. M., Coplan, J. O., O'Hara, S., Melkonian, A., Arko, R., Weissel, R. A., Ferrini, V., Goodwillie, A., Nitsche, F., Bonczkowski, J., and Zemsky, R. (2009). Global multi-resolution topography synthesis. *Geochemistry, Geophysics, Geosystems*, 10(3).

Rymer, H., Cassidy, J., Locke, C. A., and Murray, J. B. (1995). Magma movements in Etna volcano associated with the major 1991-1993 lava eruption: evidence from gravity and deformation. *Bulletin of Volcanology*, 57(6):451–461.

Rymer, H., Van Wyk De Vries, B., Stix, J., Williams-Jones, G., Rymer, H., Van Wyk De Vries, B., Stix, J., and Williams-Jones, G. (1998). Pit crater structure and processes governing persistent activity at Masaya Volcano, Nicaragua. *Bulletin of Volcanology*, 59(April 1994):345–355.

Rymer, H. and Williams-Jones, G. (2000). Volcanic eruption prediction: Magma chamber physics from gravity and deformation measurements. *Geophysical Research Letters*, 27(16):2389–2392.

Saccorotti, G., Petrosino, S., Bianco, F., Castellano, M., Galluzzo, D., La Rocca, M., Del Pezzo, E., Zaccarelli, L., and Cusano, P. (2007). Seismicity associated with the 2004-2006 renewed ground uplift at Campi Flegrei Caldera, Italy. *Physics of the Earth and Planetary Interiors*, 165(1-2):14–24.

Sandwell, D. T., Garcia, E., Soofi, K., Wessel, P., Chandler, M. M. T., and Smith, W. H. F. (2013). Toward 1-mGal accuracy in global marine gravity from CryoSat-2, Envisat, and Jason-1. *The Leading Edge*, (August):892–899.

Sandwell, D. T., Muller, R. D., Smith, W. H. F., Garcia, E., and Francis, R. (2014). New global marine gravity model from CryoSat-2 and Jason-1 reveals buried tectonic structure. *Science*, 346(6205):65–67.

Sandwell, D. T. and Smith, W. H. (2009). Global marine gravity from retracked Geosat and ERS-1 altimetry: Ridge segmentation versus spreading rate. *Journal of Geophysical Research: Solid Earth*, 114(1):1–18.

Saxby, J., Gottsmann, J., Cashman, K., and Gutiérrez, E. (2016). Magma storage in a strike-slip caldera. *Nature Communications*, 7:12295.

Scandone, R., Cashman, K. V., and Malone, S. D. (2007). Magma supply, magma ascent and the style of volcanic eruptions. *Earth and Planetary Science Letters*, 253(3-4):513–529.

Scandone, R. and Malone, S. D. (1985). Magma supply, magma discharge and readjustment of the feeding system of mount St. Helens during 1980. *Journal of Volcanology and Geothermal Research*, 23(34):239–262.

Schaefer, L. N., Kendrick, J. E., Oommen, T., Lavallée, Y., and Chigna, G. (2015). Geomechanical rock properties of a basaltic volcano. *Frontiers in Earth Science*, 3(29):1–15.

Scheu, B., Spieler, O., and Dingwell, D. B. (2006). Dynamics of explosive volcanism at Unzen volcano: An experimental contribution. *Bulletin of Volcanology*, 69(2):175–187.

Schiavone, D. and Loddo, M. (2007). 3-D density model of Mt. Etna Volcano (Southern Italy). *Journal of Volcanology and Geothermal Research*, 164(3):161–175.

Scintrex Limited (2012). CG-5 Scintrex autograv system Operation Manual.

Segall, P. (2010). *Earthquake and Volcano Deformation*. Princeton University Press.

Segall, P. (2013). Volcano deformation and eruption forecasting. *Geological Society, London, Special Publications*, 380:85–106.

Seigel, H., Brcic, I., and Mistry, P. (1995). A guide to high precision land gravimeter surveys. *Scintrex Limited*, 222(1):1–122.

Setyawan, A., Yudianto, H., Nishijima, J., and Hakim, S. (2015). Horizontal Gradient Analysis for Gravity and Magnetic Data Beneath Gedongsongo Geothermal Manifestations , Ungaran , Indonesia. *World Geothermal Congress 2015*, (April):1–6.

Sevilla, W. I., Ammon, C. J., Voight, B., and De Angelis, S. (2010). Crustal structure beneath the Montserrat region of the Lesser Antilles island arc. *Geochemistry, Geophysics, Geosystems*, 11(6):n/a–n/a.

Shalev, E., Kenedi, C. L., Malin, P., Voight, V., Miller, V., Hidayat, D., Sparks, R. S. J., Minshull, T., Paulatto, M., Brown, L., and Mattioli, G. (2010). Three-dimensional seismic velocity tomography of Montserrat from the SEA-CALIPSO offshore/onshore experiment. *Geophysical Research Letters*, 37(9).

Sibson, R. H. (1994). Crustal stress, faulting and fluid flow. *Geological Society, London, Special Publications*, 78(1):69–84.

Sigurdsson, H., Houghton, B., McNutt, S., Rymer, H., and Stix, J., editors (2015). *The encyclopedia of volcanoes*. Elsevier.

Sparks, R. S. (2003). Forecasting volcanic eruptions. *Earth and Planetary Science Letters*, 210(1-2):1–15.

Sparks, R. S. J., Biggs, J., and Neuberg, J. W. (2012). Monitoring Volcanoes. *Science*, 335(6074):1310–1311.

Sparks, R. S. J., Murphy, M. D., Lejune, A. M., Watts, R. B., Barclay, J., and Young, S. R. (2000). Control on the emplacement of the andesite lava dome of the Soufrière Hills volcano, Montserrat by degassing-induced crystallization. *Terra Nova*, 12:1–20.

Sparks, R. S. J. and Young, S. R. (2002). The eruption of Soufrière Hills Volcano, Montserrat (1995-1999): overview of scientific results. *Geological Society, London, Memoirs*, 21(1):45–69.

Stephens, K. J., Ebmeier, S. K., Young, N. K., and Biggs, J. (2016). Transient deformation associated with explosive eruption measured at Masaya volcano (Nicaragua) using Interferometric Synthetic Aperture Radar. *Journal of Volcanology and Geothermal Research*.

Stevenson, D. S. and Blake, S. (1998). Modelling the dynamics and thermodynamics of volcanic degassing. *Bulletin of Volcanology*, 60(2):307–317.

Stewart, R., Bass, V., Christopher, T., Dondin, F., Finizola, N., Fournier, N., Joseph, E., Komorowski, J., Legendre, Y., Robertson, R., Syers, R., and Williams, P. (2009). Report for the Scientific Advisory Committee (SAC12) on Montserrat Volcanic Activity. Technical report, Montserrat Volcano Observatory (MVO) Open File Report 09/01 (2009).

Stix, J. (2007). Stability and instability of quiescently active volcanoes: The case of Masaya,

Nicaragua. *Geology*, 35(6):535–538.

Stix, J., Torres, R. C., Narváez M, L., Cortés J, G. P., Raigosa, J. A., Gómez M, D., and Castonguay, R. (1997). A model of vulcanian eruptions at Galeras volcano, Colombia. *Journal of Volcanology and Geothermal Research*, 77(1-4):285–303.

Swanson, D. A., Casadevall, T. J., Dzurisin, D., Holcomb, R. T., Newhall, C. G., Malone, S. D., and Weaver, C. S. (1985). Forecasts and predictions of eruptive activity at Mount St. Helens, USA: 1975-1984. *Journal of Geodynamics*, 3(3-4):397–423.

Tamura, Y. (1982). A computer program for calculating the tide-generating force. *Publications of the International Latitude Observatory at Mizusawa*, 16:1–20.

Tarantola, A. (1987). *Inverse Problem Theory and Methods for Model Parameter Estimation*, volume 89. SIAM.

Tarquini, S., Isola, I., Favalli, M., Mazzarini, F., Bisson, M., Pareschi, M. T., and Boschi, E. (2007). TINITALY/01: A new Triangular Irregular Network of Italy. *Annals of Geophysics*, 50(3):407–425.

Tarquini, S., Vinci, S., Favalli, M., Doumaz, F., Fornaciai, A., and Nannipieri, L. (2012). Release of a 10-m-resolution DEM for the Italian territory: Comparison with global-coverage DEMs and anaglyph-mode exploration via the web. *Computers and Geosciences*, 38(1):168–170.

Telford, W. M., Gelart, L. P., Sheriff, R. E., and Keys, D. A. (1976). *Applied Geophysics*. Cambridge University Press, second edition.

Testo (2019). Testo 845 Leaflet. https://www.testo.com/kr-KR/testo-845/p/0563-8451, Accessed 2019-10-02.

Thomas, M. E. and Neuberg, J. (2012). What makes a volcano tick-A first explanation of deep multiple seismic sources in ascending magma. *Geology*, 40(4):351–354.

Tibaldi, A. (2015). Structure of volcano plumbing systems: A review of multi-parametric effects. *Journal of Volcanology and Geothermal Research*, 298:85–135.

Todesco, M. (2008). Hydrothermal Fluid Circulation and its Effect on Caldera Unrest. In *Developments in Volcanology*, volume 10, chapter 11, pages 393–416. Elsevier.

Todesco, M., Afanasyev, A. A., Montagna, C. P., and Longo, A. (2016). Interaction between hydrothermal and magmatic systems : modelling of magmatic gas release and ascent at Campi Flegrei (Italy). In *Geophysical Research Abstracts*, volume 18, page 8264.

Todesco, M. and Berrino, G. (2005). Modeling hydrothermal fluid circulation and gravity signals at the Phlegraean Fields caldera. *Earth and Planetary Science Letters*, 240(2):328–338.

Todesco, M., Chiodini, G., and Macedonio, G. (2003). Monitoring and modelling hydrothermal fluid emission at La Solfatara (Phlegrean Fields, Italy). An interdisciplinary approach to the study of diffuse degassing. *Journal of Volcanology and Geothermal Research*, 125(1-2):57–79.

Todesco, M., Rinaldi, A. P., and Bonafede, M. (2010). Modeling of unrest signals in heterogeneous hydrothermal systems. *Journal of Geophysical Research: Solid Earth*, 115(9):B09213.

Todesco, M., Rutqvist, J., Chiodini, G., Pruess, K., and Oldenburg, C. M. (2004). Modeling of recent volcanic episodes at Phlegrean Fields (Italy): geochemical variations and ground deformation. *Geothermics*, 33(4):531–547.

Trasatti, E., Giunchi, C., and Bonafede, M. (2003). Effects of topography and rheological

layering on ground deformation in volcanic regions. *Journal of Volcanology and Geothermal Research*, 122(1-2):89–110.

Travaglino, F., Di Crescenzo, A., Martinucci, B., and Scarpa, R. (2018). A New Model of Campi Flegrei Inflation and Deflation Episodes Based on Brownian Motion Driven by the Telegraph Process. *Mathematical Geosciences*, pages 1–15.

Troiano, A., Di Giuseppe, M., Patella, D., Troise, C., and De Natale, G. (2014). Electromagnetic outline of the Solfatara-Pisciarelli hydrothermal system, Campi Flegrei (Southern Italy). *Journal of Volcanology and Geothermal Research*, 277:9–21.

UNAVCO (2019). Synthetic Aperture Radar (SAR) Satellites. https://www.unavco.org/instrumentation/geophysical/imaging/sar-satellites/sar-satellites.html, Accessed 2019-28-02.

USGS (2017). Volcanic alert-levels characterize conditions at U.S. volcanoes. https://volcanoes.usgs.gov/vhp/about_alerts.html, Accessed 2019-12-02.

Van Camp, M., de Viron, O., Watlet, A., Meurers, B., Francis, O., and Caudron, C. (2017). Geophysics From Terrestrial Time-Variable Gravity Measurements.

Van Camp, M. and Vauterin, P. (2005). Tsoft: Graphical and interactive software for the analysis of time series and Earth tides. *Computers and Geosciences*, 31(5):631–640.

van Manen, S. M. (2014). Perception of a chronic volcanic hazard: persistent degassing at Masaya volcano, Nicaragua. *Journal of Applied Volcanology*, 3(1):9.

Vanorio, T. (2005). Three-dimensional seismic tomography from P wave and S wave microearthquake travel times and rock physics characterization of the Campi Flegrei Caldera. *Journal of Geophysical Research*, 110(B3):B03201.

Venturi, S., Tassi, F., Bicocchi, G., Cabassi, J., Capecchiacci, F., Capasso, G., Vaselli, O., Ricci, A., and Grassa, F. (2017). Fractionation processes affecting the stable carbon isotope signature of thermal waters from hydrothermal/volcanic systems: The examples of Campi Flegrei and Vulcano Island (southern Italy). *Journal of Volcanology and Geothermal Research*, 345:46–57.

Vilardo, G., Isaia, R., Ventura, G., De Martino, P., and Terranova, C. (2010). InSAR Permanent Scatterer analysis reveals fault re-activation during inflation and deflation episodes at Campi Flegrei caldera. *Remote Sensing of Environment*, 114(10):2373–2383.

Voight, B., Hidayat, D., Sacks, S., Linde, A., Chardot, L., Clarke, A., Elsworth, D., Foroozan, R., Malin, P., Mattioli, G., McWhorter, N., Shalev, E., Sparks, R. S., Widiwijayanti, C., and Young, S. R. (2010). Unique strainmeter observations of Vulcanian explosions, Soufrire Hills Volcano, Montserrat, July 2003. *Geophysical Research Letters*, 37(11).

Voight, B., Sparks, R. S., Miller, A. D., Stewart, R. C., Hoblitt, R. P., Clarke, A., Ewart, J., Aspinall, W. P., Baptie, B., Calder, E. S., Cole, P., Druitt, T. H., Hartford, C., Herd, R. A., Jackson, P., Lejeune, A. M., Lockhart, A. B., Loughlin, S. C., Luckett, R., Lynch, L., Norton, G. E., Robertson, R., Watson, I. M., Watts, R., and Young, S. R. (1999). Magma flow instability and cyclic activity at Soufrière Hills volcano, Montserrat, British West Indies. *Science*, 283(5405):1138–1142.

Wadge, G. (1986). The dykes and structural setting of the volcanic front in the Lesser Antilles island arc. *Bulletin of Volcanology*, 48(6):349–372.

Wadge, G., Voight, B., Sparks, R. S. J., Cole, P. D., Loughlin, S. C., and Robertson, R. E. A. (2014). Chapter 1 An overview of the eruption of Soufrière Hills Volcano, Montserrat from

2000 to 2010. *Geological Society, London, Memoirs*, 39(1):1.1–40.

Walker, J. A., Williams, S. N., Kalamarides, R. I., and Feigenson, M. D. (1993). Shallow open-system evolution of basaltic magma beneath a subduction zone volcano: The Masaya Caldera Complex, Nicaragua. *Journal of Volcanology and Geothermal Research*, 56(4):379–400.

Watts, R. B., Herd, R. A., Sparks, R. S. J., and Young, S. R. (2002). Growth patterns and emplacement of the andesitic lava dome at Soufrière Hills Volcano, Montserrat. *Geological Society, London, Memoirs*, 21(1):115–152.

Wauthier, C., Cayol, V., Kervyn, F., and D'Oreye, N. (2012). Magma sources involved in the 2002 Nyiragongo eruption, as inferred from an InSAR analysis. *Journal of Geophysical Research: Solid Earth*, 117(5):n/a–n/a.

Wayne Peter, B. (2008). The rock mechanics of kimberlite volcanic pipe excavation. *Journal of Volcanology and Geothermal Research*, 174(1-3):29–39.

Wessel, P. and Smith, W. H. F. (1998). New, improved version of generic mapping tools released. *Eos, Transactions American Geophysical Union*, 79(47):579–579.

West Systems (2016). High resolution Methane and Carbon Dioxide diffuse flux meter. https://www.westgroupnews.com/wp-content/uploads/2016/02/12_Portable_fluxmeter.pdf, Accessed 2019-10-02.

Widiwijayanti, C., Clarke, A., Elsworth, D., and Voight, B. (2005). Geodetic constraints on the shallow magma system at Soufrière Hills Volcano, Montserrat. *Geophysical Research Letters*, 32(11):1–5.

Williams, C. A. and Wadge, G. (1998). The effects of topography on magma chamber deformation models: Application to Mt. Etna and radar interferometry. *Geophysical Research Letters*, 25(10):1549–1552.

Williams-Jones, G. (2001). *Integrated Geophysical Studies at Masaya Volcano, Nicaragua*. PhD thesis.

Williams-Jones, G., Rymer, H., and Rothery, D. A. (2003). Gravity changes and passive SO2 degassing at the Masaya caldera complex, Nicaragua. *Journal of Volcanology and Geothermal Research*, 123(1-2):137–160.

Wilson, L., Sparks, R. S. J., and Walker, G. P. (1980). Explosive volcanic eruptions -IV. The control of magma properties and conduit geometry on eruption column behaviour. *Geophysical Journal of the Royal Astronomical Society*, 63(1):117–148.

Yamamoto, M., Kawakatsu, H., Kaneshima, S., Mori, T., Tsutsui, T., Sudo, Y., and Morita, Y. (1999). Detection of a crack-like conduit beneath the active crater at Aso volcano. *Geophysical Research Letters*, 26(24):3677–3680.

Yang, X. M., Davis, P. M., and Dieterich, J. H. (1988). Deformation from inflation of a dipping finite prolate spheroid in an elastic half-space as a model for volcanic stressing. *Journal of Geophysical Research*, 93(B5):4249–4257.

Young, N. K. and Gottsmann, J. (2015). Shallow crustal mechanics from volumetric strain data: Insights from Soufrière Hills Volcano, Montserrat. *Journal of Geophysical Research B: Solid Earth*, 120(3):1559–1571.

Young, S., Sparks, R., Aspinall, W., Lynch, L., Miller, A., Robertson, R., and Shepherd, J. (1998). Overview of the eruption of Soufrière Hills Volcano, Montserrat, 18 July 1995 to December 1997. *Geophysical Research Letters*, 25(18):3389–3392.

Zobin, V. M., Ramírez, J. J., Santiago, H., Alatorre, E., and Navarro, C. (2011). Relationship between tilt changes and effusive-explosive episodes at an andesitic volcano: The 2004-2005 eruption at Volcán de Colima, México. *Bulletin of Volcanology*, 73(1):91–99.

Zobin, V. M., Reyes, G. A., Guevara, E., and Bretón, M. (2008). Seismological constraints on the position of the fragmentation surfaces in the volcano conduit. *Earth and Planetary Science Letters*, 275(3-4):337–341.

Zollo, A., Capuano, P., and Corciulo, M. (2006). *Geophysical Exploration of the Campi Flegrei (Southern Italy) Caldera' Interiors: Data, Methods and Results*. Napoli, Italy.

Zollo, A., Maercklin, N., Vassallo, M., Dello Iacono, D., Virieux, J., and Gasparini, P. (2008). Seismic reflections reveal a massive melt layer feeding Campi Flegrei caldera. *Geophysical Research Letters*, 35(12).

Appendix A

This appendix contains information pertinent to the gravity reductions and how the caldera fill detrending was carried out.

Table A.1: Table of gravity reductions and detrended gravity data. E. height refers to the WGS84 ellipsoidal height as given by the GPS measurements and O. Height refers to the orthometric height. Stn. = station, DC = Drift Corrected data, Lat = Latitude correction, FA = Free Air correction, BS = Bouguer Slab correction, Terrain = Terrain correction, R. gravity = reduced gravity, Linear dt. = L. detrended and C. dt. = Caldera detrended.

Stn	Lat °	Long °	Easting (m)	Northing (m)	E. Height (m)	O. Height (m)	Raw Data (mGal)	DC (mGal)	Lat (mGal)	FA (mGal)	BS (mGal)	Terrain (mGal)	R. Gravity (mGal)	L. dt. (mGal)	C. dt. (mGal)
1	40.83134	14.11458	425344.80	4520411.54	94.908	43.308	6379.495	-8.822	0.372	7.380	-1.905	1.976	-1.000	-1.511	4.510
2	40.82403	14.12088	425867.95	4519595.17	56.138	4.538	6387.915	-0.393	1.026	-4.585	1.184	0.535	-2.234	-2.756	4.714
3	40.81802	14.17520	430442.18	4518883.37	68.496	16.896	6391.593	3.303	1.563	-0.771	0.199	1.510	5.804	2.332	6.377
4	40.80543	14.17363	430297.02	4517486.70	54.621	3.021	6394.900	6.620	2.690	-5.053	1.304	1.185	6.747	4.012	7.414
5	40.81499	14.16330	429435.57	4518556.42	55.848	4.248	6391.155	2.894	1.835	-4.674	1.207	0.648	1.909	-0.679	3.036
6	40.81851	14.14459	427861.59	4518962.06	57.505	5.905	6387.100	-1.151	1.520	-4.163	1.075	4.377	1.658	0.018	5.023
7	40.82118	14.12867	426521.53	4519271.79	57.093	5.493	6387.190	-1.051	1.281	-4.290	1.108	0.610	-2.343	-3.185	4.120
8	40.83189	14.12915	426573.82	4520459.95	138.206	86.606	6369.825	-18.386	0.323	20.741	-5.354	0.870	-1.806	-3.211	2.196
9	40.83081	14.15067	428386.90	4520322.59	93.319	41.719	6382.615	-5.579	0.419	6.889	-1.778	0.686	0.637	-2.014	2.189
10	40.82697	14.15990	429161.82	4519889.14	73.178	21.578	6389.026	0.846	0.763	0.674	-0.174	1.881	3.989	0.996	5.083
11	40.82814	14.13639	427180.34	4520038.18	152.042	100.442	6365.710	-21.906	0.658	25.011	-6.457	0.752	-1.941	-3.590	1.684
12	40.82813	14.13856	427363.57	4520035.60	149.344	97.744	6366.600	-21.005	0.659	24.179	-6.242	0.744	-1.666	-3.441	1.612
13	40.82795	14.13872	427376.77	4520015.16	148.431	96.831	6366.860	-20.739	0.675	23.897	-6.169	0.780	-1.557	-3.353	1.689
14	40.82777	14.13888	427389.56	4519994.38	148.126	96.526	6366.910	-20.684	0.692	23.803	-6.145	0.748	-1.586	-3.366	1.687
15	40.82758	14.13903	427401.92	4519974.17	147.987	96.387	6366.918	-20.674	0.708	23.760	-6.134	0.755	-1.585	-3.362	1.690
16	40.82739	14.13918	427414.53	4519952.95	148.006	96.406	6366.910	-20.679	0.725	23.766	-6.135	0.773	-1.551	-3.339	1.712
17	40.82721	14.13932	427426.05	4519932.19	148.002	96.402	6366.860	-20.726	0.741	23.764	-6.135	0.800	-1.555	-3.336	1.726
18	40.82703	14.13944	427436.14	4519912.33	148.026	96.426	6366.780	-20.803	0.757	23.772	-6.137	0.836	-1.575	-3.368	1.703
19	40.82689	14.13953	427443.67	4519897.15	148.068	96.468	6366.720	-20.860	0.769	23.785	-6.140	0.875	-1.571	-3.359	1.711
20	40.82670	14.13968	427456.44	4519875.27	148.742	97.142	6366.474	-21.103	0.787	23.993	-6.194	0.945	-1.572	-3.329	1.737
21	40.82651	14.13981	427467.03	4519854.63	148.837	97.237	6366.400	-21.174	0.804	24.022	-6.201	1.050	-1.499	-3.266	1.810
23	40.82703	14.13989	427474.00	4519911.84	148.947	97.347	6366.750	-20.815	0.757	24.056	-6.210	0.889	-1.323	-3.155	1.858
24	40.82741	14.13956	427447.01	4519954.29	148.177	96.577	6366.775	-20.784	0.723	23.818	-6.149	0.805	-1.587	-3.408	1.597
25	40.82779	14.13928	427423.40	4519996.94	148.228	96.628	6366.840	-20.717	0.689	23.834	-6.153	0.771	-1.576	-3.384	1.624
26	40.82817	14.13898	427398.43	4520039.37	148.980	97.380	6366.660	-20.890	0.655	24.066	-6.213	0.773	-1.608	-3.426	1.573
27	40.82854	14.13807	427322.35	4520080.86	150.085	98.485	6366.470	-21.070	0.622	24.407	-6.301	0.753	-1.588	-3.363	1.688
28	40.82827	14.13944	427437.92	4520050.08	149.438	97.838	6366.500	-21.018	0.646	24.208	-6.249	0.831	-1.583	-3.430	1.515
29	40.82784	14.13977	427465.02	4520001.52	148.547	96.947	6366.575	-20.940	0.685	23.933	-6.178	0.819	-1.681	-3.500	1.454
30	40.82746	14.14006	427489.06	4519959.32	149.023	97.423	6366.290	-21.222	0.719	24.079	-6.216	0.856	-1.783	-3.604	1.357

Table A.1: Table of gravity reductions and detrended gravity data. E. height refers to the WGS84 ellipsoidal height as given by the GPS measurements and O. Height refers to the orthometric height. Stn. = Station, DC = Drift Corrected data, Lat = Latitude correction, FA = Free Air correction, BS = Bouguer Slab correction, Terrain = Terrain correction, R. gravity = reduced gravity, Linear dt. = L. detrended and C. dt. = Caldera detrended.

Stn.	Lat °	Long °	Easting (m)	Northing (m)	E. Height (m)	O. Height (m)	Raw Data (mGal)	DC (mGal)	Lat (mGal)	FA (mGal)	BS (mGal)	Terrain (mGal)	R. Gravity (mGal)	L. dt. (mGal)	C. dt, (mGal)
31	40.82709	14.14036	427513.86	4519917.78	149.137	97.537	6366.050	-21.459	0.752	24.115	-6.225	0.957	-1.861	-3.733	1.223
32	40.82677	14.14066	427539.24	4519882.34	149.443	97.843	6365.865	-21.641	0.781	24.209	-6.250	1.166	-1.735	-3.592	1.359
33	40.82704	14.14122	427586.67	4519911.63	150.184	98.584	6365.630	-21.872	0.757	24.438	-6.309	1.205	-1.782	-3.659	1.219
34	40.82721	14.14185	427639.81	4519930.20	152.963	101.363	6364.700	-22.799	0.741	25.295	-6.530	1.494	-1.799	-3.736	1.072
35	40.82746	14.14096	427565.12	4519958.91	150.619	99.019	6365.570	-21.924	0.719	24.572	-6.343	1.008	-1.969	-3.873	1.002
36	40.82779	14.14062	427536.89	4519995.93	149.927	98.327	6365.440	-22.051	0.689	24.358	-6.288	0.933	-2.359	-4.238	0.641
37	40.82818	14.14028	427508.56	4520039.06	149.926	98.326	6366.075	-21.412	0.655	24.358	-6.288	0.896	-1.791	-3.655	1.217
38	40.82860	14.14002	427486.59	4520085.57	150.422	98.822	6366.060	-21.425	0.617	24.511	-6.328	0.930	-1.694	-3.574	1.280
39	40.82900	14.13980	427468.48	4520130.83	152.348	100.748	6365.680	-21.801	0.581	25.106	-6.481	0.989	-1.607	-3.514	1.332
40	40.82772	14.14162	427621.22	4519987.22	151.131	99.531	6365.124	-22.350	0.695	24.730	-6.384	1.319	-1.990	-3.951	0.837
41	40.82833	14.14144	427605.95	4520055.32	152.346	100.746	6364.882	-22.588	0.641	25.105	-6.481	1.414	-1.909	-3.883	0.874
42	40.82871	14.14104	427573.22	4520097.27	151.620	100.020	6365.415	-22.051	0.607	24.881	-6.423	1.439	-1.547	-3.466	1.294
43	40.82915	14.14050	427527.74	4520146.23	152.219	100.619	6365.750	-21.713	0.568	25.066	-6.471	1.355	-1.196	-3.122	1.649
44	40.82801	14.13814	427328.01	4520021.96	148.151	96.551	6366.771	-20.675	0.670	23.810	-6.147	0.726	-1.616	-3.376	1.723
45	40.82758	14.13837	427346.77	4519974.60	147.962	96.362	6366.700	-20.741	0.708	23.752	-6.132	0.722	-1.691	-3.436	1.686
46	40.82721	14.13866	427370.91	4519932.95	147.874	96.274	6366.643	-20.793	0.741	23.725	-6.125	0.752	-1.700	-3.446	1.686
47	40.82679	14.13890	427390.52	4519886.46	147.952	96.352	6366.530	-20.904	0.779	23.749	-6.131	0.826	-1.682	-3.419	1.735
48	40.82643	14.13938	427430.43	4519845.66	148.732	97.132	6366.170	-21.259	0.811	23.990	-6.193	0.992	-1.659	-3.411	1.714
49	40.82624	14.13889	427388.82	4519824.97	149.104	97.504	6366.090	-21.336	0.828	24.104	-6.223	1.071	-1.555	-3.261	1.950
50	40.82664	14.13862	427366.74	4519869.60	148.036	96.436	6366.463	-20.959	0.792	23.775	-6.138	0.829	-1.700	-3.419	1.772
51	40.82702	14.13832	427341.53	4519912.59	147.900	96.300	6366.550	-20.867	0.758	23.733	-6.127	0.750	-1.753	-3.464	1.729
52	40.82741	14.13801	427316.31	4519955.58	147.881	96.281	6366.590	-20.825	0.723	23.727	-6.125	0.715	-1.785	-3.478	1.704
54	40.83016	14.14720	428093.61	4520252.94	118.928	67.328	6373.830	-12.998	0.478	14.792	-3.819	0.928	-0.619	-3.041	1.276
55	40.82501	14.14454	427863.91	4519683.77	172.842	121.242	6359.561	-27.257	0.938	31.430	-8.114	1.345	-1.658	-3.650	1.038
56	40.83289	14.13823	427340.51	4520563.61	241.440	189.840	6343.440	-43.365	0.233	52.599	-13.579	1.927	-2.185	-4.212	0.416
57	40.83163	14.13900	427404.05	4520422.88	230.529	178.929	6346.255	-40.545	0.346	49.232	-12.710	2.051	-1.626	-3.630	1.059
58	40.82759	14.13789	427305.81	4519976.22	148.416	96.816	6365.430	-20.879	0.707	23.892	-6.168	0.767	-1.681	-3.406	1.776
59	40.82705	14.13767	427287.16	4519915.46	148.257	96.657	6365.412	-20.895	0.756	23.843	-6.155	0.729	-1.722	-3.388	1.880
60	40.82676	14.13793	427308.77	4519883.49	148.004	96.404	6365.400	-20.905	0.782	23.765	-6.135	0.768	-1.726	-3.413	1.842

Table A.1: Table of gravity reductions and detrended gravity data. E. height refers to the WGS84 ellipsoidal height as given by the GPS measurements and O. Height refers to the orthometric height. Stn. -= Station, D = Drift Corrected data, Lat = Latitude correction, FA = Free Air correction, BS = Bouguer Slab correction, Terrain = Terrain correction, R. gravity = reduced gravity, L.dt. = Linear detrended and C. dt. = Caldera detrended.

Stn.	Lat °	Long °	Easting (m)	Northing (m)	E. Height (m)	O. Height (m)	Raw Data (mGal)	DC (mGal)	Lat (mGal)	FA (mGal)	BS (mGal)	Terrain (mGal)	R. Gravity (mGal)	L. dt. (mGal)	C. dt, (mGal)
61	40.82636	14.13835	427343.67	4519838.96	148.238	96.638	6365.262	-21.042	0.817	23.837	-6.154	0.895	-1.646	-3.322	1.943
62	40.82699	14.14393	427814.79	4519903.73	228.239	176.639	6344.910	-41.385	0.761	48.525	-12.527	2.593	-2.033	-4.081	0.559
63	40.82761	14.14332	427764.36	4519973.17	226.343	174.743	6345.420	-40.872	0.706	47.940	-12.376	2.602	-2.001	-4.047	0.606
64	40.82796	14.14309	427745.26	4520012.10	226.680	175.080	6345.200	-41.088	0.674	48.044	-12.403	2.904	-1.868	-3.918	0.727
65	40.82792	14.14380	427804.67	4520007.19	223.988	172.388	6346.250	-40.036	0.678	47.214	-12.188	2.304	-2.028	-4.114	0.486
66	40.82897	14.14270	427713.31	4520125.43	233.831	182.231	6343.305	-42.977	0.583	50.251	-12.973	3.254	-1.861	-3.930	0.688
67	40.83351	14.13993	427484.95	4520631.58	209.116	157.516	6351.635	-34.641	0.177	42.624	-11.004	2.139	-0.705	-2.836	1.658
68	40.82871	14.13844	427354.16	4520099.64	150.201	98.601	6365.160	-21.082	0.607	24.443	-6.310	0.786	-1.556	-3.351	1.646
69	40.82935	14.13903	427403.93	4520170.32	154.717	103.117	6364.085	-22.154	0.550	25.837	-6.670	0.959	-1.478	-3.362	1.521
70	40.82956	14.13934	427430.80	4520192.70	153.798	102.198	6364.370	-21.866	0.531	25.553	-6.597	1.123	-1.256	-3.167	1.668
71	40.82954	14.13756	427280.70	4520192.40	152.225	100.625	6364.620	-21.611	0.533	25.068	-6.471	1.014	-1.468	-3.264	1.735
72	40.82861	14.13633	427175.63	4520090.41	152.001	100.401	6364.270	-21.958	0.616	24.998	-6.454	0.998	-1.799	-3.466	1.751
73	40.83539	14.13980	427475.95	4520839.94	202.197	150.597	6353.015	-33.200	0.009	40.489	-10.452	1.580	-1.574	-3.807	0.572
75	40.84905	14.15762	428992.63	4522341.83	241.570	189.970	6348.492	-37.710	-1.213	52.639	-13.589	2.802	2.929	-1.055	3.545
76	40.85547	14.15055	428403.83	4523059.92	189.665	138.065	6363.052	-23.142	-1.788	36.622	-9.454	1.073	3.310	-0.590	3.906
77	40.87610	14.13694	427279.17	4525361.03	97.740	46.140	6386.333	0.143	-3.634	8.254	-2.131	0.639	3.271	-0.866	3.626
78	40.82893	14.12901	426559.26	4520131.48	118.994	67.394	6371.124	-14.502	0.588	14.812	-3.824	0.563	-2.363	-3.610	2.335
79	40.83027	14.13485	427052.82	4520275.36	197.311	145.711	6352.582	-33.043	0.468	38.981	-10.063	1.245	-2.412	-4.090	1.071
80	40.83325	14.13252	426859.38	4520607.99	168.590	116.990	6360.131	-25.492	0.201	30.118	-7.775	0.976	-1.972	-3.652	1.305
81	40.83633	14.13764	427294.61	4520946.64	268.417	216.817	6335.540	-50.082	-0.075	60.924	-15.728	2.565	-2.396	-4.542	-0.145
82	40.82511	14.13693	427222.14	4519701.39	170.298	118.698	6359.545	-26.075	0.929	30.645	-7.911	1.157	-1.256	-2.803	2.788
83	40.85003	14.11510	425410.03	4522485.84	119.904	68.304	6376.250	-9.362	-1.301	15.093	-3.896	1.153	1.688	0.194	3.323
84	40.84002	14.11840	425676.68	4521371.96	129.333	77.733	6370.880	-14.730	-0.405	18.003	-4.648	0.749	-1.031	-2.215	2.092
85	40.84000	14.12837	426517.53	4521361.65	205.284	153.684	6352.985	-32.624	-0.404	41.442	-10.698	1.051	-1.233	-3.010	1.295
86	40.83977	14.13762	427296.34	4521327.75	300.683	249.083	6327.616	-57.991	-0.383	70.882	-18.299	3.864	-1.927	-4.243	-0.047

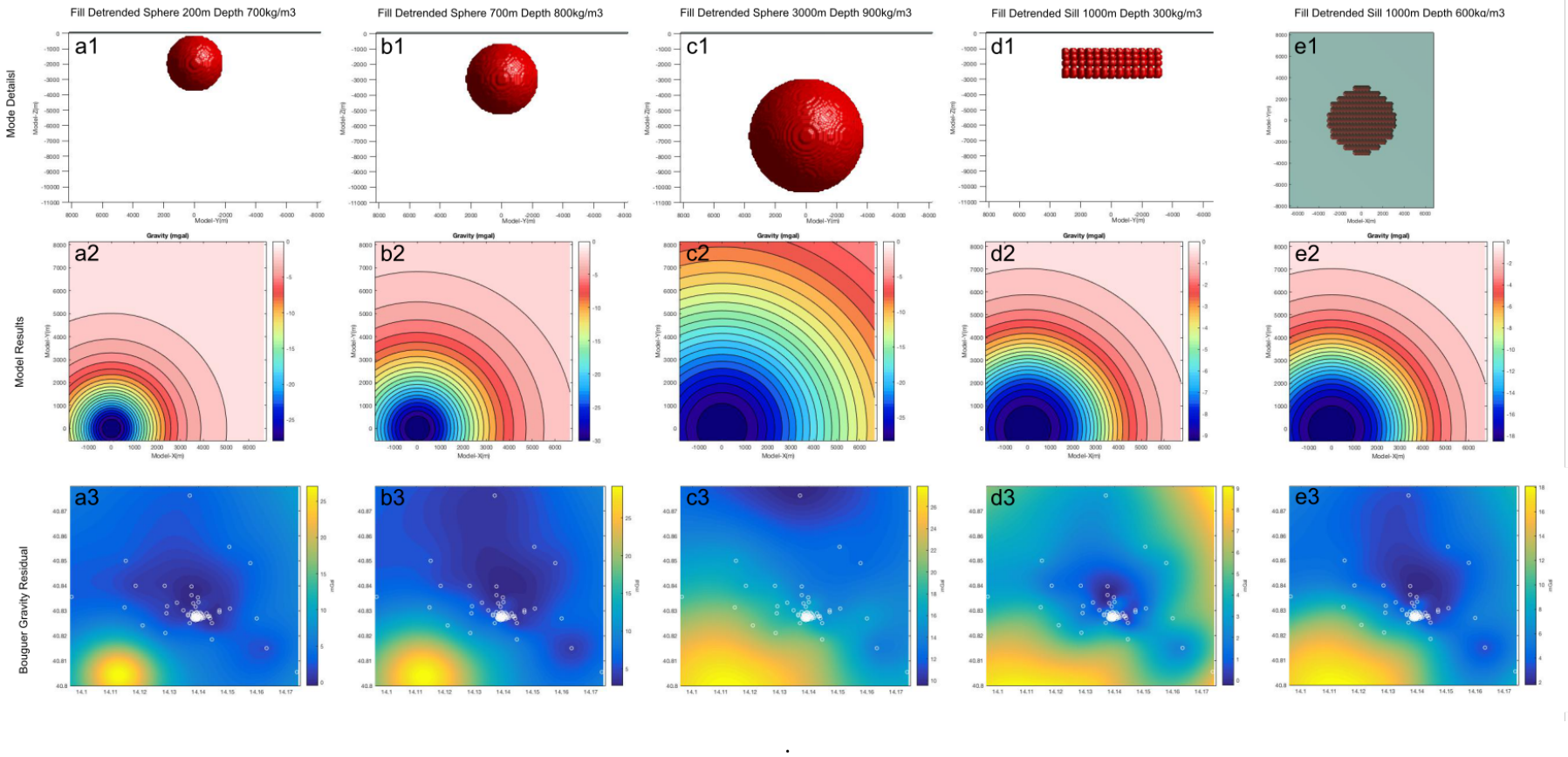

Figure A.1: Figures depicting tested caldera fill effects. The first row (all panels numbered 1) shows the model cross section, however e1 illustrates the same model as d1 in plan view. The second row (all panels numbered 2) shows the resultant gravity anomaly at the surface. The third row (all panels numbered 3) demonstrates the resultant gravity anomaly once the caldera fill anomaly has been subtracted from the regional anomaly shown in Fig. 2.7a. The single sphere models (panels a-c) were rejected; the sill models (panels d-e) were selected as a more appropriate representation based on data from [Capuano et al., 2013] as explained in Section 2.2.2. d3 is therefore identical to Fig. 2.7c

Appendix B

This appendix contains information on benchmarking of analytical and numerical deformation models and inverse model runs, as supplied in the supplementary materials in **Young, N. K.**, & Gottsmann, J. (2015). Shallow crustal mechanics from volumetric strain data: Insights from Soufrire Hills Volcano, Montserrat. *Journal of Geophysical Research: Solid Earth*, 120(3), 1559-1571.

a) Benchmarking

ai) Analytical Conduit Model

The conduit model was set up according to the model by Yang et al. [1988]. The Yang model is for a shallowly dipping finite prolate ellipsoidal body in a HOHS. It produces vertical and horizontal displacements. The model was adapted from the original script to produce 2D output graphs for displacement and strain. Strain was calculated using equations B.1-B.3 presented by Lisowski [2006], derived from Fung [1977] where $\varepsilon_{\theta\theta}$ is tangential strain, ε_{rr} is radial strain and ε_v is volumetric strain.

$$\varepsilon_{\theta\theta} = \frac{u}{r} \tag{B.1}$$

$$\varepsilon_{rr} = \frac{\partial u}{\partial r} \tag{B.2}$$

$$\varepsilon_v = \frac{1-2v}{1-v}(\varepsilon_{rr} + \varepsilon_{\theta\theta}) \tag{B.3}$$

aii) Numerical Conduit Model

An axisymmetric half-space was built on a scale large enough to prevent the boundary conditions from interfering with results, but small enough to be computationally quick [Hickey and Gottsmann, 2014]. This half-space obeys Hookes Law and has a planar surface which extends infinitely in all directions. An infinite element domain was created on the lower and right bounds of the half-space as shown in Fig. 3.3 (main text), with the following boundary conditions; (1) a fixed constraint on the bottom boundary to prevent deformation, (2) a roller on the right boundary to prevent deformation perpendicular to the boundary and (3) a free top boundary [Hickey and Gottsmann, 2014]. An oval cavity was embedded in the half-space and numerical rotation during computation causes the oval to become an ellipsoid. The domain was built as an HOHS. A positive pressure change was imposed on the boundary of this cavity. The horizontal and vertical displacement and the volumetric strain were computed.

aiii) Conduit Benchmark

The Yang model for a slightly dipping prolate spheroid was used to benchmark the conduit. The Yang model source code cannot accept a 0 value for the angle of dip. As the SHV conduit is thought to be vertical this problem was overcome by using a value extremely close to 90○ so as to render negligible the error produced by the code. These model dimensions were then set at the dimensions of the SHV conduit for realism. The desired depth to model the top of the conduit at was -1 m (as the SHV conduit begins at the surface) but unfortunately, the Yang script did not permit using any depths above 10 m. Model parameters are as in Tables B.1 and B.2. Residuals from benchmarking of horizontal and vertical displacement and volumetric strain are shown in Figures B.1-B.3.

b) Inverse Modeling

We used the optimisation module in COMSOL 5.0 to invert for geometrical properties of conduit length l, conduit radius rc and halo radius rh, and pressure drops, and material properties of domain 2 Youngs Modulus E and domain 3 Youngs Modulus E.

The optimisation was set to minimise the objective function, which was set up as follows;

AIRS = AIRS predicted
TRNT = TRNT predicted
AIRS_strain = AIRS observed
TRNT_strain = TRNT observed
AIRS_error = 1σ error on AIRS
TRNT_error= 1σ error on TRNT

a_1=AIRS/AIRS_error
a_2= TRNT/TRNT_error

asum=a_1+a_2

$weight_1$ = a_1/asum
$weight_2$=a_2/asum

$functionweight_1$= (AIRS_strain$\times 10e^8$-AIRS$\times 10e^8 \times weight_1)^2$
$functionweight_2$= (TRNT_strain$\times 10e^8$-TRNT$\times 10e^8 \times weight_2)^2$

functionweightsum = $functionweight_1$+$functionweight_2$ (objective function).

We first inverted for geometrical properties as described above and the pressure drop. The algorithm was permitted to search for these properties within set ranges as given in Table 3.2 (main text) while material properties remained constant.

Results within our σ error for AIRS and TRNT for this inversion were selected and averaged. The average geometric properties (or within their standard deviation) were made constant in the next iteration, which then inverted for material properties within the ranges in Table 3.2 (main text). This iteration process continued until the results converged or remained within their standard deviations.

Table B.1: Analytical conduit model benchmarking parameters using the dipping prolate spheroid model according to Yang et al. [1988]

Depth (km)	Semi-Major Axis (km)	Semi-minor Axis (km)	Poisson's Ratio	Young's Modulus (GPa)	Density kg m^{-3}	Pressure Change (MPa)
0.01	0.5	0.015	0.25	8	2800	10

Table B.2: Numerical conduit model benchmarking parameters

Domain Area (km)	Depth (km)	Semi-Major Axis (km)	Semi-minor Axis (km)	Poisson's Ratio	Young's Modulus (GPa)	Pressure Change (MPa)
50×50	0.01	0.5	0.015	0.25	8	10

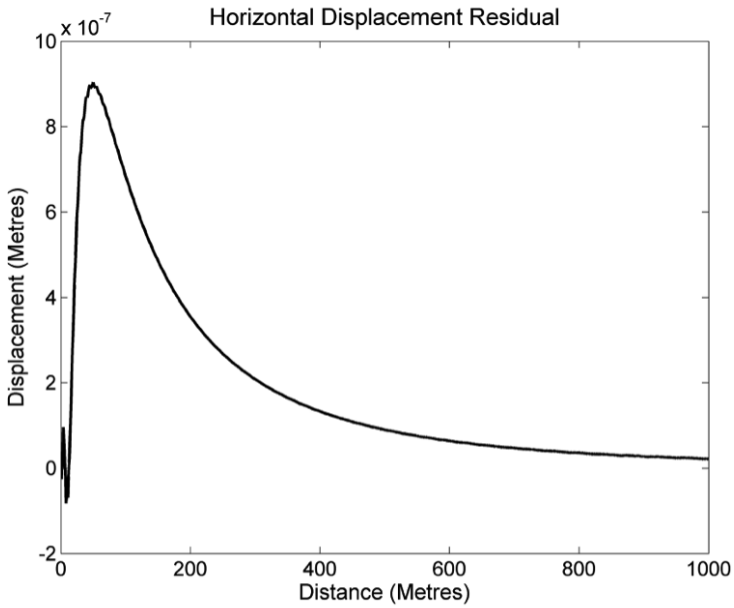

.

Figure B.1: Horizontal displacement residual

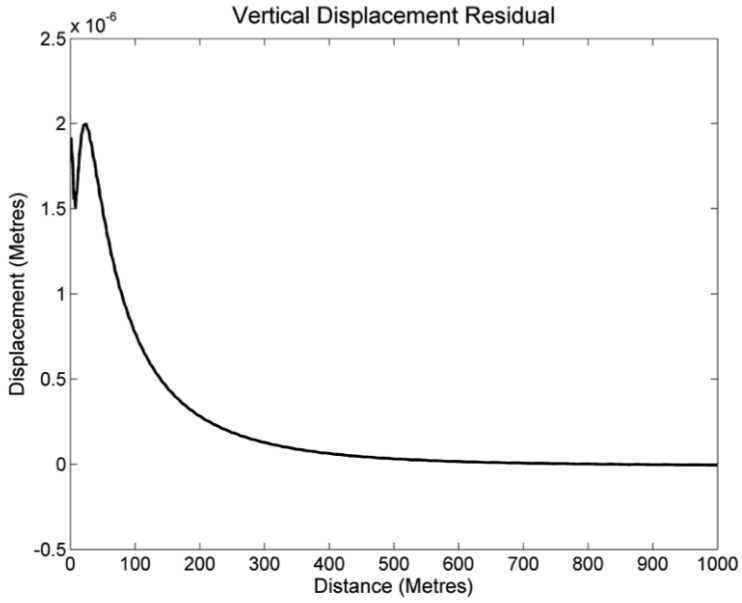

.

Figure B.2: Vertical displacement residual

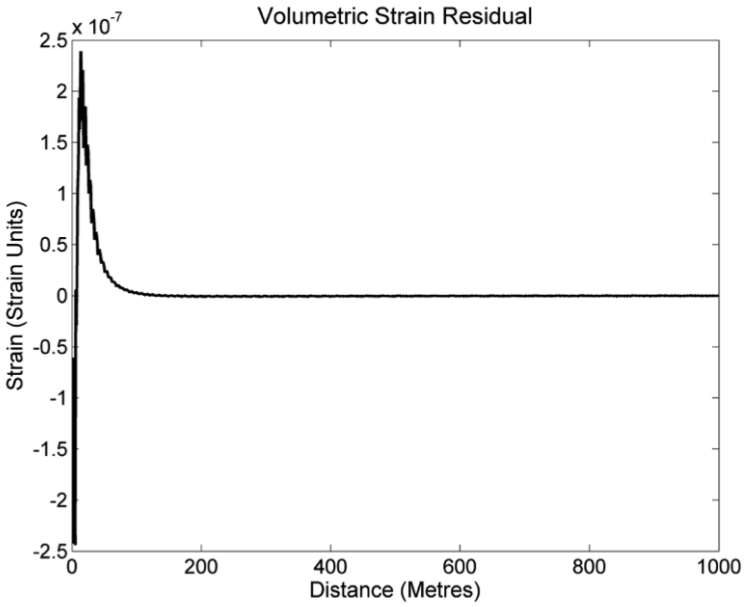

.

Figure B.3: Volumetric Strain residual

Appendix C

This appendix contains the relevant modelling parameters used in Chapter 5 which are included in the online supplements in Stephens, K. J., Ebmeier, S. K., **Young, N. K.,** & Biggs, J. (2017). Transient deformation associated with explosive eruption measured at Masaya volcano (Nicaragua) using Interferometric Synthetic Aperture Radar. *Journal of Volcanology and Geothermal Research*, 344, 212-223.

Table C.1: Model parameter sweeps performed for the homogeneous and heterogeneous domain models. E1 = whole domain Youngs modulus, and E2 = halo domain Youngs modulus.

a) Homogeneous model parameters						
Parameters	Radius (m)	Length (m)	Top depth (m)	Pressure (MPa)		E1 (GPa)
	110:10:370	200:200:3000	100:100:2300	-10		20
b) Heterogeneous model results						
Parameters	Radius (m)	Halo Radius (m)	Length (m)	Top depth (m)	Pressure (MPa)	E1 (GPa)	E2 (GPa)
	90:10:250	500	200:100:1400	10:20:1290	-10	20	5:5:15